Controlling and Monitoring Intracellular Drug Delivery Using PHPMA-Based Polymer Nanomedicines

PAR

Claudia BATTISTELLA

EPFL

ÉCOLE POLYTECHNIQUE
FÉDÉRALE DE LAUSANNE

Suisse
2017

Acknowledgments

being such good friends. I will take with me all your sincere advices and all the beautiful memories about these five years together!

I would like also to express my gratitude to special people that I met in my first months at EPFL. My sincere gratitude goes to Prof. Vassily Hatzimanikatis, for his understanding and humanity. Sylvain, Mathieu, Emrah, Gena it was a pleasure meeting you. My dear Tina and Raha, you supported me since the first day I arrived here, thanks for being the best colleagues and friends I could ever wish. And of course, Nicolas and Stéphane it was a pleasure meeting you! Thanks for all the nice moments we spent together.

Thanks also to all who have contributed in one way or another to this chapter of my life. Grazie mille to Alessandra, Fabio, Federica, Marta, Matteo, Damiano and Alice for all the nice moments we spent together in Lausanne. Thanks to Sandra for taking care of me and Tommaso and to Alexandros, Gabriella and Giuseppe for the nice chats along the MXD corridors. Of course sincere thanks also to Meriç, for your cheerfulness and for your help with Matlab! I can't forget all the friends that always made me happy during my trips back to Italy: Alessandra, Anna, Eleonora, Elena, Mariel, Michela, Chiara, Martina M., Alexandra, Martina R., Diego, Veronica, Deborah, Diletta, Laura and Francesca.

Warm thoughts go to all my family. Oscar, Silvana, Sophia, Olivia and Oscar Charles, there are not enough words to express all my gratitude for your advices, for your generosity and hospitality. You have made me feel at home since my first day in Switzerland. *Un grazie di cuore va ai miei genitori Giovanna e Alberto e a mio fratello Nicola per tutto il supporto e l' affetto. Questa traguardo lo dedico a voi!*

Finally, the most special thoughts are for Tommaso, whose help and support in these years have been fundamental. *Grazie per avermi consolata nei periodi piu difficili e per aver gioito con me nei momenti felici, per avermi insegnato che vale la pena inseguire i propri sogni e per essere la mia fonte di felicità.*

Table of contents

Summary

Polymer nanomedicine is an attractive approach for the delivery of anticancer drugs. Firstly designed to increase drug bioavailability, polymer conjugates and polymer nanoparticles have rapidly emerged in the field of cancer therapy after the discovery of the enhanced permeation and retention (EPR) effect. The leaky and disordered tumor neovascularization provides opportunities to guide the accumulation of polymer nanomedicines to the tumor tissue therefore enhancing therapy selectivity and reducing off-target-associated side effects. However, since many chemotherapeutics act on targets that are located in well-defined subcellular compartments, controlling the intracellular fate of polymer nanomedicines and/or their payload is another important factor that contributes to therapy efficiency. Polymer conjugates and polymer nanoparticles generally access the cell interior *via* endocytosis. The physiochemical and biochemical parameters that distinguish the endolysosomal compartments from the extracellular environment have been widely exploited to trigger intracellular drug release from the polymer carriers.

Amongst a range of other polymers and polymer nanoparticles that have been investigated over the past 30 years, poly(*N*-(2-hydroxypropyl) methacrylamide) (PHPMA)-based conjugates have been extensively explored for the endolysosomal release of anticancer drugs. While the modern polymer chemistry toolbox provides many opportunities to tailor the molecular weight and functionality of PHPMA and to introduce features that allow the polymer to respond to the different endolysosomal environments, the development of tools and methods to monitor these processes is also crucial for the future development of advanced delivery systems.

The aim of this Thesis is to design dual-functional PHPMA polymers that offer the possibility to control the endolysosomal release of anticancer drug combinations as well as to monitor the PHPMA endolysosomal trafficking.

Chapter 1 of this Thesis provides an overview of the different approaches that have been described in literature to control and monitor the intracellular delivery of polymer nanomedicines.

Chapter 2 describes a synthetic approach to prepare α- and α,ω-fluorine labeled pentafluorophenyl methacrylate (PPFMA) polymers *via* reversible addition fragmentation chain transfer (RAFT) polymerization. Both R- and R, Z-fluorinated chain transfer agents

(F-CTAs) will be used to introduce fluorine labels at the α- and α,ω- end groups of the polymer. These labels will be further used to investigate RAFT polymerization parameters *via* ^{19}F-NMR studies. The synthesized α-fluorinated PPFMA will serve in **Chapter 3** and **Chapter 4** as a polymer precursor for the preparation of the dual functional PHPMA polymers.

   Chapter 3 describes the preparation of a dual PHPMA conjugate for the reversion of P-glycoprotein-mediated multidrug resistance in ovarian carcinoma cells. Post-polymerization modification of the PPFMA precursor will be used to prepare a series of PHPMA conjugates carrying either the anticancer drug doxorubicin (Dox) or the P-glycoprotein inhibitor zosuquidar (Zos) or both drugs at the polymer side chains. The first part of this Chapter will investigate the feasibility of PHPMA conjugates bearing a pendant zosuquidar derivative *via* hydrazone linker to overcome doxorubicin efflux in resistant ovarian carcinoma cells. In the second part, the cytotoxic activity of the dual delivery system in which both drugs are conjugated to the PHPMA backbone *via* orthogonal cleavable linkers will be assessed.

   Finally, **Chapter 4** will study the cellular internalization and endolysosomal trafficking of PHPMA. First, the synthesis of a dual-labeled PHPMA polymer containing both a fluorescent as well as a fluorinated label will be described. Second, the fluorescent label will be used to investigate cellular internalization and endolysosomal trafficking *via* flow cytometry and confocal fluorescence microscopy, respectively. In a final step, the potential of nanoscale secondary ion mass spectrometry (NanoSIMS) to map and localize fluorine-containing polymers in cells will be assessed.

Keywords: polymer nanomedicine, PHPMA-conjugates, PPFMA, post-polymerization modification, multidrug resistance, intracellular trafficking, co-localization studies, NanoSIMS.

Riassunto

L'uso di nanomedicine di matrice polimerica rappresenta un approccio interessante per il trasporto e il rilascio controllato dei farmaci antitumorali. Inizialmente ideati per incrementare la disponibilità dei farmaci, i coniugati e le nanoparticelle di natura polimerica sono emersi rapidamente nel campo della terapia anticancro grazie alla scoperta dell'*enhanced permeation and retention (EPR) effect*. La maggiore permeabilità che caratterizza i vasi sanguigni tumorali offre infatti l' opportunità di dirigere l'accumulo dei polimeri coniugati e delle nanoparticelle nel tessuto tumorale, aumentando di coseguenza la selettività e riducendo gli effetti collaterali dei farmaci trasportati. Tuttavia, dato che molti farmaci antitumorali agiscono in target localizzati in organelli cellulari, il controllo della destinazione intracellulare del polimero e/o del farmaco trasportato è un fattore altrettanto determinante per l'efficacia della terapia. I coniugati polimerici e le nanoparticelle, in genere, vengono internalizzati dalle cellule *via* endocitosi. Di conseguenza, i parametri fisiochimici e biochimici che contraddistinguono gli endosomi e lisosomi dall'ambiente extracellulare sono stati ampiamente utilizzati per stimolare il rilascio dei farmaci dalla matrice polimerica nei compartimenti endolisosomali.

Tra una vasta gamma di polimeri e di nanoparticelle esaminati negli ultimi 30 anni, i coniugati polimerici di poli(*N*-(2-idrossipropil) metacrilammide) (PHPMA) sono stati ampiamente esplorati per il rilascio di farmaci antitumorali in risposta ai diversi ambienti che caratterizzano gli endosomi e lisosomi. Nonostante la chimica dei polimeri moderna fornisca svariate opportunità per controllare il peso molecolare e le funzionalità dei coniugati polimerici di PHPMA e per introdurre caratteristiche che permettono al polimero di rispondere ai diversi ambienti che caratterizzano endosomi e lisosomi, lo sviluppo di mezzi e metodi per monitorare questi processi sono considerati cruciali per lo sviluppo di sistemi avanzati di trasporto dei farmaci.

L'obiettivo di questa Tesi è quello di preparare polimeri bifunzionali di PHPMA per il rilascio controllato di combinazioni di farmaci antitumorali negli endosomi e lisosomi e per il monitoraggio di questi processi.

Il **Capitolo 1** di questa Tesi fornisce una panoramica dei diversi approcci che sono stati descritti in letteratura per controllare e monitorare il trasporto e il rilasco intracellulare di nanomedicine di matrice polimerica.

Il **Capitolo 2** descrive un approccio sintetico per preparare polimeri di pentafluorofenile metacrilato (PPFMA) contenete sonde fluorurate nei due gruppi terminali attraverso polimerizzazione *reversible addition fragmentation chain transfer (RAFT)*. Due *chain transfer agents* fluorurati (F-CTAs) contenenti una sonda nel gruppo R, o in entrambi i gruppi R e Z, saranno utilizzati per introdurre le sonde fluorurate in entrambi i gruppi terminali α e α,ω del polimero. Queste sonde saranno poi utilizzate per determinare i diversi parametri della polimerizzazione RAFT attraverso studi di ^{19}F-NMR. Il PPFMA analogo contenente la sonda fluorurata in posizione α sarà successivamente utlizzato nei capitoli **Capitoli 3** e **4** di questa Tesi come precursore per la preparazione dei polimeri bifunzionali di PHPMA.

Il **Capitolo 3** descrive la preparazione di un PHPMA bifunzionale per evadere i meccanismi di resistenza multifarmaco in cellule di carcinoma ovarico resistenti attraverso l'inibizione della P-glicoproteina. Il precursore polimerico PPFMA sarà modificato al fine di sintetizzare una serie di coniugati contenenti il farmaco antitumorale doxorubicina (Dox), o l'inibitore della P-glicoproteina zosuquidar (Zos) o una combinazione dei due farmaci. La prima parte di questo capitolo investigherà l'abilità dei coniugati di PHPMA contenenti un derivato di zosuquidar coniugato attraverso un linker di idrazone, di minimizzare l'efflusso di doxorubicina dalle cellule di carcinoma ovarico resistente. Nella seconda parte invece, sarà investigata l'attivita citotossica del polimero contenente la combinazione dei due farmaci collegati attraverso linkers ortogonali.

Infine, il **Capitolo 4** studia l'internalizzazione cellulare e il *trafficking* nel tratto endolisosomiale di un polimero di PHPMA. In un primo step, sarà descritta la sintesi di un PHPMA bifunzionale contenente sia una sonda fluorescente che una fluorurata. Successivamente, la sonda flurescente sarà usata per investigare l'internalizzazione cellulare del polimero e il *trafficking* endolisosomiale utilizzando citometria a flusso e microscopia di fluorescenza. Lo step finale consisterà nel dimostrare il potenziale di *nanoscale secondary ion mass spectrometry (NanoSIMS)* di mappare e localizzare polimeri fluorurati nei compartimenti endolisosomiali.

Parole chiave: nanomedicine polimeriche, coniugati polimerici di PHPMA, PPFMA, modificazione post-polimerizzazione, resistenza multifarmaco, trafficking intracellulare, studi di colocalizzazione, NanoSIMS.

1. Controlling and Monitoring Intracellular Delivery of Anticancer Polymer Nanomedicines

1.1. Introduction

Conventional chemotherapeutic agents are small molecule drugs that once administered diffuse throughout the body without any particular selectivity toward the tumor. As a consequence, the use of such drugs is limited, in terms of dose and frequency, by the onset of severe side effects. In order to achieve a balance between proper dose, generating the desired response and tolerable adverse effects, strategies that allow to deliver chemotherapeutics with a higher selectivity toward the tumor are needed. Polymer nanomedicine has emerged as an attractive approach to enhance the efficacy of small molecule therapeutics for the treatment of cancer and beyond.[1] Polymer conjugates and polymer nanocarriers can help to prevent rapid renal clearance and recognition from the reticuloendothelial system (RES) thereby increasing plasma half-life and drug bioavailability.[1,2] Another asset of the use of polymers and polymer nanoparticles for the delivery of cancer chemotherapeutics is that it allows passive tumor targeting by the enhanced permeation and retention (EPR) effect.[2,3] The EPR effect was discovered by Maeda *et al*. who recognized the rapid and disordered tumor neovascularization, together with the defective or absent lymphatic drainage of solid tumors, as an attractive way to selectively and passively deliver macromolecules to the cancer tissue.[3]

The most common route for polymers, polymer nanoparticles, or nanomaterials in general, to be internalized by cells is *via* clathrin-mediated endocytosis.[4,5] This pathway, which uses dynamic vesicles that transport the cargo from the plasma membrane to the cell inward, begins with the engulfment of the cargo in the cell membrane. This can occur as a consequence of specific ligand targeting, as in the case of receptor-mediated endocytosis, or *via* a nonspecific adsorptive mechanism. The thus formed intracellular vesicles, which are called early endosomes and characterized by slightly acidic pH, represent the main cargo sorting station. The internalized material can either be recycled

to the cell membrane or shuttled from early endosomes to the more acidic late endosomes before finally being sorted to the lysosomes, where enzymatic digestion occurs.[6,7] To further enhance the selectivity toward the cancer cells and to maximize cellular internalization, polymer-based delivery systems have been decorated with targeting ligands that bind to receptors that are overexpressed by cancer cells.[8] The folate receptor is frequently used as target since it is overexpressed in the plasma membrane of several types of cancers such as epithelial, ovarian, cervical, breast, lung, kidney, colorectal, and brain.[9] The decoration of nanoparticles, micelles and linear polymers with folic acid (FA) has been shown to result in enhanced intracellular accumulation in folate positive cell lines as compared to the receptor-negative cells.[9-11] The $\alpha_v\beta_3$ integrin is another receptor that is frequently targeted and exploited to enhance cellular internalization by decorating delivery systems with the arginine-glycine-aspartic acid (RGD) tripeptide ligand.[12-14] A third example of a receptor that is exploited for tumor targeting is the epidermal growth factor receptor (EGFR), which is generally overexpressed and therefore used in the treatment of neck cancer, glioblastoma and lung adenocarcinoma.[15] To this purpose, antibodies, aptamers and peptides were designed as targeting ligands.[16,17] Targeting the human epidermal growth factor receptor-2 (HER2) *via* the monoclonal antibody Trastuzumab has been reported to facilitate breast cancer cellular internalization of block copolymer micelle-based nanoparticles as well as polyplexes.[18,19] Upregulation of the transferrin receptor in pancreas, colon, lung and bladder cancers was also exploited using transferrin-nanoparticle and linear polymer conjugates,[20-23] as well as transferrin-modified polyplexes.[24] Another example of a ligand used for prostate and lung cancer targeting is anisamide, which binds to the overexpressed sigma receptor.[25-27]

Efficient tumor targeting and cellular internalization are important to maximize the efficacy of anticancer drugs and reduce side effects. Another important factor that determines drug action is intracellular transport. This is due to the fact that many drugs act on targets that are located in well-defined subcellular compartments. The aim of this chapter is to give an overview of the different approaches that have been developed to control intracellular delivery of polymer nanomedicines and to present the methods that can be used to monitor these processes. While a range of other nanomaterials, including inorganic or metal nanoparticles or liposomes are also intensively used as carriers in nanomedicine, this chapter will exclusively focus on polymers and polymer nanoparticle-based nanomedicines. The remainder of this chapter will first describe the advances that have been made in the field of polymer nanomedicine to enhance delivery to specific

subcellular targets. The second part of this chapter will present an overview of techniques that have been used to monitor intracellular trafficking of polymer nanomedicines.

1.2.   Controlling intracellular delivery

This part of this chapter will provide an overview of the different strategies that have been developed to guide delivery of polymer nanomedicines to specific subcellular compartments. In what follows below, first, the various approaches that have been used to enhance access to the cytosol will be summarized. After that, strategies will be described, which have been elaborated to target specific organelles including the mitochondria, the nucleus as well as the Golgi apparatus (GA) and endoplasmic reticulum (ER). A schematic illustration of the different approaches reported to control intracellular delivery is shown in **Figure 1**.
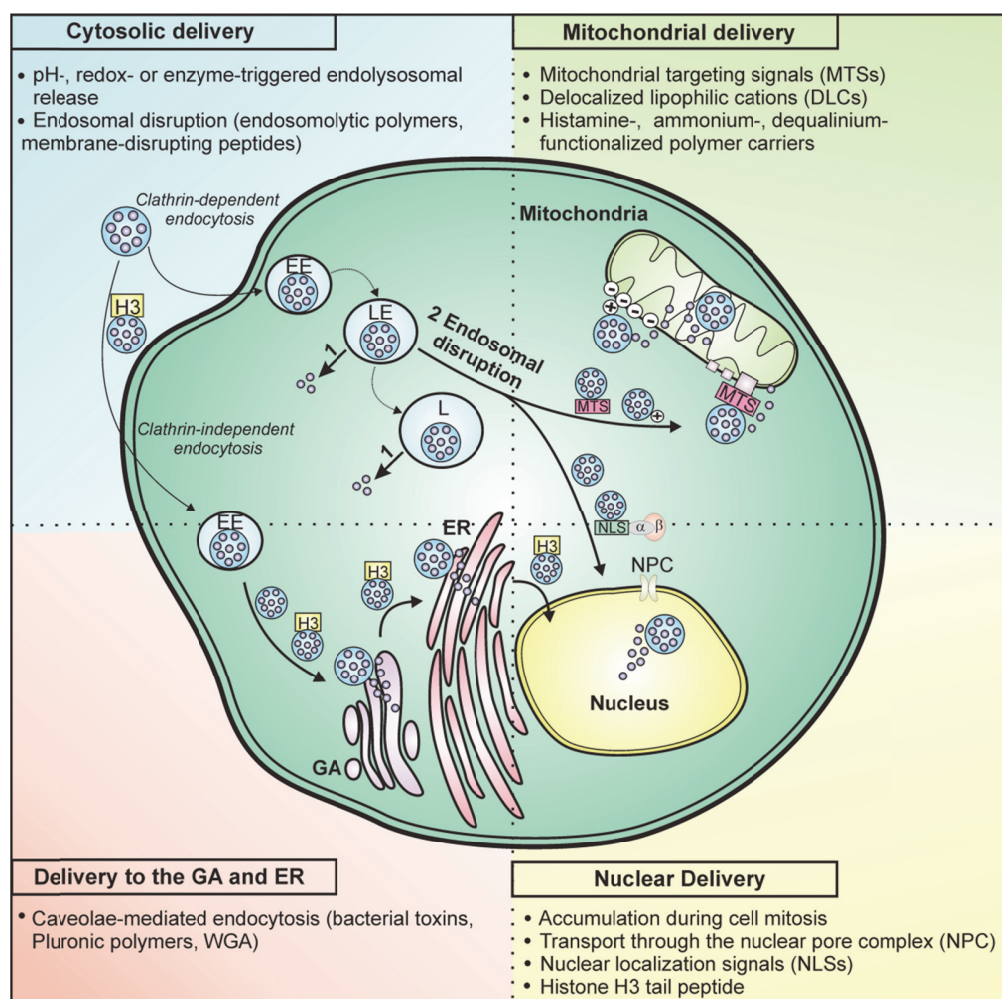
Figure 1. Schematic overview of approaches that have been developed to control intracellular delivery of polymer nanomedicines. After clathrin-mediated endocytosis, the environment of early endosomes (EE), late endosomes (LE) and lysosomes (L) can be exploited to trigger drug release into the cytoplasm (**1**) or to promote endosomal escape (**2**) with consequent accumulation of the delivery system in the cytoplasm. Internalization of polymer nanomedicines *via* clathrin-independent mechanisms has been used to deliver cargo to Golgi apparatus (GA) and endoplasmic reticulum (ER) and more recently to the nucleus by using histone H3 tail peptide-functionalized polyplexes.

1.2.1. Cytosolic Delivery

Endocytosis represents a very attractive strategy to facilitate cellular internalization of polymer nanomedicines. The entrapment of polymers or polymer nanoparticles in intracellular endosomal compartments, however, also presents an additional barrier that needs to be overcome in order to deliver the drug to the appropriate target site in the cell. In addition to the fact that the membrane of these intracellular vesicles (endosomal and lysosomal) prevents translocation to the cytoplasm, lysosomal accumulation may also result in enzymatic degradation of therapeutic cargo. **Table 1** provides an overview of the different approaches that have been explored to enhance cytosolic delivery. The different approaches can be organized in two main classes. One group of approaches are those that involve release of the drug in the endosomes or lysosomes by taking advantage of specific environmental parameters (pH, redox, enzyme) in these compartments. While other stimuli, such as UV-light can also be used, **Table 1** only lists those strategies that explore endogenous stimuli that are characteristic of the intracellular (micro)environment. The second class of approaches focuses on disrupting the endosomal membrane using endosomolytic polymers, either alone or in combination with membrane-disrupting peptides. The entries in **Table 1** are organized according to the mechanism that is exploited to trigger endolysosomal release or endosomal disruption. For each of these mechanisms, **Table 1** lists a number of functionalities that have been incorporated in the polymer conjugates and polymer nanoparticles and which have been successfully used to mediate endolysosomal release or endosomal disruption. For several of the functionalities listed in **Table 1**, however, the number of examples that have been reported in the literature is too numerous to be included. Therefore, for each functionality, **Table 1** cites several key review articles as well as selected examples, some of which are highlighted in the text below.

Table 1. Overview of the various strategies that have been explored to enhance cytosolic delivery of polymer nanomedicines.

Mechanism	Intracellular location	Functionality	Examples	
pH	Endosomes/Lysosomes	**Acetal**		28,29,30,31,32,33
			Linear polymers	34,35,36
			Micelles	37
			Polymersomes	38,39
			Nanoparticles	40
		Ortho ester		28,30,31
			Micelles	41,42
			Polymersomes	43
		Imine		28,30,31, 32
			Micelles	44,45,46,47
		Oxime		29,30,32
			Nanoparticles	48
			Micelles	49,50
		Cis-aconityl		28,31,33
			Micelles	51
			Nanoparticles	52
		Hydrazone		29,33,28,30,31,32
			Linear polymers	53,54,55,56,57,58,59,60
			Nanoparticles	10,61
			Dendrimers	62,63
			Micelles	64,65,66,67,26,68
Enzyme	Lysosomes	**GFLG**		69,33,29,
			Linear polymers	70,71,72,73,74,75 76,77,78,79
			Dendrimers	80,81,82,83
			Micelles	84,85
			Polymersomes	17
Redox	Endosomes/Lysosomes/ Cytoplasm	**Disulfide**		33,86
			Linear polymer	87,88
			Micelle	89,90,91,92,93
			Polymersomes	94,95,96
		α,β-unsaturated carbonyl	Micelles	97
		Selenium-based compounds		98,86
			Nanogels	99
			Micelles	100,101

*(Leftmost rotated label spanning all rows: **Endolysosomal Release**)*

Table 1. (Continued).

Mechanism		Intracellular location	Functionality	Examples	
Endosomal Disruption	**Endosomolytic polymers**	Endosomes/Lysosomes	**Positive charges**		102
				Linear polymers	103,104,105,106,107,108,109,24, 110,111,112,113,114,115,116
				Branched polymers	104,117,118,119,109,24,115,120
				Dendrimers	121,122,123, 124,125,109
			Charge-reversal		102
				Linear polymers	22,126,127,11,128,129
				Micelles	130,131,132,133,134
				Dendrimers	135
			Volumetric expansion	Nanoparticles	136
	Membrane-disrupting peptides	Endosomes/Lysosomes	**N-terminal HA2 peptide derivative**		137
				Linear polymers	21
			INF-7 peptide	Linear polymers	138,139
			GALA	PEGylated liposomes	23
				Dendrimers	123
			KALA	Micelles	140
				Nanoparticles	112
			HIV gp41 derivative	Branched polymers	141
			Melittin	Linear polymers	142,143

1.2.1.1. Endolysosomal Release

This approach involves the use of polymer conjugates or polymer nanoparticles, which are stable in the blood stream but allow rapid drug release in the endolysosomal environment. The use of stimuli responsive carriers is particularly suitable for the delivery of small molecule drugs since after release from the carrier, these molecules can passively diffuse through the endolysosomal membrane and reach the cytoplasm. There is a number of physiochemical (pH, glutathione concentration) and biochemical (enzymes) parameters that differentiate the endolysosomal from the extracellular environment and which have been explored to trigger drug release.[29,33] In what follows below, the use of pH, enzyme and redox responsive polymer conjugates and polymer nanoparticles to trigger endolysosomal release will be discussed.

pH-triggered release. Acid-labile chemical bonds that are stable in the bloodstream (pH 7.4) but upon endocytic internalization are cleaved in the slightly acidic late endosomal (pH 5-6) and lysosomal (pH 4-5) environments, have been used to promote endolysosomal release.[28,30,31] Among the different pH sensitive linkers, which are available, such as acetal/ketal,[28-40] ortho ester,[28,30,31,41-43] imine,[28,30-32,44-47] oxime[29,30,32,48-50] and cis-aconityl,[28,31,33,51,52] the hydrazone linker[28-33] is the most widely used.[30] In order to illustrate the various possibilities in which the pH-responsiveness of these linkers can be used to enhance endolysosomal drug release, some examples of hydrazone-based polymer nanomedicines will be highlighted here. Hydrazone-linked polymer nanomedicines can be obtained by coupling ketone or aldehyde functional drugs to hydrazide modified polymers or polymer nanoparticles, or *vice versa*. Doxorubicin (Dox) is a particularly attractive candidate for the preparation of pH sensitive polymer nanomedicines as it contains a ketone group. Both linear poly(*N*-(2-hydroxypropyl)methacrylamide) (PHPMA) as well as poly(amidoamine) (PAMAM) dendrimers modified with hydrazide groups have been used to couple Dox *via* hydrazone linkers.[31,53-58,60,62,63] HPMA polymers bearing hydrazone linkages have also been explored for the delivery of other anticancer drugs such as paclitaxel and docetaxel.[59] The hydrazone motif has also been used to prepare micelles and nanoparticles that allow pH-dependent release of doxorubicin as well as other anticancer drugs.[32,66,67] For instance, Dox has been coupled to poly(ethylene glycol) (PEG)-folic acid (FA) conjugates to generate hydrophobically modified PEG derivatives that self-assembled into nanoparticles, which showed an enhanced Dox release at pH 5 as compared to pH 7.4.[10] Instead of using the hydrazone bond to couple the drug to a polymer carrier, this pH sensitive motif can also be used to connect the hydrophobic and hydrophilic segments of amphiphiles that are designed to self-assemble into polymer micelles or nanoparticles. Cleaving the hydrazone bond in the endolysosomal compartments lead to dissociation of these nanoparticles and concomitant release of the entrapped drug.[26,32,33,64,65] Another interesting example are sub 200-nm polymeric nanoparticles that are designed to simultaneously deliver doxorubicin and docetaxel. These particles were obtained *via* self-assembly of the aliphatic copolymer poly(butylene succinate-*co*-butylene dilinoleate) (PBS-*co*-PBDL) and a hydrophobically modified HPMA copolymer. The hydrophobic drug docetaxel (DTX) was physically entrapped within the (PBS-*co*-PBDL) core and the hydrophilic doxorubicin hydrochloride (Dox·HCl) was chemically conjugated to the HPMA copolymer shell *via* a hydrazone bond. This strategy enabled the combination chemotherapy by the simultaneous Dox and DTX delivery.[61]

Enzyme-triggered release. Cathepsin B is a cysteine protease, which is upregulated in tumors and located in the lysosomes.[69] This provides opportunities for the design of polymer nanomedicines that release their payload in the lysosomes.[29,33,69] Kopecek and co-workers first reported the design of Dox-modified HPMA copolymers in which the pendant doxorubicin groups were linked to the polymer backbone *via* the GFLG peptide spacer, which is a substrate for cathepsin B.[70,71,74] The authors showed that release of Dox in the lysosomes, in relatively close proximity to the nucleus allowed to reduce P-gp-mediated drug efflux.[77] The same concept was applied to prepare HPMA copolymers that were modified with other anticancer drugs such as cisplatin[73] as well as paclitaxel and gemcitabine.[75] In addition to a number of other linear PHPMA conjugates,[76,78,79] the GFLG peptide linker has also been used to develop micellar-[84,85] and dendrimer-based carriers that are able to release their payload in the lysosomes.[80-83] The GFLG peptide linker has not only been used to trigger cathepsin B-mediated drug release from various polymer-based systems, but has also been exploited to prepare polymersomes that disintegrate upon exposure to this enzyme. This was accomplished by Lee *et al*. who used this peptide to connect PEG and poly(D,L-lactide) to form diblock copolymers, which could self-assemble to form polymersomes with an average size 124 nm. Complete release of the encapsulated model fluorescent dye was observed after incubation with cathepsin B for three days. The result was confirmed with *in vitro* cell studies using fluorescence microscopy.[17]

Redox-triggered release. Redox-responsive delivery systems have been extensively explored for the endolysosomal release of anticancer drugs. This approach takes advantage from the highly reducing environment of cell cytoplasm, nucleus and endolysosomal pathway as compared to the extracellular matrix and circulation system.[33,86] Disulfide bonds are most frequently used for the development of redox responsive delivery systems as they are readily cleaved intracellularly. Cuchelkar *et al*., for example, prepared linear HPMA polymer conjugates in which the drug was conjugated to the polymer backbone *via* disulfide linker.[87,88] Similarly, Cao *et al*. designed poly(ethylene glycol)-*b*-poly(lactic acid) copolymer (PEG-*b*-PLA) micelles in which the drug curcumin was conjugated to the polymer chains *via* a disulfide bond. The redox-sensitive micelles could enhance curcumin delivery while avoiding premature release as compared to control micelles containing an ester linker.[89] Poly(ethylene glycol)

methyl ether methacrylate-*b*-poly(2-hydroxyethyl methacrylate), in which the poly(2-hydroxyethyl methacrylate) segment was modified with 3-(pyridin-2-yldisulfanyl)propanoic acid (PDP) (PEGMEA-*b*-PDPHEMA), allowed the linkage of paclitaxel *via* esterification reaction and subsequent self-assembly of the amphiphilic copolymer into micelles.[91] While the disulfide bond has been mostly used, another interesting motif that can be used to prepare redox-responsive polymer nanomedicines is the α,β-unsaturated carbonyl group. In a recent example, Shi *et al.* used this motif to couple a 6-mercaptopurine (6-MP) prodrug to poly(ethylene glycol) monomethyl ether. In water, these drug conjugates self-assemble to form micelles. Drug release from these micelles occurs upon the influence of glutathione and proceeds *via* a Michael addition-elimination pathway.[97] In addition to using the reducing intracellular environment to trigger drug release, the elevated intracellular glutathione concentration can also be exploited to induce disassembly of polymer-based carriers.[33,86] As an example, Liu *et al.* described self-assembled micelles based on a disulfide linked poly(methacrylic acid)-*b*-poly(ε-caprolactone) copolymer (PMAA-*b*-PCL-SS-PCL-*b*-PMAA), which were used for paclitaxel delivery.[92] Hubbell *et al.* prepared reduction-sensitive polymersomes, which were based on PEG-SS-poly(propylene sulfide) (PEG-SS-PPS) diblock copolymers and quickly disrupted inside cells leading to fast release of the cargo.[95] Poly(ethylene glycol)-*b*-poly(L-lysine)-*b*-poly(ε-caprolactone) triblock copolymers bearing a disulfide bond (PEG-*b*-PLL-SS-PCL) have also been used for the formation of redox responsive polymersomes. These polymersomes were stable in physiological solution (pH 7.4), whereas they readily disintegrated under a reductive environment similar to the intracellular one. Both the hydrophobic camptothecin (CPT) and the hydrophilic doxorubicin hydrochloride (Dox·HCl) could be loaded in the polymersome membrane and in the aqueous core, respectively.[96] Selenium-based compounds have been also used recently to promote carrier disassembly as a response to glutathione as well as reactive oxygen species (ROS) such as hydrogen peroxide.[86,98] For instance, Yan and co-workers designed an amphiphilic hyperbranched polymer alternating hydrophobic selenide groups and hydrophilic phosphate segments in the dendritic backbone. These polymers self-assembled in water to form core-shell micelles, which could incorporate the anticancer drug doxorubicin. Upon exposure to the intracellular oxidative microenvironment of cancer cells, the selenide groups were converted into hydrophilic selenone moieties. The transition from amphiphilic hyperbranched precursor to hydrophobic one caused rapid micelles disassembly and drug release. The cytotoxicity of this system was ascribed to both the release of Dox and the release of selenium derivatives which can induce

14

apoptosis.[101] In addition to serving as reduction sensitive linkers, that can facilitate intracellular drug release or the cleavage of amphiphilic block copolymers that act as the constituents of micellar nanoparticles or polymersomes, redox responsive bonds have also been explored as reversible crosslinkers.[33,93] Zou *et al.*, for instance, prepared polymersomes from poly(ethylene glycol)-*b*-poly(trimethylene carbonate-*co*-dithiolane trimethylene carbonate) (PEG-*b*-P(TMC-DTC)) block copolymers. The addition of a catalytic amount of DTT promoted the formation of stable particle cores due to disulfide crosslinking. Upon cellular internalization, disulfide bond cleavage allowed disassembly of the polymersomes and drug release.[94] Based on the same principle, biodegradable poly(ethylene glycol)-*b*-poly(dithiolane trimethylene carbonate) (PEG-*b*-PDTC) block copolymer micelles were also prepared. Interestingly, doxorubicin (DOX)-loaded micelles showed high stability, minimal drug leakage, long circulation time and triggered drug release inside the tumor cells. [90] In addition to disulfide bond, the diselenide linker has also been used to prepare reversible crosslinked polymer nanoparticles. Deepagan *et al.*, for instance, prepared diselenide-crosslinked micelles by using selenol-bearing triblock copolymers consisting of PEG and polypeptide derivatives. Upon Dox incorporation in the hydrophobic core, diselenide crosslinks were formed in the micelle shell. Exposure of these micelles to reactive oxygen species (ROS) resulted in cleavage of the hydrophobic diselenide bond into hydrophilic selenic acid derivatives and consequent Dox release. These diselenide cross-linked micelles were found to deliver up to 3.73-fold higher amount of Dox in mice tumor as compared to non-crosslinked micelles.[100] The diselenide group was also used for the redox responsive PEGylated poly(diselenide-phosphate) nanogels. While the polyphosphate block cross-linked by hydrophobic diselenide bonds formed the inner core, the PEG chains constituted the outer shell. Interestingly, these nanogels were found to be intrinsically cytotoxic toward cancer cells. This effect was attributed to the presence of overexpressed reactive peroxides and gluthatione in cancer cells.[99]

1.2.1.2. Endosomal disruption.

Endosomal disruption and cytoplasmic release are fundamental prerequisites for the delivery of peptide-based drugs as well as plasmid DNA and oligonucleotides,[102,137] Inefficient cytoplasmic release of these biological drugs can result in accumulation in the highly degradative lysosomal environment and have a negative impact on the therapeutic

efficacy.[102] As a consequence, considerable efforts have been made to develop strategies that facilitate endosomal escape of polymer nanomedicines. These efforts can be broadly categorized in two groups (**Table 1**). One approach involves the use of polymers that possess intrinsic endosomolytic properties. A second strategy is based on the functionalization of the polymer or polymer nanoparticles with membrane-disrupting peptides. In what follows below, a number of examples of both of these two strategies will be described.

Endosomolytic polymers. Endosomolytic polymers are generally cationic polymers that are able to interact and destabilize endolysosomal membranes.[102] Poly(L-Lysine) (PLL) and poly(ethylenimine) (PEI) are the first examples of amino-functionalized polymers carriers used to enhance endosomal escape of plasmid DNA and oligonucleotides.[102-106] Other amine functionalized polymers that have been widely used to provide cytosolic release of oligonucleotides and pDNA were PAMAM and poly(propyleneimine) (PPI) dendrimers.[102,121-125] PEI has been proposed to act *via* the proton sponge effect.[102,137] According to this hypothesis, PEI, and more in general polymers that contain a large number of secondary and tertiary amine groups with pKa values between physiological and lysosomal pH, can be protonated in the endosomal environment. Hence, upon endocytic internalization, the increased polymer positive charges give rise to buffering of the endosomal pH inducing ion and water influx into the endosomal vesicles with consequent osmotic swelling. This, together with carrier swelling due to electrostatic repulsions, leads to vesicle rupture and release of the cargo into the cytoplasm.[102,137] The *in vivo* implementation of PLL and PEI-based delivery systems, however, has been hampered by two limitations. First, PLL failed to provide satisfactory endosomal escape due to the lack of buffering capacity.[102] Second, *in vitro* and *in vivo* studies revealed significant toxicities of both PLL and PEI.[109,115,120,144] PAMAM and PPI dendrimers have also been shown *in vitro* and *in vivo* to be cytotoxic and hemolytic.[121] A number of approaches has been proposed to reduce the cytotoxicity of PLL and PEI and enhance transfection efficiency. First, to shield the positive charges and to reduce toxicity, the grafting of PEG chains on PEI and PLL,[24,107,111,112] as well as the modification of PLL with PHPMA was explored.[114] Another strategy involves the preparation of PEI polymers that are reductively degradable inside cells minimizing the risk of interactions with cellular components. This was achieved using disulfide cross-

linked low molecular-weight linear PEI carriers. The use of this polymer led to a cell viability of 90% after the transfection process.[108] The linkage of PEI and PEG chains *via* disulfide bond was also proposed as a strategy to further reduce cytotoxicity and increase transfection efficiency.[110] The same principle was used to prepared PLL-*b*-HPMA block copolymers containing redox-responsive disulfide bond.[113,116] Derivatization of the PEI amine groups was also investigated. In particular, it was found that *N*-acylation of PEI with alanine nearly doubled its transfection efficiency and also lowered its toxicity.[117] A similar result was obtained upon partial acetylation of PEI amine functionalities with acetic anhydride.[118,119] The limited buffering capacity of PLL and the cytotoxicity of PLL and PEI have stimulated the development of alternative polymers that are neutral at physiological pH, but become charged once internalized *via* the endolysosomal pathway. Poly(L-histidine) or in general, imidazole-rich polymers, micelles and nanoparticles have found interest since the pKA of the imidazole group (6.15) allows a rapid transition from an uncharged state in the extracellular milieu to a positively charged state upon endocytic internalization.[22,102,126,127,130,132,133] Another strategy that has been pursued is to mask positively charged groups with another functionality that is cleaved under acidic conditions and restore the positive charges. In one example, the primary amine groups of PLL were amidized with 1,2-dicarboxylic-cyclohexene anhydride. The negatively charged polymer showed low toxicity as well as low interaction with the cell membrane. Upon endocytic internalization and lysosomal accumulation, the acidic pH caused cleavage of acid β-carboxylic acid-amide bond and restoration of the positively charged lysine amine groups.[11] Kataoka and co-workers developed a series of charge-reversal delivery systems that were used to deliver pDNA and small interfering RNA (siRNA). In one example, polyplexes assembled from poly(aspartamide) derivatives bearing 1,2-diaminoethane side chains and pDNA were designed. While at physiological pH the flanking diamino groups on the polymer chains were found in a monoprotonated gauche form and showed minimal membrane interaction, upon endocytic internalization, the drop in pH caused a transition to a diprotonated anti form. Interaction of the amine groups with endosomal membrane led to cytoplasmic cargo release.[129] In a following work, the same authors, designed a diblock copolymer composed of poly(ethylene glycol) and a polyaspartamide derivative containing a pH cleavable 2-propionic-3-methylmaleic (PMM) amide as an anionic protective group in the side chains. The PMM-based polymer was incorporated into calcium phosphate nanoparticles together with small interfearing RNA (siRNA) for the formation of sub-100 nm size PEGylated hybrid micelles. The

lower endosomal pH allowed cleavage of the PMM side chain groups with consequent exposure of the membrane destabilizing polyaspartamide and cytosolic delivery.[134] Stayton *et al.* explored another strategy to develop polymers that are hydrophilic and have a net neutral charge under physiological conditions, but rapidly protonate and switch into an endosomolytic state upon endocytic internalization. A series of well-defined block copolymers containing 2-(dimethylamino)ethyl methacrylate (DMAEMA) as a siRNA-condensing block and an endosomolytic block incorporating DMAEMA, propyl acrylic acid (PAA) and butyl methacrylate (BMA) (DMAEMA-*b*-DMAEMA-*co*-PAA-*co*-BMA) was prepared. At physiological conditions the endosomolytic block is a hydrophilic polyampholyte containing both positive and negative charges. However, upon internalization, the drop in pH causes protonation of the acrylic acid residues resulting in the formation of a hydrophobic polycationic polymer able to interact and disrupt the endosomal membranes.[128] As for other cationic polymers, in order to avoid unspecific interaction and minimize the cytotoxicity of positively charged PAMAM, charge-reversal poly(amidoamine) dendrimers, that are uncharged in the extracellular milieu, but shifts to a positively charged state upon endocytic internalization, were also proposed.[135]

Membrane-disrupting peptides. In addition to the use of polymer or polymeric nanoparticles that possess intrinsic endosomolytic properties, a second strategy that has been used to facilitate cytosolic delivery is to functionalize the polymer or particle of interest, which may or may not possess endosomolytic properties by itself, with a membrane-disrupting peptide. This class of peptides mimics the natural endosomal escape properties of viruses and are usually peptide sequences that are based upon or derived from the respective viral membrane subunits.[137] Among the variety of peptides that has been proposed as membrane destabilizing agents, this section will only focus on those sequences that have been used in combination with polymers to enhance or impart endosomolytic properties.

In order to enhance PLL-mediated gene delivery, Wagner and co-workers conjugated PLL-modified transferrin to a peptide sequence derived from the N-terminus of the influenza HA2 subunit.[21] While the transferrin ligand was used as receptor-binding module to promote receptor-mediated endocytosis, the PLL acted as pDNA binding site and as endosomolytic polymer. The conjugation with the influenza-derived peptide maximized endosomal destabilization in a pH-dependent manner. The construct resulted

in a substantial increase of the transferrin-mediated gene transfer. Similarly, Funhoff *et al*. conjugated an influenza-derived fusogenic peptide (INF-7) to copolymers of (2-methyl-acrylic acid 2-((2-(dimethylamino)-ethyl)-methyl-amino)-ethyl ester) (DAMA), 2-dimethylamino-ethyl ester 1-methyl-2-(2-methacryloylamino)-ethyl ester (HPMA-DMAE) or DMAEMA with the amino side chain functional monomer *N*-(3-aminopropyl) methacrylamide hydrochloride (NAPMAm) using *N*-succinimidyl 3-(2-pyridyldithio)propionate (SPDP) as coupling agent.[138] The peptide-decorated polyplexes enhanced transfection activity while maintaining a similar toxicity. The INF-7 peptide was also used for the decoration of poly(3-guanidinopropyl methacrylate)-based polyplexes and resulted in two fold increase in transfection efficiency.[139] Szoka *et al*. designed a 30 amino acid synthetic peptide (GALA), which contains the EALA repeat unit and can interact with lipid bilayers in a pH-dependent manner. The membrane activity of this peptide is due to the fact that it can undergo a transition from a random coil at pH 7.4 to an amphipathic α-helix at pH 5.[145] The capability of this peptide to mimic pH-dependent virus-membrane interactions has been exploited to facilitate cytoplasmic delivery in several reports. Sasaki *et al*., for example, loaded pDNA inside PEGylated transferrin-liposomes to form core shell nanoparticles. Cholesterol-GALA, which inserted in the liposome membrane, and PEGylated GALA, constituting the outer shell, were used to induce interaction and fusion between liposomes and endosome membranes.[23] Due to its negative charge, GALA is not able to bind electrostatically plasmid DNA or oligonucleotides. However, by replacing several of the negatively charged glutamic acid residues by positively charged lysine amino acids, Szoka *et al*. prepared a peptide that is referred to KALA and which combines membrane-disrupting activity with the ability to form polyplexes with DNA and oligonucleotides.[145] In one example, KALA was used to coat the surface of PEG-*g*-PLL-DNA polyplexes *via* ionic interactions. The decoration of the polyplexes with KALA peptide allowed higher transfection efficiency.[112] In a following work, KALA was used to form polyelectrolyte complex micelles with PEG-oligonucleotide conjugate. The anionic oligonucleotide, interacting with KALA, constituted the inner shell, while the outer corona was formed by the PEG chains. The micelles enhanced oligonucleotide uptake as well as transfection efficiency.[140] Another peptide that has been used to enhance cytoplasmic release is derived from the HIV gp41 envelope glycoprotein.[137] In particular, linkage of this peptide to PEI-based polyplexes allowed higher transfection efficiency as compared to unmodified polyplexes. This result was attributed to the enhanced endosomal membrane

destabilization, which was confirmed *via* confocal microscopy imaging.[141] A final example of a peptide that has been conjugated to polymer carriers to improve endosomal release is Melittin (MLT). MLT does not derives from viruses, but is the main active component of the bee venom and has a pH independent membrane lytic activity *via* membrane pore-formation.[137] The ability of this peptide to interact and disrupt membranes at physiological pH limits its application. In an attempt to decrease the cytotoxicity and confine the membrane-disrupting properties at the endosomal level, the conjugation to polymeric carriers was explored. To this purpose, MLT was linked to a HPMA-*b*-PLL copolymer. The system efficiently condensed DNA into 100-200 nm particles and resulted in higher transfection efficiency compared to control polymers lacking MLT.[142] MLT was also used to potentiate the endosomolytic efficiency of 2 different poly(amidoamine)s. The authors hypothesized that the use of a carrier system could partially shield the peptide and therefore reduce its haemolytic activity. However, although MLT conjugation was beneficial for endosomal disruption, at least for one of the conjugates, its haemolytic activity at pH 7.4 was still considered unacceptable.[143]

1.2.2. Organelle specific delivery

A large number of active compounds act on intracellular targets that are located in specific organelles. To direct the transport of polymer-based nanomedicines towards specific organelles, a number of approaches have been developed. One possibility is to decorate the polymer-based carrier with specific functional groups that promote targeting of the organelle of interest. An alternative strategy, which is used to target the Golgi apparatus (GA) and endoplasmic reticulum (ER), is to promote internalization *via* clathrin-independent endocytosis. **Table 2** provides a summary of the various approaches that have been used to guide delivery of polymer-based nanomedicines to four major organelles, viz. the mitochondria, the nucleus and Golgi apparatus and endoplasmic reticulum. For several organelles, in particular the mitochondria and the nucleus, the number of examples that have been reported is too numerous to allow each of these to be cited. **Table 2** instead lists several key review articles, as well as some selected examples, some of which will be highlighted in the remainder of this section.

Table 2. Overview of the strategies that have been used for organelle specific delivery of polymer nanomedicines.

Organelle	Targeting mechanism	Targeting Signal	Functionality	Examples	
Mitochondria					146,147, 148,149
	Mitochondrial protein import machinery	**Mitochondrial targeting signals (MTSs)**	MALLRGVFIVAAKRTPF	Linear polymers	150
			MLSNL RILLN KAALR-KAHTSMVRNF RYGKP VQC	Branched polymers	151
	Transmembrane potential	**Delocalized lipophilic cations (DLCs)**	Triphenylphosphonium (TPP)		152
				Dendrimers	153,154
				Linear polymers	87
				Nanoparticles	155,156 157,158
				Polymersomes	159
			Rhodamine 123	PEGylated liposomes	160
		Positive charges	Histamine	Micelles	130
			N-quarternary ammonium	Nanoparticles	161
			Dequalinium	Vesicles	162,163
				Micelles	26
Nucleus					164
	Temporary disassembly of the nuclear envelope during mitosis	-			165,166, 167
			-	Nanoparticles	168
			-	Linear polymers	169
			-	Branched polymers	170
	Nuclear pore complex (NPC)	-			164
			-	Linear polymers	171
		NPC dilation	Dexamethasone (Glucocorticoid receptor)	Linear polymer	172
	α,β-Importins	**Nuclear localization signals (NLSs)**			165,166, 167,173
			CGYGPKKKRKVGG	Micelles	18
			DRQIKIWFQNRRMKWKK	Nanoparticles	174
			PKKRKV	Nanoparticles	175
			CVKRKKKP	Linear polymers	79,60
			Cytoplasmic NF*k*B	Linear polymers	176,177
	Caveolae-mediated endocytosis	**Histone H3 tail peptide**	ARTKQTARKSTGGKAPRKQL ATKAA	Branched polymers	178,179, 180
Golgi apparatus and endoplasmic reticulum	Caveolae-mediated endocytosis	**Cholera Toxin**	B subunit	Nanoparticles	181
		Others	Pluronic	Linear polymers	182,183 184
			Wheat germ agglutinin	Nanoparticles	185

1.2.2.1. Mitochondrial delivery

Several chemotherapeutic agents act on mitochondria by targeting the transition of cell metabolism, the cellular damage caused by abnormal reactive oxygen species (ROS) production, the disabled apoptosis pathway or mutated mitochondrial DNA (mtDNA).[146] Polymers and polymer-based particles can be used to promote the accumulation of these drugs in the mitochondria. To guide the transport of polymer nanomedicines and delivery of active compounds to this organelle, various strategies have been developed.[146]

One approach that has been used to guide the delivery to the mitochondria involve the use of mitochondrial targeting peptides (MTS)s. MTSs are peptide sequences that allow the translocation of proteins, which are synthesized in the cytoplasm, to the mitochondria *via* the mitochondrial protein import machinery.[146,186] MTSs have been used for the targeting of DNA to the mitochondria.[146,147] A drawback of the use of MTSs for the delivery of polymer nanomedicines to the mitochondria is the limited size of the cargo that can be transported using this pathway. Generally, this strategy cannot be used to mediate mitochondrial uptake of unfolded proteins or macromolecules such as plasmid DNA.[146,147] However, it was shown that the localization of the polymer carrier to the mitochondrial membrane using MTSs as a targeting (rather than translocation) signal and the consequent release of pDNA in close proximity of the targeted organelle, can enhance mitochondrial delivery.[148,150] In one example, Lee *et al.* modified a PEI carrier with MTS and investigated the mitochondrial co-localization and *in vitro* toxicity of the targeted PEI/DNA complex. *In vitro* experiments using a rhodamine-DNA conjugate revealed that the use of the targeting peptide allowed higher mitochondrial localization as well as lower toxicity compared to naked DNA or untargeted PEI/DNA complex.[150] Flierl *et al.* used another approach to overcome the size limitations. In this work, a MTS peptide-peptide nucleic acid (PNA) conjugate was annealed to an oligonucleotide with a complementary PNA sequence and the complex was transferred into the cytosol using a PEI carrier. While the carrier allowed endosomal escape, the MTS targeting peptide directed the oligonucleotide to the mitochondria.[151]

A second strategy that has been used to guide delivery of polymer nanomedicines to the mitochondria explores the high transmembrane potential of these organelles (-180 to -200 mV). This negative potential allows the selective accumulation of delocalized lipophilic cations (DLCs),[146,152] such as triphenylphosphonium (TPP).[149,152] Conjugation of TPP to PAMAM dendrimers allowed endosomal escape and efficient mitochondrial targeting.[153,154] In a similar manner, a construct containing TPP and the photosensitizer

mesochlorine ce6 (Mce6) was connected to the side chains of a PHPMA conjugate *via* a disulfide linker.[87] The disulfide bond was selected to promote rapid intracellular release and subsequent mitochondrial targeting of the TPP-Mce6 drug conjugate. The substitution of Mce6 with a fluorescent dye allowed to monitor the localization of the targeting construct in the mitochondria with confocal microscopy. Moreover, cytotoxicity studies revealed the higher efficacy of the targeted compound as compared to non-targeted PHPMA-Mce6 conjugate. TPP has also been used for the targeting of nanoparticle-based delivery systems. For example, nanoparticles prepared by blending a poly(D,L-lactic-*co*-glycolic acid)-*b*-poly(ethylene glycol)-triphenylphosphonium block copolymer (PLGA-*b*-PEG-TPP) with non-targeted poly(D,L-lactic-*co*-glycolic acid)-*b*-poly(ethylene glycol) (PLGA-*b*-PEG-OH) or poly(D,L-lactic-*co*-glycolic acid) (PLGA-COOH) were found to exhibit compete endosomal escape and were found to localize in the mitochondria of Hela cells.[155] This behavior was attributed to the cationic charge that facilitated endosomal escape through buffering effect and provided mitochondria localization. The use of the TPP functional nanoparticles for the delivery of Lonidamine and α-tocopheryl succinate resulted in a significant improvement of the therapeutic index as compared to administration of these drugs with the non-targeted TPP-modified nanoparticles or the free drug.[155] More recently, α-tocopheryl succinate was delivered in combination with obatoclax (a Bcl-2 inhibitor) using TPP-coated positively charged nanoparticles. The nanoparticles entered into acidic lysosomes *via* macropinocytosis, followed by lysosomal escape and accumulated into mitochondria over a period of 24 h.[156] In another example, conjugation of (4-carboxybutyl)triphenylphosphonium (4-carboxybutyl TPP) to poly(ε-caprolactone) (PCL) diol resulted in the formation of amphiphilic TPP-*b*-PCL-*b*-TPP (TPCL) polymers, which self-assembled into less than 50 nm cationic nanoparticles. These nanoparticles were used for the simultaneous delivery of both the hydrophilic Dox·HCl and the hydrophobic Dox to the mitochondria.[157] Along the same lines, poly(lactic acid)-*b*-poly(ethylene glycol) (PLA-PEG) polymersomes decorated with a fluorescent TPP derivative were used to mediate mitochondrial delivery of Dox.[159] This resulted in a significantly reduced viability of cultured pancreatic cancer cell spheroids. Grancharov *et al*. prepared TPP functionalized micellar nanocarriers by co-assembly of poly(ethylene oxide)-*b*-poly(ε-caprolactone)-*b*-poly(ethylene oxide) (PEO-*b*-PCL-*b*-PEO) and a poly(2-(dimethylamino)ethylmethacrylate)-*b*-poly(ε-caprolactone)-*b*-poly(2-(dimethylamino)ethylmethacrylate) (PDMAEMA-*b*-PCL-*b*-PDMAEMA) triblock copolymer, which was partially functionalized with TPP.[158] These

nanoparticles were used to direct the delivery of the anticancer drug curcumin to the mitochondria. Apart from TPP, another DLC that has been used for mitochondrial targeting of polymer nanomedicines is rhodamine 123 (Rho).[149] Biswas *et al*. coupled Rho to amphiphilic PEG-phosphatidylethanolamine conjugates, which were subsequently used to prepare PEGylated liposomes.[160] Enhanced mitochondrial targeting was observed as well as enhanced cytotoxicity upon paclitaxel incorporation as compared to untargeted liposomes.

In addition to the use of mitochondrial targeting sequences or delocalized lipophilic cations to guide trafficking of polymer nanomedicines to the mitochondria, there are also several reports that describe the use of positively charged nanocarriers to enhance drug accumulation in the mitochondria. Zhang *et al*., for instance, prepared histamine functionalized poly(allyl glycidyl ether)-*b*-poly(ethylene glycol) (PAGE-*b*-PEG) micelles. It was found that the histamine functionality facilitated endosomal escape and enhanced doxorubicin targeting to the mitochondria as compared to free Dox.[130] Chen *et al*. have prepared nanoparticles that were composed of a quaternary ammonium-functionalized chitosan (NQC) derivative and a chitosan derivative modified with N-glycyrrhetinic acid (GA) moieties *via* schiff base PEG spacer. These nanoparticles were used for the delivery of brucine.[161] After endocytosis, the drop in pH caused Schiff base cleavage, which resulted in an increased positive surface charge of the particles and facilitated endosome disruption and cytosolic cargo release. Meanwhile, the positive charge on the particle surface allowed mitochondrial targeting. Brucine accumulation in the mitochondria of hepatocellular carcinoma HepG2 cells increased toxicity both *in vitro* and *in vivo* as compared to the use of the free drug. Dequalinium (DQA) is a dicationic amphiphilic compound generally used as antimicrobial agent but which has also found application in mitochondrial targeting.[146,147] This compound can self-assemble to form vesicles called DQAsomes that have the ability to condense DNA. Those vesicles could escape the endosomes, localize at the mitochondrial membrane and release the pDNA in close proximity of the targeted organelle.[163] DQA was also conjugated to PEG chains for the decoration of liposomes. This allowed endosomal escape and subsequent mitochondrial targeting.[162] Targeted liposomes enhanced the cytotoxicity of the potential anticancer drug resveratrol compared to non-targeted carriers. A similar approach was used by Zhou and co-workers for the delivery of Dox and Dox-DQA conjugates to the mitochondria and nucleus simultaneously. Dox and Dox-DQA were delivered using micelles that were generated by self-assembly of a hydrazone-linked PEG-1,2-distearoyl-

sn-glycero-3-phosphorylethanolamine (DSPE) conjugate that was modified with anisamide (AA), which is a tumor cell targeting ligand. When the loaded micelles were internalized by tumor cells, hydrazone bond cleavage allowed Dox and Dox-DQA release, which mainly accumulated in the nucleus and mitochondria, respectively. [26]

1.2.2.2. Nuclear delivery

A large number of anticancer therapeutics act by interfering with DNA replication. Doxorubicin and other anthracyclines act by inhibiting the enzyme topoisomerase II and through DNA intercalation. Antimetabolites like 5-Fluorouracil and mercaptopurine are based on nucleoside analogs that once incorporated in the DNA prevent chain elongation, whereas DNA alkylating agents such as platinum (e.g. cisplatin) and nitrogen mustards (e.g. cyclophosphamide, ifosfamide) give rise to DNA crosslinking.[187,188] Cancer gene therapy focuses on introducing foreign genes into cancer cells or the surrounding tissue.[189] As a consequence, the nucleus is a main target in anticancer therapy. While escape from endocytic vesicles can be promoted by using, for example, endosomolytic polymers, access to the nucleus is further limited by the presence of a double-layer membrane separating and protecting the genetic material *via* a series of tightly regulated pores called the nuclear pore complex (NPC).[190] There are a number of approaches that have been explored to enhance nuclear uptake of polymer nanomedicines. These are summarized in **Table 2** and discussed in more detail below.

A first pathway for polymer nanomedicines to enter the nucleus takes advantage of the fact that the nuclear membrane disassembles during mitosis.[164-166,168] This path represents the primary enabler for the entry of pDNA or polyplexes into the nuclear compartment.[165,168] A drawback of this approach, however, is that it is strictly dependent on the cell cycle and cannot be used in the case of non-dividing cells.[165,168] An interesting example of the use of the mitotic cycle for nuclear delivery of polymer nanomedicines was described by Li *et al*. To enhance the nuclear translocation of the c-Myc inhibitor H1-S6A,F8A (H1) peptide during cell division, the authors used a combination of two different polymer conjugates. First, cells were treated with a PHPMA-docetaxel (DTX) conjugate (P-DTX), which arrested cells in the G2/M phase and prolonged the period when the nuclear membrane was disassembled. In a second step, the cells were treated with the PHPMA-H1 conjugate (P-H1), which entered the nucleus and efficiently

inhibited c-Myc. *In vitro* studies demonstrated that the administration of P-DTX followed by the P-H1 conjugates was significantly more effective than reverse sequential delivery as well as the simultaneous co-delivery or monotherapy with P-DTX or P-H1 alone.[169] Another approach reported by Shen *et al*. involved the use of the CDK1 inhibitor RO-3306 to control the G2/M transition of the cell cycle and increase the proportion of mitotic cells during transfection. It was found that combination of RO-3306 and PEI/DNA complex remarkably increased the transfection efficiency.[170] Moreover, the transfection efficiency of the PEI carrier was compared to that of the (ROS)-labile charge-reversal poly((2-acryloyl)ethyl(p-boronic acid benzyl)diethylammonium bromide) (B-PDEAEA), which was recently reported by the same authors.[171] B-PDEAEA is a positively charged linear polymer that packages DNA into nanoparticles, but turns into a negatively charged polymer releasing the DNA in response to intracellular reactive oxygen species (ROS).[171] It was demonstrated that the DNA was localized in the cell nucleus quickly after B-PDEAEA mediated transfection and RO-3306 co-administration only slightly increased the transfection efficiency.[170] Based on these results, the authors concluded that, while most of the PEI/DNA complexes enter the nucleus in the intact form during mitosis, cytoplasmic DNA released from the negatively charged B-PDEAEA may enter the nucleus passing through the NPC.

Passive trafficking through the nuclear pore complex (NPC) represents a second access path to the nucleus. However, due to the tiny size of the pores, the access through this way is limited to the diffusion of ions, small metabolites and molecules with molecular weight less than 40-60 KDa.[164,165,190] As a consequence, pDNA alone, or in combination with cationic carrier-based polymers (polyplexes) is believed to rarely undertake this pathway, therefore resulting in a poor transfection efficiency.[167,173,190] One approach that has been used to enhance nuclear permeation *via* NPCs involves the use of dexamethasone (Dex), a glucocorticoid steroid that upon binding to its nuclear receptor enables NPC dilation up to 140 nm.[191] Low molecular weight PEI-Dex conjugates complexed with DNA showed enhanced translocation efficiency compared to the untargeted PEI-DNA system.[172]

A third strategy to enhance nuclear uptake exploits the nuclear import machinery, which controls the translocation of cytoplasmic proteins into the nucleus by means of nuclear localization signals (NLS)s.[173] These small cationic peptide sequences access the nucleus by interaction with nuclear importing proteins called importins.[190] This pathway allows active transport of molecules that are too large to passively diffuse through the

NPC. Polymers and nanoparticles have been decorated with NLSs to direct the intracellular trafficking of both anticancer drugs and pDNA.[164,167] Hoang and co-workers aimed to localize Auger electron emitting radionuclides in the perinuclear and nuclear regions of cells. To this purpose, PEG-*b*-PCL block copolymer micelles labeled with the Auger electron emitter indium-111 (111In) and loaded with the radiosensitizer methotrexate (MTX) were decorated with NLS peptides to promote nuclear uptake. Successful nuclear targeting was shown to improve the antiproliferative effect of the Auger electrons. Moreover, significant radiation enhancement was observed by the co-delivery of low-dose MTX and 111In in breast cancer cell lines.[18] A similar strategy has been used to enhance nuclear delivery of doxorubicin using NLS-modified PLGA nanoparticles.[174] In another example, covalent conjugation of a NLS derived from the SV40 virus on PLGA nanospheres was demonstrated to enhance the gene transfection efficiency of the encapsulated pDNA.[175] While decoration of polymers or polymer nanoparticles with NLSs provides a powerful strategy to enhance nuclear delivery, *in vivo* the positively charged nature of these peptides may lead to non-specific cellular uptake in the blood stream.[167] One way to address this drawback is to mask the NLS such that it is negatively charged in circulation but upon internalization undergoes charge reversal. This was demonstrated by Zhong *et al*. for the design of an HPMA copolymer in which the therapeutic H1 peptide-modified with an octaarginine-NLS sequence (R8NLS-H1) was linked to the polymer backbone *via* the lysosomally cleavable linker GFLG spacer. The positive charges of the octaarginine-NLS peptide were modified with anionic 2, 3-dimethylmaleicanhydrides (DMA). This allowed the shielding of the cationic properties of the peptide in physiological conditions as well as rapid cleavage and unmasking of the positively charged amino-rich residues after mild-acidic (pH 6.5) tumor tissue accumulation. After cellular internalization *via* endocytosis, the lysosomal release of the R8NLS-H1 peptide allowed lysosomal escape through the octaarginine motif and nuclear transport *via* the NLS sequence.[79] In another report, the same authors described a PHPMA nanoparticle-based nuclear delivery system that was designed to successively reduce size upon trafficking towards the tumor environment and subsequently the intracellular environment. The particles were composed of an anionic DMA protected *N*-3-aminopropylmethacrylamide-HPMA copolymer and a second (cationic) HPMA copolymer, which is functionalized *via* a pH cleavable hydrazone linker with a Dox peptide conjugate (R8NLS-Dox). The Dox-peptide conjugate included a fusion peptide (R8NLS) that is composed of an octaarginine motif (R8) and a NLS. The mild-acidic pH of the tumor environment allowed dissociation of the two conjugates and resulted in

enhanced cellular internalization due to reduction of carrier size. After endocytosis, a second reduction in size occurred in the more acidic endolysosomal compartments, which allowed cleavage of the hydrazone linker, R8NLS-doxorubicin release and nuclear entry *via* nuclear localization signal assistance. Based on the stepwise size reduction and on-demand R8NLS exposure, the PNV inhibited the growth of HeLa tumors in mice by 75%.[60] Another interesting approach to enhance nuclear delivery is based on the nuclear factor kappa B (NF*k*B) transcription factor. NF*k*B is a transcription factor containing both a DNA binding domain and a NLS domain. The latter, under specific conditions, directs the translocation from the cytoplasm to the nucleus and *vice versa*. Hence, a pDNA containing a NF*k*B-binding motif was delivered in the cell cytoplasm *via* a PEI carrier. The binding of the pDNA to the cytoplasmic NF*k*B resulted in translocation to the nucleus *via* the NF*k*B NLS domain.[176] Jeong *et al.* used reducible poly(amido ethylenimine)s for intracellular release of a plasmid DNA having binding sequences for NF*k*B. The highly reductive cytosolic environment allowed cytosolic release of the pDNA from the carrier therefore enhancing NF*k*B binding and nuclear targeting.[177]

The nuclear delivery strategies that have been discussed so far all involve cellular internalization of the polymer nanomedicines *via* clathrin-mediated endocytosis. In a series of studies, Sullivan and co-workers have demonstrated the power of other internalization pathways, more specifically, caveolae-mediated uptake to promote efficient nuclear delivery.[164] In a first study, Reilly *et al.* found that conjugation of histone H3 tails to PEI-based polyplexes enhanced both the rate of gene expression as well as the efficiency of gene transfection and reduced the dependence on endocytic pathways that involve lysosomal trafficking, indicating a possible increase reliance on caveolar uptake.[178] A subsequent study that used a variety of endocytic inhibitors indeed demonstrated that the H3 functionalized polyplexes are internalized *via* caveolae-mediated endocytosis and also indicated that the polyplexes used retrograde Golgi-to-ER pathways to reach the nucleus.[179] Ross *et al.* demonstrated that H3-targeted polyplexes were not released into the cytoplasm after internalization, but instead entered the nucleus in association with ER membranes. A post-mitotic increase in nuclear localization, that was coincident with nuclear envelope (NE) reassembly, suggested that the nuclear entry *via* the NLS contained in the H3 tails was enhanced during nuclear envelope dismantle.[180]

1.2.2.3. *Delivery to the Golgi apparatus (GA) and Endoplasmic Reticulum (ER).*

In the endoplasmic reticulum (ER), proteins are synthesized, folded and transported to the Golgi apparatus (GA) where they are modified and sorted before secretion. Interfering with those specific functions can be exploited as anticancer therapy.[192] Moreover, the ER is a main Ca^{2+} storage and stress signals in this organelle can trigger rapid Ca^{2+} release and apoptosis.[192] ER targeting is also interesting for antigen presentation in antigen presenting cells, which can be exploited for antitumor immunotherapy.[193] So far, however, only a relatively small number of polymer nanomedicines designed to mediate delivery to the GA and ER have been reported.

One possible strategy to guide polymer nanomedicines to the GA and ER is to exploit some of the intracellular trafficking pathways of bacteria toxins such as Shiga and Cholera toxins. These toxins are internalized by the cells *via* both clathrin-dependent and independent endocytosis. After accumulation in the early endosomes, these toxins retrograde through the GA and ER, therefore avoiding the highly degradative lysosomal environment.[194] The Shiga toxin accesses the cell by binding to the globotriaosylceramide (Gb3) receptor before being redirected to GA and ER.[194] The overexpression of Gb3 receptor on the plasma membrane of various cancers such as lymphomas, ovarian carcinoma, breast and colon cancer has been recognized as an appealing opportunity to develop highly selective targeting methods.[193,195,196] Moreover, since the targeting mechanism is dictated by the B subunit of the Shiga toxin, which is not toxic,[197] the use of toxins subunits to promote GA and ER targeting was proposed.[195] The Shiga toxin B subunit has been conjugated to low molecular weight cytotoxic compounds such as benzodiazepine RO5-4864,[196] the topoisomerase I inhibitor Sn38[196] and photosensitizer drugs.[198,199] The Cholera B toxin subunit can be used in a conceptually similar way. Vivero-Escoto and co-workers, for example, conjugated the B subunit of cholera toxin (CT-B) to PEG-modified fluorescein isothiocyanate (FITC)-mesoporous silica nanoparticles.[181] This work demonstrated that the cellular internalization occurred *via* both clathrin-dependent and -independent mechanisms allowing partial trafficking through the trans-Golgi network and the ER. These examples highlight the possibility to use toxins-derived subunits to target the GA and ER bypassing the degradative compartments, which provides new opportunities for the delivery of macromolecular cargo to these organelles.

In addition to the use of bacterial toxins, Pluronic polymers and wheat germ agglutinin (WGA)-targeted nanoparticles have also been used to promote cellular internalization *via*

different mechanisms and in particular *via* caveolae-mediated endocytosis. Kabanov and co-workers have reported that, while the cellular internalization of P85 block copolymer micelles at high concentrations occurs mainly through clathrin-mediated endocytosis, P85 unimers at concentrations below the CMC, enter the cell mainly *via* caveolae-mediated endocytosis.[182] These block copolymers were seen to bypass the cell lysosomes and transport to the ER and then to the mitochondria.[183] Shen *et al.* showed that coating the surface of silicon quantum dots with Pluronic F127 allowed selective labeling of the ER.[184] Gao *et al.* reported that quantum dots labeled poly(ethylene glycol)-*b*-poly(lactid acid) (PEG-*b*-PLA) nanoparticles, that were decorated with wheat germ agglutinin (WGA) were internalized by both clathrin- and caveolae-mediated mechanisms and found to accumulate in the lysosomes and Golgi apparatus.[185]

1.3. Monitoring Intracellular Drug Delivery

The advances made in the field of polymer nanomedicine to control and direct active compounds to the proper intracellular target also call for methods that allow to monitor these processes. While assessing drug activity[35,54] or transfection efficiency provides indirect evidence for successful delivery,[104,125,128] these experiments do not afford quantitative insight into the intracellular trafficking pathways and single cell pharmacokinetics of the polymer nanomedicines. Detailed and quantitative information about the intracellular routing and release profiles of polymer nanomedicines is essential to further improve the performance of these delivery systems.

Owing to the broad variety of organelle-specific fluorescent markers and the wide range of fluorescence probes that can be used to label polymers or polymer nanoparticles, fluorescence microscopy, and in particular confocal laser scanning microscopy (CLSM), has become the most commonly used technique to monitor intracellular delivery. Intracellular trafficking is generally monitored in co-localization studies between targeted organelles or cellular compartments and fluorescent polymer-drug systems. Often, co-localization studies are performed in combination with other techniques such as flow cytometry,[200,201] transmission electron microscopy (TEM)[151,202,203] as well as with subcellular fractionation.[204] In addition to fluorescence-based techniques, there are also various label-free methods that have been used to monitor intracellular delivery of

polymer nanomedicines. These label-free methods are highly attractive as they allow to overcome some of the drawbacks of fluorescence-based techniques such as potential cleavage of the label, interference of the label with biological processes and the need to introduce labels.[205-207]

The second part of this chapter will highlight the use of the techniques mentioned above to study and monitor transport of polymer nanomedicines to the cytosol as well as specific organelles. As fluorescence microscopy and CLSM for example are very widely used, it is impossible to provide a comprehensive overview that covers all the work that has been done to monitor intracellular delivery of polymer nanomedicines. Instead, the aim of this section is to highlight how these techniques (or a combination thereof) can be used to answer specific questions with regards to the intracellular trafficking of polymer nanomedicines.

1.3.1. Monitoring cytosolic delivery

The use of the fluorescence and label-free methods allows to address a number of important questions that are related to the cytosolic delivery of polymer nanomedicines and/or the active compounds that these transport. In what follows below, selected examples will be presented, which illustrate the use of various fluorescence-based techniques to monitor (i) endolysosomal release, which occurs upon cleavage of linkers in polymer-drug conjugates, (ii) endosomal escape as well as (iii) the acidification kinetics of the endolysosomal compartments. Finally, two examples of label-free methods that have been used to study the intracellular trafficking and degradation of polymer nanomedicines in the endolysosomal compartments will be presented.

Endolysosomal release of anticancer drugs is generally accomplished by using stimuli-responsive drug delivery carriers that are stable under physiological conditions, but release the active compound upon endocytic internalization in response to an intracellular stimulus. In general, the most used technique to monitor endolysosomal release is CLSM. In particular, if the transported drug is fluorescent, the release from the carrier can be directly observed by tracking the fluorescent drug.[48] When the active compound is non-fluorescent, endolysosomal release can be assessed by substituting the drug with a fluorescent dye.[17,95] Doxorubicin is very attractive not only since it is a very potent

chemotherapeutic, but also due to its intrinsic fluorescence. A simple experiment to assess escape of Dox from the endocytic pathway consists in cellular CLSM imaging after long cellular incubation time. A diffuse red Dox fluorescence throughout the cells confirms cytosolic release of Dox or Dox-linked polymer nanomedicines.[80] A deeper understanding of the time-dependent release process can be obtained by monitoring the intracellular path of the drug. In this case, co-localization studies need to be performed at different incubation times. While the Dox red fluorescence appeared as punctual cytoplasmic fluorescence for short incubation times, indicating the entrapment of the polymer-bound drug inside the endocytic vesicles, after longer incubation time, the red fluorescence spreads throughout the cells confirming the release of the drug from the carrier. Markers for the endolysosomal vesicles as well as for the target organelle can be used for time-dependent co-localization studies.[44,48,62]

Förster resonance energy transfer (FRET) experiments are a powerful tool to monitor linker cleavage and drug release from polymer conjugates. In one example, the FRET donor Cy5 was attached to a HPMA polymer backbone and the acceptor Cy7 was conjugated *via* the enzyme-cleavable GFLG peptide linker. Cells were incubated with the polymer conjugate and at different incubation times the cell lysate was analysed *via* fluorescence spectroscopy. Upon cellular internalization and exposure to the lysosomal enzyme cathepsin B, cleavage of the peptide linker led to separation of the two dyes and loss of the FRET signal.[208] In another study, the same authors used the intrinsically fluorescent anticancer drug epirubicin (EPI) as a FRET donor to prepare PHPMA-GFLG-EPI conjugates that also incorporated the FRET acceptor Cy5. The FRET effect, generated by the close proximity of the pair Cy5/EPI, significantly decreased after 24 h incubation due to the complete GFLG cleavage and EPI release.[76] A similar approach was used also to determine the release of Dox from *N*-palmitoyl chitosan nanoparticles containing a Cy5 moiety as FRET acceptor. HT1080 cells were incubated with the nanoparticles for 24 hours and at different time points, the FRET effect was visualized with CLSM. For the first 30 min incubation the nanoparticles fluorescence was observed in the Cy5 channel, while no Dox signal was observed. After 1 hour incubation, the Cy5 signal significantly decreased while a weak Dox signal appeared in the cytoplasm. At longer incubation times the Cy5 fluorescence was not observed anymore, while Dox signal in the cytoplasm further increased. Incubation times of 12 and 24 hours highlighted the accumulation of Dox in the cell nucleus.[209] FRET was also used to monitor intracellular pH-dependent release of doxorubicin from a carbon nanodot (CDot)-based

drug delivery system. CDots were used both as drug carriers and as the FRET donor. The FRET-CDots were obtained by coupling PEG chains onto the CDot surface followed by trapping of doxorubicin molecules within the PEG network *via* π–π stacking. The close proximity of the CDot core and Dox generated a strong FRET signal. Upon release of Dox from the CDot surface, the FRET signal was quenched. This change in FRET signal was used to monitor the release of doxorubicin from the CDot surface as a response to the decreased endolysosomal pH.[210] In a similar way, PEGylated quantum dots (QDs) were used to monitor the cytosolic release of the anticancer drug STAT3 inhibitor in response to cytosolic glutathione. To this purpose, CdS:Mn/ZnS QDs were functionalized *via* a disulfide linker with the STAT3 inhibitor, folate as targeting motif as well as with PEG chains. The surface modified QDs were then used to decorate superparamagnetic iron oxide nanoparticles to generate a multimodal/multifunctional nanocomposite probe. Conjugation of the electron rich STAT3 inhibitor and the folate ligand quenches the QDs luminescence. QDs luminescence is restored once the surface-bound ligands are detached. Hence, the modification of the QDs surface and linkage to the iron oxide core resulted in the formation of nanocomposites in an OFF state due to the QD quenching. Upon intracellular uptake, the higher glutathione concentration allowed QD and drug release with consequent increase in the QD fluorescence. The increased QD fluorescence could be used to track STAT3 release from the nanocomposite and the iron oxide core allowed MRI analysis of the nanocomposite in the cell cytoplasm.[211]

In addition to follow drug release from polymer conjugates or polymer nanomedicines, a second important challenge is to monitor endosomal escape of polymer nanomedicines and/or their cargo. The use of CLSM and suitable labels allows to monitor either drug or carrier. Their intracellular trafficking can be visualized observing the co-localization, first with endocytic vesicles and after with the targeted cytoplasmic organelle. As an example, the intracellular trafficking of endosomolytic dendrimers and linear polymer-FITC conjugates was investigated after 6 and 12 hours incubation in cancer cells. The use of the lysosomal marker Lyso Tracker green allowed the determination of lysosomal co-localization in the first 6 hours incubation. Mixed co-localization with cytoplasm, lysosomes and nucleus after 12 hours incubation confirmed the endolysosomal destabilization and cytoplasmic release.[11,135] Jiang *et al*. used α,β-unsaturated ketone-caged coumarin derivatives to monitor endosomal escape and consequent cytosolic disintegration of polymer nanocarriers. These micellar nanoparticles were obtained by temperature-induced self-assembly of a diblcok copolymer composed of a hydrophilic

PEG block and a thermosensitive poly(di(ethylene glycol) monomethyl ether methacrylate) that was modified with an α,β-unsaturated ketone-caged coumarin derivative. Upon endosomal escape, Michael addition reaction of thiols (from cytosolic glutathione as well as protein cysteine residues) and the α,β-unsaturated ketone groups, led to unmasking of the coumarin moieties resulting in a blue fluorescence as well as an elevation of the critical micellization temperature and disintegration of the polymer nanoparticles.[212]

FRET has also been used to monitor polymer-mediated endosomal escape of DNA and RNA. In one example, a FRET-capable single stranded oligonucleotide molecular beacon (OMB) was used to monitor intracellular DNA release as well as its stability in the cytosol. The OMB contained the FRET dye pair Alexa-Fluor 488 and 594 and was used to form mixed polyplexes with a plasmid DNA encoding green fluorescent protein (GFP) using jetPEI and generation 5 (G5) PAMAM dendrimer as vectors. Confocal microscopy studies revealed that the OBM delivered *via* PAMAM was retained inside the endocytic vesicles up to 24 h, whereas the PEI vector allowed cytoplasmic release already after 2 h incubation in HEK 293A cells. Moreover, FRET confocal microscopy showed a decrease in FRET signal after 12 h incubation due to the cleavage of the cytoplasmic OBM released from the PEI carrier by cytoplasmic proteases.[213] In another example QDs were used to monitor the endosomal escape of PEI-siRNA complexes *via* FRET analysis. PEI covalently conjugated on the surface of the QDs was complexed with cyanine dye labeled vascular endothelial growth factor siRNA (cy5-VEGF siRNA) to generate nanosized polyelectrolyte complexes (PEC). FRET was achieved between cy5-VEGF siRNA and PEI conjugated QDs in the complex. CLSM was used to monitor the intracellular trafficking and release of siRNA from the complex as a function of incubation time. The extent of cy5-siRNA release from the PEC was quantitatively evaluated by flow cytometry analysis.[214]

Significant efforts have been made to monitor and measure the acidification kinetics in the endolysosomal system. Insights in the acidification kinetics could aid the development of novel polymer nanomedicines that are designed e.g. for the pH triggered release of drugs. In one example, Chang *et al*. prepared hydrophilic, fluorescent nanoprobes that consist of hybrid polystyrene-*b*-poly(acrylic acid) (PS-*b*-PAA) micelles encapsulating the hydrophobic pH responsive fluorophore *N,N'*-di-*n*-dodecyl-2,6-di(4-methyl-piperazin-1-yl)naphthalene-1,4,5,8-tetracarboxylic acid diimide (NDI). The fluorescence intensity of the nanoparticles was enhanced 55-fold upon changing from

neutral (7.4) or basic pH (8.4) to acidic (3.4) pH. MCF-7 cells stained with endolysosomal markers were incubated with TAT-peptide modified nanoparticles for 1, 4 and 8 hours and analysed both *via* CLSM and flow cytometry. After 8 hours, bright red fluorescence of the hybrid nanoparticles was found to overlap with that of the green-fluorescent stained lysosomal compartments.[200] Similarly, Lerch *et al.* reported the synthesis of polystyrene nanoparticles modified with the dual-wavelength pH-sensitive dye seminaphthorhodafluor-1 (SNARF-1). SNARF-1 is a fluorescent dye with emission maxima that shifts from $\lambda = 580$ nm to $\lambda = 640$ nm upon protonation.[203] Hela cells were incubated with the nanoparticles and imaged at different time points. While the subcellular localization of the nanoparticles was mapped by TEM and co-localization with endolysosomal Rab family proteins using CLSM, the acidification process was visualized as pseudo-color CLSM images. Bao *et al.* prepared ratiometric pH sensors by decorating hyperbranched polylactide nanoparticles with both a pH sensitive as well as a pH-insensitive naphthalimide-based fluorophore. These probes were successfully used to quantitatively analyse the intracellular pH of Hela cells.[215] Choi *et al.* developed a colourimetric polyaniline nanoindicator composed of silica-coated polyaniline (PANI) nanoparticles. The fluorophores Cy3 ($\lambda = 570$) and Cy7 ($\lambda = 770$) were absorbed on particle surface to give Cy3 and Cy7-labeled proton-sensitive nanoindicators. The ability of the nanoprobes to sense the endolysosomal pH was tested in HT1080 cells using CLSM. To this purpose, cells were incubated with the nanoprobes for 0.5, 1.5, and 4 hours. Co-localization experiments with EEA1 as early endosomal marker and Lyso Tracker Blue as lysosomal marker revealed that after 30 min and 1.5 h the nanoparticles were located in the early endosomes, whereas after an incubation time of 4 hours the nanoparticles were found in the lysosomes. In the early endosomes, the fluorescence intensity of Cy7-labeled nanoparticles was strong whereas the Cy3 dye fluorescence was quenched. This is due to the fact that in the endosomes (pH 6), PANI is in its deprotonated form and causes quenching of the Cy3 dye. On the other hand, after 4 hours incubation, the decreased pH of the lysosomes resulted in PANI protonation and a shift of its absorption peak to 770 nm. This caused the quenching of Cy7 emission and increase of Cy3 fluorescence.[216] Ratiometric pH sensitive probes based on silica nanoparticles incorporating Atto647 as pH-insensitive reference dye and FITC as pH sensor have been used to monitor intracellular pH upon internalization of various polyplexes. It was found that the FITC:Atto647 fluorescence ratio was highly correlated with the pH over the pH range 4 - 7.5. These particles were used to monitor real-time intracellular trafficking in

BT-20 cells. The environmental pH of the nanoprobes dropped from pH 7.4 to 4 over the first 2 hours suggesting rapid internalization *via* endocytosis, followed by acidification within endolysosomal compartments. The pH remained around 4 for 24 hours, indicating the inability of the nanoprobes to escape from the acidic vesicles. To further confirm that the nanoprobes were trapped in the endolysosomal vesicles, cells were incubated with both the nanoprobes and branched PEI, a polymer known to mediate endosomal disruption. The PEI co-treatment not only prevented a complete acidification by retaining the pH at 5.5 in the first few hours, but also reversed the pH to 7.4 at 24 hours post-incubation indicating endolysosomal escape. Co-incubation of the nanoprobes and different endosomal disrupting polymer-DNA complexes was used to correlate the ability of the polymers to trigger endosomal release with the endocytic compartments acidification.[201] Hu *et al*. prepared ratiometric fluorescent pH imaging probes, which also possess endosomolytic properties. These nanoparticles were generated from dual-labeled pH responsive block copolymers, which were composed of a pH-responsive *N,N*-diethylaminoethyl methacrylate-*co*-butyl methacrylate (PDEA-*b*-PBMA) block incorporating tetramethylrhodamine (TMR) and a hydrophilic poly(*N,N*-dimethylacrylamide) (PDMA) segment that incorporates a small fraction of the fluorescent pH sensitive dye 7-hydroxycoumarin (HCCME) (**Figure 2A**). While the red TMR emission was detected during the entire incubation period, the blue HCCME emission was almost not detected for the first 4 hours incubation due to the acidic environment. After 8 hours, the blue emission increased suggesting endosomal escape (**Figure 2B**). The presence of the internal standard TMR and the use of calibration curves allowed the determination of the pH gradient to which the micelles were exposed. For the first 5 hours, the pH was around 5, whereas for longer incubation times, such as 16 and 24 hours, the pH was close to neutral as shown in **Figure 2B.** This result was confirmed by the co-localization between TMR and the late endosomal-lysosomal marker for the first 4 hours. After 8 hours, the co-localization between TMR and endocytic vesicles decreased going from 92% at 4 hours to less than 32% after 24 hours incubation.[217]
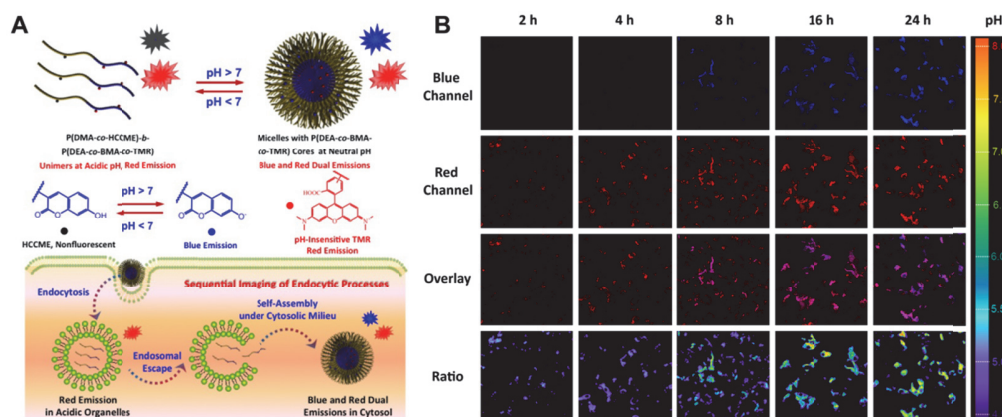
Figure 2. (A) Schematic illustration of a ratiometric fluorescent imaging probe generated from dual-labeled pH responsive block copolymers. (B) Incubation time-dependent CLSM images of live HepG2 cells upon exposure to the imaging probe at 37 °C. The ratio panel indicates the pH sensed by the micelle at different incubation times. Adapted with permission from J. M. Hu, G. H. Liu, C. Wang, T. Liu, G. Y. Zhang, S. Y. Liu, Spatiotemporal Monitoring Endocytic and Cytosolic pH Gradients with Endosomal Escaping pH-Responsive Micellar Nanocarriers, Biomacromolecules 2014, 15 (11), 4293-4301. Copyright (2014) American Chemical Society.[217]

In addition to the techniques used in the examples discussed above, another attractive technique to study cellular interaction and trafficking of polymer nanomedicines is Raman spectroscopy since it is a non-invasive and label-free method.[218] Chernenko *et al*. used Raman spectroscopy to study the subcellular degradation of poly(ε-caprolactone) (PCL) and poly(L-lactide-*co*-glycolide) (PLGA) nanoparticles (**Figure 3A**).[219] Comparison of polymer and cell associated signals and the use of a mathematical algorithm allowed the reconstruction of pseudocolor images. **Figure 3B** shows results of examples carried out with fixed Hela cells which were incubated with PCL and PLGA nanoparticles for 7 h and 2 h, respectively. While, PLGA nanoparticles were internalized faster than the PCL nanoparticles, both types of nanoparticles were found to localize inside endocytic vesicles. In order to investigate the degradation pattern of the internalized nanoparticles, in a second experiments cells were first incubated with the nanoparticles (7 h in the case of PCL and 2 h in the case PLGA) and subsequently incubated with fresh medium, fixed and analysed at different time intervals. Disappearance of the 1735 cm^{-1} PCL peak corresponding to the C=O ester bonds, suggests that endosomal metabolic activity gives rise to the hydrolysis of ester moieties of

PCL particles. However, these particles were not fully degraded even after 24 h. On the contrary, disappearance of the characteristic ester linkage (1765 cm^{-1}) of PLGA particles was observed already after 3-6 hours incubation in fresh medium and complete digestion was observed after 6 h incubation. In a following study, the same authors used Raman spectroscopy to investigate the internalization behaviour of non-targeted and EGFR-targeted PEG-PLGA\PCL blend nanoparticles in SKOV-3 human ovarian adenocarcinoma cells. Raman analysis of cells incubated with the nanoparticles for different incubation times indicated a much rapid cellular internalization of targeted nanoparticles as compared to the non-targeted ones. This led to a faster accumulation of the targeted particles within large vesicular compartments in the perinucelar region of the cells. In a second step, the nanoparticles were loaded with the model drug C6 ceramide, which is known to accumulate in the mitochondria. To study the drug release profile and mitochondria co-localization of the targeted and non-targeted nanoparticles, Raman spectroscopy was combined with fluorescence microscopy. C6 ceramide delivered using the EGFR-targeted nanoparticles was found to accumulate faster in the cell mitochondria. This result indicated a faster release of the cargo, transported *via* the targeted nanoparticles, in the subcellular matrix.[220] In another study, Raman spectroscopy has been used together with fluorescence microscopy to study the subcellular distribution of fluorescent polystyrene nanoparticles. After 24 h incubation the nanoparticles were co-localized with lipid rich environments in proximity of the endoplasmic reticulum.[221]
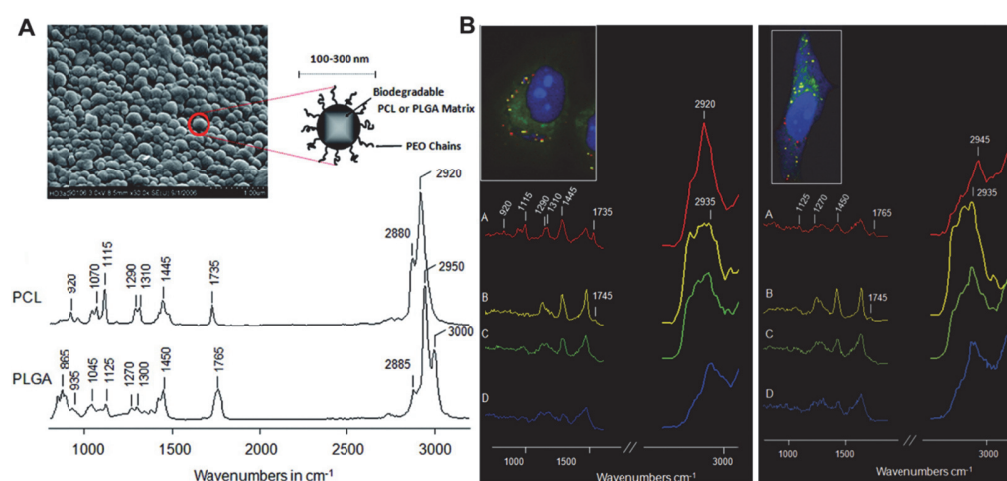

Figure 3. (A) SEM image of PCL nanoparticles and Raman spectra of PCL and PLGA nanoparticles with the characteristic peaks at 1735 and 2920 cm^{-1} for PCL and 1765 and 2950 cm^{-1} for PGLA, respectively. (B) Pseudocolor Raman image of a Hela cell

incubated with PCL-particle-containing medium (left) for 7 h as well as PLGA-particle-containing medium for 2 h (right). Red regions, PCL or PLGA aggregates; yellow regions, lipid/phospholipids inclusions; green regions, membrane rich organelles such as ER, Golgi, mitochondria; blue regions, proteins of the cell body. Traces A-D represent the Raman spectra of the corresponding regions. Adapted with permission from T. Chernenko, C. Matthaus, L. Milane, L. Quintero, M. Amiji, M. Diem, Label-Free Raman Spectral Imaging of Intracellular Delivery and Degradation of Polymeric Nanoparticle Systems, Acs Nano 2009, 3 (11), 3552-3559. Copyright (2009) American Chemical Society.[219]

NanoSIMS is another powerful, label-free technique to monitor cellular internalization and intracellular trafficking of polymer nanomedicines. NanoSIMS uses a focused primary ion beam to erode the sample and provides secondary ions that can be analysed to trace elements and isotopes. The focusing of this ion beam to a very narrow beam spot allows spatial resolutions down to 50 nm. The high resolution, together with the capability of multi-element and isotope selective analysis, resulted in the application of NanoSIMS in a variety of different fields such as cosmochemistry, biological geochemistry, materials chemistry and cell biology.[222] NanoSIMS has been used to track the subcellular pathway drug distribution of metal-based anticancer drugs.[223-225] Recently, the NanoSIMS technique has also been used, in combination with fluorescence microscopy, to monitor cellular internalization and trafficking of polymer nanomedicines. Proetto *et al*. investigated the intracellular accumulation of ^{15}N-labeled polymer nanoparticles containing a covalently linked Pt(II)-based anticancer drug as well as a Cy5.5 fluorescent tag.[226] First, HeLa cells were incubated with the nanoparticles for 4 hours and subsequently analysed with fluorescence structured illumination microscopy (SIM). Co-localization of the nanoparticles with fluorescently labelled vesicles indicated cellular internalization *via* endocytosis. Analysis of ^{15}N and ^{195}Pt co-localization with NanoSIMS suggested significant release of the drug from the nanoparticles after 24 h as compared to 4 h incubation (**Figure 4A**). **Figure 4B** shows an overlay of SIM and NanoSIMS images. The overlaid images confirmed weak correlation between ^{195}Pt with the carrier signals at long incubation time. This example demonstrates the feasibility of using NanoSIMS combined with fluorescence microscopy as a tool to simultaneously monitor polymer and cargo in cells in a qualitative and quantitative manner and opened new possibilities for the monitoring of intracellular delivery processes.
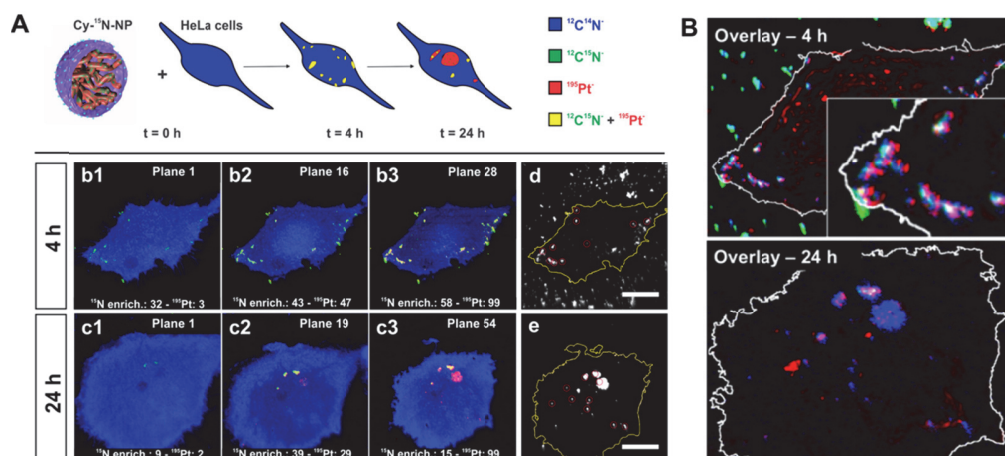
Figure 4. (A) Time dependent NanoSIMS analysis of HeLa cells treated with Cy-^{15}N-Pt for 4 h (b1-3) or 24 h (c1-3). Removal of layers of organic matter from the cell surface followed by imaging shows co-localization (yellow) of the ^{195}Pt (red) and ^{15}N (green) on the NP inside the cells. Red circles are the ROIs selected for ^{15}N/^{14}N quantification where ^{195}Pt counts are observed. The averaged ^{15}N and ^{195}Pt signals per selected Region of Interest (ROI) at each of the selected planes are shown for panels b and c. Scale bar represents 10 μm. (B) Overlay of NanoSIMS and SIM images showing the co-localization of the fluorescent tag (red) with ^{195}Pt (blue) and ^{15}N (green) after 4 and 24 h incubation. Overlay of ^{195}Pt and fluorescent tag is shown in magenta and overlay of ^{195}Pt, ^{15}N and fluorescent tag is represented in white. Adapted with permission from M. T. Proetto, C. R. Anderton, D. Hu, C. J. Szymanski, Z. Zhu, J. P. Patterson, J. K. Kammeyer, L. G. Nilewski, A. M. Rush, N. C. Bell, J. E. Evans, G. Orr, S. B. Howell, N. C. Gianneschi, Cellular Delivery of Nanoparticles Revealed with Combined Optical and Isotopic Nanoscopy, Acs Nano 2016, 10 (4), 4046-4054. Copyright (2016) American Chemical Society.[226]

1.3.2. Monitoring mitochondrial delivery

Mitochondrial targeting is generally assessed in co-localization experiments using CLSM. When the transported drug is fluorescent, such as e.g. doxorubicin, these experiments are relatively straightforward and only require the use of an appropriate mitochondrial marker.[26,157] In case of non-fluorescent cargo, this can be accomplished in model experiments with polymer nanomedicines that transport fluorescent dye instead of

the active compound. Cuchelkar *et al.* for example used a BOBIPY labeled PHPMA-TPP conjugates to validate mitochondrial targeting.[87] Alternatively, modification of the active compound such as oligonucleotides has also been used to investigate the mitochondrial co-localization.[151] Another possibility is to modify the polymer carrier with a suitable fluorescent dye.[153] The use of fluorescent, or fluorescent labeled, delocalized lipophilic cations (DLCs) is attractive as they simultaneously allow to target the mitochondria as well as to visualize the localization of the polymer nanomedicines in these organelles. For instance, enhanced mitochondrial targeting of liposomes modified with the DLC rhodamine-123 (Rho) was observed by co-localization studies with stained mitochondria.[160] In another example, PLA-PEG polymersomes were decorated with a naphthalene-modified TPP derivative, which enabled to directly visualize the co-localization of these nanoparticles with MitoView stained mitochondria.[159] Fluorescent quantum dots (QDs) have been also proposed to monitor mitochondria targeting. To this end, targeted and non-targeted nanoparticles were prepared by blending PLGA-*b*-PEG-QD with PLGA-*b*-PEG-TPP and with PLGA-*b*-PEG-OH, respectively. Fluorescence microscopy analysis of treated HeLa cells indicated significantly greater mitochondrial uptake of targeted nanoparticles as compared to non-targeted ones as shown in **Figure 5**.[155]
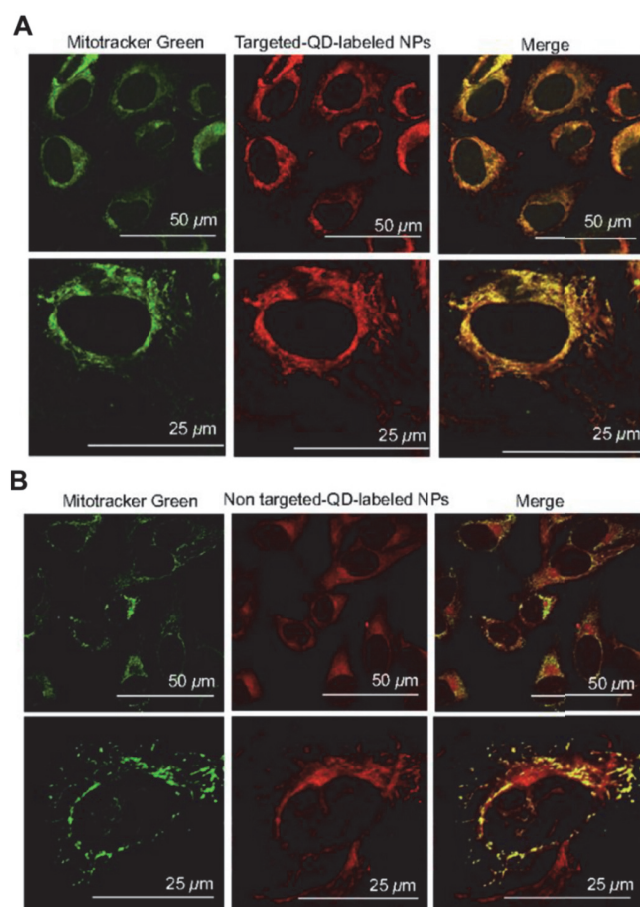
Figure 5. Subcellular localization of (A) red fluorescent-targeted PLGA-*b*-PEG-TPP/PLGA-*b*-PEG-QD and (B) non-targeted PLGA-*b*-PEG-OH/PLGA-*b*-PEG-QD blended nanoparticles (NPs). HeLa cells were exposed to targeted and non-targeted NPs at 10 μM for 4 h. The cells were then stained with the mitochondrial marker MitoTracker Green, fixed, and observed by wide-field fluorescence microscopy. The merged images and higher-magnification images show effective overlap of mitochondrial staining (green) and targeted NPs (red). No significant overlap was observed with non-targeted NPs. Adapted with permission from S. Marrache, S. Dhar, P*., Engineering of blended nanoparticle platform for delivery of mitochondria-acting therapeutics, Proceedings of the National Academy of Sciences of the United States of America, 2012, 109 (40), 16288-16293. Copyright (2012) National Academy of Sciences.[155]

1.3.3. Monitoring nuclear delivery

Nuclear targeting is generally visualized using CLSM *via* co-localization studies. This can be achieved by labeling the polymer carrier with a fluorescent dye and measuring the co-localization with the nucleus, which can be stained with nuclear specific markers such as DAPI, Hoechest 33342 and Draq 5.[79,169,172] Alternatively, the cargo can be tracked in case of fluorescent drugs such as doxorubicin[174] or when labeled pDNA are delivered.[176,179,180] Labeling both the polymer carrier and the cargo with a fluorescent dye allows to monitor release of the active compound, e.g. plasmid DNA.[170] In case of pDNA delivery, co-localization studies can also be correlated to transfection efficiency when reporter genes such as luciferase are used.[176]

Co-localization studies *via* CLSM, have also been used to answer specific questions such as the nuclear entry of nanoparticles during cell division. Symens *et al*. investigated the ability of fluorescent carboxylated polystyrene beads (100, 200 and 500 nm), which were either functionalized with Pluronic F127 or dimethylamine-ethylamine (DMAEA) to generate PEGylated and positive charged particles, to accumulate in the cell nucleus using an *in vitro* Xenopus nuclear envelope reassembly (XNER) assay. pDNA/PEI fluorescent polyplexes were also tested as a comparison. It was found that, 100 and 200 nm polystyrene particles were better included than the 500 nm ones and that positively charged polystyrene and PEI particles were better included than negatively charged or PEGylated polystyrene particles. Moreover, the coupling of chromatin-targeting peptides to the polystyrene beads or pDNA/PEI complex improved their inclusion by 2- to 3-fold. An unexpected but interesting result was obtained upon direct microinjection of the particles in the cytoplasm of HeLa cells. In this case, the nanoparticles were never observed in the nuclei of cells post-division but accumulated instead in specific perinuclear regions. **Figure 6A** represent an example of images of the distribution of 100 nm positively charged polystyrene beads (green), pDNA/PEI polyplexes (red) and chromatin-targeted pDNA/PEI polyplexes (red) in Hela cells during cell division. In order to investigate the site of the particles, cells were stained with early endosomal and lysosomal markers (green) and red polystyrene beads were used instead of green ones to prevent signal overlap. As shown in **Figure 6B**, the nanoparticles were never co-localized with early endocytic vesicles, however, 24 hours post-injection high co-localization was observed with lysosomal vesicles. These results demonstrate that nanoparticles can accumulate in the lysosomes even if they have not been internalized *via* endocytosis.[227]
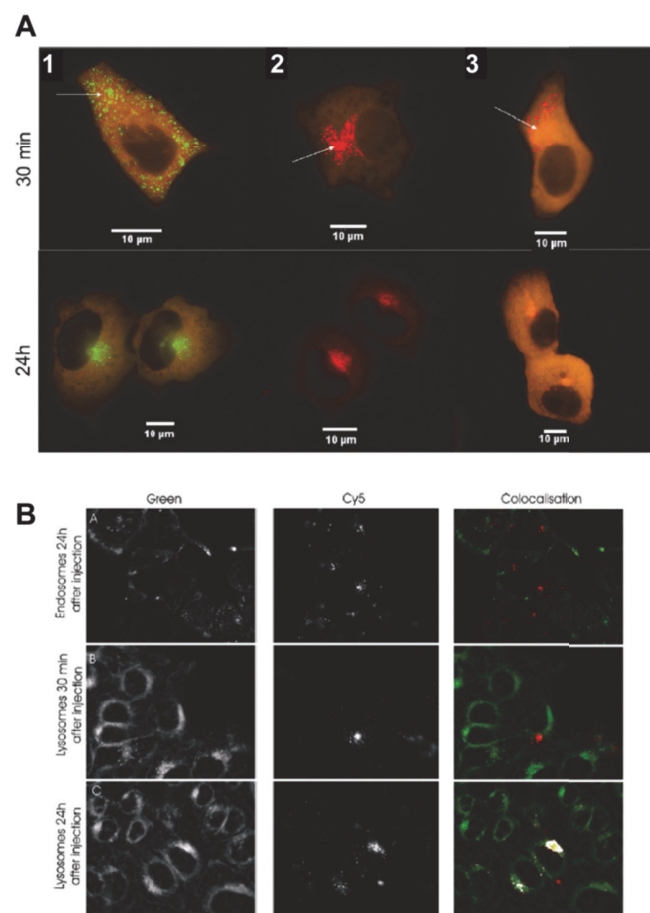
Figure 6. (A) Intracellular distribution upon microinjection of nanoparticles in HeLa cells. 100 nm polystyrene beads positively charged are labeled in green (1), 170 nm pDNA/PEI polyplexes positively charged are labeled in red (2) and 240 nm chromatin-targeted pDNA/PEI polyplexes positively charged are labeled in red (3). 70 kDa TRITC dextran (orange) was used to identify the place of injection and whether or not the cells divide. Pictures of the injected cells were taken 30 min (top panel) and 24 hours (bottom panel) after injection. (B) Identification of the perinuclear region upon microinjection of red polystyrene beads in HeLa cells. Pictures of the injected cells were taken 30 min or 24 hours after injection. The green panel shows the labeling of the endosomes (top panel) or the lysosomes (bottom panels). The Cy5 panel shows the injected red beads. Co-localized pixels appear white in the co-localization image. Adapted with permission from N. Symens, R. Walczak, J. Demeester, I. Mattaj, S. C. De Smedt, K. Remaut, Nuclear Inclusion of Nontargeted and Chromatin-Targeted Polystyrene Beads and Plasmid DNA Containing Nanoparticles, Molecular Pharmaceutics, 2011, 8 (5), 1757-1766. Copyright (2011) American Chemical Society. [227]

44

Combining CLSM with quantum dots mediated Förster resonance energy transfer (QDs-FRET) does not only allow to visualize nuclear targeting but also enables to monitor nucleic acid release. In one example, hydrophobic CdSe/ZnS QDs were loaded in the core of PEG-PCL-PEI based nanocarriers that were used to release Alexa Fluor 647 (AF647)-labeled siRNA. *In vitro* experiments with SKOV3 cells revealed co-localization of the carrier and the siRNA in the form of intact polyplexes in the cytosol.[228] Shaheen *et al.* also used QDs-FRET to monitor decondensation of pDNA in the nuclear subdomains. In this study, polyplexes of QD-labeled pDNA and a rhodamine-labeled cationic polyrotaxane (PRX) were entrapped in a tetra-lamellar multifunctional envelope-type nanodevice (T-MEND), which was designed to overcome the endosomal and nuclear membranes, respectively. CLSM was used to investigate the subcellular distribution and pDNA/polycation dissociation. To this end, the nuclear subdomains were distinguished by Hoechst 33342 staining and pDNA condensation/decondensation was quantified based on the pixel area of the signals derived from the QDs and rhodamine. In particular, some red clusters with a maximum peak at 590 nm (Rhodamine) were localized in the cytoplasm and nucleus, suggesting the presence of pDNA in the condensed form. Green signals at 550 nm (QDs), which derive from the pDNA dissociation, were localized in the nucleus. Finally, the pixel areas of red, green and yellow (partial dissociation) cluster, in the nuclear euchromatin and heterochromatin regions were independently integrated and quantified.[229] Chen *et al.* investigated the intracellular uptake and dissociation of polyplexes through QD-FRET at different incubation times in HEK 293 cells. To this purpose, pDNA and the polymeric carrier were individually labeled with quantum dots (QDs) and Cy5 dyes, respectively, as a FRET donor and acceptor. Co-localization studies allowed the quantitative analysis of the distribution of released plasmid within the endo/lysosomal, cytosolic, and nuclear compartments. Polyplex unpacking kinetics for chitosan, polyethylenimine and polyphosphoramidate-based polyplexes were measured and found to correlate well with the transcription efficiencies.[230] Bryson *et al.* combined fluorescent microscopy with MRI to visualize pDNA delivery at different biological length scales. This was accomplished using oligoethyleneamine-based polycations that incorporated either luminescent europium (Eu^{3+}) or paramagnetic gadolinium (Gd^{3+}) chelators.[231] The use of Gd^{3+} enables MRI of bulk cells, which showed bright image contrast and allowed the visualization of effective intracellular delivery on the tissue scale. At the nm/µm length scale, pDNA delivery was measured by fluorescence microscopy using the Eu^{3+} labeled beacons and FITC labeled pDNA. Co-localization of

FITC-pDNA and Eu^{3+} polymer luminescence could be observed as cytoplasmic punctate staining and a lower fraction was localized in the cell nucleus, which was proposed as a contributing factor to the low luciferase reporter gene expression that was obtained.

1.3.4. Monitoring Golgi Apparatus (GA) and Endoplasmic Reticulum (ER) delivery

ER and GA delivery can be monitored with co-localization studies using dye-labeled carriers[183] or fluorescent drugs[232] and GA and ER compartments stained with specific fluorescent markers. Vivero-Escoto and co-workers performed detailed studies to assess the intracellular trafficking pathways of fluorescein-labeled mesoporous silica nanoparticles (FMSNs) that presented the cholera toxin subunit B (CTxB) tethered *via* a PEG spacer on their surface. As controls, unmodified fluorescein-labeled MSNs (FMSNs) and PEG modified FMSNs (PEGC-MSNs) were used. Intracellular trafficking was studied by CLSM using lysosomal, ER and GA specific stains. FMSNs and PEGC-FMSNs were co-localized exclusively in the cell lysosomes. Interestingly, a significantly lower amount of CTxB-FMSNs was found in the lysosomes. Co-localization of CTxB-FMSNs with the GA confirmed that a certain number of CTxB-FMSN particles targeted the GA following uptake and a little amount was finally localized in the ER. In a second step, the ability of the CTxB-FMSN particles to deliver a model fluorescent dye to ER was investigated. To this end, propidium iodide (PI) loaded particles were incubated with Hela cells for 1 hour. Imaging 24 hours post-incubation revealed the co-localization of PI with ER, indicating that the membrane impermeable dye was transported by the CTxB-FMSN particles *via* the GA and finally accumulated in the ER.[181]

QDs have also been used to monitor trafficking of polymer nanomedicines to the ER and GA. In one example Shen *et al*. prepared Si-QDs coated with Pluronic F127 and demonstrated the selective labeling of the ER within live human umbilical vein endothelial cells (HUVECs).[184] Gao *et al*. encapsulated CdSe/ZnS QDs in the core of PEG-*b*-PLA nanoparticles, which were subsequently functionalized to present wheat germ agglutinin (WGA) on the surface. Co-localization studies revealed that the cellular uptake occurred *via* WGA-mediated receptor endocytosis and both clathrin and caveolae-mediated mechanisms were involved. Intracellular tracking of the carried QDs revealed

co-localization of the nanoparticles with both GA and lysosomes.[185]

1.4. Conclusions

Polymer conjugates and other polymer-based nanocarriers have been shown to be very efficient to improve the delivery of chemotherapeutics. There are, however, still various important (and scientifically interesting) challenges ahead, which if they can be addressed, will help to further improve the performance of polymer-based anticancer nanomedicines. One important objective (which is outside the scope of this Thesis) is to improve control on biodistribution as most *in vivo* studies still show very significant accumulation of polymer nanomedicines in off-target organs. Also on the cellular level there are several challenges. How to design nanomedicines that are efficiently internalized by cancer cells? In addition to clathrin-mediated endocytosis, are there other internalization pathways that can be used? Can polymer nanomedicines be designed in such a way that their intracellular trafficking pathways can be guided to the location where the drug is needed? The last questions are particularly pertinent in case of delivery of biologics that are prone to degrade. The aim of this chapter has been to illustrate the progress that has been made towards answering (some of) these questions. This progress rests on three pillars: (i) cell biology and the continuously growing insights in cellular internalization and trafficking mechanisms and pathways; (ii) polymer science and the ever growing possibilities to synthesize carriers and particles and (iii) biological imaging and analysis techniques, which make it possible to study live cells and provide resolutions that now proves insights at the subcellular level. The examples discussed in this chapter, show that, while great advances have been made in controlling cellular internalization and intracellular trafficking pathways, there is still room and need for further improvement. We are confident that further advances at the exciting intersection of cell biology, polymer science and biological analysis and imaging will pave the way to a further improved polymer nanomedicines and therapies.

1.5. References

(1)   Duncan, R., *Nat. Rev. Cancer* **2006**, *6*, 688.

(2)   Wang, A. Z.; Langer, R.; Farokhzad, O. C., *Annu. Rev. Med.* **2012**, *63*, 185.

(3)   Maeda, H.; Nakamura, H.; Fang, J., *Adv. Drug. Deliver. Rev.* **2013**, *65*, 71.

(4)   Bareford, L. A.; Swaan, P. W., *Adv. Drug. Deliver. Rev.* **2007**, *59*, 748.

(5)   Akinc, A.; Battaglia, G., *Csh Perspect. Biol.* **2013**, *5*.

(6)   Duncan, R.; Richardson, S. C. W., *Mol. Pharm.* **2012**, *9*, 2380.

(7)   Gruenberg, J., *Nat. Rev. Mol. Cell. Biol.* **2001**, *2*, 721.

(8)   Bertrand, N.; Wu, J.; Xu, X. Y.; Kamaly, N.; Farokhzad, O. C., *Adv. Drug. Deliver. Rev.* **2014**, *66*, 2.

(9)   Zwicke, G. L.; Mansoori, G. A.; Jeffery, C. J., *Nano Rev.* **2012**, *3*.

(10)   Ye, W. L.; Du, J. B.; Zhang, B. L.; Na, R.; Song, Y. F.; Mei, Q. B.; Zhao, M. G.; Zhou, S. Y., *PloS one* **2014**, *9*, e97358.

(11)   Zhou, Z. X.; Shen, Y. Q.; Tang, J. B.; Fan, M. H.; Van Kirk, E. A.; Murdoch, W. J.; Radosz, M., *Adv. Funct. Mater.* **2009**, *19*, 3580.

(12)   Byrne, J. D.; Betancourt, T.; Brannon-Peppas, L., *Adv. Drug. Deliver. Rev.* **2008**, *60*, 1615.

(13)   Nasongkla, N.; Shuai, X.; Ai, H.; Weinberg, B. D.; Pink, J.; Boothman, D. A.; Gao, J., *Angew. Chem. Int. Ed.* **2004**, *43*, 6323.

(14)   Graf, N.; Bielenberg, D. R.; Kolishetti, N.; Muus, C.; Banyard, J.; Farokhzad, O. C.; Lippard, S. J., *ACS nano* **2012**, *6*, 4530.

(15)   Herbst, R. S.; Shin, D. M., *Cancer* **2002**, *94*, 1593.

(16)   Master, A. M.; Sen Gupta, A., *Nanomedicine* **2012**, *7*, 1895.

(17)   Lee, J. S.; Groothuis, T.; Cusan, C.; Mink, D.; Feijen, J., *Biomaterials* **2011**, *32*, 9144.

(18)   Hoang, B.; Reilly, R. M.; Allen, C., *Biomacromolecules* **2012**, *13*, 455.

(19)   Mann, K.; Kullberg, M., *Cancer Gene Ther.* **2016**, *23*, 221.

(20)   Bellocq, N. C.; Pun, S. H.; Jensen, G. S.; Davis, M. E., *Bioconjug. Chem.* **2003**, *14*, 1122.

(21)   Wagner, E.; Plank, C.; Zatloukal, K.; Cotten, M.; Birnstiel, M. L., *Proc. Natl. Acad. Sci. USA* **1992**, *89*, 7934.

(22)   Pack, D. W.; Putnam, D.; Langer, R., *Biotechnol. Bioeng.* **2000**, *67*, 217.

(23)   Sasaki, K.; Kogure, K.; Chaki, S.; Nakamura, Y.; Moriguchi, R.; Hamada, H.; Danev, R.; Nagayama, K.; Futaki, S.; Harashima, H., *Anal. Bioanal. Chem.* **2008**, *391*, 2717.

(24)   Kursa, M.; Walker, G. F.; Roessler, V.; Ogris, M.; Roedl, W.; Kircheis, R.; Wagner, E., *Bioconjug. Chem.* **2003**, *14*, 222.

(25)   Fitzgerald, K. A.; Malhotra, M.; Gooding, M.; Sallas, F.; Evans, J. C.; Darcy, R.; O'Driscoll, C. M., *Int. J. Pharm.* **2016**, *499*, 131.

(26)   Song, Y. F.; Liu, D. Z.; Cheng, Y.; Liu, M.; Ye, W. L.; Zhang, B. L.; Liu, X. Y.; Zhou, S. Y., *Sci. Rep.* **2015**, *5*.

(27)   Lu, L.; Zou, Y.; Yang, W. J.; Meng, F. H.; Deng, C.; Cheng, R.; Zhong, Z. Y., *Biomacromolecules* **2015**, *16*, 1726.

(28)   Liu, J.; Huang, Y. R.; Kumar, A.; Tan, A.; Jin, S. B.; Mozhi, A.; Liang, X. J., *Biotechnol. Adv.* **2014**, *32*, 693.

(29)   Mura, S.; Nicolas, J.; Couvreur, P., *Nat. Mater.* **2013**, *12*, 991.

(30)   Kanamala, M.; Wilson, W. R.; Yang, M. M.; Palmer, B. D.; Wu, Z. M., *Biomaterials* **2016**, *85*, 152.

(31)   Binauld, S.; Stenzel, M. H., *Chem. Commun.* **2013**, *49*, 2082.

(32)   Meng, F. H.; Zhong, Y. A.; Cheng, R.; Deng, C.; Zhong, Z. Y., *Nanomedicine* **2014**, *9*, 487.

(33)   Meng, F. H.; Cheng, R.; Deng, C.; Zhong, Z. Y., *Mater. Today* **2012**, *15*, 436.

(34)   Knorr, V.; Russ, V.; Allmendinger, L.; Ogris, M.; Wagner, E., *Bioconjug. Chem.* **2008**, *19*, 1625.

(35)   Tomlinson, R.; Heller, J.; Brocchini, S.; Duncan, R., *Bioconjug. Chem.* **2003**, *14*, 1096.

(36)   Gillies, E. R.; Goodwin, A. P.; Frechet, J. M. J., *Bioconjug. Chem.* **2004**, *15*, 1254.

(37)   Huang, F. S.; Cheng, R.; Meng, F. H.; Deng, C.; Zhong, Z. Y., *Biomacromolecules* **2015**, *16*, 2228.

(38)   Wang, L.; Liu, G. H.; Wang, X. R.; Hu, J. M.; Zhang, G. Y.; Liu, S. Y., *Macromolecules* **2015**, *48*, 7262.

(39)   Liu, X. F.; Yaszemski, M. J.; Lu, L. C., *Biomater. Sci.* **2016**, *4*, 245.

(40)   Wang, Y.; Chang, B. S.; Yang, W. L., *J. Nanosci. Nanotechno.* **2012**, *12*, 8266.

(41)   Thambi, T.; Deepagan, V. G.; Yoo, C. K.; Park, J. H., *Polymer* **2011**, *52*, 4753.

(42)   Tang, R. P.; Ji, W. H.; Wang, C., *Macromol. Biosci.* **2010**, *10*, 192.

(43)   Qiao, Z. Y.; Cheng, J.; Ji, R.; Du, F. S.; Liang, D. H.; Ji, S. P.; Li, Z. C., *Rsc Adv.* **2013**, *3*, 24345.

(44)   Li, J. G.; Zhang, L.; Lin, Y. J.; Xiao, H.; Zuo, M. X.; Cheng, D.; Shuai, X. T., *Rsc Adv.* **2016**, *6*, 9160.

(45)   Mao, J.; Li, Y.; Wu, T.; Yuan, C. H.; Zeng, B. R.; Xu, Y. T.; Dai, L. Z., *Acs Appl. Mater. Inter.* **2016**, *8*, 17109.

(46)   Qiu, L.; Hong, C. Y.; Pan, C. Y., *Int. J. Nanomed.* **2015**, *10*, 3623.

(47)   Wang, Y.; Luo, Q. J.; Sun, R.; Zha, G. Y.; Li, X. D.; Shen, Z. Q.; Zhu, W. P., *J. Mater. Chem. B* **2014**, *2*, 7612.

(48)   Zhang, Y. M.; Yang, C. H.; Wang, W. W.; Liu, J. J.; Liu, Q.; Huang, F.; Chu, L. P.; Gao, H. L.; Li, C.; Kong, D. L.; Liu, Q.; Liu, J. F., *Sci. Rep.* **2016**, *6*.

(49)   Jin, Y.; Song, L.; Su, Y.; Zhu, L. J.; Pang, Y.; Qiu, F.; Tong, G. S.; Yan, D. Y.; Zhu, B. S.; Zhu, X. Y., *Biomacromolecules* **2011**, *12*, 3460.

(50)   Liu, B.; Chen, H. Y.; Li, X.; Zhao, C. N.; Liu, Y. K.; Zhu, L. J.; Deng, H. P.; Li, J. C.; Li, G. L.; Guo, F. L.; Zhu, X. Y., *Rsc Adv.* **2014**, *4*, 48943.

(51)   Jiang, L.; Gao, Z. M.; Ye, L.; Zhang, A. Y.; Feng, Z. G., *Biomater. Sci.* **2013**, *1*, 1282.

(52)   Guan, X. W.; Li, Y. H.; Jiao, Z. X.; Lin, L. L.; Chen, J.; Guo, Z. P.; Tian, H. Y.; Chen, X. S., *Acs Appl. Mater. Inter.* **2015**, *7*, 3207.

(53)   Rihova, B.; Etrych, T.; Pechar, M.; Jelinkova, M.; Stastny, M.; Hovorka, O.; Kovar, M.; Ulbrich, K., *J. Control. Release* **2001**, *74*, 225.

(54)   Etrych, T.; Chytil, P.; Jelinkova, M.; Rihova, B.; Ulbrich, K., *Macromol. Biosci.* **2002**, *2*, 43.

(55)   Ulbrich, K.; Etrych, T.; Chytil, P.; Jelinkova, M.; Rihova, B., *J. Control. Release* **2003**, *87*, 33.

(56)   Rihova, B.; Etrych, T.; Sirova, M.; Kovar, L.; Hovorka, O.; Kovar, M.; Benda, A.; Ulbrich, K., *Mol. Pharm.* **2010**, *7*, 1027.

(57)   Etrych, T.; Subr, V.; Laga, R.; Rihova, B.; Ulbrich, K., *Eur. J. Pharm. Sci.* **2014**, *58*, 1.

(58)   Subr, V.; Sivak, L.; Koziolova, E.; Braunova, A.; Pechar, M.; Strohalm, J.; Kabesova, M.; Rihova, B.; Ulbrich, K.; Kovar, M., *Biomacromolecules* **2014**, *15*, 3030.

(59)   Etrych, T.; Sirova, M.; Starovoytova, L.; Rihova, B.; Ulbrich, K., *Mol. Pharm.* **2010**, *7*, 1015.

(60)   Li, L.; Sun, W.; Zhong, J. J.; Yang, Q. Q.; Zhu, X.; Zhou, Z.; Zhang, Z. R.; Huang, Y., *Adv. Funct. Mater.* **2015**, *25*, 4101.

(61)   Jager, E.; Jager, A.; Chytil, P.; Etrych, T.; Rihova, B.; Giacomelli, F. C.; Stepanek, P.; Ulbrich, K., *J. Control. Release* **2013**, *165*, 153.

(62)   Lai, P. S.; Lou, P. J.; Peng, C. L.; Pai, C. L.; Yen, W. N.; Huang, M. Y.; Young, T. H.; Shieh, M. J., *J. Control. Release* **2007**, *122*, 39.

(63)   Chang, Y. L.; Liu, N. A.; Chen, L.; Meng, X. L.; Liu, Y. J.; Li, Y. P.; Wang, J. Y., *J. Mater. Chem.* **2012**, *22*, 9594.

(64)   Koutroumanis, K. P.; Holdich, R. G.; Georgiadou, S., *Int. J. Pharm.* **2013**, *455*, 5.

(65)   Kale, A. A.; Torchilin, V. P., *Bioconjug. Chem.* **2007**, *18*, 363.

(66)   Hami, Z.; Amini, M.; Ghazi-Khansari, M.; Rezayat, S. M.; Gilani, K., *Colloids Surf. B* **2014**, *116*, 309.

(67)   Wang, X.; Wu, G.; Lu, C.; Zhao, W.; Wang, Y.; Fan, Y.; Gao, H.; Ma, J., *Eur. J. Pharm. Sci.* **2012**, *47*, 256.

(68)   Su, Z. H.; Liang, Y. C.; Yao, Y.; Wang, T. Q.; Zhang, N., *J. Mater. Chem. B* **2016**, *4*, 1122.

(69)   Zhong, Y. J.; Shao, L. H.; Li, Y., *Int. J. Oncol.* **2013**, *42*, 373.

(70)   Rihova, B.; Bilej, M.; Vetvicka, V.; Ulbrich, K.; Strohalm, J.; Kopecek, J.; Duncan, R., *Biomaterials* **1989**, *10*, 335.

(71)   Rejmanova, P.; Kopecek, J.; Pohl, J.; Baudys, M.; Kostka, V., *Makromol. Chem.* **1983**, *184*, 2009.

(72)   Kopecek, J.; Kopeckova, P.; Minko, T.; Lu, Z. R., *Eur. J. Pharm. Biopharm.* **2000**, *50*, 61.

(73)   Gianasi, E.; Wasil, M.; Evagorou, E. G.; Keddle, A.; Wilson, G.; Duncan, R., *Eur. J. Cancer* **1999**, *35*, 994.

(74)   Malugin, A.; Kopeckova, P.; Kopecek, J., *J. Control. Release* **2007**, *124*, 6.

(75)   Zhang, R.; Yang, J. Y.; Sima, M.; Zhou, Y.; Kopecek, J., *Proc. Natl. Acad. Sci. USA* **2014**, *111*, 12181.

(76)   Yang, J. Y.; Zhang, R.; Radford, D. C.; Kopecek, J., *J. Control. Release* **2015**, *218*, 36.

(77)   Minko, T.; Kopeckova, P.; Pozharov, V.; Kopecek, J., *J. Control. Release* **1998**, *54*, 223.

(78)   Lammers, T.; Subr, V.; Ulbrich, K.; Peschke, P.; Huber, P. E.; Hennink, W. E.; Storm, G., *Biomaterials* **2009**, *30*, 3466.

(79)   Zhong, J. J.; Li, L.; Zhu, X.; Guan, S.; Yang, Q. Q.; Zhou, Z.; Zhang, Z. R.; Huang, Y., *Biomaterials* **2015**, *65*, 43.

(80)   Lee, S. J.; Jeong, Y. I.; Park, H. K.; Kang, D. H.; Oh, J. S.; Lee, S. G.; Lee, H. C., *Int. J. Nanomed.* **2015**, *10*, 5489.

(81)   Zhang, C. Y.; Pan, D. Y.; Luo, K.; She, W. C.; Guo, C. H.; Yang, Y.; Gu, Z. W., *Adv. Healthc. Mater.* **2014**, *3*, 1299.

(82)   Zhang, C. Y.; Pan, D. Y.; Luo, K.; Li, N.; Guo, C. H.; Zheng, X. L.; Gu, Z. W., *Polym. Chem.* **2014**, *5*, 5227.

(83)   Li, N.; Li, N.; Yi, Q.; Luo, K.; Guo, C.; Pan, D.; Gu, Z., *Biomaterials* **2014**, *35*, 9529.

(84)   Veronese, F. M.; Schiavon, O.; Pasut, G.; Mendichi, R.; Andersson, L.; Tsirk, A.; Ford, J.; Wu, G. F.; Kneller, S.; Davies, J.; Duncan, R., *Bioconjug. Chem.* **2005**, *16*, 775.

(85)   Cheng, Y. J.; Cheng, H.; Zhao, X.; Xu, X. D.; Zhuo, R. X.; He, F., *Polym. Chem.* **2015**, *6*, 3512.

(86)   Cheng, R.; Feng, F.; Meng, F. H.; Deng, C.; Feijen, J.; Zhong, Z. Y., *J. Control. Release* **2011**, *152*, 2.

(87)   Cuchelkar, V.; Kopeckova, P.; Kopecek, J., *Mol. Pharm.* **2008**, *5*, 776.

(88)   Cuchelkar, V.; Kopeckova, P.; Kopecek, J., *Macromol. Biosci.* **2008**, *8*, 375.

(89)   Cao, Y.; Gao, M.; Chen, C.; Fan, A.; Zhang, J.; Kong, D.; Wang, Z.; Peer, D.; Zhao, Y., *Nanotechnology* **2015**, *26*, 115101.

(90)   Zou, Y.; Fang, Y.; Meng, H.; Meng, F.; Deng, C.; Zhang, J.; Zhong, Z., *J. Control. Release* **2016**.

(91)   Yan, Q. F.; Yang, Y. C.; Chen, W. L.; Hu, J. H.; Yang, D., *Mat. Sci. Eng. C-Mater.* **2016**, *58*, 580.

(92)   Liu, Y. S.; Huang, S. J.; Huang, X. S.; Wu, Y. T.; Chen, H. Y.; Lo, Y. L.; Wang, L. F., *Rsc Adv.* **2016**, *6*, 75092.

(93)   Zhang, X. J.; Dong, H.; Fu, S. L.; Zhong, Z. L.; Zhuo, R. X., *Macromol. Rapid Commun.* **2016**, *37*, 993.

(94)   Zou, Y.; Meng, F.; Deng, C.; Zhong, Z., *J. Control. Release* **2016**, *239*, 149.

(95)   Cerritelli, S.; Velluto, D.; Hubbell, J. A., *Biomacromolecules* **2007**, *8*, 1966.

(96)   Thambi, T.; Deepagan, V. G.; Ko, H.; Lee, D. S.; Park, J. H., *J. Mater. Chem.* **2012**, *22*, 22028.

(97)   Shi, L.; Ding, K.; Sun, X.; Zhang, L.; Zeng, T.; Yin, Y.; Zheng, H., *J. Biomater. Sci., Polym. Ed.* **2016**, *27*, 472.

(98)   Xu, H. P.; Cao, W.; Zhang, X., *Acc. Chem. Res.* **2013**, *46*, 1647.

(99)   Li, C. T.; Huang, W.; Zhou, L. Z.; Huang, P.; Pang, Y.; Zhu, X. Y.; Yan, D. Y., *Polym. Chem.* **2015**, *6*, 6498.

(100)   Deepagan, V. G.; Kwon, S.; You, D. G.; Nguyen, V. Q.; Um, W.; Ko, H.; Lee, H.; Jo, D. G.; Kang, Y. M.; Park, J. H., *Biomaterials* **2016**, *103*, 56.

(101)   Liu, J. Y.; Pang, Y.; Zhu, Z. Y.; Wang, D. L.; Li, C. T.; Huang, W.; Zhu, X. Y.; Yan, D. Y., *Biomacromolecules* **2013**, *14*, 1627.

(102)   Pack, D. W.; Hoffman, A. S.; Pun, S.; Stayton, P. S., *Nat. Rev. Drug. Discov.* **2005**, *4*, 581.

(103)   Lungwitz, U.; Breunig, M.; Blunk, T.; Gopferich, A., *Eur. J. Pharm. Biopharm.* **2005**, *60*, 247.

(104)   Boussif, O.; Lezoualch, F.; Zanta, M. A.; Mergny, M. D.; Scherman, D.; Demeneix, B.; Behr, J. P., *Proc. Natl. Acad. Sci. USA* **1995**, *92*, 7297.

(105)   Wagner, E.; Ogris, M.; Zauner, W., *Adv. Drug. Deliver. Rev.* **1998**, *30*, 97.

(106)   Plank, C.; Zatloukal, K.; Cotten, M.; Mechtler, K.; Wagner, E., *Bioconjug. Chem.* **1992**, *3*, 533.

(107)   Petersen, H.; Fechner, P. M.; Martin, A. L.; Kunath, K.; Stolnik, S.; Roberts, C. J.; Fischer, D.; Davies, M. C.; Kissel, T., *Bioconjug. Chem.* **2002**, *13*, 845.

(108)   Breunig, M.; Lungwitz, U.; Liebl, R.; Goepferich, A., *Proc. Natl. Acad. Sci. USA* **2007**, *104*, 14454.

(109)   Kadlecova, Z.; Baldi, L.; Hacker, D.; Wurm, F. M.; Klok, H. A., *Biomacromolecules* **2012**, *13*, 3127.

(110)   Zhao, N.; Roesler, S.; Kissel, T., *Int. J. Pharm.* **2011**, *411*, 197.

(111)   Rimann, M.; Luhmann, T.; Textor, M.; Guerino, B.; Ogier, J.; Hall, H., *Bioconjug. Chem.* **2008**, *19*, 548.

(112)   Lee, H.; Jeong, J. H.; Park, T. G., *J. Control. Release* **2002**, *79*, 283.

(113)   Tappertzhofen, K.; Beck, S.; Montermann, E.; Huesmann, D.; Barz, M.; Koynov, K.; Bros, M.; Zentel, R., *Macromol. Biosci.* **2016**, *16*, 106.

(114)   Tappertzhofen, K.; Weiser, F.; Montermann, E.; Reske-Kunz, A.; Bros, M.; Zentel, R., *Macromol. Biosci.* **2015**, *15*, 1159.

(115)   Hunter, A. C., *Adv. Drug. Deliver. Rev.* **2006**, *58*, 1523.

(116)   Shi, J.; Johnson, R. N.; Schellinger, J. G.; Carlson, P. M.; Pun, S. H., *Int. J. Pharm.* **2012**, *427*, 113.

(117)   Thomas, M.; Klibanov, A. M., *Proc. Natl. Acad. Sci. USA* **2002**, *99*, 14640.

(118)   Forrest, M. L.; Meister, G. E.; Koerber, J. T.; Pack, D. W., *Pharm. Res.* **2004**, *21*, 365.

(119)   Gabrielson, N. P.; Pack, D. W., *Biomacromolecules* **2006**, *7*, 2427.

(120)   Paul, A.; Eun, C. J.; Song, J. M., *Polymer* **2014**, *55*, 5178.

(121)   Kaur, D.; Jain, K.; Mehra, N. K.; Kesharwani, P.; Jain, N. K., *J. Nanopart. Res.* **2016**, *18*.

(122)   Dufes, C.; Uchegbu, I. F.; Schatzlein, A. G., *Adv. Drug. Deliver. Rev.* **2005**, *57*, 2177.

(123)   Haensler, J.; Szoka, F. C., *Bioconjug. Chem.* **1993**, *4*, 372.

(124)   KukowskaLatallo, J. F.; Bielinska, A. U.; Johnson, J.; Spindler, R.; Tomalia, D. A.; Baker, J. R., *Proc. Natl. Acad. Sci. USA* **1996**, *93*, 4897.

(125)   Patil, M. L.; Zhang, M.; Minko, T., *ACS nano* **2011**, *5*, 1877.

(126)   Putnam, D.; Gentry, C. A.; Pack, D. W.; Langer, R., *Proc. Natl. Acad. Sci. USA* **2001**, *98*, 1200.

(127)   Midoux, P.; Monsigny, M., *Bioconjug. Chem.* **1999**, *10*, 406.

(128)   Convertine, A. J.; Benoit, D. S. W.; Duvall, C. L.; Hoffman, A. S.; Stayton, P. S., *J. Control. Release* **2009**, *133*, 221.

(129)   Miyata, K.; Oba, M.; Nakanishi, M.; Fukushima, S.; Yamasaki, Y.; Koyama, H.; Nishiyama, N.; Kataoka, K., *J. Am. Chem. Soc.* **2008**, *130*, 16287.

(130)   Zhang, Y.; Lundberg, P.; Diether, M.; Porsch, C.; Janson, C.; Lynd, N. A.; Ducani, C.; Malkoch, M.; Malmstrom, E.; Hawker, C. J.; Nystrom, A. M., *J. Mater. Chem. B* **2015**, *3*, 2472.

(131)   Berguig, G. Y.; Convertine, A. J.; Frayo, S.; Kern, H. B.; Procko, E.; Roy, D.; Srinivasan, S.; Margineantu, D. H.; Booth, G.; Palanca-Wessels, M. C.; Baker, D.; Hockenbery, D.; Press, O. W.; Stayton, P. S., *Mol. Ther.* **2015**, *23*, 907.

(132)   Zhang, X. J.; Chen, D. W.; Ba, S.; Chang, J.; Zhou, J. Y.; Zhao, H. X.; Zhu, J.; Zhao, X. L.; Hu, H. Y.; Qiao, M. X., *Colloids Surf. B* **2016**, *140*, 176.

(133)   Yin, H. Q.; Lee, E. S.; Kim, D.; Lee, K. H.; Oh, K. T.; Bae, Y. H., *J. Control. Release* **2008**, *126*, 130.

(134)   Maeda, Y.; Pittella, F.; Nomoto, T.; Takemoto, H.; Nishiyama, N.; Miyata, K.; Kataoka, K., *Macromol. Rapid Commun.* **2014**, *35*, 1211.

(135)   Shen, Y. Q.; Zhou, Z. X.; Sui, M. H.; Tang, J. B.; Xu, P. S.; Van Kirk, E. A.; Murdoch, W. J.; Fan, M. H.; Radosz, M., *Nanomedicine* **2010**, *5*, 1205.

(136)   Lee, E. S.; Kim, D.; Youn, Y. S.; Oh, K. T.; Bae, Y. H., *Angew. Chem. Int. Edit.* **2008**, *47*, 2418.

(137)   Varkouhi, A. K.; Scholte, M.; Storm, G.; Haisma, H. J., *J. Control. Release* **2011**, *151*, 220.

(138)   Funhoff, A. M.; Van Nostrum, C. F.; Lok, M. C.; Kruijtzer, J. A. W.; Crommelin, D. J. A.; Hennink, W. E., *J. Control. Release* **2005**, *101*, 233.

(139)   Funhoff, A. M.; van Nostrum, C. F.; Lok, M. C.; Fretz, M. M.; Crommelin, D. J. A.; Hennink, W. E., *Bioconjug. Chem.* **2004**, *15*, 1212.

(140)   Jeong, J. H.; Kim, S. W.; Park, T. G., *Bioconjug. Chem.* **2003**, *14*, 473.

(141)   Kwon, E. J.; Bergen, J. M.; Pun, S. H., *Bioconjug. Chem.* **2008**, *19*, 920.

(142)   Schellinger, J. G.; Pahang, J. A.; Johnson, R. N.; Chu, D. S. H.; Sellers, D. L.; Maris, D. O.; Convertine, A. J.; Stayton, P. S.; Horner, P. J.; Pun, S. H., *Biomaterials* **2013**, *34*, 2318.

(143)   Lavignac, N.; Lazenby, M.; Franchini, J.; Ferruti, P.; Duncan, R., *Int. J. Pharm.* **2005**, *300*, 102.

(144)   Chollet, P.; Favrot, M. C.; Hurbin, A.; Coll, J. L., *J. Gene Med.* **2002**, *4*, 84.

(145)   Li, W. J.; Nicol, F.; Szoka, F. C., *Adv. Drug. Deliver. Rev.* **2004**, *56*, 967.

(146)   Zhang, E. L.; Zhang, C.; Su, Y. P.; Cheng, T. M.; Shi, C. M., *Drug. Discov. Today* **2011**, *16*, 140.

(147)   Yamada, Y.; Harashima, H., *Adv. Drug. Deliver. Rev.* **2008**, *60*, 1439.

(148)   Yoon, Y. G.; Koob, M. D.; Yoo, Y. H., *Anat. Cell Biol.* **2010**, *43*, 97.

(149)   Pathak, R. K.; Kolishetti, N.; Dhar, S., *Wires Nanomed. Nanobi.* **2015**, *7*, 315.

(150)   Lee, M.; Choi, J. S.; Choi, M. J.; Pak, Y. K.; Rhee, B. D.; Ko, K. S., *J. Drug Target.* **2007**, *15*, 115.

(151)   Flierl, A.; Jackson, C.; Cottrell, B.; Murdock, D.; Seibel, P.; Wallace, D. C., *Mol. Ther.* **2003**, *7*, 550.

(152)   Murphy, M. P., *Bba-Bioenergetics* **2008**, *1777*, 1028.

(153)   Biswas, S.; Dodwadkar, N. S.; Piroyan, A.; Torchilin, V. P., *Biomaterials* **2012**, *33*, 4773.

(154)   Paleos, C. M.; Tsiourvas, D.; Sideratou, Z., *Mol. Pharm.* **2016**, *13*, 2233.

(155)   Marrache, S.; Dhar, S., *Proc. Natl. Acad. Sci. USA* **2012**, *109*, 16288.

(156)   Mallick, A.; More, P.; Syed, M. M. K.; Basu, S., *Acs Appl. Mater. Inter.* **2016**, *8*, 13218.

(157)   Cho, D. Y.; Cho, H.; Kwon, K.; Yu, M.; Lee, E.; Huh, K. M.; Lee, D. H.; Kang, H. C., *Adv. Funct. Mater.* **2015**, *25*, 5479.

(158)   Grancharov, G.; Gancheva, V.; Kyulavska, M.; Momekova, D.; Momekov, G.; Petrov, P., *Polymer* **2016**, *84*, 27.

(159)   Kulkarni, P. S.; Haldar, M. K.; Confeld, M. I.; Langaas, C. J.; Yang, X.; Qian, S. Y.; Mallik, S., *Polym. Chem.* **2016**, *7*, 4151.

(160)   Biswas, S.; Dodwadkar, N. S.; Sawant, R. R.; Koshkaryev, A.; Torchilin, V. P., *J. Drug Target.* **2011**, *19*, 552.

(161)   Chen, Z.; Zhang, L.; Song, Y.; He, J.; Wu, L.; Zhao, C.; Xiao, Y.; Li, W.; Cai, B.; Cheng, H.; Li, W., *Biomaterials* **2015**, *52*, 240.

(162)   Wang, X. X.; Li, Y. B.; Yao, H. J.; Ju, R. J.; Zhang, Y.; Li, R. J.; Yu, Y.; Zhang, L.; Lu, W. L., *Biomaterials* **2011**, *32*, 5673.

(163)   D'Souza, G. G. M.; Rammohan, R.; Cheng, S. M.; Torchilin, V. P.; Weissig, V., *J. Control. Release* **2003**, *92*, 189.

(164)   Munsell, E. V.; Ross, N. L.; Sullivan, M. O., *Curr. Pharm. Design* **2016**, *22*, 1227.

(165)   Elouahabi, A.; Ruysschaert, J. M., *Mol. Ther.* **2005**, *11*, 336.

(166)   Pouton, C. W.; Wagstaff, K. M.; Roth, D. M.; Moseley, G. W.; Jans, D. A., *Adv. Drug. Deliver. Rev.* **2007**, *59*, 698.

(167)   Sui, M.; Liu, W.; Shen, Y., *J. Control. Release* **2011**, *155*, 227.

(168)   Larsen, J. D.; Ross, N. L.; Sullivan, M. O., *J. Gene Med.* **2012**, *14*, 580.

(169)   Li, L.; Sun, W.; Zhang, Z. R.; Huang, Y., *J. Control. Release* **2016**, *232*, 62.

(170)   Zhou, X.; Liu, X.; Zhao, B.; Liu, X.; Zhu, D.; Qiu, N.; Zhou, Q.; Piao, Y.; Zhou, Z.; Tang, J.; Shen, Y., *J. Control. Release* **2016**, *234*, 90.

(171)   Liu, X.; Xiang, J.; Zhu, D.; Jiang, L.; Zhou, Z.; Tang, J.; Liu, X.; Huang, Y.; Shen, Y., *Adv. Mater.* **2016**, *28*, 1743.

(172)   Bae, Y. M.; Choi, H.; Lee, S.; Kang, S. H.; Kim, Y. T.; Nam, K.; Park, J. S.; Lee, M.; Choi, J. S., *Bioconjug. Chem.* **2007**, *18*, 2029.

(173)   Cartier, R.; Reszka, R., *Gene Ther.* **2002**, *9*, 157.

(174)   Misra, R.; Sahoo, S. K., *Eur. J. Pharm. Sci.* **2010**, *39*, 152.

(175)   Jeon, O.; Lim, H. W.; Lee, M.; Song, S. J.; Kim, B. S., *J. Drug Target.* **2007**, *15*, 190.

(176)   Goncalves, C.; Ardourel, M. Y.; Decoville, M.; Breuzard, G.; Midoux, P.; Hartmann, B.; Pichon, C., *J. Gene Med.* **2009**, *11*, 401.

(177)   Jeong, J. H.; Kim, S. H.; Christensen, L. V.; Feijen, J.; Kim, S. W., *Bioconjug. Chem.* **2010**, *21*, 296.

(178)   Reilly, M. J.; Larsen, J. D.; Sullivan, M. O., *Mol. Pharm.* **2012**, *9*, 1031.

(179)   Reilly, M. J.; Larsen, J. D.; Sullivan, M. O., *Mol. Pharm.* **2012**, *9*, 1280.

(180)   Ross, N. L.; Sullivan, M. O., *Mol. Ther.* **2015**, *23*, S195.

(181)   Walker, W. A.; Tarannum, M.; Vivero-Escoto, J. L., *J. Mater. Chem. B* **2016**, *4*, 1254.

(182)   Sahay, G.; Batrakova, E. V.; Kabanov, A. V., *Bioconjug. Chem.* **2008**, *19*, 2023.

(183)   Sahay, G.; Gautam, V.; Luxenhofer, R.; Kabanov, A. V., *Biomaterials* **2010**, *31*, 1757.

(184)   Shen, P.; Ohta, S.; Inasawa, S.; Yamaguchi, Y., *Chem. Commun.* **2011**, *47*, 8409.

(185)   Gao, X. L.; Wang, T.; Wu, B. X.; Chen, J.; Chen, J. Y.; Yue, Y.; Dai, N.; Chen, H. Z.; Jiang, X. G., *Biochem. Biophys. Res. Commun.* **2008**, *377*, 35.

(186)   Omura, T., *J. Biochem.* **1998**, *123*, 1010.

(187)   Nussbaumer, S.; Bonnabry, P.; Veuthey, J. L.; Fleury-Souverain, S., *Talanta* **2011**, *85*, 2265.

(188)   Hurley, L. H., *Nat. Rev. Cancer* **2002**, *2*, 188.

(189)   Cross, D.; Burmester, J. K., *Clin. Med. Res.* **2006**, *4*, 218.

(190)   Wente, S. R.; Rout, M. P., *Csh Perspect. Biol.* **2010**, *2*.

(191)   Kastrup, L.; Oberleithner, H.; Ludwig, Y.; Schafer, C.; Shahin, V., *J. Cell. Physiol.* **2006**, *206*, 428.

(192)   Wlodkowic, D.; Skommer, J.; McGuinness, D.; Hillier, C.; Darzynkiewicz, Z., *Leuk. Res.* **2009**, *33*, 1440.

(193)   Tarrago-Trani, M. T.; Storrie, B., *Adv. Drug. Deliver. Rev.* **2007**, *59*, 782.

(194)   Sandvig, K.; van Deurs, B., *FEBS Lett.* **2002**, *529*, 49.

(195)   Engedal, N.; Skotland, T.; Torgersen, M. L.; Sandvig, K., *Microb. Biotechnol.* **2011**, *4*, 32.

(196)   Johannes, L.; Romer, W., *Nat. Rev. Microbiol.* **2010**, *8*, 105.

(197)   Falguieres, T.; Mallard, F.; Baron, C.; Hanau, D.; Lingwood, C.; Goud, B.; Salamero, J.; Johannes, L., *Mol. Biol. Cell* **2001**, *12*, 2453.

(198)   Tarrago-Trani, M. T.; Jiang, S.; Harich, K. C.; Storrie, B., *Photochem. Photobiol.* **2006**, *82*, 527.

(199)   Amessou, M.; Carrez, D.; Patin, D.; Sarr, M.; Grierson, D. S.; Croisy, A.; Tedesco, A. C.; Maillard, P.; Johannes, L., *Bioconjug. Chem.* **2008**, *19*, 532.

(200)   Chang, S.; Wu, X. M.; Li, Y. S.; Niu, D. C.; Gao, Y. P.; Ma, Z.; Gu, J. L.; Zhao, W. R.; Zhu, W. H.; Tian, H.; Shi, J. L., *Biomaterials* **2013**, *34*, 10182.

(201)   Deng, Z. J.; Morton, S. W.; Bonner, D. K.; Gu, L.; Ow, H.; Hammond, P. T., *Biomaterials* **2015**, *51*, 250.

(202)   Panyam, J.; Sahoo, S. K.; Prabha, S.; Bargar, T.; Labhasetwar, V., *Int. J. Pharm.* **2003**, *262*, 1.

(203)   Lerch, S.; Ritz, S.; Bley, K.; Messerschmidt, C.; Weiss, C. K.; Musyanovych, A.; Landfester, K.; Mailander, V., *Nanomed.-Nanotechnol.* **2015**, *11*, 1585.

(204)   Seib, F. P.; Jones, A. T.; Duncan, R., *J. Drug Target.* **2006**, *14*, 375.

(205)   Salvati, A.; Aberg, C.; dos Santos, T.; Varela, J.; Pinto, P.; Lynch, I.; Dawson, K. A., *Nanomed.-Nanotechnol.* **2011**, *7*, 818.

(206)   Ostrowski, A.; Nordmeyer, D.; Boreham, A.; Holzhausen, C.; Mundhenk, L.; Graf, C.; Meinke, M. C.; Vogt, A.; Hadam, S.; Lademann, J.; Ruhl, E.; Alexiev, U.; Gruber, A. D., *Beilstein J. Nanotech.* **2015**, *6*, 263.

(207)   Richardson, S. C. W.; Wallom, K. L.; Ferguson, E. L.; Deacon, S. P. E.; Davies, M. W.; Powell, A. J.; Piper, R. C.; Duncan, R., *J. Control. Release* **2008**, *127*, 1.

(208)   Zhang, R.; Yang, J.; Radford, D. C.; Fang, Y.; Kopecek, J., *Macromol. Biosci.* **2016**.

(209)   Chen, K. J.; Chiu, Y. L.; Chen, Y. M.; Ho, Y. C.; Sung, H. W., *Biomaterials* **2011**, *32*, 2586.

(210)   Tang, J.; Kong, B.; Wu, H.; Xu, M.; Wang, Y. C.; Wang, Y. L.; Zhao, D. Y.; Zheng, G. F., *Adv. Mater.* **2013**, *25*, 6569.

(211)   Mitra, R. N.; Doshi, M.; Zhang, X. L.; Tyus, J. C.; Bengtsson, N.; Fletcher, S.; Page, B. D. G.; Turkson, J.; Gesquiere, A. J.; Gunning, P. T.; Walter, G. A.; Santra, S., *Biomaterials* **2012**, *33*, 1500.

(212)   Jiang, Y. Y.; Liu, G. H.; Wang, X. R.; Hu, J. M.; Zhang, G. Y.; Liu, S. Y., *Macromolecules* **2015**, *48*, 764.

(213)   Vaidyanathan, S.; Chen, J.; Orr, B. G.; Holl, M. M. B., *Mol. Pharm.* **2016**, *13*, 1967.

(214)   Lee, H.; Kim, I. K.; Park, T. G., *Bioconjug. Chem.* **2010**, *21*, 289.

(215)   Bao, Y. Y.; De Keersmaecker, H.; Corneillie, S.; Yu, F.; Mizuno, H.; Zhang, G. F.; Hofkens, J.; Mendrek, B.; Kowalczuk, A.; Smet, M., *Chem. Mater.* **2015**, *27*, 3450.

(216)   Choi, E. B.; Choi, J.; Bae, S. R.; Kim, H. O.; Jang, E.; Kang, B.; Kim, M. H.; Kim, B.; Suh, J. S.; Lee, K.; Huh, Y. M.; Haam, S., *Nano Res.* **2015**, *8*, 1169.

(217)   Hu, J. M.; Liu, G. H.; Wang, C.; Liu, T.; Zhang, G. Y.; Liu, S. Y., *Biomacromolecules* **2014**, *15*, 4293.

(218)   Smith, R.; Wright, K. L.; Ashton, L., *Analyst* **2016**, *141*, 3590.

(219)   Chernenko, T.; Matthaus, C.; Milane, L.; Quintero, L.; Amiji, M.; Diem, M., *ACS nano* **2009**, *3*, 3552.

(220)   Chernenko, T.; Buyukozturk, F.; Miljkovic, M.; Carrier, R.; Diem, M.; Amiji, M., *Drug. Deliv. Transl. Res.* **2013**, *3*.

(221)   Dorney, J.; Bonnier, F.; Garcia, A.; Casey, A.; Chambers, G.; Byrne, H. J., *Analyst* **2012**, *137*, 1111.

(222)   Hoppe, P.; Cohen, S.; Meibom, A., *Geostand. Geoanal. Res.* **2013**, *37*, 111.

(223)   Wedlock, L. E.; Kilburn, M. R.; Cliff, J. B.; Filgueira, L.; Saunders, M.; Berners-Price, S. J., *Metallomics* **2011**, *3*, 917.

(224)   Wedlock, L. E.; Kilburn, M. R.; Liu, R.; Shaw, J. A.; Berners-Price, S. J.; Farrell, N. P., *Chem. Commun.* **2013**, *49*, 6944.

(225)   Lee, R. F. S.; Escrig, S.; Croisier, M.; Clerc-Rosset, S.; Knott, G. W.; Meibom, A.; Davey, C. A.; Johnsson, K.; Dyson, P. J., *Chem. Commun.* **2015**, *51*, 16577.

(226)   Proetto, M. T.; Anderton, C. R.; Hu, D.; Szymanski, C. J.; Zhu, Z.; Patterson, J. P.; Kammeyer, J. K.; Nilewski, L. G.; Rush, A. M.; Bell, N. C.; Evans, J. E.; Orr, G.; Howell, S. B.; Gianneschi, N. C., *ACS nano* **2016**, *10*, 4046.

(227)   Symens, N.; Walczak, R.; Demeester, J.; Mattaj, I.; De Smedt, S. C.; Remaut, K., *Mol. Pharm.* **2011**, *8*, 1757.

(228)   Endres, T.; Zheng, M. Y.; Kilic, A.; Turowska, A.; Beck-Broichsitter, M.; Renz, H.; Merkel, O. M.; Kissel, T., *Mol. Pharm.* **2014**, *11*, 1273.

(229)   Shaheen, S. M.; Akita, H.; Yamashita, A.; Katoono, R.; Yui, N.; Biju, V.; Ishikawa, M.; Harashima, H., *Nucleic Acids Res.* **2011**, *39*, E48.

(230)   Chen, H. H.; Ho, Y. P.; Jiang, X.; Mao, H. Q.; Wang, T. H.; Leong, K. W., *Mol. Ther.* **2008**, *16*, 324.

(231)   Bryson, J. M.; Fichter, K. M.; Chu, W. J.; Lee, J. H.; Li, J.; Madsen, L. A.; McLendon, P. M.; Reineke, T. M., *Proc. Natl. Acad. Sci. USA* **2009**, *106*, 16913.

(232)   Zeng, X. H.; Morgenstern, R.; Nystrom, A. M., *Biomaterials* **2014**, *35*, 1227.

2. Synthesis of α,ω-Fluorine Labeled PPFMA *via* RAFT Polymerization

2.1. Introduction

Reversible addition-fragmentation chain transfer (RAFT) polymerization is a controlled/living radical polymerization carried out using thiocarbonylthio compounds of general structure Z-C(=S)S-R that act as chain transfer agents (CTA).[1] While initiation and termination occur as in conventional radical polymerization, the presence of the CTA allows the establishment of an equilibrium between addition and fragmentation steps as illustrated in **Scheme 1**.

Scheme 1. Mechanism of RAFT polymerization.

First, in the pre-equilibrium stage, the addition of propagating radicals ($P_n\cdot$) to the CTA leads to the formation of the intermediate radical **1**, which upon fragmentation yields the

macro chain transfer agent **2** and a new radical R·. The propagation of R· results in the formation of a new polymer chain $P_m·$. The establishment of the main equilibrium between the two propagating species $P_n·$ and $P_m·$ and the dormant macro CTA **2** and **2'** provides rapid interchange of all the radical species from a dormant to a propagating stage, therefore allowing equal probability for all polymer chains to grow.[1,2]

As a consequence, RAFT polymerization results in the formation of α,ω-end-functionalized polymer chains characterized by a low dispersity, a linear increase in molecular weight with the conversion and by a match between theoretical predictable M_n and experimental data, if the following conditions are fulfilled: (i) the CTA must be quickly consumed with a consumption rate (k_{tr}) higher than that of the propagation (k_p) in the pre-equilibrium stage, (ii) the dormant species (**2** and **2'**) and the $P_n·/P_m·$ active species must exchange quickly.[1,2] As a result, the optimal control in RAFT polymerization requires choosing an appropriate CTA for the selected monomer. The Z and R groups both play critical roles in determining the outcome of the polymerization. While the Z-group activates the thiocarbonyl double bond toward radical addition and stabilizes the intermediate radicals **1** and **3** (high k_{add}), the R-group should enable rapid fragmentation ($k_β > k_{-add}$) as well as an efficient re-initiation process (high k_{iR}).[1,3] The efficiency of a CTA depends on two transfer constants C_{tr} (= k_{tr}/k_p) and C_{-tr} (=k_{-tr}/k_{iR}), which take into account the reactivity of the propagating radical $P_n·$ and the reactivity of the expelled radical R·, respectively. The rate constants for chain transfer (k_{tr} and k_{-tr}) are given by the following equations:[2,3]

$$k_{tr}=k_{add}\ \frac{k_β}{k_{-add}+k_β} \qquad\qquad k_{-tr}=k_{-β}\ \frac{k_{-add}}{k_{-add}+k_β} \qquad\qquad (1, 2)$$

The determination of C_{tr} and C_{-tr} provides important information about the CTA compatibility for the given monomer and polymerization conditions, while it also predicts the control over the polymerization.

These transfer constants can be estimated if the consumption rate of the CTA during the polymerization reaction is known. The CTA consumption during the polymerization is generally indirectly estimated by the discrepancy between theoretical and experimental polymer molecular weights.[45-7] However, a lot of reports also explain discrepancies between theoretical and experimental molecular weight as due, at least in part, to the use

of size exclusion chromatography (SEC) for the estimation of experimental molecular weights.[7-10] Although the availability of standards for polymers such as poly(methyl methacrylate) (PMMA) or poly(styrene) (PS), allow a relatively reliable estimation of the molecular weight for these polymers, it is well known that the analysis of non-conventional polymers often requires optimization in terms of standards and solvents. As an alternative to SEC analysis, polymer molecular weight can also be estimated *via* ^{1}H-NMR, in particular by comparing the integrals of the polymer end group signals with those of the polymer backbone.[9,10] However, also in this case, due to the weak intensity of the end group-derived signals as compared to those of the polymer chains and due to the broad nature of polymer peaks and overlapping signals, polymer molecular weights can be only poorly estimated.[11] These limitations can be overcome with the establishment of methods to directly monitor the residual CTA during RAFT polymerization. In one example, Chiefari *et al.* estimated the concentration of residual CTA in the reaction mixture *via* ^{1}H-NMR studies.[12] However, also in this case, overlapping signals and the broad nature of the polymer peaks make this method applicable only to limited cases. More recently, Han *et al.* monitored the cumyl dithiobenzoate (CDB) CTA conversion *via* flash chromatography combined with HPLC.[5] This method allowed the correlation between residual CTA and polymer molecular weights determined by SEC analysis and showed the effect of the reaction conditions on the CTA consumption rate and therefore on polymerization behavior. A more simple and direct approach to monitor CTA consumption during the iodine transfer polymerization of vinyldiene fluoride is the one proposed by Boyer *et al.*[13] In this work the author monitored the conversion of fluorinated CTAs *via* ^{19}F-NMR studies.

^{19}F-NMR provides spectra with characteristics very similar to that of the proton, with the additional benefit of having a broader range of chemical shifts and no interference from the solvent peaks. For these reasons, even in the presence of compounds containing multiple fluorine atoms, the risk of signal overlap is drastically reduced.[14] Moreover, the unique sensitivity of fluorine chemical shifts to local conformational and structural environments results in a powerful tool to monitor chemical reactions. As a result, the design of fluorinated CTAs (F-CTAs) for RAFT polymerization represents a direct and simple method to monitor CTA consumption *via* ^{19}F-NMR studies. This method becomes even more attractive when the RAFT polymerization of fluorinated monomers is investigated. Fluorine-containing polymers are considered as an interesting class of polymers with unique features that have found applications in a variety of different

fields.[15-17] The determination of several polymerization parameters *via* unique ^{19}F-NMR measurement represents a very appealing opportunity for further development of these polymers. In this case, apart from monitoring F-CTA consumption, the use of ^{19}F-NMR also allows for the determination of monomer conversion as well as the estimation of the experimental polymer molecular weight based on end group analysis.

The aim of this work is to investigate the use of F-CTAs and ^{19}F-NMR to monitor CTA consumption during RAFT polymerization and to demonstrate the potential of this approach to access several polymerization parameters during the RAFT polymerization of fluorinated polymers. Poly(pentafluorophenyl methacrylate) (PPFMA) was selected as a candidate for this study, as it is considered as an interesting active-ester precursor polymer for the generation of biocompatible functional polymers.[8,18-22] However, the efficiency of the used CTA and the effect of different polymerization conditions have never been investigated in detail. Hence, a fluorinated label was introduced at the R group of the chain transfer agent 4-cyanopentanoic acid dithiobenzoate (CTA-1) to give the fluorinated F-CTA-1, which was used to monitor the RAFT polymerization of pentafluorophenyl methacrylate (PFMA) *via* ^{19}F-NMR. The first part of this work aims to prove that the insertion of a fluorinated label at the R position of the CTA-1 does not affect the polymerization process and that the CTA-derived fluorine label incorporated on the PPFMA α-end group can be used to determine the experimental polymer molecular weights *via* ^{19}F-NMR analysis. The second part aims to demonstrate how ^{19}F-NMR analysis can be used to monitor F-CTA-1 consumption during the RAFT polymerization and to investigate the effect of different polymerization conditions on the transfer constants. Finally, a second CTA containing fluorine on both the R and Z groups (F-CTA-2) was synthesized in order to explore the feasibility of using F-CTAs and ^{19}F-NMR, not only to monitor CTA consumption during RAFT polymerization and to determine the molecular weights of fluorinated polymers, but also to investigate the α-ω-end group fidelity during the polymerization process.

2.2. Experimental Section

2.2.1. Materials

All chemicals were used as received unless described. 4-Cyanopentanoic acid dithiobenzoate (CTA) (>97%), N-(3-dimethylaminopropyl)-N′-ethylcarbodiimide hydrochloride (97%) and 2,2′-azobis(2-methylpropionitrile) (98%) (AIBN), which was re-crystalized from methanol prior use, were purchased from Sigma-Aldrich. 1,4-Dioxane and trimethylamine (Et$_3$N) were purchased from Acros Organics and 3,3,3-trifluoro-propylamine hydrochloride was obtained from Apollo Scientific. Pentafluorophenol was purchased from MatrixScientific. Dichloromethane (DCM), tetrahydrofuran (THF), hexane and ethyl acetate were purchased from Reactolab. Sodium methoxide, elemental sulfur, 4-chlorobenzotrifluoride, 4, 4'-azobis (4-cyanovaleric acid) (ACVA) were purchased from J&K Scientific Ltd. 4'-Azobis (4-cyanovaleric acid) (ACVA) was crystallized from ethanol and sodium methoxide was used in 30 % solution in methanol. Pentafluorophenyl methacrylate (PFMA) was synthesized as reported by Eberhardt *et al.*[23] 1,4-Dioxane was dried under molecular sieves and Et$_3$N was freshly distilled prior use. THF was dried using a Pure Solv solvent purification system prior use.

2.2.2. Methods

^{1}H- and ^{19}F-NMR spectra were recorded on a Bruker AV-400 instrument at room temperature using CDCl$_3$ as solvent. For ^{1}H-NMR, chemical shifts are reported relative to the residual proton signal of the solvent. Size exclusion chromatography (SEC) of PPFMA in THF was performed using an Agilent 1260 infinity system equipped with a refractive index (RI) Varian detector 390-LC, two PLgel 5 µm Mixed C (Agilent) columns and a PLgel guard column. THF was used as eluent with a flow rate of 1 mL/min and the temperature was 40 °C. Samples were analysed using conventional calibration with polystyrene (PS) standards ranging from 4910 Da to 549 KDa and poly (methyl methacrylate) (PMMA) standards from 2370 Da to 201 KDa. SEC in DMF was performed with a Waters Alliance GPCV 2000 system equipped with a RI, three Styragel HR4, HR2 and HR 0.5 columns and a Styragel guard column. The eluent was DMF containing 0.01 wt % LiCl at a flow rate of 0.6 mL/min at 60 °C. Samples were analysed

using conventional calibration with poly (methyl methacrylate) (PMMA) standards ranging from 2200 Da to 520 KDa.

2.2.3. Procedures

Synthesis of F-CTA-1. 500.0 mg (1.79 mmol) 4-cyanopentanoic acid dithiobenzoate (CTA-1) and 411.6 mg (2.15 mmol) EDC HCl were dissolved in 8 mL dry DCM, the solution was cooled down to 0 °C and stirred under nitrogen. In a second flask, 214.0 mg (1.43 mmol) 3,3,3-trifluoropropyl amine hydrochloride were dissolved in 8 mL dry DCM and 250 µL (1.43 mmol) triethylamine were added. After 10 minutes the 3,3,3-trifluoropropyl amine solution was added dropwise to the first solution and the reaction was stirred at room temperature for 2 h. The solution was washed with 5 % NaHCO$_3$ and brine, dried over MgSO$_4$ and finally dried under vacuum. The crude product was purified by flash chromatography using ethyl acetate / hexane 4.5:5.5 to give the dark pink product (73 % yield).

Synthesis of F-CTA-2. 69.4 g 30 % Sodium methoxide solution (0.39 mol) was added to the flask at room temperature under a dry nitrogen atmosphere followed by 13.3 g anhydrous methanol and rapid addition of 5.4 g (0.17 mol) elemental sulfur. The mixture was heated in an oil bath at 70 °C with continuous stirring for 30 min. 15.0 g (0.08 mol) 4-chlorobenzotrifluoride was then added dropwise *via* the addition funnel over a period of 1 h. The reaction mixture was kept at 70 °C in nitrogen atmosphere for 10 h. After this time, the reaction was stopped by cooling it down to 0 °C using an ice bath. The salt was removed by filtration, and the solvent was removed in vacuum. 50 mL deionized water was then added to the residue. The solution was filtered again. The crude product was washed with diethyl ether (3 × 40 mL) in an extraction funnel. Diethyl ether (20 mL) and 1.0 mol/L HCl (50 mL) were added, and the product was extracted into the ethereal layer. Deionized water (30 mL) and 1.0 M NaOH (60 mL) were added, and the product was extracted to the aqueous layer. 36.3 g (0.11 mol) potassium ferricyanide (III) was dissolved in 100 mL deionized water and then was added dropwise to the first solution *via* an addition funnel over a period of 1 h under vigorous stirring. Then the solution was transferred to an extraction funnel. 30 mL anhydrous ethyl acetate was added to wash the product and the product was extracted to the ethyl acetate layer. This washing process

was repeated two more times. The red solution was dried over anhydrous $MgSO_4$ and in vacuum to remove the solvent at room temperature overnight. The obtained 4-(trifluoromethylthiobenzoyl) disulphide was dissolved in 50 mL anhydrous ethyl acetate and the solution was transferred to a flask. 2.6 g (9.19 mmol) dry 4, 4'-Azobis (4-cyanovaleric acid) was added to the flask. The reaction solution was heated at 75 °C for 14 h. The ethyl acetate was removed in vacuum. The crude product was isolated by column chromatography using ethyl acetate: hexane (1:1.5) as eluent. The solvent mixture was removed in vacuum, and the red oily 4-cyanopentanoic acid-4-(trifluoromethyl) dithiobenzoate was kept at 4 °C. 2.0 g (5.8 mmol) 4-cyanopentanoic acid-4-(trifluoromethyl) dithiobenzoate and 1.34 g (6.96 mmol) EDC HCl were dissolved in 20 mL of dry DCM. The solution was cooled down to 0 °C and stirred under nitrogen. In a second flask, 0.7 g (4.60 mmol) of 3,3,3-trifluoropropyl amine hydrochloride were dissolved in 10 mL dry DCM and 465 µL (4.60 mmol) triethylamine were added. After 10 min the trifluoropropylamine solution was added dropwise to the first solution and the reaction was stirred at room temperature for 2 h. The solution was washed with 5% $NaHCO_3$ solution and brine, dried over anhydrous $MgSO_4$ and dried under vacuum. The crude product was purified by column chromatography using ethyl acetate/hexane 1:1.5 to give the dark pink F-CTA-2.

   PPFMA polymerization. 1.4 g (5.56 mmol) PFMA was added to the Schlenk tube followed by 2.08 mL dry dioxane containing 0.0028, 0.0055 or 0.011 mmol AIBN and 0.028, 0.055 or 0.11 mmol CTA in the case of [M:CTA] = 200, 100 and 50, respectively. The solutions were degassed by four freeze-pump-thaw cycles and the tubes were filled with argon. The flasks were immersed in an oil bath at 90 °C or 75 °C. At different time intervals 150 µL samples were removed, 50 µL were diluted in 400 µL $CDCl_3$ for ^{19}F-NMR analysis, the remaining part was precipitated in ice-cold hexane three times. The isolated pink product was dried under vacuum overnight and analysed by SEC.

2.3. Results and Discussion

2.3.1. Design and synthesis of the fluorinated CTAs (F-CTAs)

Elberhardt *et al.* investigated the RAFT polymerization of PFMA by using the two different 4-cyanopentanoic acid dithiobenzoate (CTA-1) and cumyl dithiobenzoate CTAs.[24] Both CTAs have an activating phenyl Z group and a good tertiary cumyl or cyanopentanoic acid leaving radical R·, which are suitable for activated monomers such as methacrylates. In the case of PFMA, CTA-1 was found to be a more effective CTA[24] and therefore it has been extensively used for PFMA polymerization.[8,19,21,22] For this reason, in this study CTA-1 (**Chart 1**) was chosen as the precursor for the preparation of two fluorinated CTAs (F-CTAs). Two different factors were taken into account for the choice of the labels and their respective positions. First, the labels should give rise to two different ^{19}F-NMR chemical shifts and those signals should be well separated from that of the PFMA monomer units. For this purpose, trifluoromethyl groups were selected as suitable labels. Second, the insertion of the labels should not affect the polymerization process. The modification of both the R (α-end of the polymer) and Z (ω-end of the polymer) CTA groups have been already explored to introduce functionalities in the polymer chains.[25] In this particular case, the modification of the Z group, required a more careful selection in order to minimize the electron-withdrawing effect of the fluorinated label on the dithiobenzoate moiety. To this purpose, the label was introduced in para position of the aromatic ring. Hence, two different fluorinated derivatives, F-CTA-1 and F-CTA-2 were prepared (**Chart 1**). While F-CTA-1 contains a trifluoromethyl label in the R group, F-CTA-2 contains two trifluoromethyl labels in both R and Z groups. F-CTA-1 was used to investigate the PFMA polymerization kinetics and to determine the experimental molecular weights and the transfer constants. In a final step, F-CTA-2 was used to investigate α-ω end group fidelity during PFMA RAFT polymerization. The synthetic scheme of the two F-CTAs, as well as the detailed characterization, is reported in Supporting Information in **Scheme S1** and **Figure S1-S4,** respectively**.**
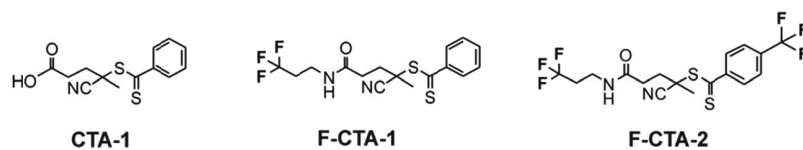
Chart 1. Chemical structures of 4-cyanopentanoic acid dithiobenzoate (CTA-1), R-labeled CTA (F-CTA-1) and R-Z-labeled CTA (F-CTA-2).

2.3.2. PFMA polymerization using F-CTA-1

PFMA polymerization conditions reported in literature generally employ monomer concentrations $[M]_0$ about 2 M, $[CTA]_0 : [I]_0$ ratio 8-10 and dioxane as solvent.[19,22,24,26] Relatively low reaction temperature (65-75°C)[22,26,27] and long polymerization time (up to 42 hours) have been used.[22] However, to the best of our knowledge, a study of the polymerization kinetics using such conditions has not been reported. The only available kinetics using similar monomer concentration and $[CTA]_0 : [I]_0$ ratio was reported by Eberhardt and co-workers. However, in this work, the polymerization was carried out at higher temperature (90°C) and the highest molecular weight obtained using CTA-1 was around 10000 g/mol.[24]

Hence, the first set of experiments aimed to assess the feasibility of using fluorinated CTAs to monitor the polymerization parameters *via* ^{19}F-NMR and to investigate the PFMA RAFT polymerization kinetics using low temperature conditions. To this end, both F-CTA-1 and CTA-1 were used for the PFMA polymerization which was carried out at 75°C using $[M]_0 = 1.8$ M, $[CTA]_0 : [I]_0 = 10$, AIBN as initiator and dioxane as solvent. A $[M]_0 : [CTA]_0$ ratio of 200 was used. The monomer conversion ρ (%) at the different polymerization time was determined by ^{19}F-NMR. An example of ^{19}F-NMR spectra of the PPFMA prepared using F-CTA-1 is given in **Figure 1A**. The monomer conversion at a given polymerization time was determined by comparing the area of the polymer peaks with that of the remaining monomer peaks indicated in **Figure 1** as **e*** and **e**, respectively. To this purpose Equation (3) was used.

$$\rho \ (\%) = \frac{\int e^*}{\int e^* + \int e} \times 100 \tag{3}$$

Subsequently, the monomer conversion ρ, the initial $[M]_0:[CTA]_0$ ratio and the number of initiator (AIBN) derived side chains $df([I]_0-[I])$ were used to calculate the theoretical degree of polymerization (DP^{TH}) as shown in Equation (4). $df[I]_0-[I]$ was expressed as $df[I]_0(1-e^{-kd})$, where k_d is the rate constant for initiator decomposition at 75 °C (7.33×10^{-5} s^{-1}) and 90 °C ($4.79 \times 10^{-4}\,s^{-1}$),[28] f is the initiator efficiency ($f = 0.6$)[28] and d is the number of chains produced from radical-radical reaction. Since this value is not available for this specific system, the value reported for MMA was used ($d = 1.67$).[4,7] The theoretical molecular weights (M_n^{TH}) were calculated taking into account the monomer (mM) and the CTA (mCTA) molecular weights as given in Equation (5).

$$DP^{TH} = \rho \frac{[M]_0}{[CTA]_0 + df[I]_0(1-e^{-kd})} \qquad M_n^{TH} = DP^{TH} \times mM + mCTA \qquad (4, 5)$$

Experimental molecular weights of the polymers obtained using both CTA-1 and F-CTA-1 for the different polymerization time were first determined by SEC analysis using THF as solvent and polystyrene (PS) as standard.
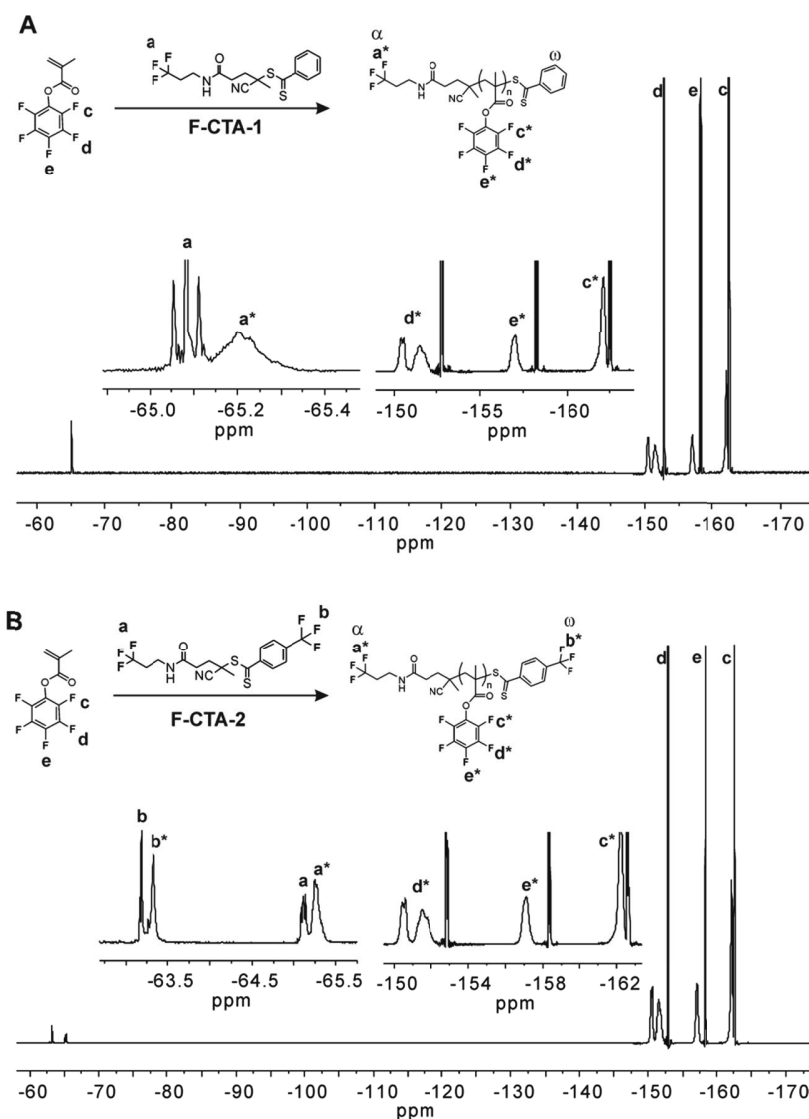
Figure 1. Examples of ^{19}F-NMR spectra of (A) α-fluorinated PPFMA obtained using F-CTA-1 and (B) α,ω-fluorinated PPFMA obtained using F-CTA-2.

Both polymerizations revealed a similar first order kinetics plot (**Figure 2A**), and in both cases, the experimental molecular weights, determined by SEC, were found to increase linearly with the monomer conversion in a similar manner (**Figure 2B**). These results confirmed that the insertion of the fluorinated label did not affect the polymerization process and therefore suggested that F-CTA-1 can be used to investigate PFMA polymerization. However, in both cases, especially in the early stage of the polymerization, the experimental molecular weights determined by SEC were higher than the theoretical predictions (**Figure 2B** and **Table S1**). This, together with relatively high

polydispersity values in the early stage of the process (above 1.5), which tended to decrease during the course of the polymerization (1.44), might indicate a slow consumption of both CTAs. This effect derives from the fact that, in an ideal case, the degree of polymerization at each particular polymerization time is expressed as [monomer consumed]:[CTA]$_0$. Therefore, a CTA with a low transfer constant C_{tr} will be slowly consumed and will generate polymer chains having an experimental molecular weight higher than the expected. The early stage of the polymerization therefore proceeds *via* a hybrid free radical-RAFT mechanism.[3,7,29] As the polymerization time increases, the higher CTA conversion shifts the process toward a RAFT mechanism and the experimental molecular weights tend to correspond with the theoretical values. This type of polymerization is therefore characterized by high polydispersity values in the early polymerization stage, which slowly decreases as the RAFT agent is consumed. This behavior has been extensively observed during the RAFT polymerization of methacrylate monomers even in the presence of the highly reactive dithiobenzoate CTAs.[4,5,7,29,30] However, since this behavior was never reported before for the given system, and since the use of SEC for the molecular weight determination of non-conventional polymers often depends on standards and solvents,[7-9] the fluorinated label at the α-end group of the polymers prepared using F-CTA-1 was used to estimate the polymer molecular weights *via* ^{19}F-NMR. To this end, the integral of the ^{19}F-NMR signal generated by the three fluorine atoms at the α-end groups of PPFMA (**a*** in **Figure 1A**) was set at 3. As a consequence, the integral deriving from PFMA polymer side chains (**e***) gave the experimental degree of polymerization (DP). The experimental molecular weights (M_n) were subsequently determined as shown in Equation (6).

$$Mn = DP \times mM + mCTA \qquad (6)$$

It should be mentioned, that due to the presence of initiator-derived polymer chains, the determination of molecular weight by ^{19}F-NMR, which is based on end group analysis, might slightly overestimate the polymer molecular weights. SEC analysis was also performed using different conditions previously reported in literature such as THF and DMF as solvents and PMMA and PS were used as standards.[8,24] As shown in **Figure 2B**, a good match was found between NMR data and SEC results for the samples analyzed using THF as solvent and both PS and PMMA standards gave comparable results (**Table**

S2). On the other hand, only poor correlation was observed when DMF was used (**Table S2**). These results indicate that THF solvent is preferred to DMF for SEC analysis of PPFMA and more important, confirm the discrepancy between experimental and theoretical molecular weights. Moreover, as shown in **Figure 1A**, the sensitivity of ^{19}F-NMR to changes in the local environment, resulted in a shift between the signals of the unreacted F-CTA-1 (**a**) and the one of the F-CTA-1 incorporated in the polymer chains (**a***, α-end group). From the ^{19}F-NMR spectra it was possible to observe that the amount of residual F-CTA-1 was quite significant and the intensity of this signal decreased while increasing the polymerization time due to the F-CTA-1 incorporation in the polymer chains. This observation further proves that the observed discrepancy between theoretical and experimental data, as well as the relatively high polydispersity of the polymers derives from a slow consumption of the CTA.
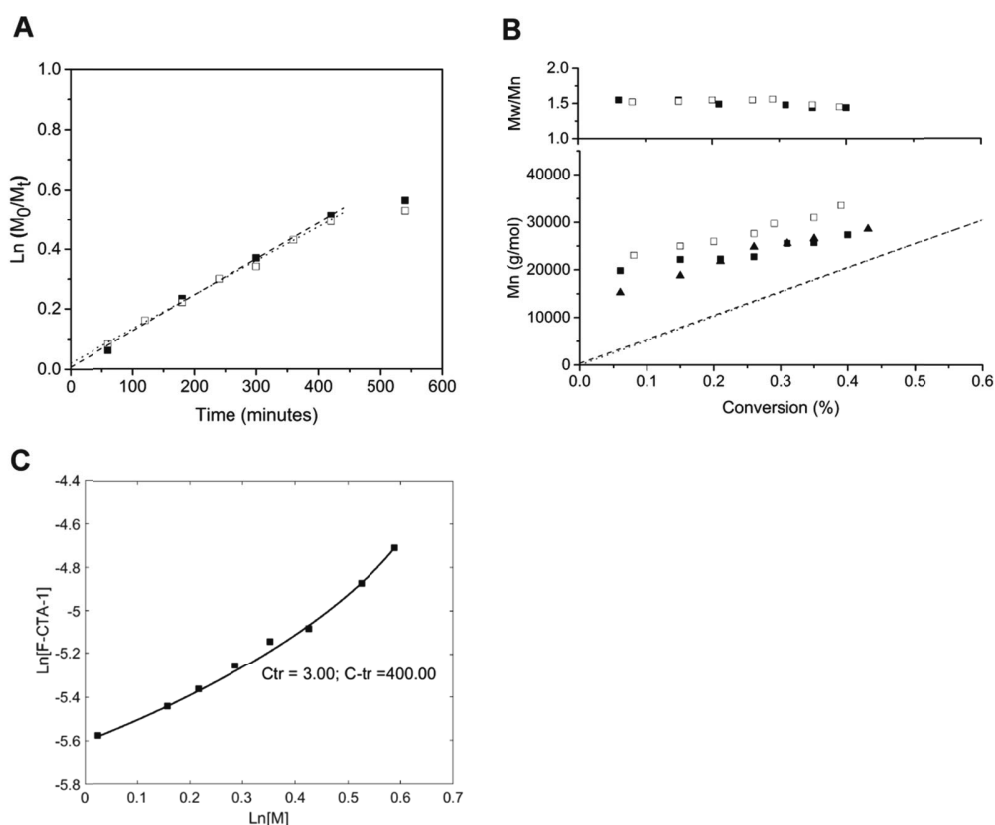
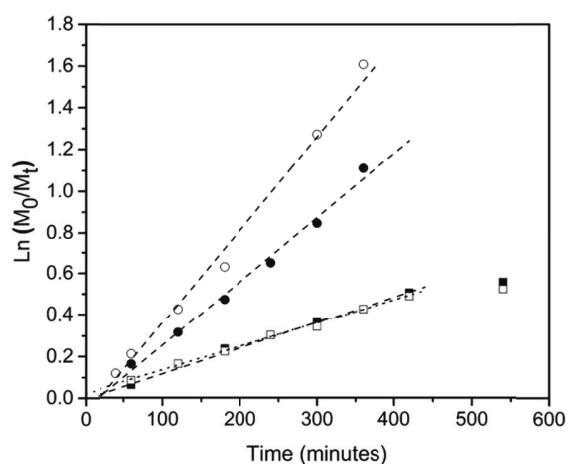**Figure 2.** (A) First-order kinetics plot for the RAFT polymerization of PFMA as determined by ^{19}F-NMR. Polymerization conditions: dioxane, 75°C, $[M]_0 = 1.8$ M, $[M]_0:[CTA-1]_0 = 200$ (□) and $[M]_0:[F-CTA-1]_0 = 200$ (■), $[F-CTA-1/CTA-1]_0:[I]_0 = 10$. (B) Evolution of experimental M_n and M_w/M_n as a function of monomer conversion for

CTA-1 as determined by SEC (□) and F-CTA-1 as determined by SEC (■) and ^{19}F-NMR (▲). SEC analysis was performed using THF as solvent and PS standards were used for conventional calibration. Dotted lines (CTA-1) and dashed lines (F-CTA-1) indicate the theoretical M_n (M_n^{TH}) expected for the different conditions. (C) Double logaritmic plot of F-CTA-1 concentration *vs* monomer concentration determined by ^{19}F-NMR, experimental points were fitted using Equation (8).

2.3.3. Determination of the transfer constants C_{tr} and C_{-tr} of F-CTA-1

The next series of experiments aimed to determine the F-CTA-1 conversion and therefore the transfer constants C_{tr} and C_{-tr} *via* ^{19}F-NMR studies and to investigate the effect of different $[M]_0:[CTA]_0$ and temperature on the efficiency of the CTA. Chong *et al.*, reported a method to estimates the transfer constants C_{tr} and C_{-tr} from the decay of CTA concentration during the polymerization using the following Equation:[4]

$$\frac{d[CTA]}{d[M]} \approx C_{tr} \frac{[CTA]}{[M]+C_{tr}[CTA]+C_{-tr}[2]} \tag{8}$$

Where [CTA] and [M] are the CTA and monomer concentrations, respectively, at each particular polymerization time and [**2**], also shown in **Scheme 1**, is the concentration of dormant polymer chains which can be directly related to the [CTA] and the initial CTA concentration $[CTA]_0$. Hence, if both monomer and CTA consumptions can be experimentally determined at each polymerization time, Equation (8) can be fitted to the experimental data using independent pairs of input C_{tr} and C_{-tr}. The F-CTA-1 conversion at different polymerization time and for different polymerization conditions was monitored via ^{19}F-NMR. In particular, the signal of the α-fluorinated polymer end groups (**a***) was compared to the unreacted F-CTA-1 integral peaks (**a**) using Equation (9). The CTA concentration at each particular polymerization time was determined with Equation (10) and related to [M] in order to determine the transfer constants using Equations (8).

$$\alpha_{CTA}\,(\%)= \frac{\int a^*}{\int a^* + \int a}\,100 \qquad [CTA]= (1-\alpha_{CTA})\times [CTA]_0 \tag{9, 10}$$

Figure 2C illustrates the experimental values Ln[F-CTA-1] *vs* Ln[M] determined by ^{19}F-NMR for the different polymerization time. The fitting of these experimental data with Equation (8) allowed the determination of C_{tr} and C_{-tr}, which were found to be 3 and 400, respectively (**Table 1**). As expected, the relatively low C_{tr} value, together with a significant C_{-tr} contribution explained the discrepancy between predicted and experimental data as well as the relatively high polydispersity obtained. Desirable characteristics such as the straight line dependence of molar mass on conversion and low polydispersity (< 1.2) require indeed CTA/monomer systems having a C_{tr} of at least 10.[3]

Table 1. C_{tr} and C_{-tr} values for the different PFMA polymerization conditions using F-CTA-1 and F-CTA-2.

F-CTA	$[M]_0$ (mol/L)	$[M]_0$:$[F-CTA]_0$	$[F-CTA]_0$:$[I]_0$	Temperature (°C)	C_{tr}*	C_{-tr}*
F-CTA-1	1.8	200	10	75	3.0	400.0
		100	10	75	3.2	390.0
				90	4.1	399.9
		50	10	75	3.5	390.0
				90	4.7	391.0
F-CTA-2		100	10	90	4.0	390.1
		50	10	90	4.8	370.1

*Determined using Equation 8.

In a following step, F-CTA-1 was used to investigate the effect of different targeted chain lengths, and therefore $[M]_0$:$[CTA]_0$ ratios on the polymerization behaviour. As illustrated in **Figure 3**, a lower $[M]_0$:$[CTA]_0$ ratio, resulted in an increased polymerization kinetics due to an higher initiator concentration and, more important, significantly lowered the polydispersity values. In particular, polydispersity values ranging from 1.41 to 1.34 and 1.38 to 1.32, were found for $[M]_0$:$[CTA]_0$ = 100 and 50, respectively (**Figure 4A** and **4B** and **Table S1**), compared to values around 1.56-1.44 previously found for $[M]_0$:$[CTA]_0$ = 200 (**Figure 2B** and **Table S1**). However, the discrepancy between theoretical and experimental molecular weights was still observed. A plot of the experimental Ln[F-CTA-1] *vs* Ln[M] data is shown in **Figure 5**. **Table 1** summarize the C_{tr} and C_{-tr} values obtained for the polymerization conditions using different $[M]_0$:$[CTA]_0$

ratios, whereas the fitted experimental points are reported in **Figure S5**. First, C_{tr} values obtained for different targeted chain lengths did not change significantly. Although variation of C_{tr} with $[M]_0$:$[CTA]_0$ ratios were observed in literature,[5] the results found here are in agreement with the definition of transfer constants as intrinsic property for a given CTA/monomer system.[5]
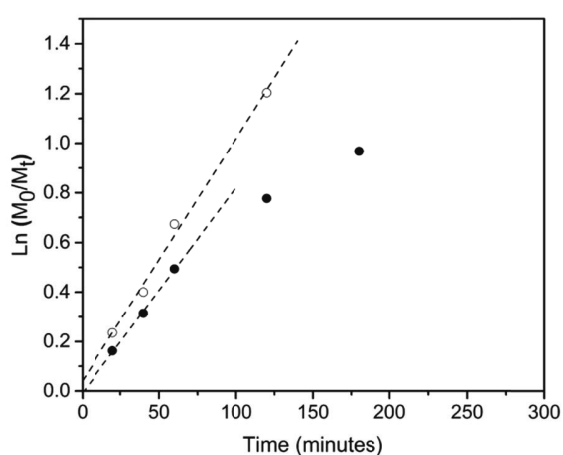

Figure 3. First-order kinetics plot for the RAFT polymerization of PFMA as determined by ^{19}F-NMR. Polymerization conditions: dioxane, 75°C, $[M]_0 = 1.8$ M, $[M]_0$:$[F$-CTA-1$]_0$ = 200 (■), 100 (●) and 50 (○), $[F$-CTA-1$]_0$:$[I]_0 = 10$.
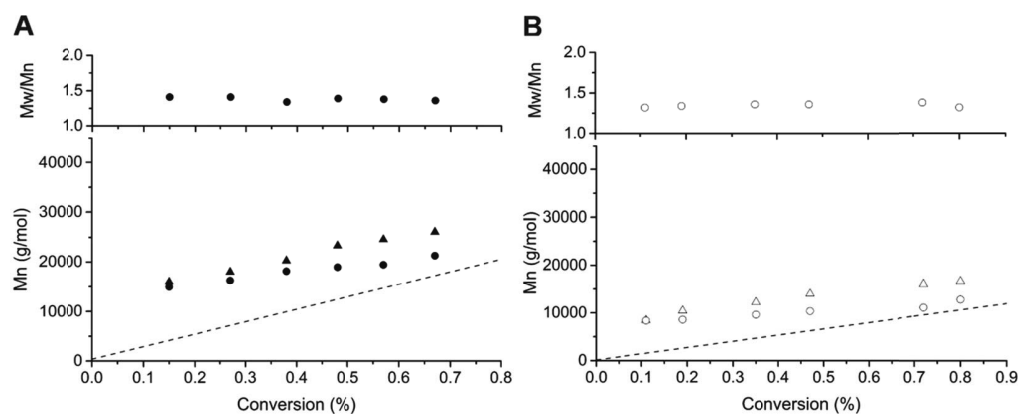
Figure 4. Polymerization conditions: dioxane, 75°C, $[M]_0 = 1.8$ M, $[M]_0$:$[F$-CTA-1$]_0$ = 100 (●) and 50 (○), $[F$-CTA-1$]_0$:$[I]_0 = 10$. (A) Evo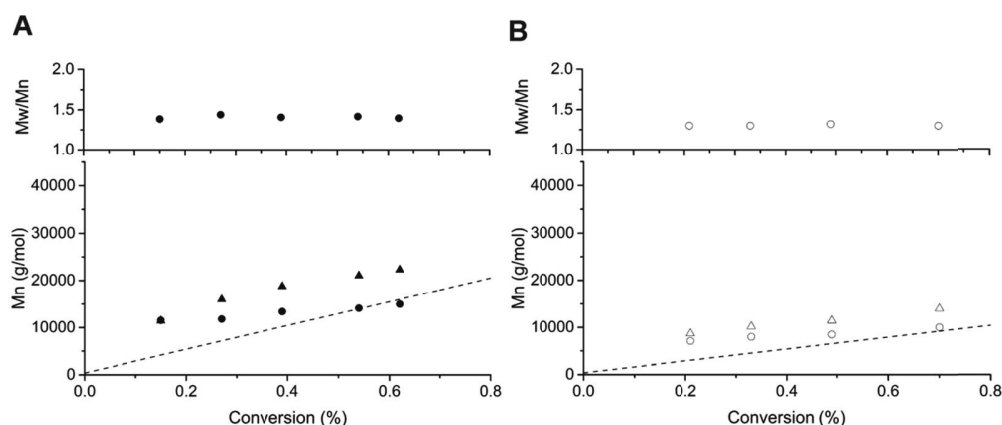lution of experimental M_n and M_w/M_n as a function of monomer conversion for $[M]_0$:$[F$-CTA-1$]_0$ = 100 as determined by SEC (●) and ^{19}F-NMR (▲) and (B) $[M]_0$:$[F$-CTA-1$]_0$ = 50 as determined by SEC (○) and ^{19}F-

NMR (Δ) . SEC analysis was performed using THF as solvent and PS standards were used for conventional calibration. Dashed lines indicates the theoretical M_n (M_n^{TH}) expected for the different conditions.
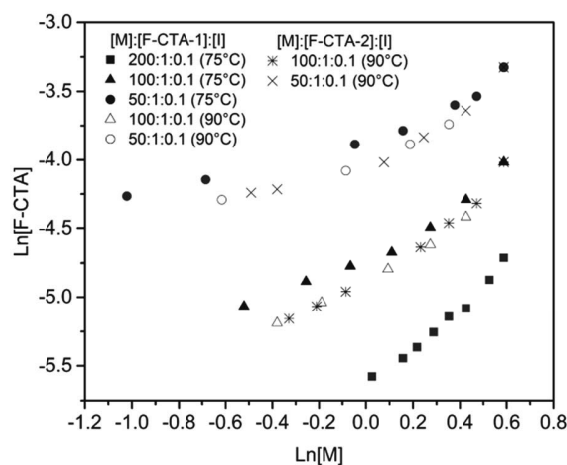
Figure 5. Double logaritmic plot of F-CTAs concentration *vs* monomer concentration during the polymerization of PFMA at 75 and 90 °C for different $[M]_0$:$[CTA]_0$ ratios as determined by ^{19}F-NMR measurements.

An interesting approach that have been proposed to enhance control over the polymerization in case of slow consumption of the CTA, is the one proposed by Benaglia *et al*. The author investigated the effect of the polymerization temperature on the RAFT polymerization of MMA using different CTAs[29] and reported that, higher polymerization temperature (90°C *vs* 60°C) increased the propagation chain constant as expected, but also enhanced the rate of chain transfer allowing for very narrow polydispersity from the beginning of the polymerization process. Hence, the effect of the temperature on the PFMA polymerization was investigated. To this purpose, F-CTA-1 and ^{19}F-NMR were used to investigate the PFMA polymerization conditions reported in literature employing higher temperature (90°C).[24] Two different $[M]_0$:$[CTA]_0$ ratios, 50 and 100, were compared. Examples of ^{19}F-NMR spectra of the polymers obtained using $[M]_0$:$[CTA]_0$ = 50 are reported in **Figure S6-S9**. As shown in **Figure 6**, at 90°C both conditions showed a higher polymerization rate as compared to 75°C (**Figure 3**). This effect derives from both the enhanced propagation chain and initiator decomposition rates. This allowed a given conversion to be achieved in a shorter reaction time. However, in the case of

$[M]_0:[CTA]_0$ = 100, the lower initiator concentration, together with the higher polymerization temperature, contributed to a decrease in radical species and resulted in a relatively fast deviation from linearity. This phenomenon is associated with the lower half-life of the initiator at 90°C which is 24 minutes compared to 2.6 h at 75°C, as calculated from the k_d.[28] As reported in **Table 1**, for both conditions, C_{tr} values slightly increased. In particular, for $[M]_0:[CTA]_0$ = 50, C_{tr} increased from 3.5 at 75 °C to 4.7 at 90 °C, while in the case of $[M]_0:[CTA]_0$ = 100, C_{tr} increased from 3.2 to 4.1. This increase, even though modest, further lowered the polydispersity, especially for $[M]_0:[CTA]_0$ = 50, for which values around 1.3 were obtained from the early stage of the process (**Figure 7A** and **7B** and **Table S3**). This result clearly confirms what reported by Benaglia *et al.* and suggests that higher polymerization temperatures can increase the polymerization control by increasing the chain transfer rate.[29]

Figure 6. First-order kinetics plot for the RAFT polymerization of PFMA as determined by ^{19}F-NMR. Polymerization conditions: dioxane, 90°C, $[M]_0$ = 1.8 M, $[M]_0:[F\text{-}CTA\text{-}1]_0$ = 100 (●) and 50 (○), $[F\text{-}CTA\text{-}1]_0:[I]_0$ = 10.

Figure 7. Polymerization conditions: dioxane, 90°C, $[M]_0 = 1.8$ M, $[M]_0$:$[F\text{-}CTA\text{-}1]_0 = 100$ (●) and 50 (○), $[F\text{-}CTA\text{-}1]_0$:$[I]_0 = 10$. (A) Evolution of experimental M_n and M_w/M_n as a function of monomer conversion for $[M]_0$:$[F\text{-}CTA\text{-}1]_0 = 100$ as determined by SEC (●) and ^{19}F-NMR (▲) and (B) $[M]_0$:$[F\text{-}CTA\text{-}1]_0 = 50$ as determined by SEC (○) and ^{19}F-NMR (△). SEC analysis was performed using THF as solvent and PS standards were used for conventional calibration. Dashed lines indicate the theoretical M_n (M_n^{TH}) expected for the different conditions.

2.3.4. PFMA polymerization using F-CTA-2

Apart from the establishment of simple and reliable methods to investigate CTA efficiency and to determine experimental molecular weights, another important objective is the development of methods to analyze polymer end groups. α,ω-end group analysis of RAFT polymers gives important information about the presence of chain termination reactions, ω end group loss, which can occur at high polymerization time and temperature and livingness of the polymerization. Moreover, high end group fidelity is a fundamental prerequisite for the synthesis of block copolymers *via* macroRAFT agents[11,31,32] as well as an important parameter for end group post-polymerization reactions.[33] In order to establish a simple method to determine α,ω-end group fidelity, Päch *et al*. designed a series of RAFT agents labeled with two complementary trimethylsilyl (TMS) groups in both R and Z positions and proposed this as a tool for universal polymer analysis by ^{1}H-NMR spectroscopy. The ratios between the two TMS signals allowed the determination of ω/α end group ratio for different polymerization conditions and highlighted high loss (up to 60%) of Z active polymer chain ends for certain polymerization conditions even when low polydispersity (1.2) were achieved.[11] Hence, we decided to further extend the

scope of this work and investigate the use of F-CTAs and ^{19}F-NMR for end group analysis. A second fluorinated CTA derivative (F-CTA-2) bearing a fluorinated label in both R (α) and Z(ω) groups was prepared and used for PFMA polymerization at 90°C using both $[M]_0:[CTA]_0 = 100$ and $[M]_0:[CTA]_0 = 50$. The resulting kinetics and transfer coefficients were compared to that obtained using F-CTA-1 and confirmed that the insertion of the trifluoromethyl group in Z position of the CTA only slightly affected the polymerization process. The kinetics of the polymerizations were only slightly slower than that obtained for F-CTA-1 and the experimental molecular weights and polydispersity were also comparable (**Figure S10** and **Table S3**). Examples of ^{19}F-NMR spectra of the polymers obtained using $[M]_0:[CTA]_0 = 50$ are reported in Supporting Information in **Figure S11-S14**. The found C_{tr} and C_{-tr} values, 4.0 and 390.1 and 4.8 and 370.1, for $[M]_0:[CTA]_0 = 100$ and 50, respectively, were close to those obtained for F-CTA-1 as reported in **Table 1** and **Figure 5.** One example of ^{19}F-NMR spectrum of PPFMA prepared using F-CTA-2 is given in **Figure 1B**. The ω/α ratios were determined using the integrals deriving from the **a*** (α) and **b*** (ω) fluorine peaks incorporated in the polymer. It should be mentioned that due to the presence of initiator derived side-chains the ω/α values might be slightly underestimated, however, in general, when high $[CTA]_0:[I]_0$ ratios are used, the extent of polymer chains lacking α-end group functionalities can be neglect.[11] The obtained ω/α ratios for the two polymerization conditions for the different polymerization times are reported in **Table 2**. It was found that for both conditions, the initial ω/α ratios were close to unity and only slightly decrease up to values around 0.86 while increasing the polymerization time. This result suggests that only a minor loss of ω-end group might occur during the course of the polymerization.

Table 2. Determination of ω/α end group ratios *via* ^{19}F-NMR for the different PFMA polymerization times using F-CTA-2, $[M]_0$:$[F-CTA-2]_0$ = 100 and 50 and T = 90 °C.

$[M]_0$:$[F-CTA-2]_0$	Time (min.)	ω/α
100	20	0.97
	40	1.07
	60	0.97
	120	0.88
	180	0.89
	240	0.93
50	20	0.95
	40	0.9
	60	0.92
	120	0.86

2.4.   Conclusions

In this work the use of fluorinated chain transfer agents (F-CTAs) and ^{19}F-NMR analysis was proposed as a simple method to prepare α- and α,ω-fluorine labeled PPFMA and to monitor PFMA RAFT polymerization.

First, it was demonstrated that the insertion of a fluorinated label in the R group of the CTA-1 (F-CTA-1) had no effect on the PFMA RAFT polymerization therefore proving the feasibility of the proposed method. Second, the presence of the fluorinated label on the α-PPFMA end group allowed the determination of the experimental polymer molecular weights *via* ^{19}F-NMR studies. The comparison of the experimental molecular weights with that determined *via* SEC analysis allowed the selection of the best conditions for SEC analysis of PPFMA. The estimation of F-CTA-1 conversion *via* ^{19}F-NMR allowed the determination of the transfer constants and revealed that, due to the slow consumption of the CTA, the early stage of the PFMA polymerization proceeds *via* a hybrid conventional free radical-RAFT mechanism. The analysis of different polymerization conditions suggested that the polymerization control can be slightly enhanced by increasing the temperature of the polymerization. Finally, a second CTA-1 derivative bearing a fluorinated label on both R and Z groups (F-CTA-2) was used for the

preparation of α,ω-fluorinated PPFMA. Comparison between ω and α fluorine signals *via* ^{19}F-NMR analysis was used to determine α,ω-end group fidelity.

The use of fluorinated CTAs to monitor RAFT polymerization *via* ^{19}F-NMR was found an easy, fast and effective approach. This method offers the opportunity to directly determine the CTA consumption and therefore the transfer constants during RAFT polymerization. Moreover, the design of CTAs containing fluorine in both R and Z groups allows to investigate end groups fidelity during RAFT polymerization. As demonstrated, this approach is particularly attractive in case of fluorinated polymers since it allows the determination of several polymerization parameters *via* a single ^{19}F-NMR measurement. The α-fluorine labeled PPFMA prepared in this Chapter was used in **Chapter 3** and **Chapter 4** as a precursor polymer for the preparation of PHPMA polymers.

This work was carried out in collaboration with Prof. Jie Chen (Biological and Medical Materials Research Center, Shanghai University) and the PhD student Yuejiao Young who contributed with the synthesis of the F-CTA-2.

2.5.   References

(1)   Moad, G.; Rizzardo, E.; Thang, S. H., *Aust. J. Chem.* **2005**, *58*, 379.

(2)   Barner-Kowollik, C., "*Handbook of RAFT polymerization*", Wiley-VCH, Weinheim, 2008, p. xi.

(3)   Keddie, D. J.; Moad, G.; Rizzardo, E.; Thang, S. H., *Macromolecules* **2012**, *45*, 5321.

(4)   Chong, Y. K.; Krstina, J.; Le, T. P. T.; Moad, G.; Postma, A.; Rizzardo, E.; Thang, S. H., *Macromolecules* **2003**, *36*, 2256.

(5)   Han, X. Q.; Fan, J.; He, J. P.; Xu, J. T.; Fan, D. Q.; Yang, Y. L., *Macromolecules* **2007**, *40*, 5618.

(6)   Theis, A.; Feldermann, A.; Charton, N.; Stenzel, M. H.; Davis, T. P.; Barner-Kowollik, C., *Macromolecules* **2005**, *38*, 2595.

(7)   Pietsch, C.; Fijten, M. W. M.; Lambermont-Thijs, H. M. L.; Hoogenboom, R.; Schubert, U. S., *J. Polym. Sci., Part A: Polym. Chem.* **2009**, *47*, 2811.

(8)   Gibson, M. I.; Frohlich, E.; Klok, H. A., *J. Polym. Sci., Part A: Polym. Chem.* **2009**, *47*, 4332.

(9)   Gunay, K. A.; Klok, H. A., *Polym. Chem.* **2016**, *7*, 970.

(10)   Hoenders, D.; Tigges, T.; Walther, A., *Polym. Chem.* **2015**, *6*, 476.

(11)   Pach, M.; Zehm, D.; Lange, M.; Dambowsky, I.; Weiss, J.; Laschewsky, A., *J. Am. Chem. Soc.* **2010**, *132*, 8757.

(12)   Chiefari, J.; Mayadunne, R. T. A.; Moad, C. L.; Moad, G.; Rizzardo, E.; Postma, A.; Skidmore, M. A.; Thang, S. H., *Macromolecules* **2003**, *36*, 2273.

(13)   Boyer, C.; Valade, D.; Lacroix-Desmazes, P.; Ameduri, B.; Boutevin, B., *J. Polym. Sci., Part A: Polym. Chem.* **2006**, *44*, 5763.

(14)   Yu, J. X.; Hallac, R. R.; Chiguru, S.; Mason, R. P., *Prog. Nucl. Magn. Reson. Spectrosc.* **2013**, *70*, 25.

(15)   Yao, W. Q.; Li, Y. J.; Huang, X. Y., *Polymer* **2014**, *55*, 6197.

(16)   Muraro, P. I. R.; de Freitas, A. G. O.; Trindade, S. G.; Giacomelli, F. C.; Bonvent, J. J.; Schmidt, V.; dos Santos, F. P.; Giacomelli, C., *J. Fluorine Chem.* **2014**, *168*, 251.

(17)   Huang, X.; Huang, G.; Zhang, S.; Sagiyama, K.; Togao, O.; Ma, X.; Wang, Y.; Li, Y.; Soesbe, T. C.; Sumer, B. D.; Takahashi, M.; Sherry, A. D.; Gao, J., *Angew. Chem. Int. Ed.* **2013**, *52*, 8074.

(18)   Gunay, K. A.; Theato, P.; Klok, H. A., *J. Polym. Sci., Part A: Polym. Chem.* **2013**, *51*, 1.

(19)   Barz, M.; Canal, F.; Koynov, K.; Zentel, R.; Vicent, M. J., *Biomacromolecules* **2010**, *11*, 2274.

(20)   Mohr, N.; Barz, M.; Forst, R.; Zentel, R., *Macromol. Rapid Commun.* **2014**, *35*, 1522.

(21)   Barz, M.; Luxenhofer, R.; Zentel, R.; Kabanov, A. V., *Biomaterials* **2009**, *30*, 5682.

(22)   Nuhn, L.; Hirsch, M.; Krieg, B.; Koynov, K.; Fischer, K.; Schmidt, M.; Helm, M.; Zentel, R., *ACS nano* **2012**, *6*, 2198.

(23)   Eberhardt, M.; Mruk, R.; Zentel, R.; Theato, P., *Eur. Polym. J.* **2005**, *41*, 1569.

(24)   Eberhardt, M.; Theato, P., *Macromol. Rapid Commun.* **2005**, *26*, 1488.

(25)   Boyer, C.; Bulmus, V.; Davis, T. P.; Ladmiral, V.; Liu, J. Q.; Perrier, S., *Chem. Rev.* **2009**, *109*, 5402.

(26)   Barz, M.; Tarantola, M.; Fischer, K.; Schmidt, M.; Luxenhofer, R.; Janshoff, A.; Theato, P.; Zentel, R., *Biomacromolecules* **2008**, *9*, 3114.

(27)   Herth, M. M.; Barz, M.; Moderegger, D.; Allmeroth, M.; Jahn, M.; Thews, O.; Zentel, R.; Rosch, F., *Biomacromolecules* **2009**, *10*, 1697.

(28)   Medeiros, S. F.; Barboza, J. C. S.; Re, M. I.; Giudici, R.; Santos, A. M., *J. Appl. Polym. Sci.* **2010**, *118*, 229.

(29)   Benaglia, M.; Rizzardo, E.; Alberti, A.; Guerra, M., *Macromolecules* **2005**, *38*, 3129.

(30)   Johnston-Hall, G.; Theis, A.; Monteiro, M. J.; Davis, T. P.; Stenzel, M. H.; Barner-Kowollik, C., *Macromol. Chem. Phys.* **2005**, *206*, 2047.

(31)   Skrabania, K.; Miasnikova, A.; Bivigou-Koumba, A. M.; Zehm, D.; Laschewsky, A., "Examining the UV-vis absorption of RAFT chain transfer agents and their use for polymer analysis", in *Polym. Chem.*, 2011, p. 2/2074.

(32)   Vandenbergh, J.; Junkers, T., *Macromolecules* **2014**, *47*, 5051.

(33)   Willcock, H.; O'Reilly, R. K., *Polym. Chem.* **2010**, *1*, 149.

2.6. Supporting Information

Table S1. Theoretical and experimental data for different PFMA polymerization time using different $[M]_0:[CTA]_0$ ratios. CTA = CTA-1 or F-CTA-1. T= 75°C, solvent dioxane, $[M]_0 = 1.8$ M, $[CTA]_0:[I]_0 = 10$.

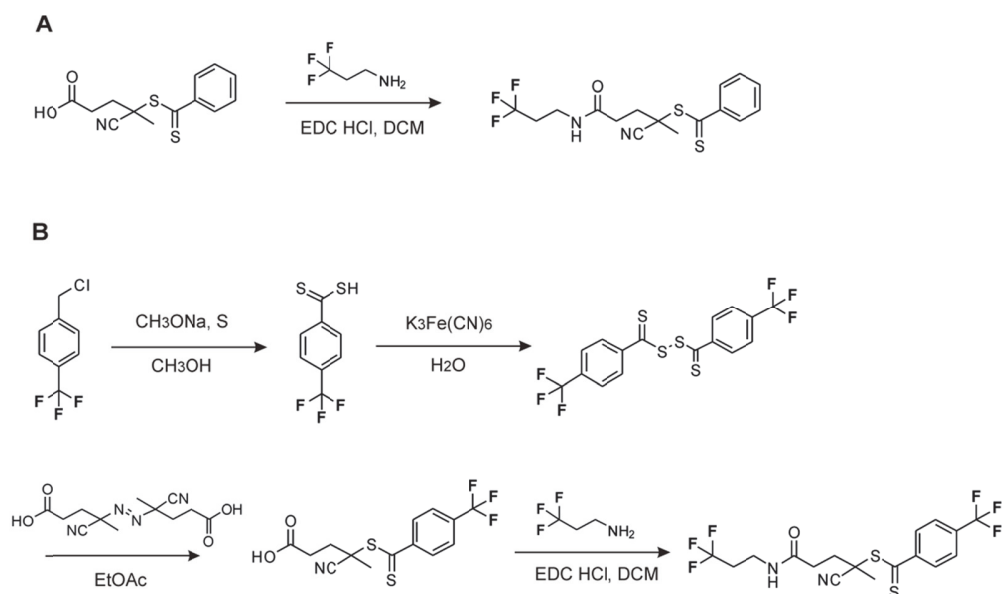| CTA	$[M]_0:[CTA]_0$	$[CTA]_0:[I]_0$	Time (min.)	ρ^a (%)	DP^{THb} (-)	M_n^{THb} (g/mol)	α^c (%)	DP^d (-)	M_n^d g/mol	SEC^e DP (-)	SEC^e M_n (g/mol)	SEC^e M_w/M_n (-)
CTA-1	200	10	60	0.08	16	4311	-	-	-	92	23061	1.52
			120	0.15	30	7839	-	-	-	99	24982	1.53
			180	0.2	40	10359	-	-	-	103	25985	1.55
			240	0.26	52	13383	-	-	-	110	27610	1.55
			300	0.29	58	14895	-	-	-	118	29739	1.56
			360	0.35	70	17919	-	-	-	123	31002	1.48
			420	0.39	78	19935	-	-	-	133	33541	1.45
			540	0.41	82	20943	-	-	-	-	-	-
F-CTA-1	200	10	60	0.06	12	3398	0.15	59	15242	79	19807	1.55
			120	0.15	30	7934	0.31	73	18770	88	22159	1.55
			180	0.21	42	10958	0.35	85	21794	88	22261	1.49
			240	0.26	52	13478	0.42	97	24818	90	22744	1.55
			300	0.31	62	15998	0.48	100	25574	101	25546	1.48
			360	0.35	70	18014	0.52	104	26582	102	25723	1.44
			420	0.4	80	20534	0.54	-	-	109	27374	1.44
			540	0.43	86	22046	0.58	112	28598	-	-	-
	100	10	60	0.15	15	4154	0.24	62	15998	59	14957	1.41
			120	0.27	27	7178	0.38	70	18014	65	16260	1.41
			180	0.38	38	9950	0.48	79	20282	72	18135	1.34
			240	0.48	48	12470	0.51	91	23306	75	18952	1.39
			300	0.57	57	14738	0.58	96	24566	77	19435	1.38
			360	0.67	67	17258	0.65	102	26078	84	21274	1.36
	50	10	40	0.11	5	1760	0.19	32	8438	33	8400	1.32
			60	0.19	9	2768	0.24	40	10454	34	8601	1.34
			120	0.35	17	4784	0.37	47	12218	38	9639	1.36
			180	0.47	23	6296	0.43	54	13982	41	10374	1.36
			300	0.72	36	9446	0.56	61	15868	44	11052	1.38
			360	0.80	40	10454	0.61	63	16439	51	12727	1.32

[a] Monomer conversion determined by ^{19}F-NMR comparing the fluorine monomer and polymer peaks.

[b] Theoretical number-average molecular weight (M_n^{TH}) and degree of polymerization (DP^{TH}) at different polymerization time calculated for each monomer conversion.

[c] CTA conversion determined by ^{19}F-NMR comparing the F-CTA-1 and macroF-CTA-1 fluorine peaks.

[d] Number-average molecular weight (M_n) and degree of polymerization (DP) calculated from ^{19}F-NMR comparing the fluorine peaks of the macroF-CTA-1 and the PFMA polymer units.

[e] Number-average molecular weight (M_n), degree of polymerization (DP) and polydispersity (M_w/M_n) determined by SEC in THF using conventional calibration using polystyrene (PS) standards.

Table S2. PPFMA molecular weights determined by both ^{19}F-NMR and SEC analysis using different solvents and standards. Polymerization conditions: CTA = F-CTA-1, $[M]_0{:}[CTA]_0 = 200$, T= 75°C, solvent dioxane, $[M]_0 = 1.8$ M and $[CTA]_0{:}[I]_0 = 10$.

CTA	$[M]_0{:}[CTA]_0$	DP^a (-)	M_n^a (g/mol)	SEC in THF$_{PS}$			SEC in THF$_{PMMA}$			SEC in DMF$_{PMMA}$		
				DP (-)	M_n (g/mol)	M_w/M_n (-)	DP (-)	M_n (g/mol)	M_w/M_n (-)	DP (-)	M_n (g/mol)	M_w/M_n (-)
F-CTA-1	200	59	15242	79	19807	1.55	94	23811	1.47	53	13374	1.4
		73	18770	88	22159	1.55	105	26491	1.47	45	11540	1.16
		85	21794	88	22261	1.49	105	26551	1.42	51	12752	1.22
		97	24818	90	22744	1.55	108	27159	1.47	52	12903	1.21
		100	25574	101	25546	1.48	120	30241	1.41	51	12790	1.20
		104	26582	102	25723	1.44	121	30395	1.38	51	12738	1.21
		-	-	109	27374	1.44	128	32221	1.38	-	-	-

[a] Number-average molecular weight (M_n) and degree of polymerization (DP) calculated from ^{19}F-NMR comparing the fluorine peaks of the macroF-CTA-1 and the PFMA polymer units.

Table S3. Theoretical and experimental data for different PFMA polymerization time using different $[M]_0:[CTA]_0$ ratios. CTA = F-CTA-1 or F-CTA-2. T= 90°C, solvent dioxane, $[M]_0 = 1.8$ M, $[CTA]_0:[I]_0 = 10$.

CTA	$[M]_0:[CTA]_0$	$[CTA]_0:[I]_0$	Time (min.)	ρ^a (%)	DP^{THb} (-)	M_n^{THb} (g/mol)	α^c (%)	DP^d (-)	M_n^d g/mol	SEC[e] DP (-)	M_n (g/mol)	M_w/M_n (-)
F-CTA-1	100	10	20	0.15	15	4154	0.33	44	11462	46	11546	1.39
			40	0.27	27	7178	0.45	62	15998	47	11812	1.44
			60	0.39	39	10202	0.54	73	18770	53	13402	1.4
			120	0.54	54	13981	0.64	82	21038	56	14111	1.42
			180	0.62	62	15997	0.69	87	22298	59	14990	1.39
	50	10	20	0.21	10	3020	0.34	33	8690	28	7112	1.3
			40	0.33	16	4532	0.43	39	10202	32	7985	1.3
			60	0.49	24	6548	0.53	44	11462	34	8477	1.32
			120	0.7	35	9194	0.61	54	13982	40	10025	1.3
F-CTA-2	100	10	20	0.11	11	3214	0.26	42	11026	55	13747	1.38
			40	0.21	21	5734	0.36	63	16318	56	14148	1.32
			60	0.3	30	8002	0.46	74	19090	62	15739	1.36
			120	0.49	49	12789	0.61	84	21610	70	17580	1.33
			180	0.55	55	14301	0.65	89	22870	73	18325	1.36
			240	0.6	60	15561	0.69	93	23715	75	18915	1.33
	50	10	20	0.15	7	2332	0.27	30	8002	42	10552	1.24
			40	0.29	14	4096	0.41	38	10018	47	11725	1.3
			60	0.4	20	5482	0.5	46	12034	50	12576	1.24
			120	0.62	31	8254	0.59	59	15310	53	13383	1.25

[a] Monomer conversion determined by ^{19}F-NMR comparing the fluorine monomer and polymer peaks.

[b] Theoretical number-average molecular weight (M_n^{TH}) and degree of polymerization (DP^{TH}) at different polymerization time calculated for each monomer conversion.

[c] CTA conversion determined by ^{19}F-NMR comparing the F-CTA-1 and macroF-CTA-1 fluorine peaks.

[d] Number-average molecular weight (M_n) and degree of polymerization (DP) calculated from ^{19}F-NMR comparing the fluorine peaks of the macroF-CTA-1 and the PFMA polymer units.

[e] Number-average molecular weight (M_n), degree of polymerization (DP) and polydispersity (M_w/M_n) determined by SEC in THF using conventional calibration using polystyrene (PS) standards.

Scheme S1. Synthesis of the (A) F-CTA-1 and (B) F-CTA-2.
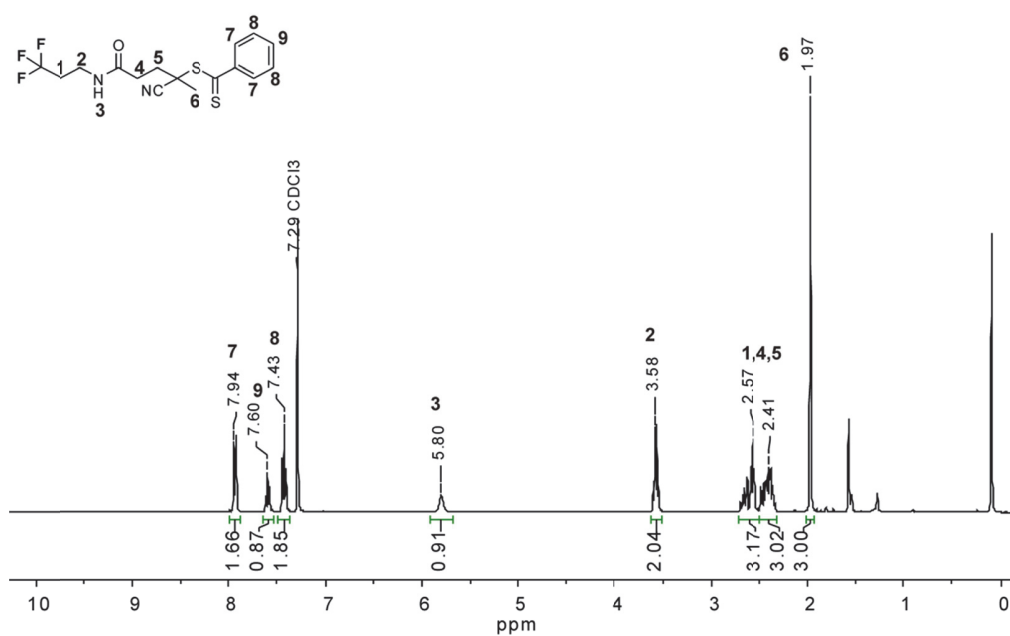
Figure S1. ^{1}H-NMR spectrum of F-CTA-1 in CDCl$_3$.
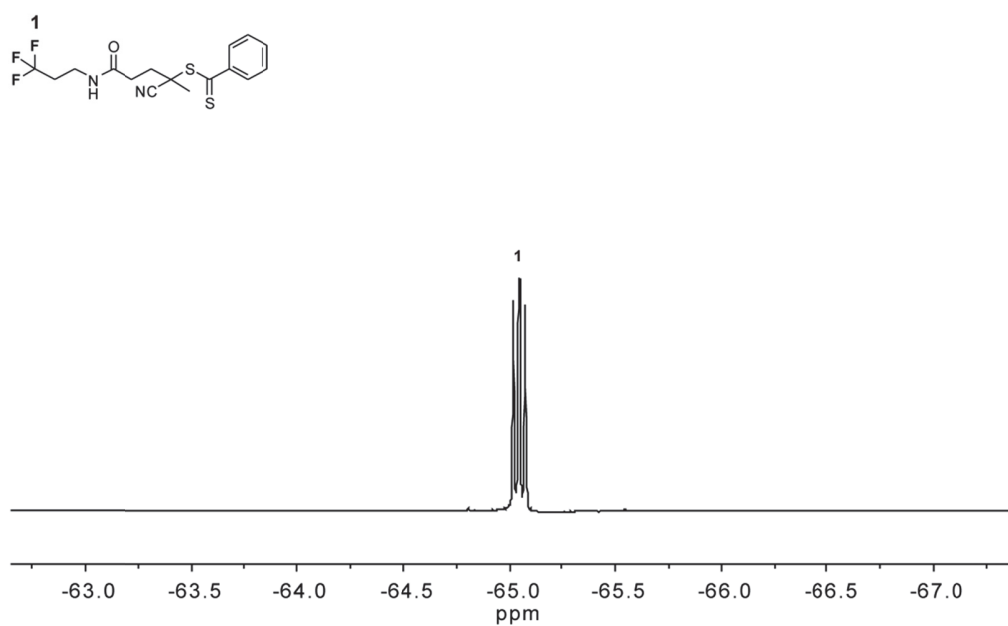
Figure S2. ^{19}F-NMR spectrum of F-CTA-1 in CDCl$_3$.
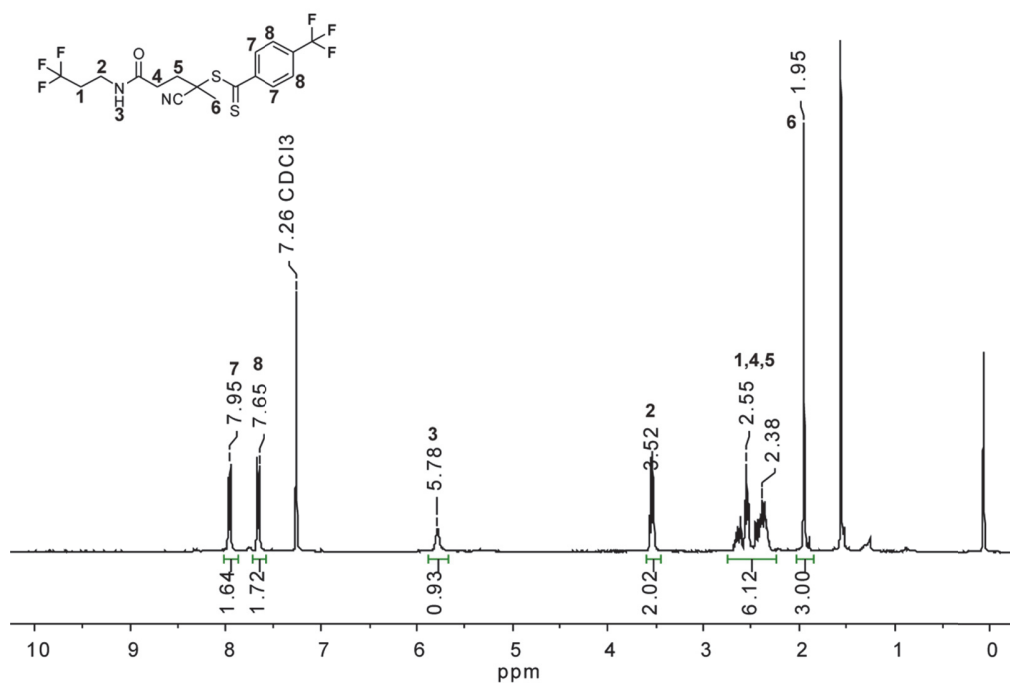
Figure S3. ^{1}H-NMR spectrum of F-CTA-2 in CDCl$_3$ (the peak at 1.56 ppm corresponds to water in CDCl$_3$).
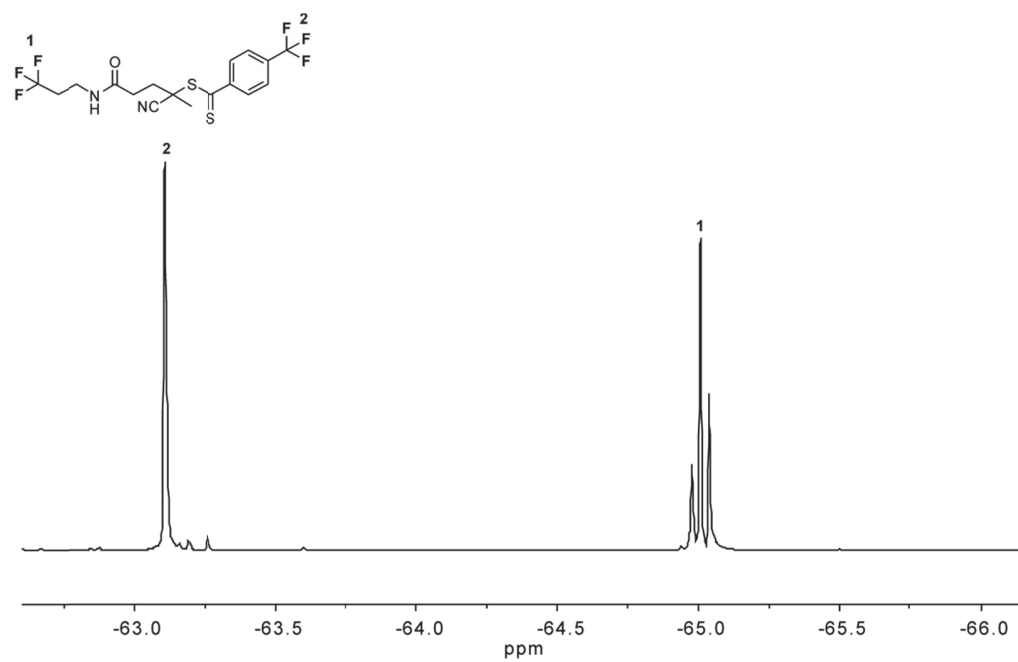
Figure S4. ^{19}F-NMR spectrum of F-CTA-2 in CDCl$_3$.
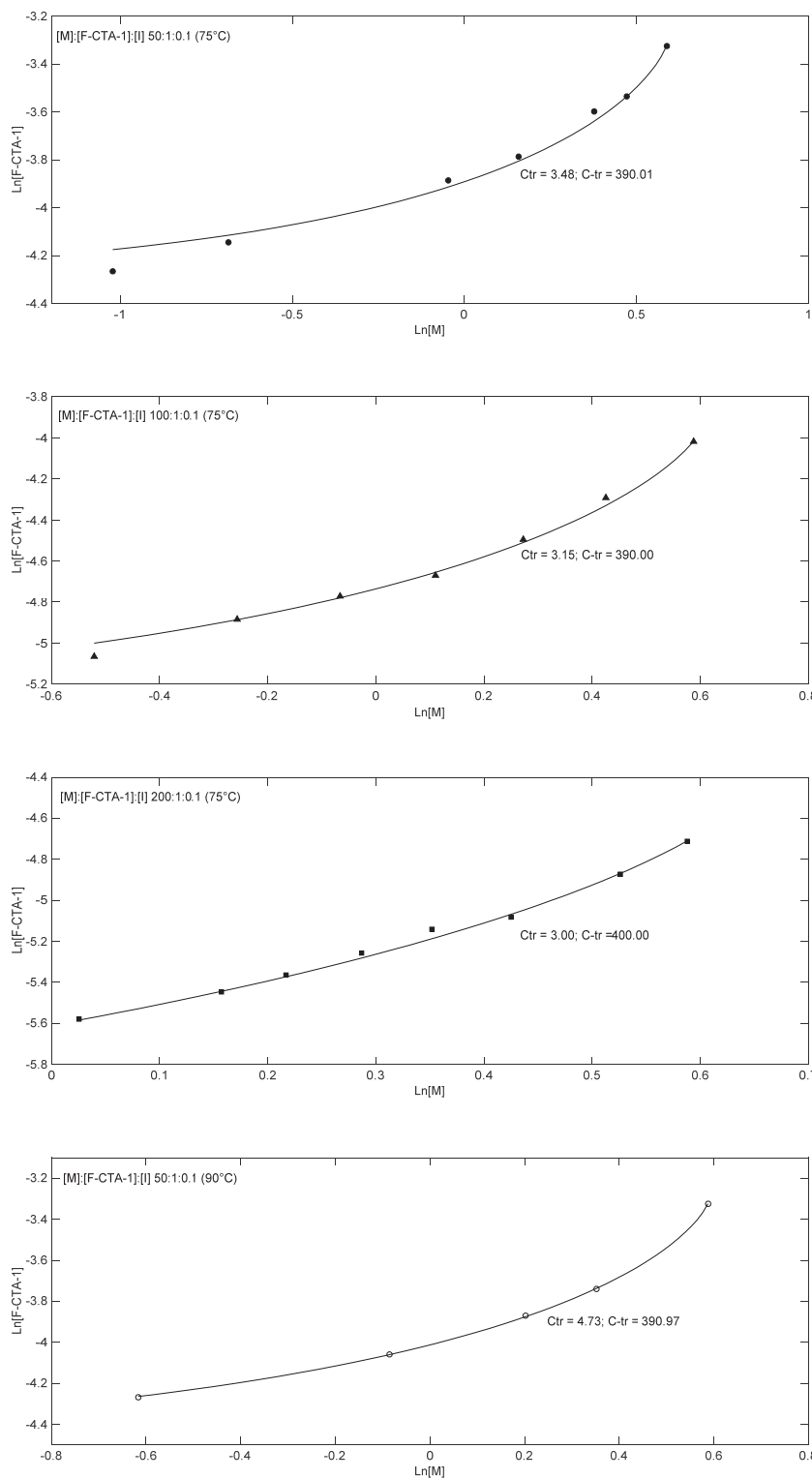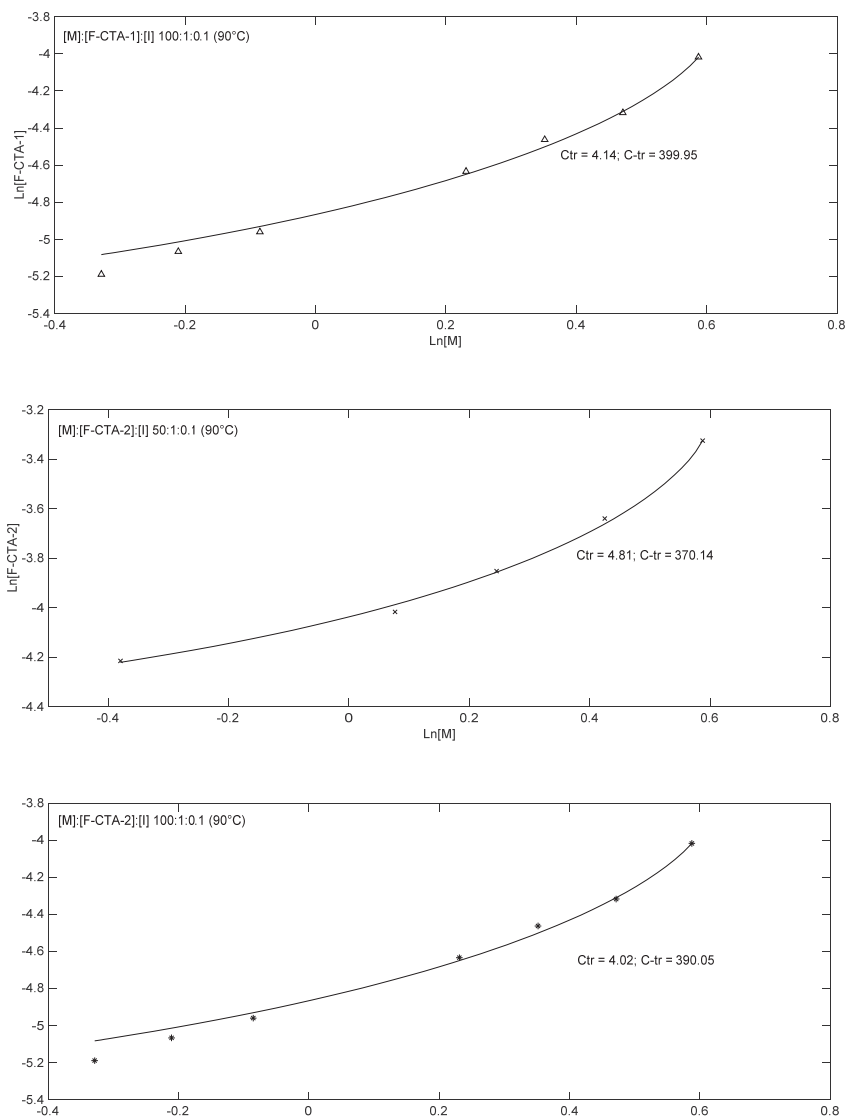
Figure S5. Double logarithmic plot of F-CTA-1 and F-CTA-2 concentrations *vs* monomer concentration for the polymerization of PFMA at 75 and 90°C for different $[M]_0:[CTA]_0$ ratios at different polymerization time. Curves are the numerical fitting results obtained using Equation (8).
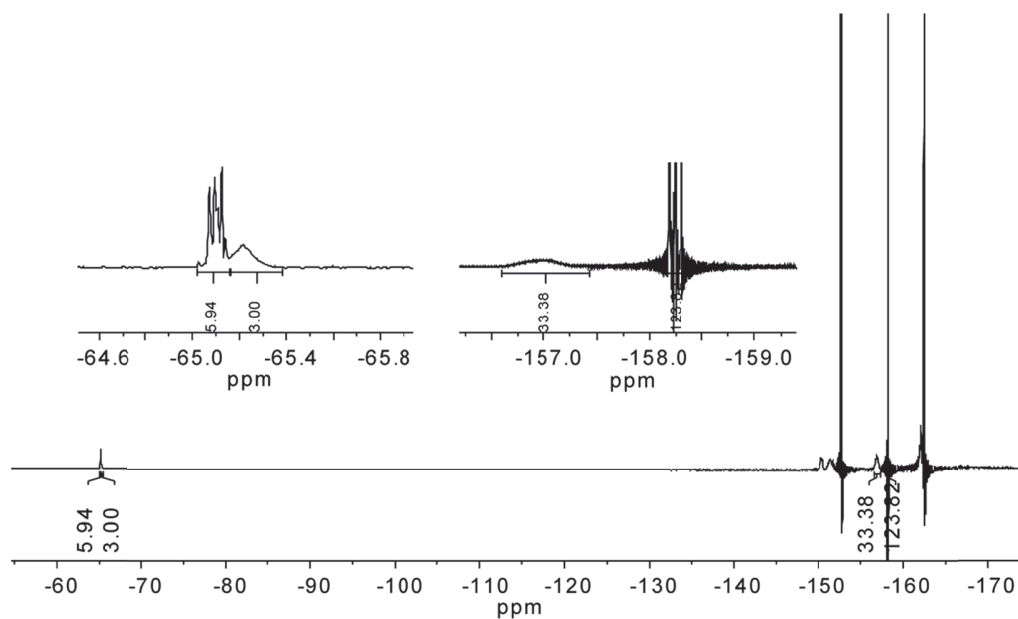
Figure S6. ^{19}F-NMR spectrum of crude PPFMA in CDCl$_3$. Polymerization conditions: [M]$_0$:[F-CTA-1]$_0$ = 50, T= 90°C, polymerization time 20 minutes.
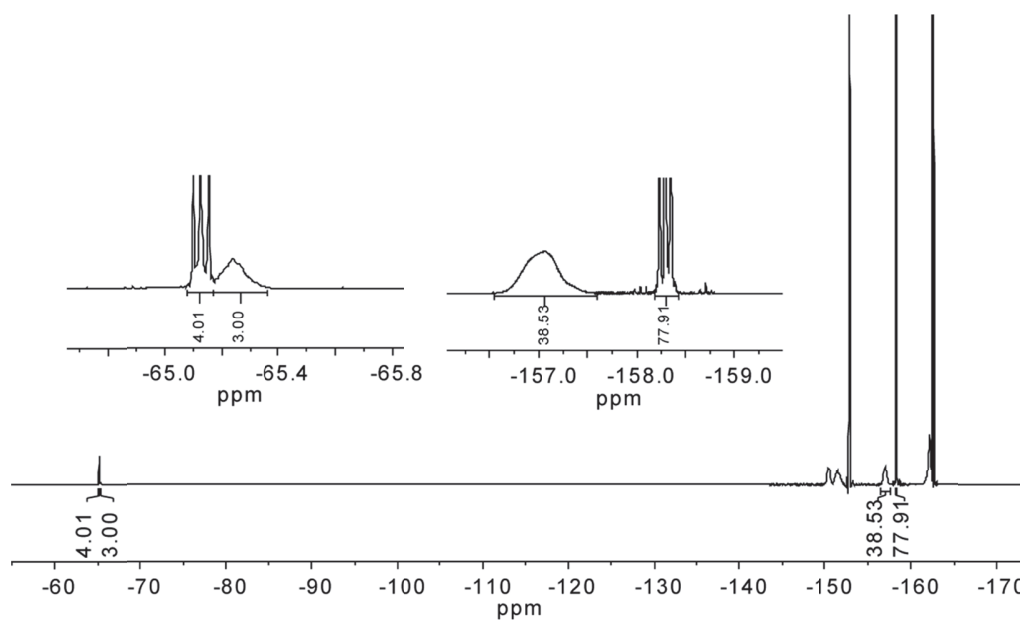
Figure S7. ^{19}F-NMR spectrum of crude PPFMA in CDCl$_3$. Polymerization conditions: [M]$_0$:[F-CTA-1]$_0$ = 50, T= 90°C, polymerization time 40 minutes.
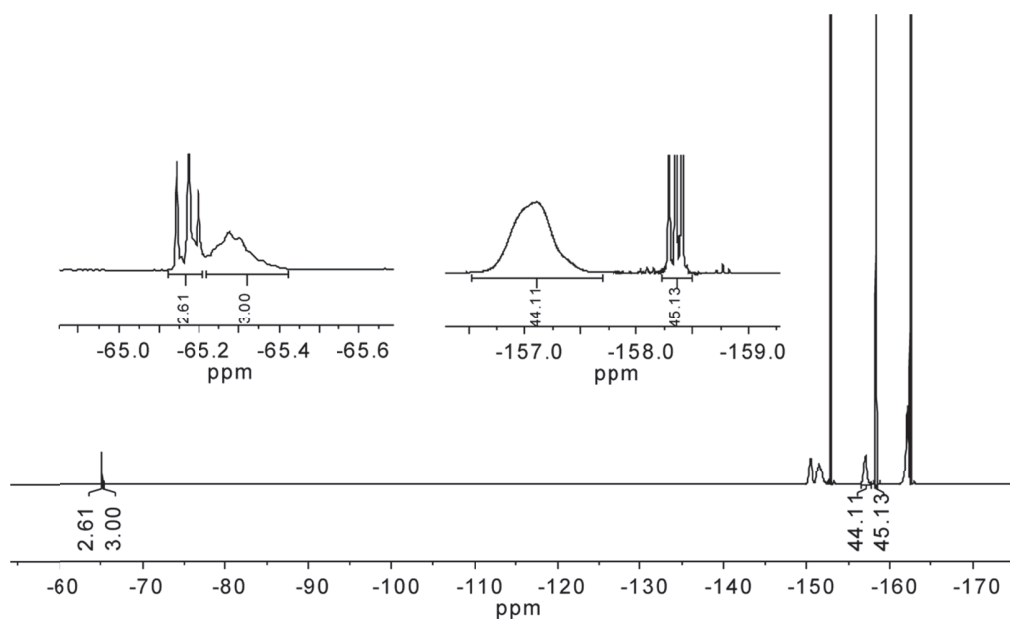
Figure S8. ^{19}F-NMR spectrum of crude PPFMA in CDCl$_3$. Polymerization conditions: [M]$_0$:[F-CTA-1]$_0$ = 50, T= 90°C, polymerization time 60 minutes.
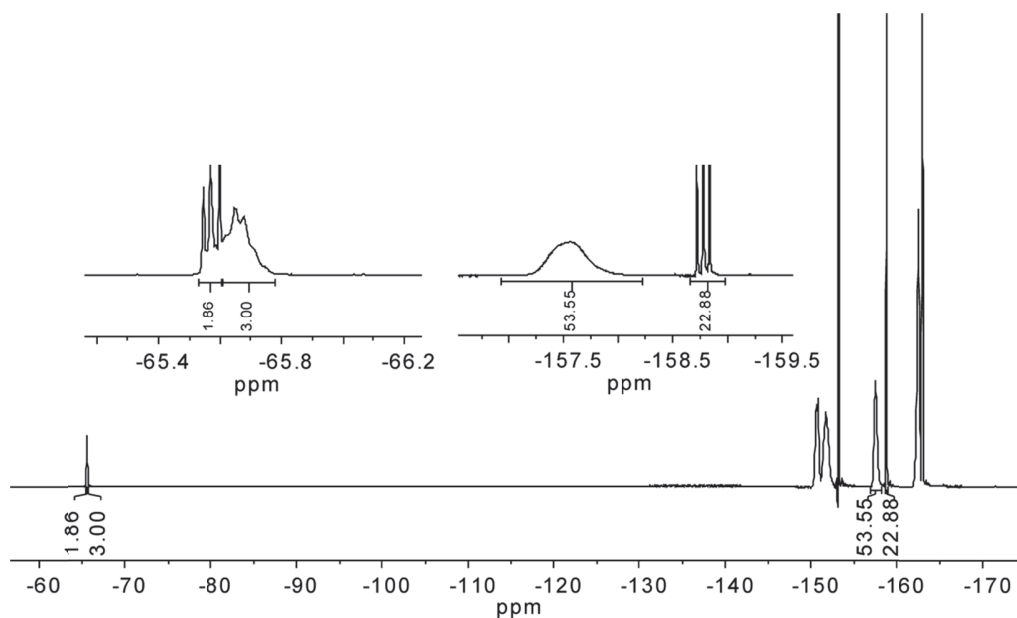
Figure S9. ^{19}F-NMR spectrum of crude PPFMA in CDCl$_3$. Polymerization conditions: [M]$_0$:[F-CTA-1]$_0$ = 50, T= 90°C, polymerization time 120 minutes.
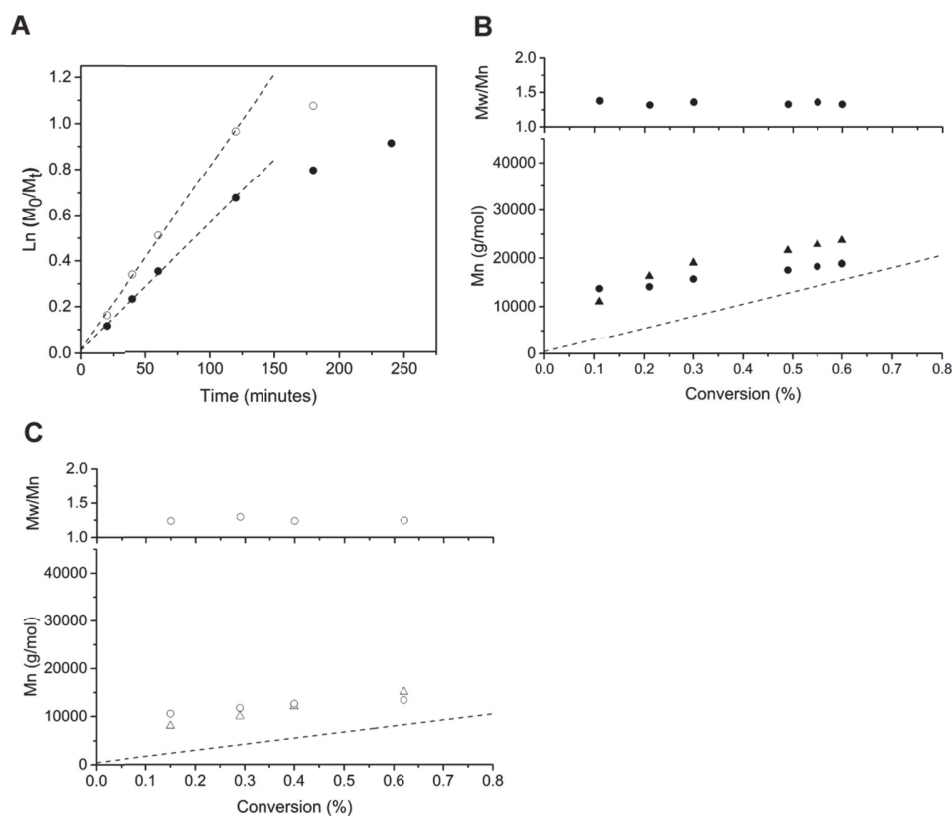
Figure S10. (A) First-order kinetics plot for the RAFT polymerization of PFMA as determined by ^{19}F-NMR. Polymerization conditions: dioxane; 90°C, $[M]_0 = 1.8$ M, $[M]_0:[F\text{-}CTA\text{-}2]_0 = 100$ (●) and 50 (○), $[F\text{-}CTA\text{-}2]_0:[I]_0 = 10$. (B) Evolution of experimental M_n and M_w/M_n as a function of monomer conversion for $[M]_0:[F\text{-}CTA\text{-}2]_0 = 100$ as determined by SEC (●) and ^{19}F-NMR (▲) and (C) $[M]_0:[F\text{-}CTA\text{-}2]_0 = 50$ as determined by SEC (○) and ^{19}F-NMR (△). SEC analysis was performed using THF as solvent and PS standards were used for conventional calibration. Dashed lines indicates the theoretical M_n (M_n^{TH}) expected for the different conditions.
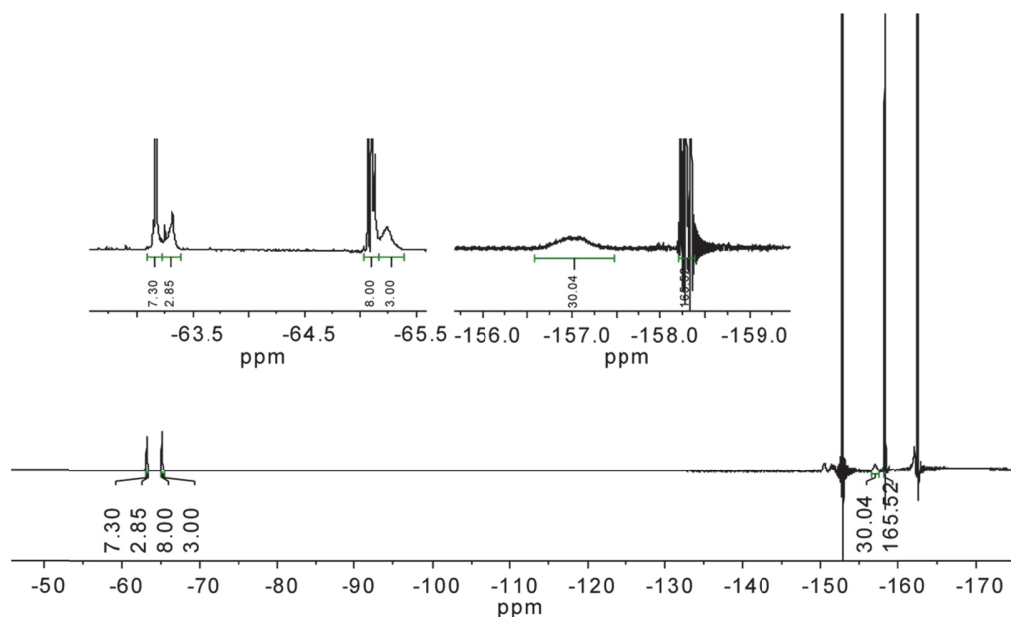
Figure S11. ^{19}F-NMR spectrum of crude PPFMA in CDCl$_3$. Polymerization conditions: [M]$_0$:[F-CTA-2]$_0$ = 50, T= 90°C, polymerization time 20 minutes.
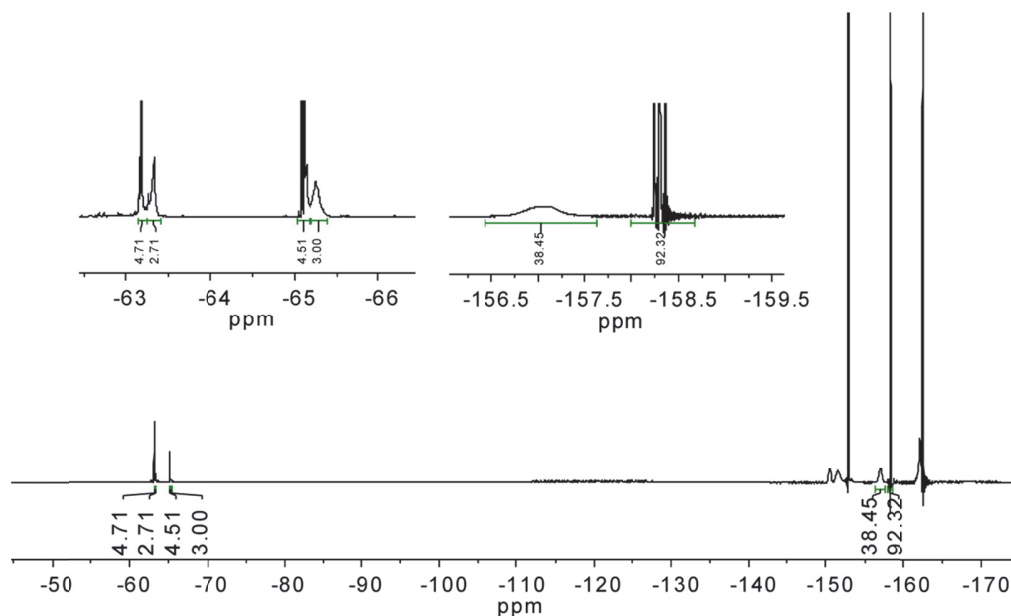
Figure S12. ^{19}F-NMR spectrum of crude PPFMA in CDCl$_3$. Polymerization conditions: [M]$_0$:[F-CTA-2]$_0$ = 50, T= 90°C, polymerization time 40 minutes.
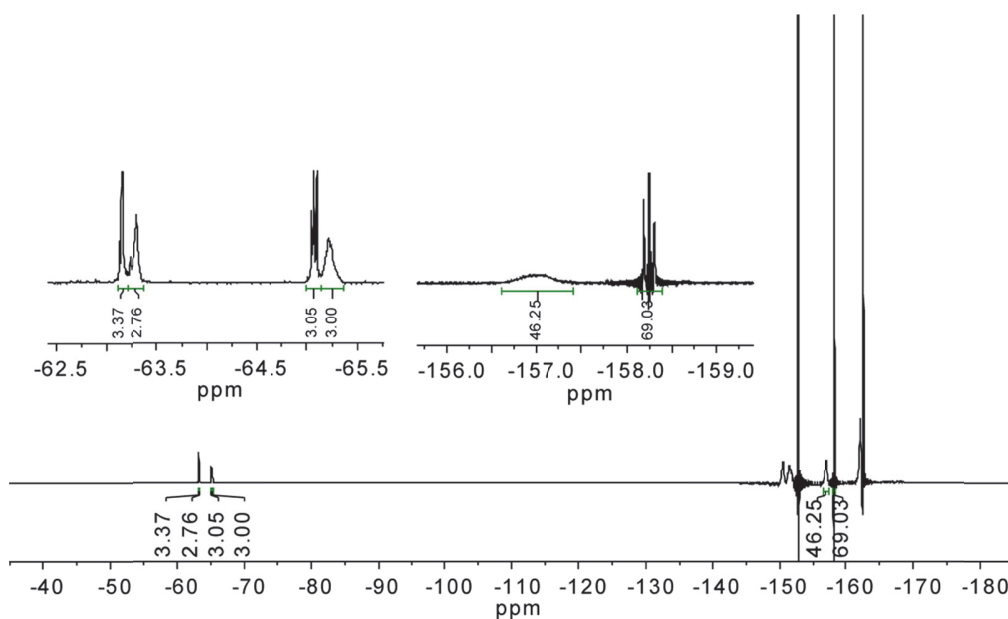
Figure S13. ^{19}F-NMR spectrum of crude PPFMA in CDCl$_3$. Polymerization conditions: [M]$_0$:[F-CTA-2]$_0$ = 50, T= 90°C, polymerization time 60 minutes.
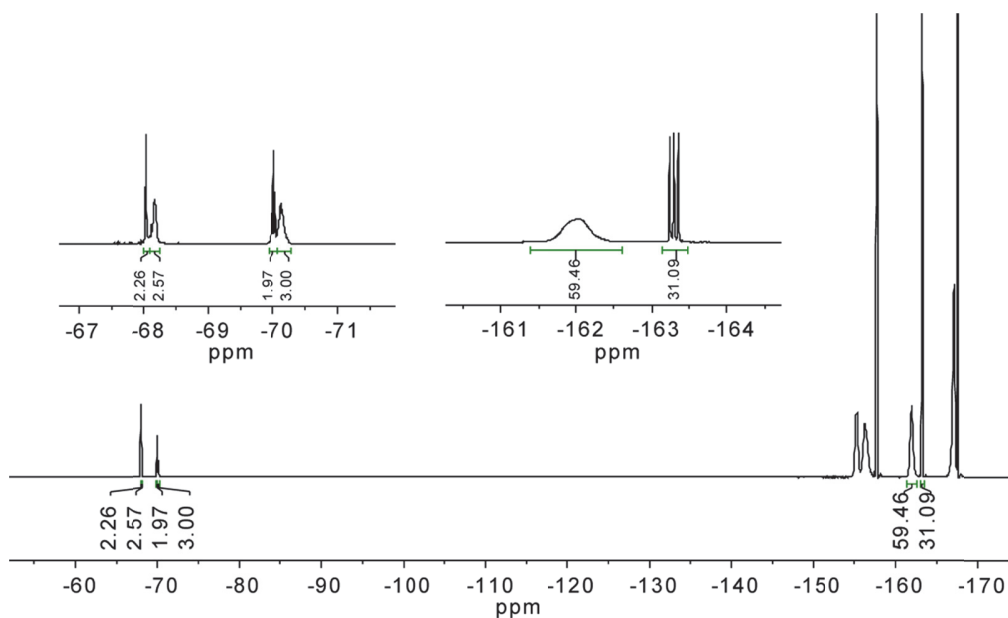
Figure S14. ^{19}F-NMR spectrum of crude PPFMA in CDCl$_3$. Polymerization conditions: [M]$_0$:[F-CTA-2]$_0$ = 50, T= 90°C, polymerization time 120 minutes.

3. Reversion of P-gp-Mediated Drug Resistance in Ovarian Carcinoma Cells with PHPMA-Zosuquidar Conjugates

3.1. Introduction

Chemotherapeutic agents are widely used to combat cancer. The onset of intrinsic or acquired multidrug resistance (MDR), however, a phenomenon in which cancer cells become resistant to an array of structurally and functionally unrelated chemotherapeutic agents, can lead to a poor clinical outcome.[1] For instance, over 90% of the metastatic cancers do not respond to chemotherapy due to resistance mechanisms and result in therapy failure.[2] One of the most common mechanisms that can lead to the resistance of cancer cells to chemotherapeutics is associated to the presence of membrane transporter proteins, which are overexpressed on cancer cells.[3-8] P-glycoprotein (P-gp), in particular, acts as an efflux pump that decreases the intracellular concentration of the chemotherapeutics. Doxorubicin, daunorubicin, vincristine, vinblastine, paclitaxel, docetaxel and bisantrene are only a few examples of widely used anticancer drugs that are also P-gp substrates.[1,3,9] The occurrence of P-gp mediated cross-resistance requires the use of higher dosages of these anticancer drugs, which further aggravates the survival rate of the patients due to the onset of numerous and intolerable side effects.[10]

A number of approaches have been developed to combat P-gp mediated MDR. A first strategy is the use of low molecular weight P-gp inhibitors.[3] The first two generations of these P-gp inhibitors, however, were hampered by relatively low binding affinities and selectivities requiring high dosages and resulting in unacceptable *in vivo* toxicity.[3,10,11] These issues could be partially resolved by a third generation of P-gp inhibitors, which were characterized by a higher specificity and affinity towards the P-gp transporter and lower toxicity.[3] In spite of these refinements, the co-administration of low molecular weight P-gp inhibitors and chemotherapeutics still suffers some limitations. First, there is

the unpredictable pharmacokinetics of the two unrelated drugs, which may lead to different time scales for their accumulation in the target cells.[10,12,13] A second problem is the lack of selectivity of small molecule drugs towards cancer tissues, which causes an undesirable accumulation of these drugs also in healthy cells.[11,12, 14] It is important to mention that P-gp is not only expressed in cancer cells, but also in healthy tissues where this transporter protein plays a central role in the detoxification and protection of the organism against xenobiotics.[1,3,11] Hence, the incapability of the P-gp inhibitors to distinguish between healthy and cancer tissues can enhance the distribution of the anticancer drugs in healthy cells and therefore further increase the chemotherapy-associated side effects.

A second promising avenue to address MDR exploits concepts from nanomedicine to co-deliver chemotherapeutics and P-gp inhibitors. Co-administration of a chemotherapeutic and a P-gp inhibitor with a single nanoparticle carrier or in the form of a single polymer conjugate offers a number of opportunities. A first consequence of the co-delivery of the two active compounds with a single nanoparticle or a single polymer carrier is that the pharmacokinetics will be governed by that of the nanoparticle or polymer carrier. The use of nanoparticles or polymer carriers also allows to exploit active or passive (enhanced permeation and retention (EPR) effect) targeting strategies that can enhance delivery to cancer cells and reduce off-target delivery.[15] Also on the cellular level the use of nanoparticles or polymer conjugates to co-deliver P-gp inhibitors and chemotherapeutics offers advantages. Macromolecules and nanoparticles are usually internalized by cells *via* endocytosis.[16-18] This process involves the compartmentalization of nanoparticles and polymers in the endosomes and lysosomes, which generates a barrier that prevents rapid efflux and also allows to release the payload deeper inside the cell and in closer proximity of the respective target (and as a consequence more distant from the membrane-bound P-gp transporter).[19,20] A number of reports describe the use of polymer or nanoparticle-based delivery strategies to combat MDR.[12,14,19-22] Minko *et al.* investigated the effect of *N*-(2-hydroxypropyl) methacrylamide (PHPMA) copolymers that carried doxorubicin (Dox) attached *via* the lysosomally cleavable GFLG peptide linker on the viability of A2780 sensitive and A2780ADR multidrug resistant human ovarian cancer cells.[19] These experiments indicated that while the IC_{50} values from the free Dox was 38 times larger on the A2780ADR resistant cells as compared to the sensitive cells, the difference between these two IC_{50} values was only about 20% for the polymer-Dox conjugate. The smaller difference in IC_{50} value between the resistant and

sensitive cells that was observed for the polymer conjugate was attributed to the lysosomal release of Dox in close proximity of the target and distant from the P-gp efflux transporter.[19] Moreover, chronic exposure of the sensitive cells to the polymer conjugate did not induce acquired MDR effect.[20] More recently, Subr *et al.* investigated the cytotoxicity of a series of PHPMA conjugates that were modified with a peptide-based P-gp inhibitor and Dox *via* a pH-sensitive hydrazone linker.[22] Whereas the hydrazone linked Dox-PHPMA conjugate did not show any cytotoxicity towards MDR cells, copolymers that incorporated both the P-gp inhibitor and Dox as well as co-administration of Dox- and P-gp inhibitor-conjugates proved effective towards MDR cells.

The findings summarized above indicate that spatiotemporal release of Dox is important to evade efflux in MDR cells. This is illustrated by the fact that lysosomal release of Dox led to a reduction of its efflux,[19] whereas the use of the pH sensitive hydrazone linker, which releases Dox earlier in the endocytic pathway in the endosomes, did have no effect in reducing P-gp mediated resistance.[22] On the other hand, the results obtained with the hydrazone linked Dox-PHPMA copolymer also indicate that the pH induced release in the early endosomes provides a relatively rapid pathway to the P-gp membrane transporter.[22] This study attempts to capitalize on these findings and reports (dual functional) PHPMA conjugates that allow spatially controlled release of the anticancer drug Dox and the third generation P-gp inhibitor zosuquidar (Zos).[3,23] The PHPMA conjugates presented here are not only able to simultaneously transport Zos and Dox into the cancer cells, but also exploit differences in the physicochemical environment in the endosomal and lysosomal compartments to release Zos and Dox by cleavage of two orthogonal linkers. Zos was attached *via* a pH sensitive hydrazone linker designed for cleavage in the endosomes,[24,25] whereas Dox was conjugated *via* the lysosomally degradable GFLG peptide linker.[19] The first part of this work investigates the feasibility of using PHPMA conjugates bearing a pendant Zos derivative *via* a hydrazone linker to overcome Dox efflux in resistant ovarian cancer cells. The second part describes a dual delivery system in which both drugs are conjugated to the PHPMA backbone *via* orthogonal cleavable linkers.

3.2. Experimental Section

3.2.1. Materials

4-Acetylbenzoic acid, 2,2′-azobis(2-methylpropionitrile) (AIBN), 4,4′-azobis(4-cyanovaleric acid), 1-amino-2-propanol (HPA), 4-cyano-4-(phenylcarbonothioylthio)pentanoic acid (CTA), cysteamine hydrochloride, *N*-(3-dimethylaminopropyl)-*N*′-ethylcarbodiimide hydrochloride (EDC HCl), *N,N*′-dicyclohexylcarbodiimide (DCC), 2,2′-dipyridyl disulphide, 4-(dimethylamino)pyridine (DMAP), isobutyl chloroformate, 2,6-lutidine, 3-(4,5-dimethylthiazol-2-yl)-2,5-diphenyltetrazolium bromide) (MTT), 6-maleimidocaproic acid, methacryloyl chloride, *N*-methylmorpholine, tert-butyl carbazate and tris(2-carboxyethyl)phosphine hydrochloride (TCEP) were obtained from Sigma Aldrich. TECP was neutralized prior use by treatment with 0.1 N NaOH (until pH 6.5 was achieved) and sebsequently lyophilized. The neutralized TCEP was then dissolved in dry methanol, filtered and dried under vacuum. Pentafluorophenol was purchased from MatrixScientific, 3,3,3-Trifluoropropylamine hydrochloride was obtained from Apollo Scientific and 3,3'-diethyloxacarbocyanine iodide (DiOC$_2$(3)) from Life Technologies. Fmoc-protected amino acids and Fmoc-Gly-Wang resin (100-200 mesh, loading 0.60 mmol/g) were obtained from Novabiochem. Ethyl(hydroxyimino)cyanoacetate (OxymaPure) and 2-(6-chloro-1*H*-benzotriazole-1-yl)-1,1,3,3-tetramethylaminium hexafluorophosphate (HBTU) were purchased from IRIS Biotech. Doxorubicin hydrochloride (Dox) was purchased from ShangHai Biochempartner and zosuquidar trihydrochloride (Zos) was obtained from NCE Biomedical. Diisopropylethylamine (DIPEA), triisopropylsilane (TIS), piperidine, dimethylformamide (DMF), dimethyl sulfoxide (DMSO), *N*-methylpyrrolidone (NMP) and trifluoroacetic acid (TFA) were obtained from VWR. Dichloromethane (DCM), tetrahydrofuran (THF) and diethylether were purchased from Reactolab and methanol (MeOH) from Merck. MeOH, DMF and THF were dried using a Pure Solv solvent purification system prior use. Triethylamine (Et$_3$N) and 1,4-dioxane were purchased from Acros Organics. 1,4-Dioxane was dried under molecular sieves and Et$_3$N was freshly distilled prior use. Pentafluorophenyl methacrylate (PFMA) was synthesized as reported by Eberhardt *et al*.[26] The synthesis of the fluorinated CTA (F-CTA), 2-(pyridyldithio)-ethylamine (PDA) and 6-maleimidocaproic acid hydrazide trifluoroacetic salt are described in the Supporting Information.

3.2.2. Methods

^{1}H-, ^{19}F- and ^{13}C-NMR spectra were recorded on a Bruker AV-400 instrument at room temperature. ^{1}H-NMR spectra of polymer conjugates were performed with a relaxation time (d_1) of 10 seconds and at least 256 scans using CD$_3$OD, CDCl$_3$ or D$_2$O as solvent. Chemical shifts are reported relative to the residual proton signal of the solvent. Size exclusion chromatography (SEC) of PPFMA was performed using an Agilent 1260 infinity system equipped with a refractive index Varian 390-LC detector, two PLgel 5 µm Mixed C (Agilent) columns and a PLgel guard column. THF was used as eluent with a flow rate of 1 mL/min and the temperature was 40 °C. Samples were analysed using conventional calibration with polystyrene (PS) standards ranging from 4910 Da to 549 KDa. PHPMA conjugates were analysed with a Waters Alliance GPCV 2000 system. The eluent was DMF containing 0.01 wt % LiCl at a flow rate of 0.6 mL/min at 60 °C. The system was equipped with a refractive index detector and samples were analysed using conventional calibration with poly(methyl methacrylate) (PMMA) standards ranging from 3670 Da to 520 KDa. The mol % of Dox and 2-(pyridyldithio)-ethylamine (PDA*)* incorporated in the conjugates as well as the pH dependent release of Zos-Ket from the conjugates were determined by UV-Vis measurements using a Varian Cary 100 Bio spectrometer using quartz cuvettes. Flow cytometry analysis was performed using a BD Accuri C6 cytometer (BD Biosciences) equipped with a blue (488 nm) and red (640 nm) laser and the data were analysed using FlowJo software.

3.2.3. Procedures

Synthesis of Zos-Ket (Scheme S4). 300 mg Zos (0.47 mmol) were dissolved in 8 mL chloroform and stirred with 3.3 equiv. (218 µL) triethylamine (Et$_3$N) for 15 minutes. The organic phase was washed twice with water, dried over MgSO$_4$, filtered and finally dried under vacuum to yield zosuquidar free base. Next, 120 mg 4-acetylbenzoic acid (0.73 mmol), 1.1 equiv. (206.3 mg) DCC and 0.2 equiv. (18 mg) DMAP were dissolved in 7 mL dry DCM. 215 mg zosuquidar free base (0.41 mmol) were dissolved in 4 mL dry DCM and subsequently added to the active ester solution. The reaction was stirred under nitrogen at room temperature for 18 h. Following the reaction, the formed *N,N'-*dicyclohexylurea was removed by filtration and the crude product was purified by flash

chromatography using ethyl acetate/hexane (6.5:3.5) to give the pure Zos-Ket (79 % yield). ^{1}H-NMR, ^{19}F-NMR and mass spectra are included in **Figure S7-S9**.

Synthesis of Zos-Mal (Scheme S5). Zos-Mal was prepared according to a literature procedure with some small modifications.[25] Briefly, 27 mg Zos-Ket (0.04 mmol) and 3 equiv. (41 mg) 6-maleimidocaproic acid hydrazide trifluoroacetic acid salt were dissolved in 2 mL dry methanol and stirred at room temperature for 1.5 h. The solvent was removed under reduced pressure and the residue was purified by preparative TLC using chloroform/methanol (10:0.3) as eluent to yield Zos-Mal (60 % yield). ^{1}H-NMR, ^{19}F-NMR and mass spectra are included in **Figure S10-S12**.

Synthesis of Fmoc-GFLG-OH. Fmoc-GFLG-OH was synthesized on a CEM Liberty automated microwave synthesizer using Fmoc-Gly-Wang resin (0.5 mmol scale) and Fmoc chemistry without final Fmoc-deprotection.[27] The peptide was purified by reversed phase high performance liquid chromatography (RP-HPLC) using a preparative HPLC Schimadzu LC-20A Prominence system equipped with a Vydac 218TP column (22 x 150 mm) that was operated at a flow rate of 20 mL/min. Peptide purification was achieved using two mobile phases. Mobile phase A consisted of a 0.05 % (v/v) solution of TFA in MilliQ water and mobile phase B consisted of a 0.05 % (v/v) solution of TFA in acetonitrile. The peptide was purified using a linear AB gradient from 35 % (v/v) to 55 % (v/v) of B over a period of 45 min and subsequently characterized *via* RP-HPLC-MS using a Vydac 218TP column (4.6x150 mm). The ^{1}H-NMR HPLC chromatogram and ESI mass spectra of the peptide are shown in **Figure S13**.

Synthesis of NH$_2$-GFLG-Dox (Scheme S6). The 200 mg Fmoc-GFLG-OH (0.32 mmol) and 1.2 equiv. Dox (226.3 mg) were dissolved in 8 mL dry DMF. Next, 2 equiv. (136 µL) DIPEA were added and the solution was stirred under nitrogen in the dark for 15 minutes. Then, 1.1 equiv. (162.7 mg) HBTU was dissolved in 1 mL dry DMF and subsequently added to the solution. The reaction mixture was stirred under nitrogen in the dark for three hours. Following the reaction, DCM was added to the solution and the organic phase was washed with 10 % acetic acid in water, passed over MgSO$_4$, filtered and dried under vacuum to yield 320 mg Fmoc-GFLG-Dox that was used without further purification. Fmoc-deprotection was performed as follows: 100 mg Fmoc-GFLG-Dox

(0.086 mmol) were dissolved in 400 μL of 10 % piperidine in DMF and the reaction was stirred for 5 minutes at 0 °C. 0.5 mL of 0.5 M formic acid solution in DMF was added dropwise until the reaction colour turned from blue to red. Next, the product was immediately precipitated in ice-cold diethyl ether. The recovered product was resuspended in fresh diethyl ether, centrifuged 2 times and finally purified by RP-HPLC using a linear AB gradient from 30 % (v/v) to 45 % (v/v) of B over a period of 30 min (yield 86 %). The purity, higher than 99 %, was determined by RP-HPLC-MS. The HPLC chromatogram and ESI mass spectra of NH_2-GFLG-Dox are shown in **Figure S14**.The ^{1}H-NMR spectrum is reported in **Figure S15**.

Synthesis of PPFMA-1 and PPFMA-2. Two different PPFMA precursors, PPFMA-1 and PPFMA-2, were used for the synthesis of the PHPMA conjugates. The synthesis of these polymers is outlined in **Scheme S7** and described in detail in the Supporting Information. **Figure S16** shows a ^{19}F-NMR spectrum of PPFMA-2. Detailed characteristics of PPFMA-1 and PPFMA-2 are summarized in **Table S1**.

Synthesis of PHPMA-PDA-1 and PHPMA-PDA-2. PHPMA-PDA-1 was obtained *via* post-polymerization modification of PPFMA-1, whereas PHPMA-PDA-2 was prepared from PPFMA-2. For the synthesis of PHPMA-PDA-1, 800 mg PPFMA-1 (3.2 mmol of PFMA reactive units) were dissolved in 10 mL dry DMF and 0.3 equiv. PDA (202.2 mg), 1.7 equiv. (417 μL) 1-amino-2-propanol (HPA) and 2 equiv. (886 μL) Et_3N were added. For PHPMA-PDA-2, 800 mg PPFMA-2 were dissolved in 10 mL dry DMF and 0.4 equiv. PDA (282.9 mg), 1.6 equiv. (392 μL) 1-amino-2-propanol (HPA) and 2 equiv. (886 μL) Et_3N were added. The solutions were stirred under nitrogen at 50 °C for 20 hours. The products were isolated by three precipitations in ice-cold diethyl ether and subsequently dialyzed against water/methanol for 2 days using a SpectraPor (MWCO 3.5 KDa) membrane and finally lyophilized. The mol % of PDA moieties incorporated in PHPMA-PDA-1and PHPMA-PDA-2 were determined by UV-Vis and ^{1}H-NMR spectroscopy and are summarized in **Table S2**. Details on the UV-Vis protocol are provided in the Supporting Information together with the UV-Vis and ^{1}H-NMR spectra (**Figure S17-S20)**.

Synthesis of PHPMA-Dox-PDA. The polymer intermediate containing PDA and Dox was prepared *via* post-polymerization modification of PPFMA-2. To this purpose, 60 mg PPFMA-2 (0.24 mmol of PFMA units) were dissolved in 3 mL dry DMF together with 0.15 equiv. (32.8 mg) NH_2-GFLG-Dox and 0.2 equiv. (7 µL) Et_3N. The solution was stirred under nitrogen at 40 °C for 24 hours in the dark. After 24 hours, 1 mL DMF solution containing 0.1 equiv. (5.3 mg) PDA, 1.9 equiv. (35 µL) HPA and 2 equiv. (66 µL) Et_3N was added and the reaction was stirred for an additional 20 hours at 40 °C. The product was precipitated three times in ice-cold diethyl ether, dialyzed against water/methanol for 2 days using a SpectraPor (MWCO 3.5 KDa) membrane and finally lyophilized. The mol % of PDA and Dox moieties incorporated in the conjugates were determined by UV-Vis and NMR spectroscopy and are indicated in **Table S2**. The UV-Vis procedure is provided in the Supporting Information together with the corresponding UV-Vis spectra (**Figure S18**).The ^{1}H-NMR spectra of the PHPMA-Dox-PDA copolymer is included in **Figure S21**.

Synthesis of PHPMA-Dox conjugate. 100 mg of PPFMA-2 (0.4 mmol of PFMA units), 0.2 equiv. (72 mg) NH_2-GFLG-Dox and 0.2 equiv. (11 µL) Et_3N were dissolved in 4 mL dry DMF and stirred in the dark at 50 °C for 20 hours under nitrogen. After 24 h, 1 mL DMF solution containing 2 equiv. (60 µL) HPA and 2 equiv. (110 µL) Et_3N was added and the reaction was stirred at 50 °C for an additional 20 hours. Following three precipitations from ice-cold diethyl ether the product was dialyzed against water/methanol for 2 days using a SpectraPor (MWCO 3500 g/mol) membrane and finally lyophilized. The Dox content in the polymer conjugate was determined by UV-Vis and ^{1}H-NMR spectroscopy. The corresponding ^{1}H-NMR and UV-Vis spectra are included in **Figure S18** and **Figure S22** and the Dox content is listed in **Table S2**.

Synthesis of PHPMA-Zos-1 and -2 and PHPMA-Dox-Zos conjugates. PHPMA-Zos-1 and -2 and PHPMA-Dox-Zos conjugates were prepared by reacting the corresponding precursors (PHPMA-PDA-1, -2 and PHPMA-Dox-PDA) with an excess of Zos-Mal. A general procedure is as follows: 30 mg polymer intermediates were dissolved in 4 mL dry methanol together with 3 equiv. of freshly prepared Zos-Mal (with respect to the PDA). After that, 3 equiv. of neutralized TCEP were added dropwise and the solution stirred under nitrogen at room temperature overnight. The products were recovered by

three precipitations from ice-cold diethyl ether and dialyzed with a SpectraPor dialysis membrane (MWCO 3.5 KDa) against PBS for 5 h and against water/methanol overnight and finally lyophilized. The Zos contents of the polymer conjugates were determined by NMR spectroscopy and are listed in **Table S2**. ^{1}H-NMR spectra of PHPMA-Zos-1, PHPMA-Zos-2 and PHPMA-Dox-Zos as well as a ^{19}F-NMR spectra of PHPMA-Zos-2 and PHPMA-Dox-Zos are included in **Figure S23-S27**.

pH triggered release of Zos-Ket from the PHPMA-Zos-1 conjugate. Zos-Ket release from PHPMA-Zos-1 was determined with a dialysis experiment by incubating the polymer conjugate in 0.1 M phosphate citrate buffer at pH 7.4 and 5.5 at 37 °C. Briefly, 2.7 mg of polymer were dissolved in 200 µL of each buffer solution and placed in SpectraPor micro dialysis cassettes with a molecular weight cut-off of 3.5 KDa. The samples were dialyzed against 2 mL of the same buffer solution. 30 % ethanol was added to all the buffers in order to assure the complete dissolution of the cleaved Zos-Ket at the tested concentrations. Over a period of 40 hours at different time intervals, 300 µL aliquots were taken and replaced with an equivalent buffer amount. The aliquots taken from the dialysis cassettes were diluted to 600 µL and the Zos-Ket content determined by UV-Vis spectroscopy by measuring the absorbance at $\lambda = 240$ nm using cuvettes with a optical path of 0.1 cm. The Zos-Ket concentration was calculated using the molar extinction coefficients $\varepsilon = 26768$ M^{-1} cm^{-1} and $\varepsilon = 25313$ M^{-1} cm^{-1} ($\lambda = 240$ nm) in the buffer solutions at pH 7.4 and 5.5, respectively. The corresponding calibration curves are shown in **Figure S28**.

Cell lines and cell cultures. The human ovarian carcinoma sensitive A2780 and resistant A2780ADR cell lines were kindly provided by Prof. S. O. Kelley, University of Toronto. Cells were cultured in RPMI 1640 glutamax (Lifetech) medium supplemented with 10 % fetal bovine serum (FBS) (Gibco) and 1% penicillin/streptomycin (Lifetech). A2780ADR cells were grown in media containing 200 nM doxorubicin in order to maintain the MDR-phenotype, 24 h before each experiment the medium was exchanged with fresh doxorubicin-free culture medium. Both cell lines were maintained in a humidified atmosphere containing 5 % (v/v) CO_2 at 37 °C.

Cytotoxicity assay. Cytotoxicities were assessed using the MTT assay. To this end, 100 μL cell suspension, corresponding to 5000 A2780ADR and 2500 A2780 cells, were added to a 96-well flat bottom plate and subsequently pre-incubated for 24 h in complete growing medium. Then, 100 μL of a solution containing the compounds to be evaluated was added and the plates were incubated for another 72 h. Subsequently, the medium was aspirated and 110 μL of MTT solution (0.5 mg/mL) in medium without phenol red was added to each well and the plates incubated for an additional 3 h. After that, the medium was removed and 100 μL DMSO was added to each well to dissolve the purple formazan crystals formed by the mitochondrial dehydrogenase activity of viable cells. Plates were incubated at 37 °C for 15 minutes and the optical density was quantified spectroscopically using a TECAN infinite 200 PRO plate reader. The optical density, directly proportional to the number of viable cells, was quantified at 570 nm using a reference filter at 690 nm. The absorbance of wells without cells was used as background and cell viabilities were calculated as a percentage relative to untreated cells. All the results are means from at least two independent experiments, each comprising triplicates per drug concentration. IC$_{50}$ values (concentration of drug necessary to inhibit 50 % of the cells growth) and standard errors were calculated using a sigmoidal dose-response curve fitting.

3,3'-Diethyloxacarbocyanine iodide (DiOC2(3)) efflux assay. Cells were trypsinized and resuspended in RPMI 1640 medium without antibiotics at a density of 1×10^6 cells/mL and transferred into different tubes. Cells were then incubated with varying concentrations of the appropriate P-gp inhibitor (Zos, Zos-Ket) or Zos-polymer conjugate (PHPMA-Zos-1, PHPMA-Zos-2) as well as with 20 μM of the positive control cyclosporine A (CsA) for 3 h at 37 °C. After 20 minutes exposure to 1 μg/mL DiOC$_2$(3) solution in ice, cells were washed and incubated at 37 °C with and without the tested compounds for an additional 90 minutes. Cells were washed twice with fresh medium, suspended in 500 μL of ice-cold medium and analysed by flow cytometry using the FL 1 channel for DiOC$_2$(3) detection. Each experiment was repeated at least twice and results are reported as relative fluorescence which represents the ratio between the geometric mean fluorescence of each sample and the positive control CsA.

Doxorubicin efflux assay. Cells were trypsinized and resuspended in RPMI 1640 medium without antibiotics at a density of 1×10^6 cells/mL and transferred into different tubes. Cells were then incubated with RPMI 1640 medium without antibiotics containing 10 μM of free doxorubicin or doxorubicin-polymer conjugate either alone or in combination with 20 μM of CsA for 4 h at 37 °C. Cells were washed twice with fresh medium, suspended in 500 μL of ice-cold medium and analysed by flow cytometry (Dox was detected in the FL 2 channel). Each experiment was repeated at least twice and results are reported as relative fluorescence that represents the ratio between the geometric mean fluorescence of each sample and the samples containing the same tested compounds and CsA.

3.3.   Results and Discussion

3.3.1.   PHPMA conjugate design and synthesis

The structure and synthesis of the PHPMA conjugates investigated in this study are shown in **Scheme 1**. In addition to the dual function PHPMA conjugate that was designed to co-deliver Dox and Zos (PHPMA-Dox-Zos) also monofunctional conjugates, which present either Zos (PHPMA-Zos-1 and -2) or Dox (PHPMA-Dox) were prepared. Zos was attached *via* a pH-sensitive hydrazone linker in order to allow release in the early stage of the endocytic process and maximize the cytosolic concentration of Zos in proximity of the P-gp transporter. Dox, in contrast, was conjugated to the PHPMA backbone *via* the lysosomally cleavable GFLG peptide linker.[19,28] This was done to enhance release of Dox in close proximity of the nucleus, which was previously demonstrated to mitigate the effect of P-gp-mediated Dox efflux.[19]
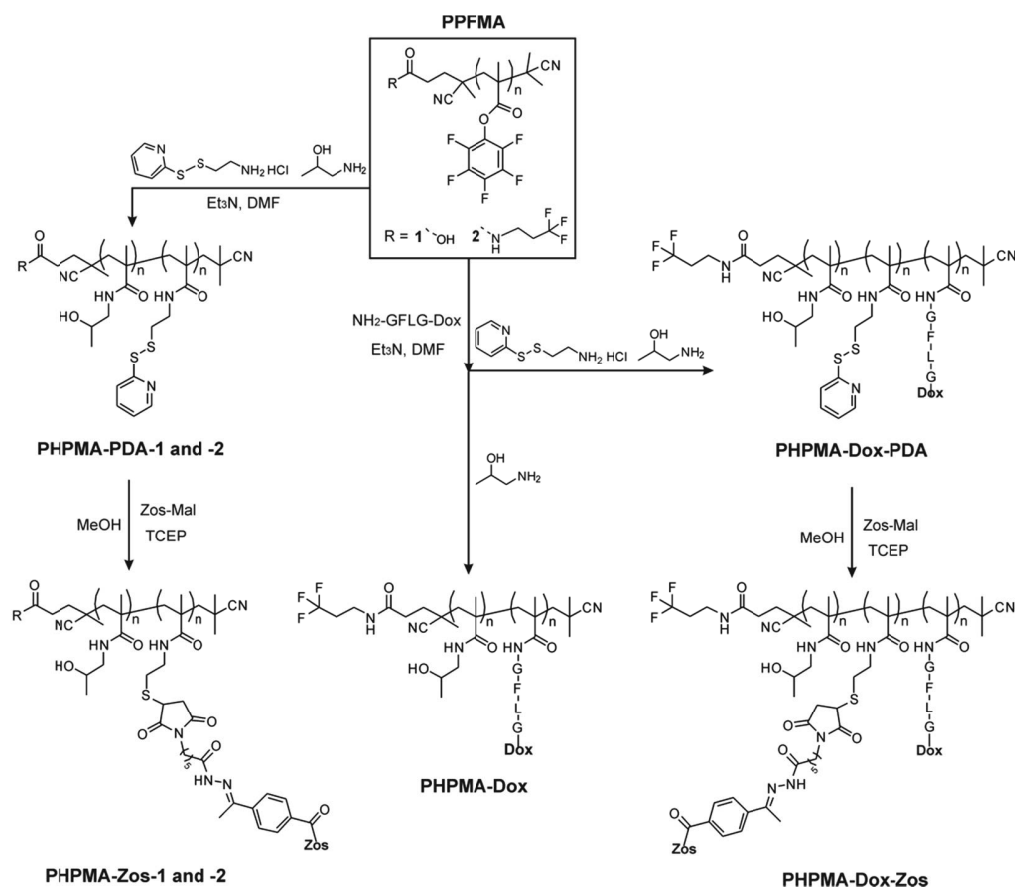
Scheme 1. Synthesis of the PHPMA-drug conjugates investigated in this study.

The Zos- and Dox-modified PHPMA copolymers were prepared *via* a two-step post-polymerization modification strategy, starting from a side-chain reactive poly(pentafluorophenyl methacrylate) PPFMA precursor. Two different PPFMA polymers were chosen as the active-ester precursors and prepared by reversible addition-fragmentation chain transfer (RAFT) polymerization. PPFMA-1 was synthesized as previously reported by Gibson *et al.*,[29] whereas the PPFMA-2 was prepared using a fluorinated RAFT agent. The fluorinated label on the polymer backbone allowed the determination of the number average molecular weight (M_n) as well as the estimation of the Zos content of PPFMA-2 by ^{19}F-NMR analysis. Both PPFMA precursors were characterized by NMR spectroscopy and SEC and the detailed characterization is provided in **Table S1**. PPFMA-1 and PPFMA-2 had number average molecular weights (M_n) of 17210 and 27630 g/mol, respectively, as revealed by SEC. ^{19}F-NMR analysis of

PPFMA-2 revealed a M_n of 28220 g/mol, which is in good agreement with the SEC results. Dox was directly coupled to the PPFMA precursor by reacting part of the active ester moieties with NH$_2$-GFLG-modified Dox derivative shown in **Chart 1**. The Dox content of PHPMA-Dox was determined by ^{1}H-NMR and UV-Vis analysis to be 2.5 mol%. To conjugate Zos, part of the PPFMA repeating units were first modified with 2-(pyridyldithio)-ethylamine (PDA) and 1-amino-2-propanol, followed by treatment with neutralized TCEP to generate side chain thiol functional groups and finally Michael addition of a maleimide-modified Zos derivative (Zos-Mal, **Chart 1**). By varying the amount of PDA used in the first post-polymerization step of PPFMA-1 and PPFMA-2, two different PHPMA-Zos conjugates were prepared, which contain 2.2 (PHPMA-Zos-1) and 4.3 (PHPMA-Zos-2) mol % Zos, respectively. The dual functional PHPMA-Dox-Zos conjugate was obtained by first reacting PPFMA-2 with PDA and NH$_2$-GFLG-Dox, followed by coupling of Zos-Mal and contains 2.9 and 0.2 mol % Dox and Zos, respectively (according to ^{1}H-NMR spectroscopy). The characteristics of the different conjugates are summarized in **Table 1** and **Table S2**
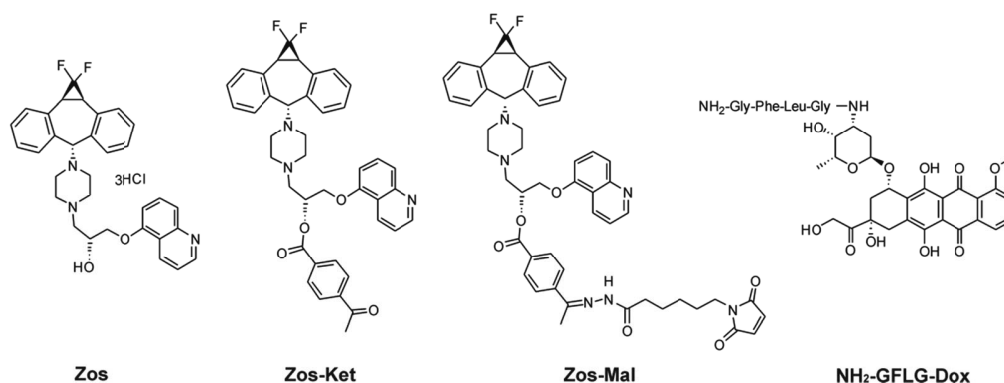
Chart 1. Chemical structures of Zos, Zos-Ket, Zos-Mal and NH$_2$-GFLG-Dox.

Table 1. Composition of the PHPMA conjugates investigated in this study.

Conjugates	Zos content (mol %)		Dox content (mol %)	
	¹H-NMR[a]	¹⁹F-NMR[b]	¹H-NMR[c]	UV[d]
PHPMA-Zos-1	2.2	-	-	-
PHPMA-Zos-2	4.3	4.6	-	-
PHPMA-Dox	-	-	2.4	2.5
PHPMA-Dox-Zos	0.2	0.4	2.9	2.9

[a] Determined comparing the integrals of Zos signals with those of the polymer backbone and with the CH proton of the hydroxypropyl polymer side chains.

[b] Determined comparing the integrals of fluorine signals of Zos with those of the polymer end group and taking into account the degree of polymerization (DP).

[c] Determined comparing the integrals of the Dox signals with those of the polymer backbone and with the CH proton of the hydroxypropyl polymer side chains.

[d] Calculated from the absorbance peak at $\lambda = 490$ nm in DMSO ($\varepsilon = 12049.6$ cm^{-1} M^{-1}).

3.3.2. pH Triggered release of Zos-Ket from the PHPMA-Zos-1 conjugate

To verify that the incorporation of the hydrazone linker can facilitate pH triggered release of Zos, the PHPMA-Zos-1 was placed in microdialysis cassettes both at pH 5.5 and 7.4 (physiological pH) and Zos release was measured spectrophotometrically. The results of these experiments are shown in **Figure 1** and confirm that the release of Zos at pH 5.5 is significantly enhanced as compared to pH 7.4. It is important to note here that pH-induced cleavage of the hydrazone linker does not result in release of Zos but rather of Zos-Ket. At pH 5.5 release of Zos-Ket was found to level off at around 80 %. The incomplete hydrolysis of hydrazone-based polymer conjugates in model experiments has been previously reported.[30] This behaviour was attributed to the reversible nature of the hydrazone bond and to the closed system used to investigate the release profile, which can results in the establishment of an equilibrium reaction between free drug and polymer-bound drug.
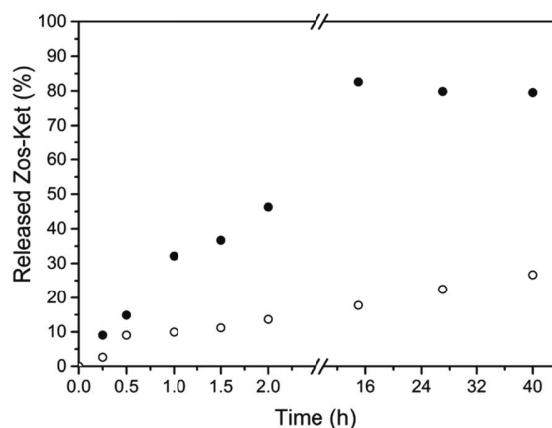
Figure 1. Cumulative release of Zos-Ket from PHPMA-Zos-1 in phosphate citrate buffer at pH 7.4 (○) and 5.5 (●) at 37 °C as a function of time over 40 hours.

3.3.3. Cytotoxicity and P-gp inhibitory activity of Zos and Zos-Ket

To identify the concentration window that can be used for Zos and Zos-Ket combination therapy with Dox as well as to assess possible effects of the 4-acetylbenzoic acid modification on the P-gp inhibitory activity of Zos, the intrinsic cytotoxicity of Zos and Zos-Ket was first determined *via* the MTT assay using multidrug resistant A2780ADR and sensitive A2780 cells. **Figure 2A** presents the viability of both the sensitive A2780 cells as well as the multidrug resistant A2780ADR cells toward Zos and Zos-Ket at concentrations ranging from 10^{-3}-10 μM, The results in **Figure 2A** shows that, while the viability of resistant cells was not significantly affected over the range of concentrations tested, the viability of the sensitive cells significantly decreased at 5 μM for both Zos as well as Zos-Ket. This result is in agreement with the previously reported IC_{50} value of Zos in A2780 cells (11 μM).[23] The results in **Figure 2A** furthermore do not reveal any significant difference between Zos and Zos-Ket, indicating that chemical modification of the inhibitor has no influence on the cytotoxicity of this compound.
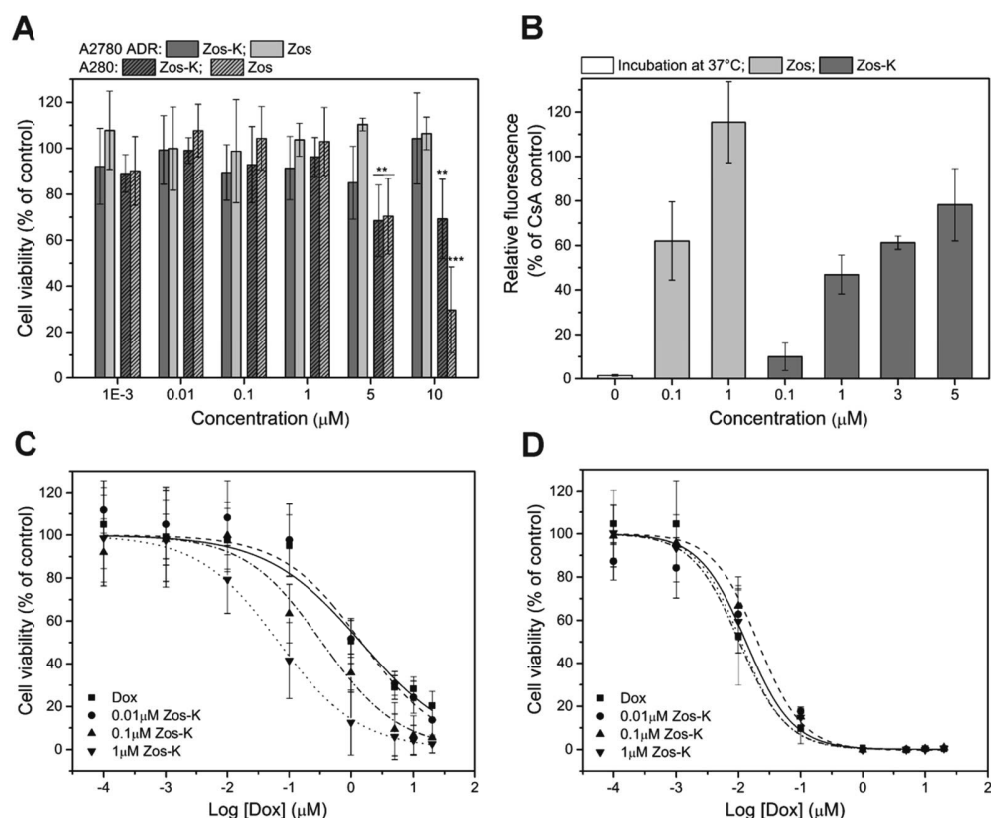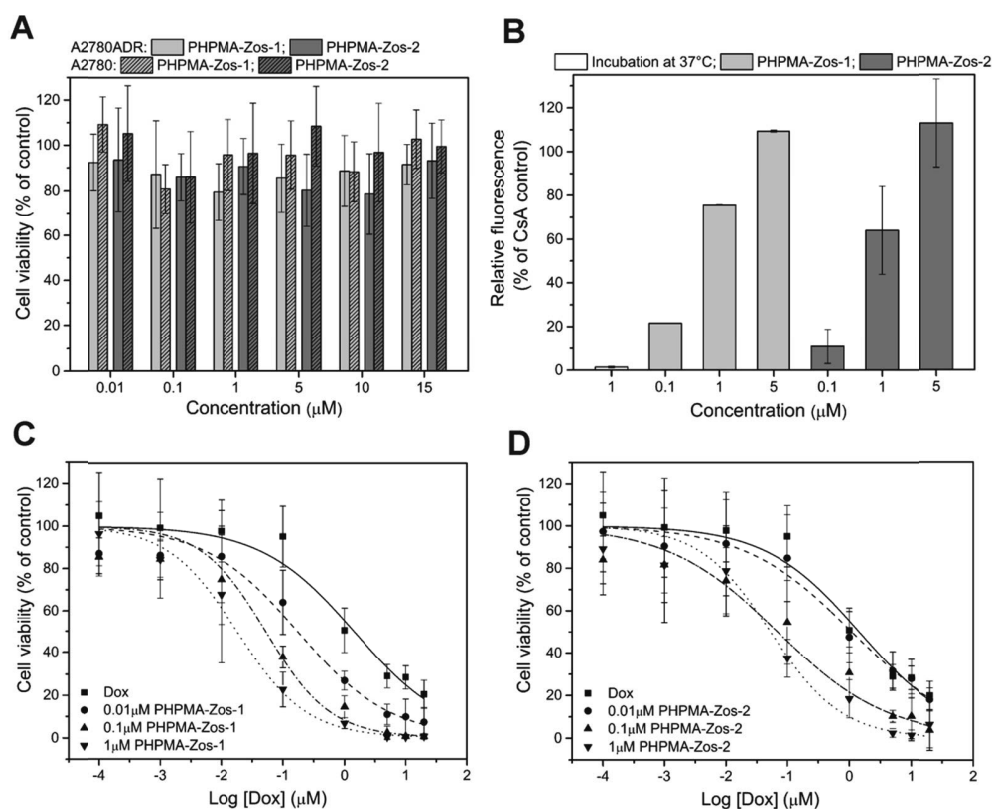
Figure 2. (A) Intrinsic cytotoxicity of Zos and Zos-Ket toward sensitive A2780 and resistant A2780ADR cells as determined by MTT assay after 72 h. Data are significantly different by Student's t test: *** ($P < 0.001$) and ** ($P < 0.01$). (B) Inhibition of $DiOC_2(3)$ efflux from A2780ADR cells. Cells were incubated with varying concentrations of Zos, Zos-Ket as well as with 20 µM cyclosporine A (CsA) at 37°C for 3 hours. After 20 minutes exposure to $DiOC_2(3)$, cells were washed and incubated at 37°C with and without the P-gp inhibitors for an additional 90 minutes and finally analyzed by flow cytometry. The relative fluorescence represents the ratio between the geometric mean fluorescence of each sample and the positive control CsA. (C) Dox cytotoxicity alone and in combination with increasing concentrations of Zos-Ket in A2780ADR and (D) A2780 cells. MTT results were read after 72 h incubation and are reported with respect to the percentage of untreated cells.

In order to investigate whether the modification of Zos with 4-acetylbenzoic acid did affect the activity of this compound, the P-gp inhibitory activity of Zos and Zos-Ket was evaluated and compared in two different experiments. First, the ability of Zos and Zos-Ket to inhibit P-gp-mediated efflux of the model fluorescent dye $DiOC_2(3)$ from resistant

A2780ADR cells was investigated by flow cytometry experiments. For these experiments, 20 µM cyclosporine A (CsA), which is known to completely inhibit P-gp, was used as a positive control.[31] Examples of flow cytometry experiments with Zos and Zos-Ket are presented in Supporting Information in **Figure S29**. **Figure 2B** presents the $DiOC_2(3)$ efflux inhibitory properties of Zos and Zos-Ket over a concentration range of 0.1-5 µM relative to that of CsA. The results show that while 1 µM Zos led to the complete inhibition of DiOC(3) efflux, 5 µM Zos-Ket were necessary to achieve 78 % dye retention. On the other hand, more than 98 % $DiOC_2(3)$ was effluxed in the absence of an inhibitor. This indicates that chemical modification of Zos with 4-acetylbenzoic acid partially decreases its activity, however, at low micromolar concentrations the modified drug still retained the ability to inhibit 78 % $DiOC_2(3)$ efflux.

In a next series of experiments, the ability of Zos and Zos-Ket to increase Dox cytotoxicity in resistant cells was examined by the MTT assay. Sensitive and resistant cells were treated with Dox concentrations ranging from 0.1 nm to 20 µM either alone or in combination with different concentrations of Zos and Zos-Ket. The results of these experiments are summarized in **Figure 2C and Figure 2D**. While resistant cells showed an expected high resistance to doxorubicin with an IC_{50} value of 1.441 µM, the IC_{50} of the sensitive cells was 0.013 µM. **Figure 2C** shows that co-administration of Dox and Zos-Ket to resistant cells resulted in a shift of the Dox cytotoxicity curve to lower concentrations in a Zos-Ket-dose dependent manner. Qualitatively similar results were obtained when resistant cells were treated with a combination of Dox and Zos (**Figure S30A**). **Table 2** compares the Dox cytotoxicity toward both cell types at various Zos and Zos-Ket concentrations. The results in **Table 2** indicate that at equal concentrations, Zos is more effective as compared to Zos-Ket in preventing efflux. For instance, when 1 µM Zos and Zos-Ket were co-administered with Dox, the IC_{50} values decreased to 0.048 and 0.068 µM, respectively, and approached the value observed for sensitive cells (0.013 µM). These IC_{50} values suggest that at a concentration of 1 µM both inhibitors can sensitize resistant ovarian cancer cells to doxorubicin, but also indicate that the modification led to a slight decrease in activity, especially at low concentrations as evident from the higher IC_{50} values for Zos-Ket as compared to Zos at equal concentration. These results are in agreement with the efflux inhibitory experiments summarized in **Figure 2B**, which also indicate that Zos-Ket at identical concentration is less active as compared to Zos. Finally, as expected, the Dox IC_{50} values measured on the

sensitive A2780 cells were not affected by co-administration of Zos or Zos-Ket (**Figure 2D** and **Figure S30B**).

Table 2. Cytotoxicity of doxorubicin alone and in combination with Zos, Zos-Ket and the PHPMA-Zos conjugates PHPMA-Zos-1 and PHPMA-Zos-2 in sensitive A2780 and resistant A2780ADR cells as determined by MTT assay.

Compound	[P-gp inhibitor] (μM)	Dox IC$_{50}$ (μM)	
		A2780	A2780ADR
Dox	**-**	**0.013 ± 0.003**	**1.441 ± 0.361**
Zos	0.01	0.022 ± 0.006	0.198 ± 0.078
	0.1	0.032 ± 0.002	0.051 ± 0.014
	1	0.017 ± 0.002	0.048 ± 0.006
Zos-Ket	0.01	0.020 ± 0.006	1.441 ± 0.361
	0.1	0.010 ± 0.004	0.341 ± 0.071
	1	0.011 ± 0.004	0.068 ± 0.006
PHPMA-Zos-1	0.01	0.008 ± 0.001	0.174 ± 0.010
	0.1	0.006 ± 0.004	0.053 ± 0.017
	1	0.007 ± 0.003	0.018 ± 0.007
PHPMA-Zos-2	0.01	0.012 ± 0.002	1.098 ± 0.194
	0.1	0.011 ± 0.007	0.069 ± 0.025
	1	0.013 ± 0.003	0.053 ± 0.015

3.3.4. Cytotoxicity and P-gp inhibitory activity of PHPMA-Zos conjugates

In a next series of experiments, the cytotoxicity and P-gp inhibitory activity of PHPMA-Zos conjugates PHPMA-Zos-1 and PHPMA-Zos-2, which contain 2.2 and 4.5 mol % Zos, respectively, were investigated. The results of the MTT assay experiments that were done to assess the cytotoxicity are summarized in **Figure 3A**. The data in this figure show that both polymers were nontoxic towards both cell lines within the concentration range investigated. In contrast, at a concentration of 10 μM both Zos and Zos-Ket resulted in a significant reduced viability of A2780 cells (**Figure 2A**).

Figure 3. (A) Intrinsic cytotoxicity of PHPMA-Zos-1 and PHPMA-Zos 2 toward sensitive A2780 and resistant A2780ADR cells as determined by MTT assay after 72 h. (B) Inhibition of $DiOC_2(3)$ efflux from A2780ADR cells. Cells were incubated with varying concentrations of PHPMA-Zos-1 and PHPMA-Zos 2 as well as with 20 μM cyclosporine A (CsA) at 37°C for 3 hours. After 20 minutes exposure to $DiOC_2(3)$, cells were washed and incubated at 37°C with and without the P-gp inhibitors for an additional 90 minutes and finally analyzed by flow cytometry. The relative fluorescence represents the ratio between the geometric mean fluorescence of each sample and the positive control CsA. (C) Dox cytotoxicity alone and in combination with increasing concentrations of PHPMA-Zos-1 and (D) PHPMA-Zos-2 in A2780ADR cells. MTT results were read after 72 h incubation and are reported with respect to the percentage of untreated cells. The concentrations of P-gp inhibitor are always expressed as polymer-bound drug.

The P-gp inhibitory activity of the polymer-Zos conjugates was assessed using both the $DiOC_2(3)$ efflux assay as well as in cytotoxicity studies with co-administration of Dox. P-gp mediated efflux of $DiOC_2(3)$ from resistant A2780ADR cells after three hours

incubation was investigated by flow cytometry. **Figure S29C** and **D** shows examples of flow cytometry results which were obtained with PHPMA-Zos-1 and PHPMA-Zos-2. From these flow cytometry experiments, the P-gp inhibitory activity of the polymer conjugates was related and expressed as a percentage relative to the CsA positive control. **Figure 3B**, which summarizes the results obtained from duplicate experiments, clearly shows that incubation of the cells with 5 µM of polymer-bound drug led to complete inhibition of $DiOC_2(3)$ efflux. In contrast, it was shown in the previous section that the same concentration of free Zos-Ket resulted only in 78 % dye retention. Moreover, **Figure 3B** also shows that the activity of PHPMA-Zos-2 is slightly lower than that of PHPMA-Zos-1 at 0.1 and 1 µM polymer-bound Zos-Ket. The enhanced P-gp inhibitory activity of PHPMA-Zos-1 as compared to free Zos-Ket at equal Zos-concentrations may be interpreted in terms of the enhanced internalization of the polymer-bound drug. In a next series of experiments A2780ADR cells were exposed to the polymer-Zos conjugates at three concentrations and Dox IC_{50} values were determined using the MTT assay. The results of these experiments are summarized in **Figure3C** and **D** and in **Table 2**. Similar to what has been observed for free Zos-Ket, the IC_{50} values of the resistant cells reached a minimum when 1 µM of polymer-bound Zos-Ket was co-administered with Dox. However, it is worth mentioning that at lower concentrations, the IC_{50} values of the polymer-bound Zos-Ket were significantly lower than those previously found for free Zos-Ket and were almost in the same range as those found for Zos. For instance, 0.1 µM of Zos-Ket delivered as PHPMA-Zos-1 and PHPMA-Zos-2 decreased the Dox IC_{50} to 0.053 and 0.069 µM, respectively, whereas these values were 0.051 µM for free Zos and 0.341 µM for Zos-Ket. Moreover, similar to what was observed when free drugs were used, the co-administration of both polymers and Dox did not show any effect on the sensitive A2780 cells (**Figure S30C** and **D**).

3.3.5. Efflux inhibition and cytotoxicity of PHPMA-Dox conjugates

In a final set of experiments, the efflux inhibition properties and cytotoxicity of the different polymer-bound Dox conjugates were evaluated. To this end, first the intrinsic cytotoxicity of PHPMA-Dox was determined and the accumulation of Dox in the A2780ADR cells when administered using the different polymer conjugates compared, before assessing the cytostatic activity of PHPMA-Dox-Zos conjugate. To determine the cytotoxicity of the PHPMA-Dox conjugate, cells were incubated with a range of

concentrations of PHPMA-Dox and their viability was determined by MTT assay. **Figure S31** illustrates the cytotoxicity curves **of PHPMA-Dox as well** as free Dox in both sensitive and resistant cells and the calculated IC_{50} values are listed in **Table S3**. While the IC_{50} of free Dox in resistant cells was 1.441 µM, the IC_{50} of the sensitive cells was 0.013 µM. The concentration of PHPMA-Dox necessary to lower the cell viability to values around 50 % was much higher for both cell lines (around 20 µM for sensitive and 100 µM for resistant cells). The IC_{50} values for free Dox indicate a resistance ratio of 111, whereas a value around 5 is estimated when doxorubicin is delivered as PHPMA-Dox. These results are in agreement with previously published data[19] and suggest that, while the IC_{50} values of the polymer conjugate are increased as compared to the free Dox, the resistance ratio is significantly decreased.

Second, Dox accumulation in A2780ADR cells when administered as free drug or delivered as PHPMA-Dox (2.4 mol % of Dox) or PHPMA-Dox-Zos (2.9 mol % of Dox and 0.2 mol % of Zos) conjugates was investigated by flow cytometry experiments. Cells were incubated with 10 µM Dox or polymer-bound Dox, either alone or in combination with 20 µM of the positive control CsA for 4 h. In the case of PHPMA-Dox-Zos, the calculated concentration of polymer-bound Zos-Ket is 0.7 µM. CsA was used to determine the maximum Dox accumulation in each experiment, allowing for the direct comparison of the results while neglecting eventual different cellular internalization rates of the tested compounds. Flow cytometry data from these experiments are shown in **Figure S32** and the Dox retention, expressed as a percentage relative to the Csa positive control cells, are presented in **Figure 4A**. The results in **Figure 4A** show that Dox retention was lowest when cells were treated with free Dox. At a Dox concentration of 10 µM treating A2780 ADR cells with PHPMA-Dox or PHPMA-Dox-Zos resulted in a 8 and 10 fold higher accumulation of Dox, respectively, as compared to the use of free Dox. These results confirm that (i) the administration of polymer-bound Dox decreases drug efflux from resistant cells and (ii) dual delivery of Dox and Zos using a single polymer conjugate even further reduces drug efflux by inhibiting the P-gp transporter.
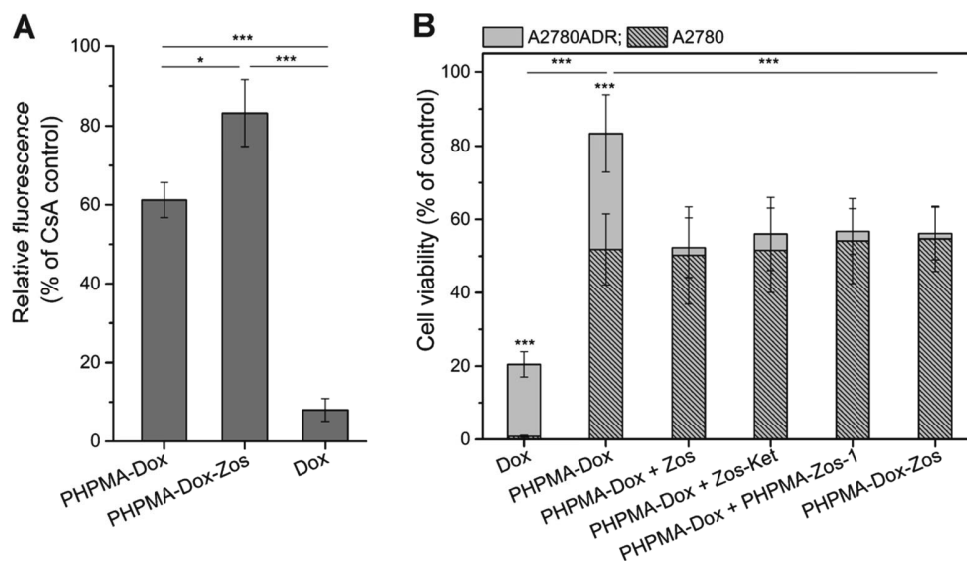
Figure 4. (A) Comparison between Dox efflux from A2780ADR cells when administered as free drug or delivered as PHPMA-Dox or PHPMA-Dox-Zos conjugate. Cells were incubated with 10 µM Dox and polymers-bound Dox either alone or in combination with 20 µM of CsA for 4 hours and subsequently washed with fresh medium twice and analyzed by flow cytometry. The relative fluorescence represents the ratio between the geometric mean fluorescence of each sample and the samples containing also the positive control CsA. (B) Sensitization of A2780ADR cells by using the PHPMA-Dox-Zos conjugate. Cells, either sensitive A2780 (slashed bars) or resistant A2780ADR (gray bars) were incubated with 20 µM of free Dox and PHPMA-bound Dox either alone or in combination with 2 µM of the P-gp inhibitors Zos, Zos-Ket and PHPMA-Zos-1 and with the PHPMA-Dox-Zos conjugate (20 µM of Dox and 1.4 µM of Zos). MTT results were read after 72 h incubation and are reported with respect to the percentage of untreated cells. In both assays data are significantly different by Student's t test: *** ($P < 0.001$) and * ($P < 0.05$).

While the experiments discussed above demonstrate that co-delivery of Dox and P-gp inhibition is an efficient strategy to reduce P-gp mediated efflux, it should be noted that the time course of these experiments may not be sufficient for all Dox and Zos to be released. Therefore, also the cytostatic activity of the PHPMA-Dox conjugate, both alone, as well as in combination with Zos, Zos-Ket and PHPMA-Zos-1 was determined and compared with that of the dual functional PHPMA-Dox-Zos conjugate using MTT assay with an incubation time of 72 h. Due to the fact that both drugs are attached to the same polymer carrier, it was not possible to determine the cytotoxicity curve and therefore the

120

IC$_{50}$ value for the PHPMA-Dox-Zos conjugate. Cell incubation with increasing amount of polymer-bound Dox, would also cause cell exposure to increasing concentrations of the polymer-bound P-gp inhibitor. Hence, for this particular experiment, the cell viability was determined at a selected Dox concentration. Based on the mol % of functionalization of the polymer carrier with the two drugs, the concentration of Zos was calculated. The selected Dox concentration in each experiment was 20 µM, which is close to the IC$_{50}$ of PHPMA-Dox in sensitive cells and do not significantly affect the viability of the resistant cells. Since the ratio between the concentration of Dox and the concentration of the inhibitor was 14.5 in the **PHPMA-Dox-Zos** conjugate, in all the experiments the concentration of polymer-bound inhibitor was 1.4 µM. **Figure 4B** illustrates that the treatment of sensitive cells with the PHPMA-Dox conjugate, either alone or in combination with 2 µM of the inhibitors (Zos, Zos-Ket and **PHPMA-Zos-1**), led to an approximate cell viability of 50 % (Experiments using PHPMA-Dox in combination with 1 µM inhibitors led to comparable results, data not shown). On the other hand, while the viability of the resistant cells in the presence of PHPMA-Dox was 83 %, the co-administration of the this conjugate with the inhibitors led to cell viabilities comparable to that of sensitive cells. Finally, treatment of the resistant cells with the dual functional PHPMA-Dox-Zos conjugate also resulted in a cell viability of ~50% similar to what was obtained for the co-administration of PHPMA-Dox with Zos, Zos-Ket or PHPMA-Zos-1. While *in vitro* co-administration of PHPMA-Dox with a polymer-bound P-gp inhibitor is equal effective in mitigating the effect of drug efflux on the viability of A2780ADR cells as using the dual functional PHPMA-Dox-Zos conjugate, the use of a combination polymer therapeutic offer a number of advantages *in vivo*. Most important, the use of a single polymer carrier allows to overcome challenges that are due to difference in the pharmacokinetics of the two low molar mass drugs, since the pharmacokinetic of the conjugate is dictated and can be controlled by engineering the polymer conjugate. Another benefit of the use of a dual functional conjugate such as PHPMA-Dox-Zos is that it allows to administer and intracellularly deliver the chemotherapeutic and the P-gp inhibitor at a precisely defined and controlled ratio.[32]

3.4.   Conclusions

This Chapter has described the design and *in vitro* activity studies of a dual-functional PHPMA conjugate that allows spatially controlled release of the anticancer drug Dox and the third generation P-gp inhibitor Zos by using two orthogonal cleavable linkers. The first part of this work investigated the feasibility of using PHPMA conjugates bearing a Zos derivative *via* a hydrazone linker as an effective polymeric system to overcome Dox efflux in resistant ovarian cancer cells. The P-gp inhibitor Zos was modified to Zos-Ket and subsequently attached to the PHPMA backbone *via* a hydrazone linker. *In vitro* activity studies using both resistant A2780ADR and sensitive A2780 ovarian carcinoma cells revealed that the modification of Zos did not significantly hinder its activity at the highest concentration of interest and resulted with any additional cytotoxicity. Two different PHPMA-Zos conjugates containing 2.2 (PHPMA-Zos-1) and 4.3 (PHPMA-Zos-2) mol % of Zos-Ket, respectively, were successfully prepared. First, both conjugates showed a reduced intrinsic cytotoxicity in sensitive cells compared to free inhibitors. Second, it was found that the polymer-mediated delivery of Zos-Ket enhanced its activity and therefore increased Dox cytotoxicity in resistant ovarian carcinoma cells. The second part of this work investigated the design of the dual delivery system in which both drugs were conjugated to the PHPMA backbone *via* orthogonal cleavable linkers. Two different conjugates containing either the anticancer drug Dox alone (PHPMA-Dox) or in combination with Zos (PHPMA-Dox-Zos) were prepared and their activity was compared with *in vitro* studies. The ability of the control PHPMA-Dox conjugate to partially overcome MDR effect in the resistant A2780ADR cells was confirmed. Finally, it was demonstrated that the presence of the two drugs attached to the polymer backbone *via* orthogonal cleavable linkers enhanced P-gp inhibition as compared to the PHPMA-Dox conjugate and led to a doxorubicin cytotoxicity comparable to that of the sensitive A2780 cells. This result is of great interest for *in vivo* applications, in which the use of a single polymer carrier for the delivery of drug combinations allow simultaneous intracellular accumulation of the two drugs in a predetermined therapeutic ratio.

3.5.   References

(1)   Eckford, P. D.; Sharom, F. J., *Chem. Rev.* **2009**, *109*, 2989.

(2)   Longley, D. B.; Johnston, P. G., *J. Pathol.* **2005**, *205*, 275.

(3)   Szakacs, G.; Paterson, J. K.; Ludwig, J. A.; Booth-Genthe, C.; Gottesman, M. M., *Nat. Rev. Drug. Discov.* **2006**, *5*, 219.

(4)   Fletcher, J. I.; Haber, M.; Henderson, M. J.; Norris, M. D., *Nat. Rev. Cancer* **2010**, *10*, 147.

(5)   Abolhoda, A.; Wilson, A. E.; Ross, H.; Danenberg, P. V.; Burt, M.; Scotto, K. W., *Clin. Cancer Res.* **1999**, *5*, 3352.

(6)   Trock, B. J.; Leonessa, F.; Clarke, R., *J. Natl. Cancer Inst.* **1997**, *89*, 917.

(7)   Arao, S.; Suwa, H.; Mandai, M.; Tashiro, H.; Miyazaki, K.; Okamura, H.; Nomura, H.; Hiai, H.; Fukumoto, M., *Cancer Res.* **1994**, *54*, 1355.

(8)   Pallis, M.; Russell, N., *Leukemia* **2004**, *18*, 1927.

(9)   Ambudkar, S. V.; Kimchi-Sarfaty, C.; Sauna, Z. E.; Gottesman, M. M., *Oncogene* **2003**, *22*, 7468.

(10)   Ozben, T., *FEBS Lett.* **2006**, *580*, 2903.

(11)   Callaghan, R.; Luk, F.; Bebawy, M., *Drug Metab. Dispos.* **2014**, *42*, 623.

(12)   Montesinos, R. N.; Beduneau, A.; Pellequer, Y.; Lamprecht, A., *J. Control. Release* **2012**, *161*, 50.

(13)   Ajaj, K. A.; Kratz, F., *Bioorg. Med. Chem. Lett.* **2009**, *19*, 995.

(14)   Parhi, P.; Mohanty, C.; Sahoo, S. K., *Drug. Discov. Today* **2012**, *17*, 1044.

(15)   Duncan, R., *Nat. Rev. Cancer* **2006**, *6*, 688.

(16)   Danhier, F.; Feron, O.; Preat, V., *J. Control. Release* **2010**, *148*, 135.

(17)   Gruenberg, J., *Nat. Rev. Mol. Cell. Biol.* **2001**, *2*, 721.

(18)   Davis, M. E.; Chen, Z. G.; Shin, D. M., *Nat. Rev. Drug. Discov.* **2008**, *7*, 771.

(19)   Minko, T.; Kopeckova, P.; Pozharov, V.; Kopecek, J., *J. Control. Release* **1998**, *54*, 223.

(20)   Minko, T.; Kopeckova, P.; Kopecek, J., *J. Control. Release* **1999**, *59*, 133.

(21)   Binichathlan, Z.; Hamdy, D. A.; Brocks, D. R.; Lavasanifar, A., *Eur. J. Pharm. Biopharm.* **2010**, *75*, 90.

(22)   Subr, V.; Sivak, L.; Koziolova, E.; Braunova, A.; Pechar, M.; Strohalm, J.; Kabesova, M.; Rihova, B.; Ulbrich, K.; Kovar, M., *Biomacromolecules* **2014**, *15*, 3030.

(23)   Dantzig, A. H.; Shepard, R. L.; Cao, J.; Law, K. L.; Ehlhardt, W. J.; Baughman, T. M.; Bumol, T. F.; Starling, J. J., *Cancer Res.* **1996**, *56*, 4171.

(24)   Tong, R.; Tang, L.; Ma, L.; Tu, C. L.; Baumgartner, R.; Cheng, J. J., *Chem. Soc. Rev.* **2014**, *43*, 6982.

(25)   Abu Ajaj, K.; Graeser, R.; Kratz, F., *Breast Cancer Res. Tr.* **2012**, *134*, 117.

(26)   Eberhardt, M.; Mruk, R.; Zentel, R.; Theato, P., *Eur. Polym. J.* **2005**, *41*, 1569.

(27)   Apostolovic, B.; Klok, H. A., *Biomacromolecules* **2008**, *9*, 3173.

(28)   Zhong, Y. J.; Shao, L. H.; Li, Y., *Int. J. Oncol.* **2013**, *42*, 373.

(29)   Gibson, M. I.; Frohlich, E.; Klok, H. A., *J. Polym. Sci., Part A: Polym. Chem.* **2009**, *47*, 4332.

(30)   Christie, R. J.; Anderson, D. J.; Grainger, D. W., *Bioconjug. Chem.* **2010**, *21*, 1779.

(31)   Ansbro, M. R.; Shukla, S.; Ambudkar, S. V.; Yuspa, S. H.; Li, L. W., *PloS one* **2013**, *8*.

(32)   Xu, X. Y.; Ho, W.; Zhang, X. Q.; Bertrand, N.; Farokhzad, O., *Trends Mol. Med.* **2015**, *21*, 223.

3.6. Supporting Information

Synthesis of fluorinated CTA (F-CTA)
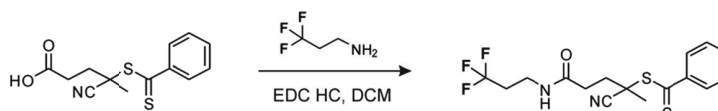
Scheme S1. Synthesis of F-CTA.

500.0 mg (1.79 mmol) 4-cyano-4-(phenylcarbonothioylthio)pentanoic acid and 411.6 mg (2.15 mmol) EDC HCl were dissolved in 8 mL dry DCM and the solution cooled down to 0 °C and stirred under nitrogen. In a second flask, 214.0 mg (1.43 mmol) 3,3,3-trifluoropropyl amine hydrochloride was dissolved in 8 mL dry DCM and 250 μL (1.43 mmol) triethylamine were added. After 10 minutes, the 3,3,3-trifluoropropyl amine solution was added dropwise to the first solution and the reaction was stirred at room temperature for 2 h. The solution was washed with 5 % NaHCO$_3$ and brine, dried over MgSO$_4$ and finally dried under vacuum. The crude product was purified by flash chromatography using ethyl acetate / hexane 4.5:5.5 to give the dark pink product (73 % yield). ^{1}H-NMR and ^{19}F-NMR spectra of the fluorinated CTA are included in **Figure S1** and **S2**.

Synthesis of 2-(pyridyldithio)-ethylamine (PDA)
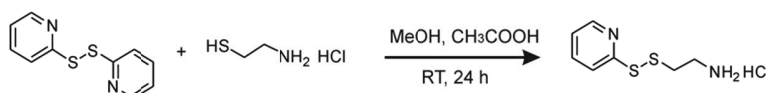
Scheme S2. Synthesis of 2-(pyridyldithio)-ethylamine (PDA).

2.20 mg (10 mmol) 2,2′-Dipyridyl disulphide were dissolved in 10 mL dry methanol and 400 μL acetic acid were added. Then, 5 mL of a methanol solution containing 568 mg (5 mmol) cysteamine hydrochloride were added dropwise over a period of 30 min.

After stirring the solution for 24 h, the solvent was removed by rotary evaporation and the product was isolated (75 % yield) by precipitation in diethyl ether followed by centrifugation (5 times). ^{1}H-NMR and ^{13}C-NMR spectra of PDA are included in **Figure S3** and **S4**.

Synthesis of 6-maleimidocaproic acid hydrazide trifluoroacetic acid salt
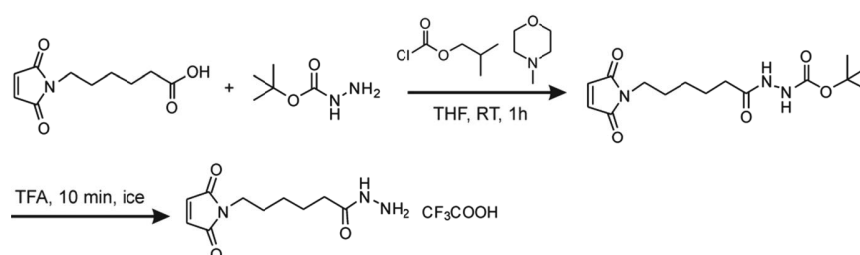
Scheme S3. Synthesis of 6-maleimidocaproic acid hydrazide trifluoroacetic acid salt.

6-Maleimidocaproic acid hydrazide trifluoroacetic acid salt was prepared as previously reported with few modifications.[27] Briefly, 400 mg (1.89 mmol) 6-maleimidocaproic acid were dissolved in 40 mL dry THF, the solution was cooled at 4 °C and 1 eq. (208 μL) of *N*-methylmorpholine was added. Next, 1 eq. (257 mg) isobutyl chloroformate in 4 mL THF was added and after 5 min an additional 4 mL of THF containing 1 eq. (250 mg) of tert-butyl carbazate were added dropwise. The reaction mixture was kept at 4 °C for 30 min and subsequently stirred at room temperature for 1 h. The solvent was evaporated and the residue dissolved in ethyl acetate and washed with water before being dried over MgSO$_4$, filtered and dried under vacuum. The crude product was purified by flash chromatography using a gradient of DCM/MeOH from 100:1 to 100:2 (0.1 % acetic acid was added to the eluent). Boc deprotection was performed by stirring the product in 4 mL ice-cold trifluoroacetic acid for 8 minutes. The acid was removed by evaporation and the product was precipitated in diethyl ether (yield 66 %). ^{1}H-NMR and ^{13}C-NMR spectra are included in **Figure S5** and **S6**.

Synthesis of Zos-Ket
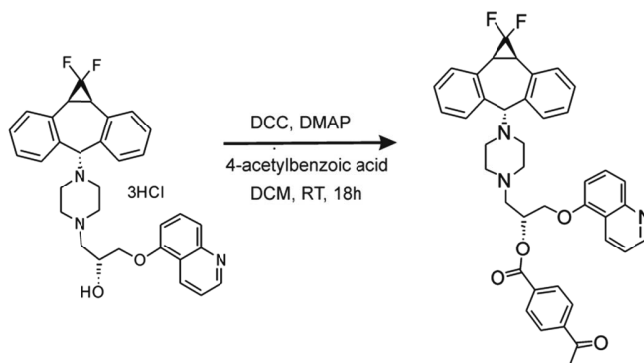
Scheme S4. Synthesis of Zos-Ket.

Synthesis of Zos-Mal
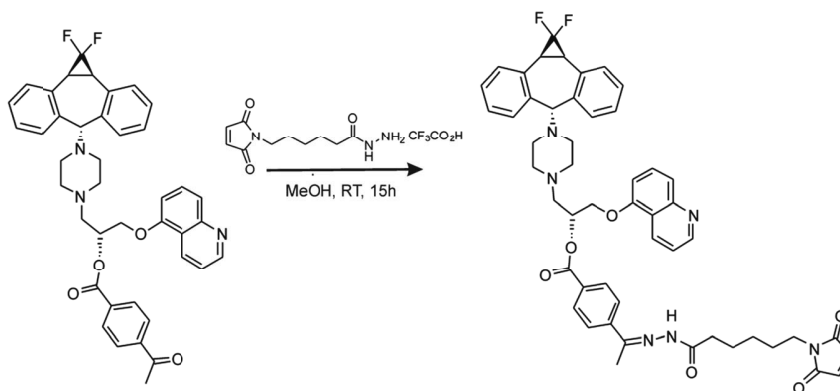
Scheme S5. Synthesis of Zos-Mal.

Synthesis of NH₂-GFLG-Dox
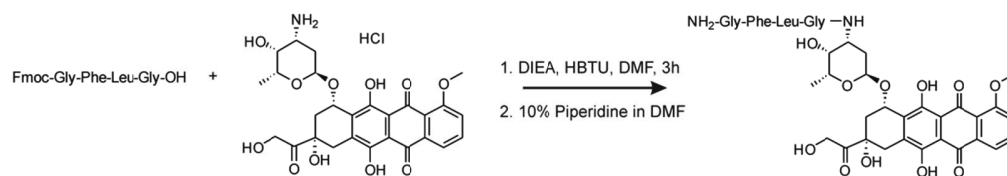
Scheme S6. Synthesis of NH2-GFLG-Dox.

Synthesis of PPFMA-1 and PPFMA-2
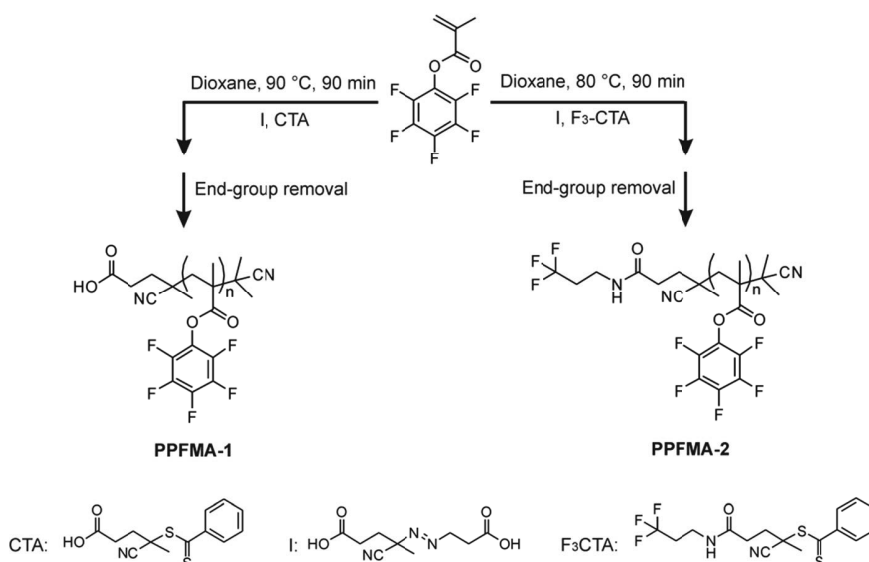
Scheme S7. Synthesis of poly(pentafluorophenyl methacrylate) precursors (PPFMA-1 and PPFMA-2). Chain transfer agent (CTA) = 4-cyano-4-(phenylcarbonothioylthio)pentanoic acid; initiator (I) = 4,4′-azobis(4-cyanovaleric acid).

PPFMA-1 was prepared as previously reported by Gibson *et al.*[23] The following conditions were used: polymerization time of 90 minutes, [PFMA]:[CTA] = 200, [CTA]:[I] = 2 and [PFMA] = 2.30 M.

PPFMA-2 was obtained using the fluorinated RAFT agent F-CTA and the following conditions were used: [PFMA]:[CTA] = 200, [CTA]:[I] = 5 and [PFMA] = 2.5 M. In a typical experiment 5 g of PFMA were added to a Schlenk tube together with 297 μL of a 0.33 M F-CTA stock solution and 277 μL of a 0.07 M initiator stock solution. 3.75 mL of dioxane were added and the solution was degassed by four freeze-pump thaw cycles. The tube was filled with argon and the reaction was stirred at 80 °C for 90 minutes. The solution was immediately cooled down in an ice bath and the polymer was isolated by precipitation in ice-cold hexane followed by centrifugation (3 times). For both polymers the end-group removal was performed using an excess of 2,2′-azobis(2-methylpropionitrile) (AIBN) as previously reported.[28] **Figure S16** shows a ^{19}F-NMR spectrum of PPFMA-2. Molecular weights and polydispersity of PPFMA-1 and PPFMA-2 are summarized in **Table S1**.

Determination of mol % of Dox and PDA in the PHPMA conjugates by UV-Vis spectroscopy
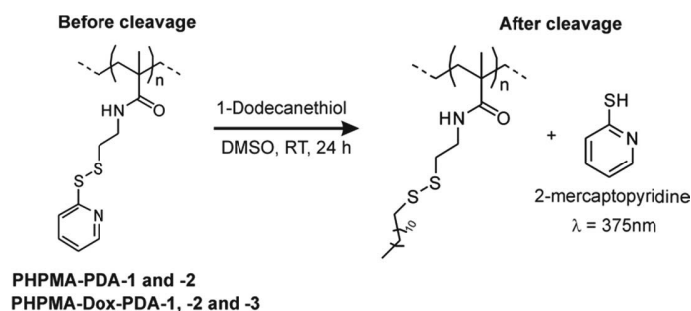
The extent of PDA incorporation in the PHPMA conjugates was determined as follows: the PHPMA intermediates PHPMA-PDA-1 and PHPMA-PDA-2 were dissolved in DMSO and stirred with 30 eq. of 1-dodecanethiol for 24 hours in order to assure complete cleavage of the linker. After 24 hours, the released 2-mercaptopyridine, which is directly proportional to the amount of PDA incorporated in the polymer was calculated form the UV absorption at $\lambda_{max} = 375$ nm. The polymer conjugate bearing both the PDA linker and Dox (PHPMA-Dox-PDA) was first analyzed by UV in order to quantify the Dox content and the Dox-related absorbance at 375 nm. In a second step, the polymer solution was treated with 1-dodecanethiol for 24 h and the PDA content was determined by UV measurements. The PDA content of the PHPMA-Dox-PDA conjugate was calculated by subtracting the Dox related absorbance at 375 nm. Dox and PDA concentrations were estimated using the calibration curves reported in **Figure S17**. The measurements were repeated at least twice and the results were averaged. On example of UV spectra per each polymer conjugate is reported in **Figure S18**.

Table S1. Molecular weights and polydispersity of PPFMA-1 and PPFMA-2 and corresponding PHPMA derivatives.

Precursor polymer	^{1}H-NMR[a] M_n^{TH} (g/mol)	^{19}F-NMR[a] M_n^{TH} (g/mol)	^{19}F-NMR[b] M_n (g/mol)	SEC in THF[c] M_n (g/mol)	DP (-)	M_w/M_n (-)
PPFMA-1	25200	-	-	17210	68	1.6
PPFMA-2	21170	21670	28220	27630	110	1.4

PHPMA intermediates	SEC in DMF[d] M_n (g/mol)	M_w/M_n (-)
PHPMA-PDA-1	36830	1.9
PHPMA-PDA-2	38105	1.2
PHPMA-Dox-PDA-1	-	-

[a] Theoretical number-average molecular weight (M_n^{TH}) calculated from the monomer conversion determined by ^{1}H- and ^{19}F-NMR.

[b] Number-average molecular weight (M_n) calculated from ^{19}F-NMR of the purified product.

[c] Conventional calibration using polystyrene (PS) standards.

[d] Conventional calibration using poly(methyl methacrylate) (PMMA) standards.

Chapter 3: Reversion of P-gp-Mediated Drug Resistance in Ovarian Carcinoma Cells with PHPMA-Zosuquidar Conjugates

Table S2. Feed ratio and percentage of functionalization of the PHPMA intermediates and final conjugates.

PHPMA intermediates	Feed ratio (eq.)			PDA content (mol %)		Dox content (mol %)	
	HPA	PDA	Dox	1H-NMR[e]	UV[f]	1H-NMR[c]	UV[d]
PHPMA-PDA-1	1.7	0.3	-	2.4	2.3	-	-
PHPMA-PDA-2	1.6	0.4	-	4.7	4.3	-	-
PHPMA-Dox	1.8	-	0.2	-	-	2.4	2.5
PHPMA-Dox-PDA	1.9	0.1	0.15	0.2	0.4	2.6	2.9

Final conjugates	Zos content (mol %)		Dox content (mol %)	
	1H-NMR[a]	19F-NMR[b]	1H-NMR[c]	UV[d]
PHPMA-Zos-1	2.2	-	-	-
PHPMA-Zos-2	4.3	4.6	-	-
PHPMA-Dox	-	-	2.4	2.5
PHPMA-Dox-Zos	0.2	0.4	2.9	2.9

[a] Determined comparing the integrals of Zos signals with those of the polymer backbone and with the CH proton of the hydroxypropyl polymer side chains.

[b] Determined comparing the integrals of fluorine signals of Zos with those of the polymer end group and taking into account the degree of polymerization (DP).

[c] Determined comparing the integrals of the Dox signals with those of the polymer backbone and with the CH proton of the hydroxypropyl polymer side chains.

[d] Calculated from the absorbance peak at λ = 490 nm in DMSO (ε = 12049.6 cm^{-1} M^{-1}).

[e] Determined comparing the integrals of the PDA aromatic signals with those of the polymer backbone and with the CH proton of the polymer hydroxypropyl side chains.

[f] Calculated from the absorbance peak at λ = 375 nm in DMSO (ε = 5898.6 cm^{-1} M^{-1}) after cleavage of the PDA linker with 1-dodecanethiol.

Table S3. Cytotoxicity of Dox and PHPMA-Dox in sensitive A2780 and resistant A2780ADR cells as determined by MTT assay.

Compounds	Dox IC$_{50}$ (μM)[a]	
	A2780	A2780ADR
Dox	0.013 ± 0.003	1.441 ± 0.362
PHPMA-Dox	~ 20	~ 100

[a] IC$_{50}$ (concentration of drug necessary to inhibit 50 % of the cells growth) were determined via MTT assay after 72 h incubation, the percentage viability was determined with respect to untreated cells. For free Dox the IC$_{50}$ values and standard errors were calculated using a sigmoidal dose-response curve fitting, in the case of PHPMA-Dox the IC$_{50}$ values were estimated from the viability profile shown in **Figure S31**.
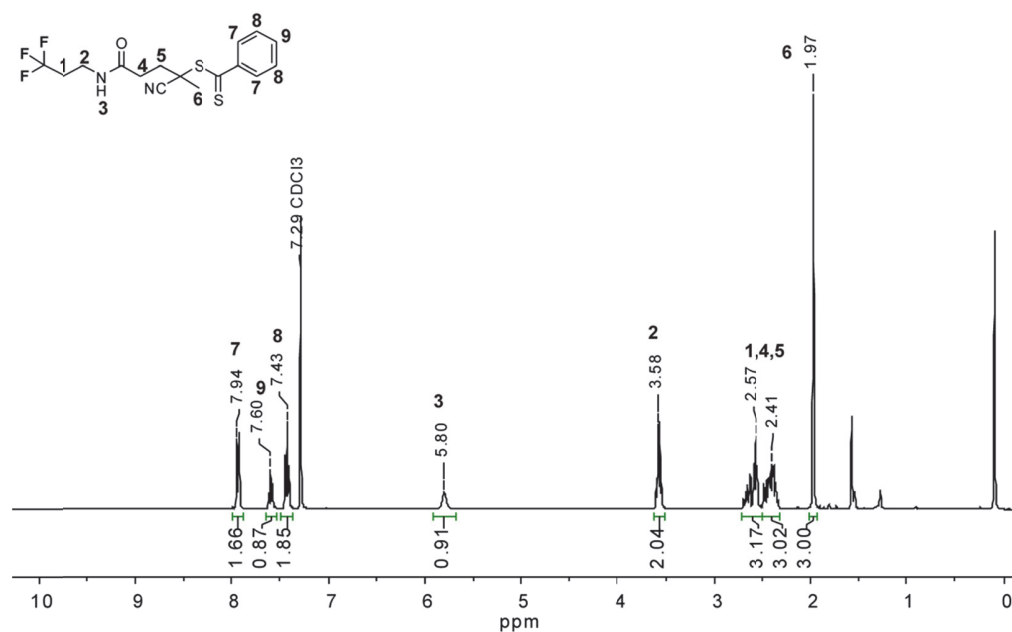
Figure S1. ^{1}H-NMR spectrum of F-CTA in CDCl$_3$.
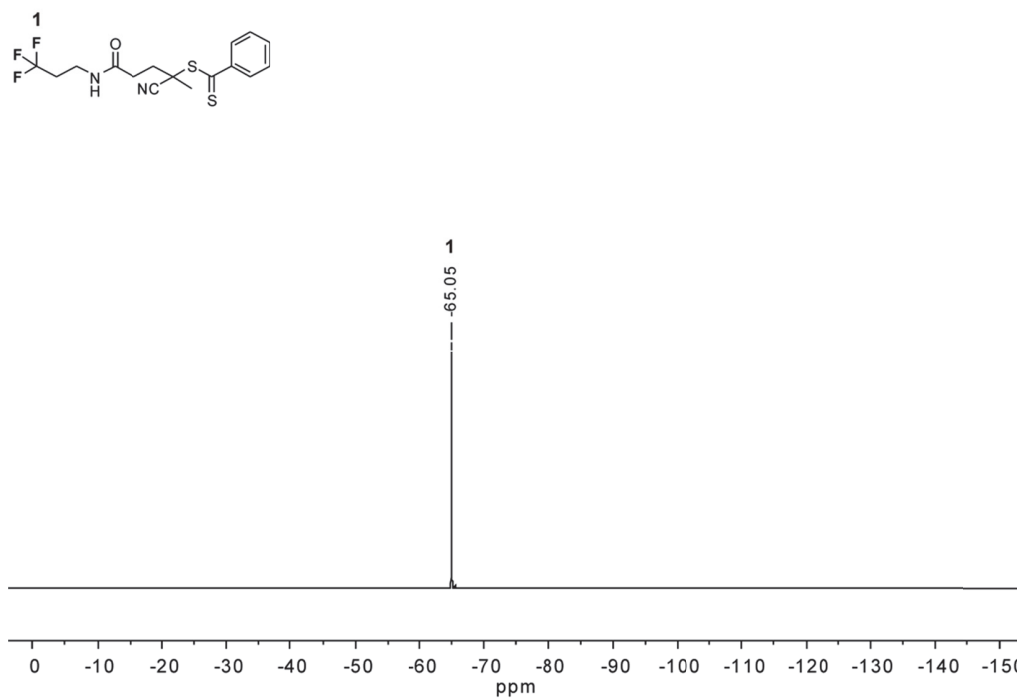
Figure S2. ^{19}F-NMR spectrum of F-CTA in CDCl$_3$.
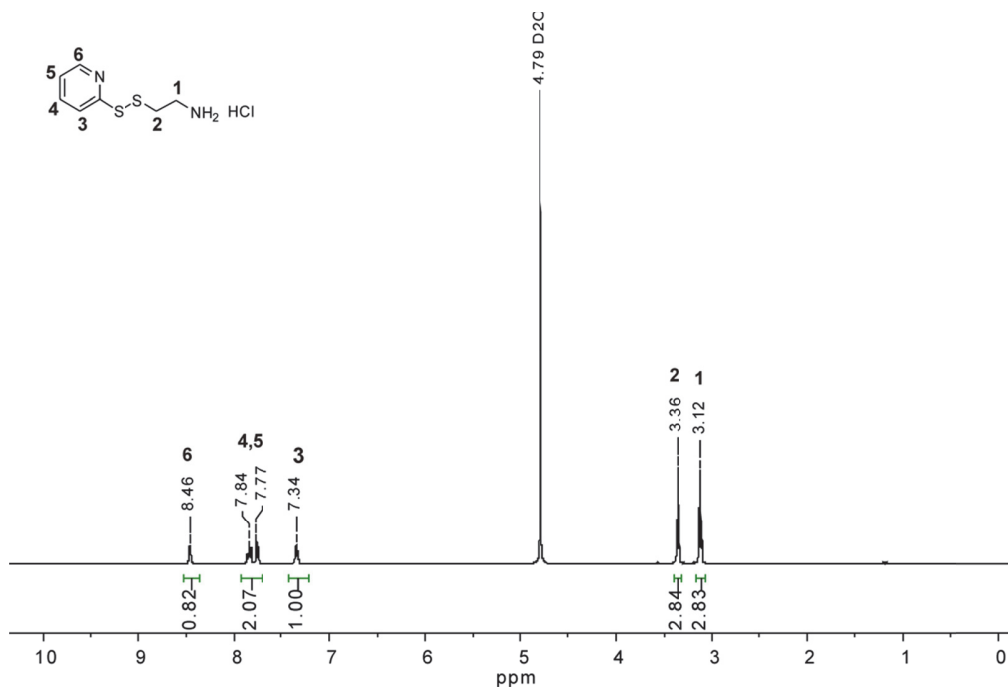
Figure S3. ^{1}H-NMR spectrum of 2-(pyridyldithio)-ethylamine (PDA) in D$_2$O.
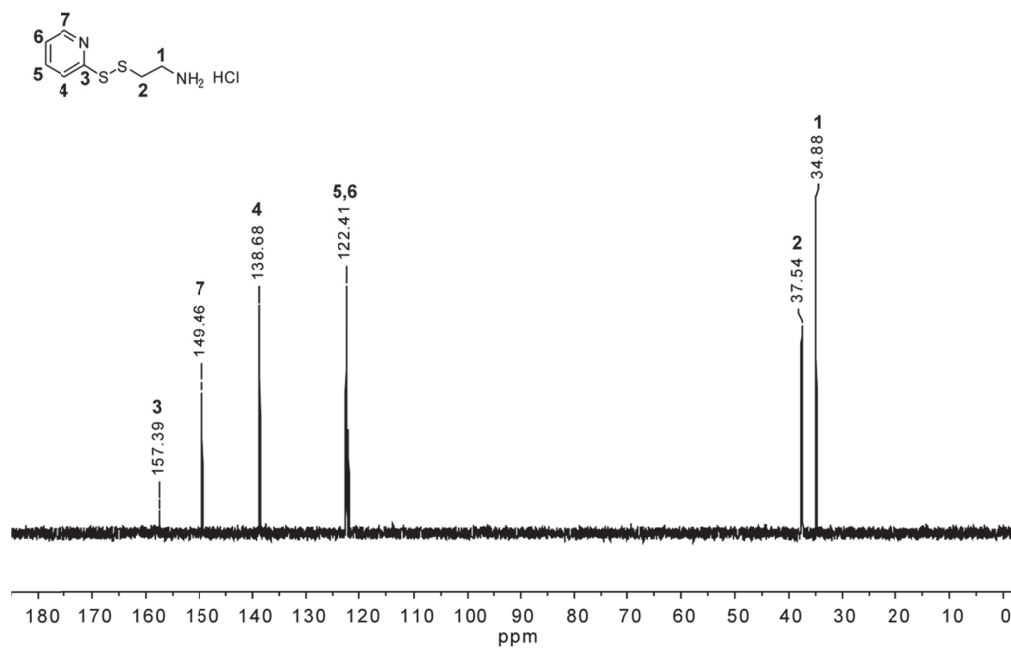
Figure S4. ^{13}C-NMR spectrum of 2-(pyridyldithio)-ethylamine (PDA) in D_2O.
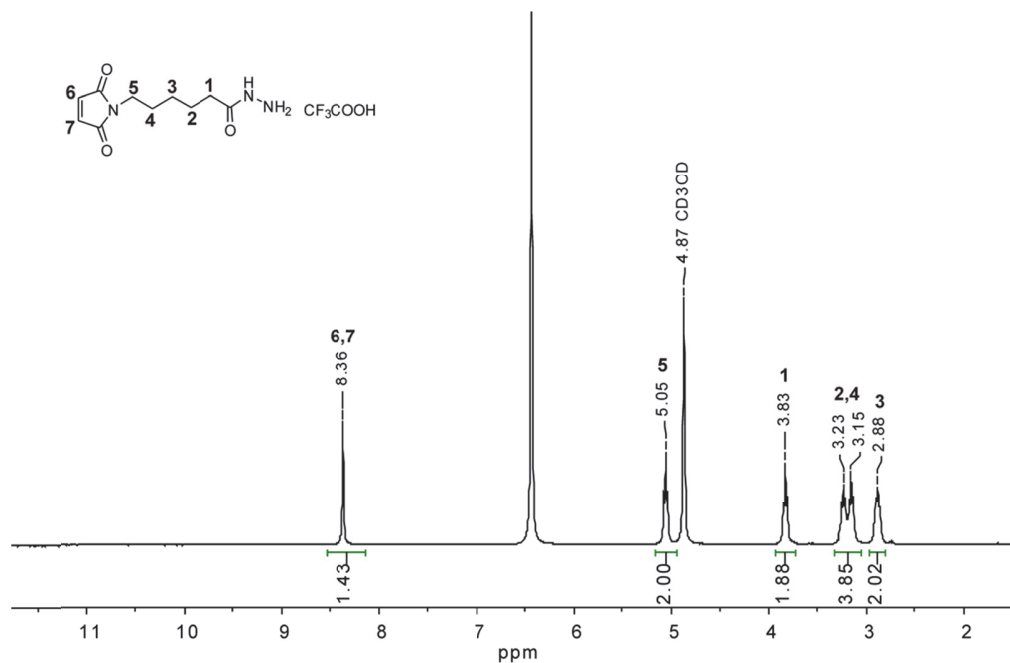
Figure S5. ^{1}H-NMR spectrum of 6-maleimidocaproic acid hydrazide trifluoroacetic acid salt in CD_3OD.
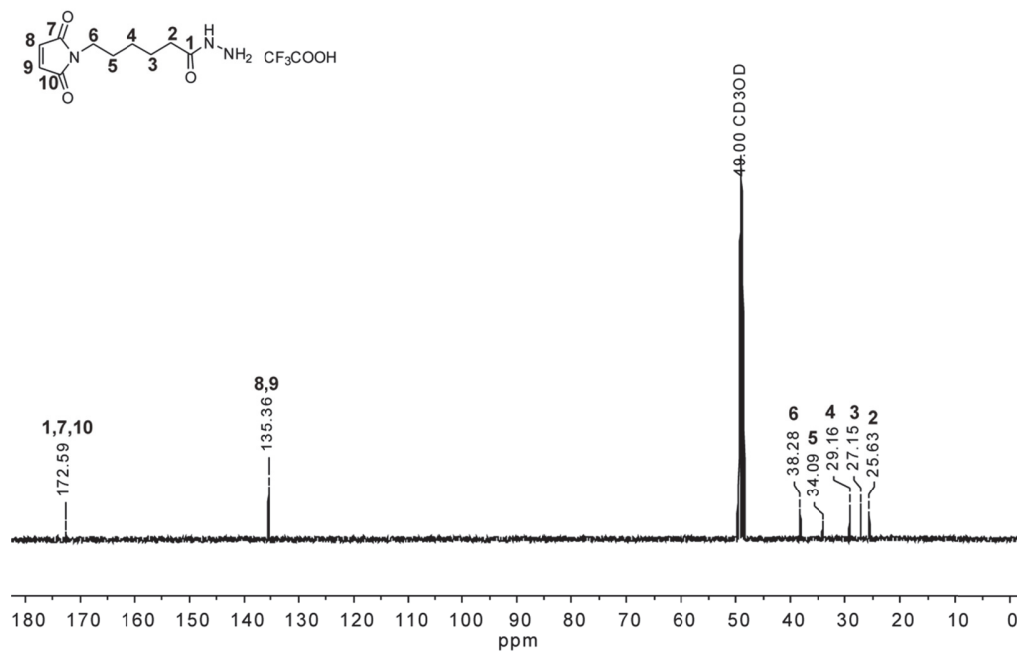
Figure S6. ^{13}C-NMR spectrum of 6-maleimidocaproic acid hydrazide trifluoroacetic acid salt in CD3OD.
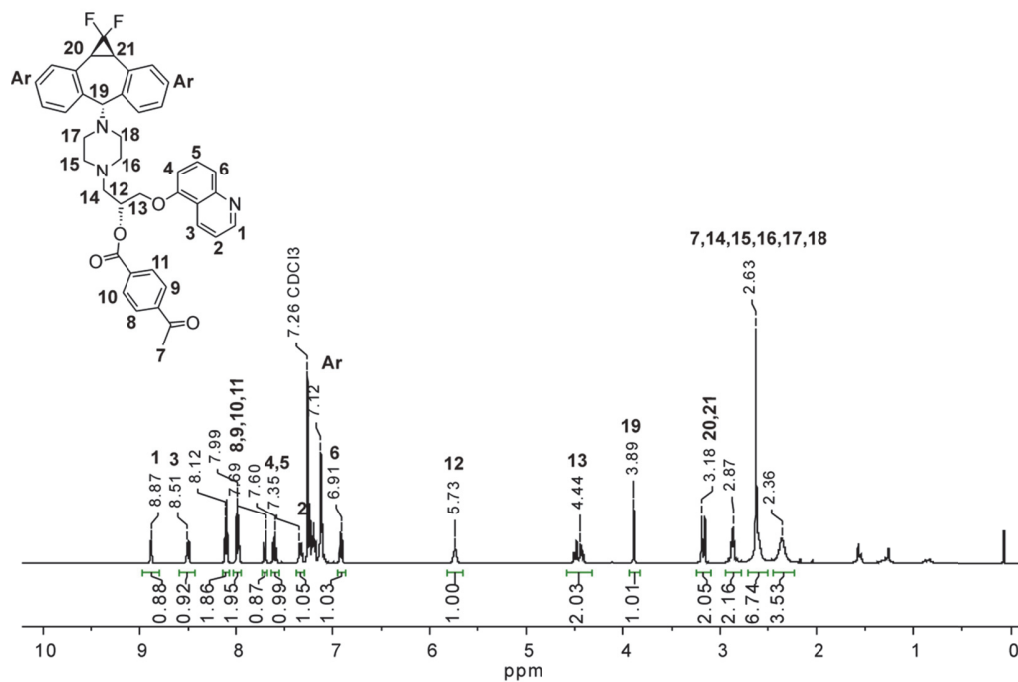
Figure S7. ^{1}H-NMR spectrum of Zos-Ket in CDCl3.
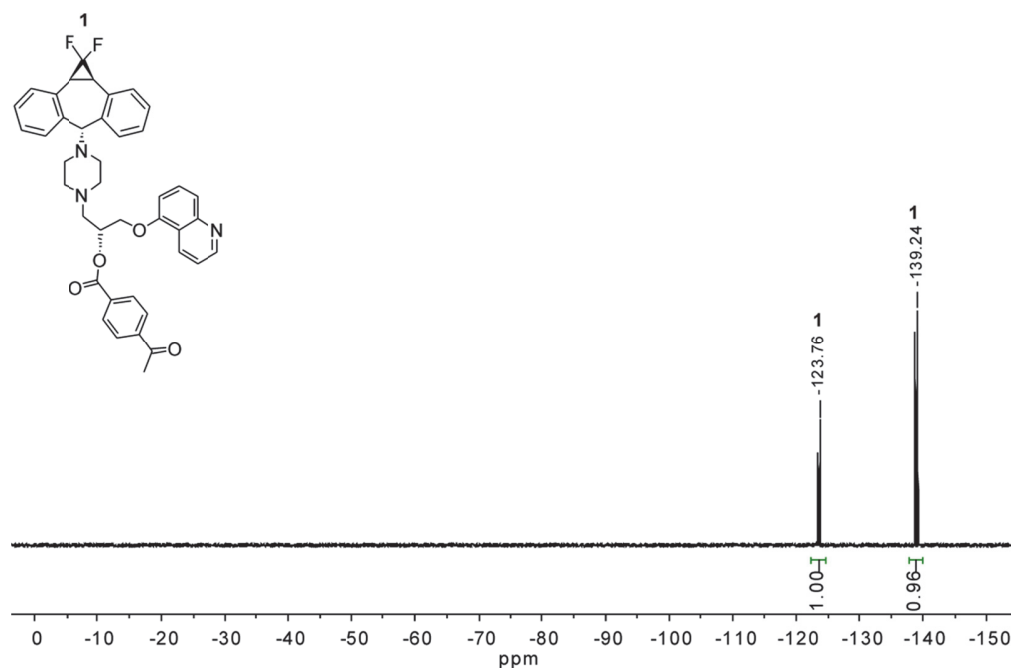
Figure S8. ^{19}F-NMR spectrum of Zos-Ket in CDCl$_3$.
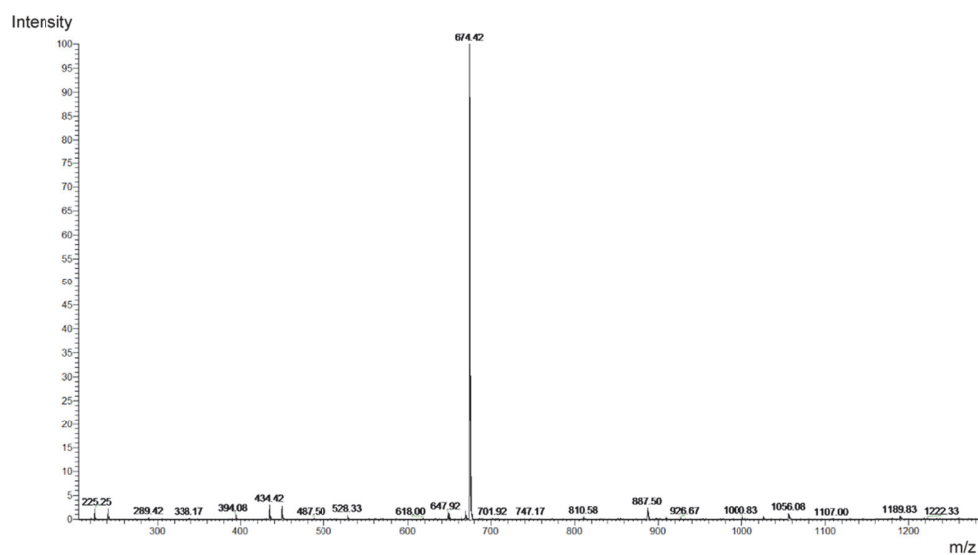
Figure S9. ESI-MS spectrum of Zos-Ket, exact mass [M] = 673.28, measured [M+H$^+$] = 674.72.

Figure S10. ^{1}H-NMR spectrum of Zos-Mal in CDCl$_3$. (* = Solvent impurity).

Figure S11. ^{19}F-NMR spectrum of Zos-Mal in CDCl$_3$.
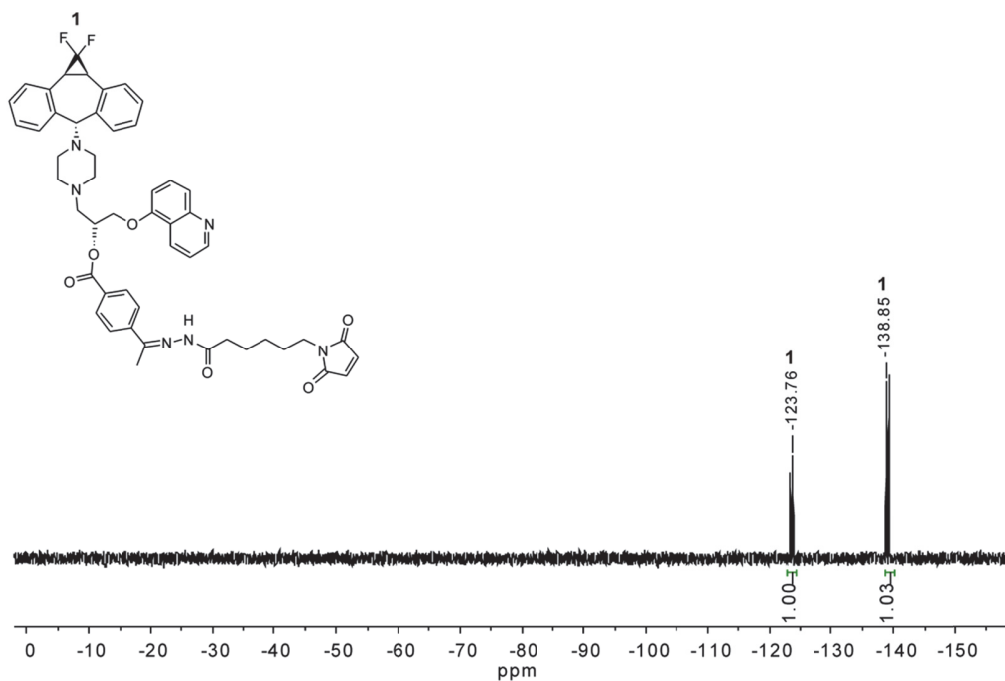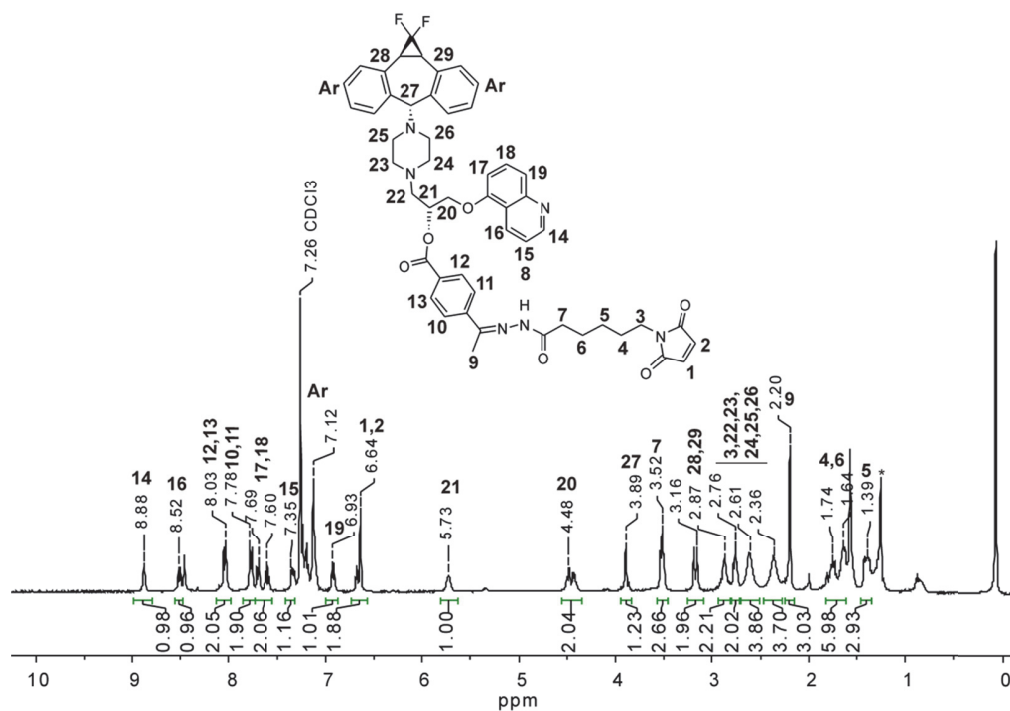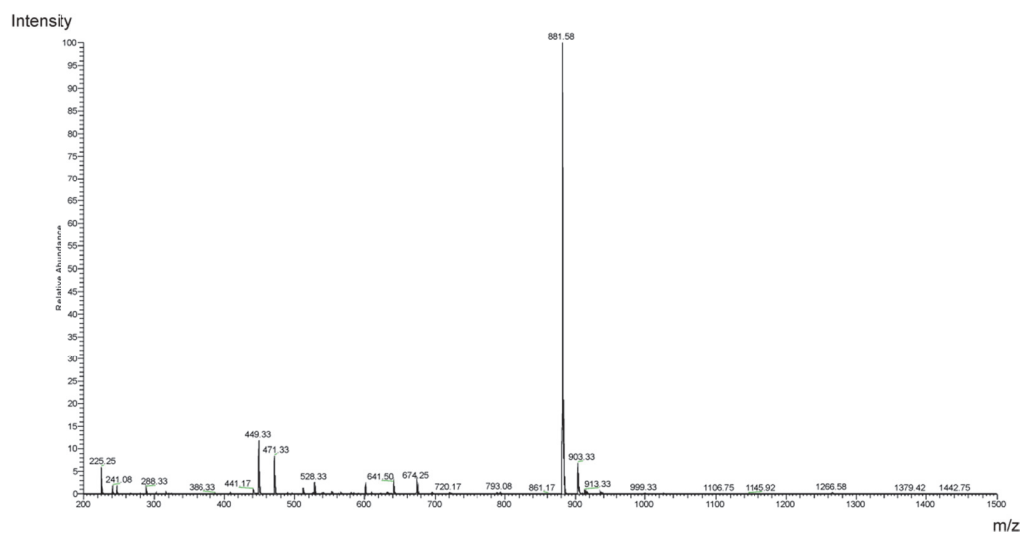
Figure S12. ESI-MS spectrum of Zos-Mal, exact mass [M] = 880.4, measured [M+H$^+$] = 881.6.
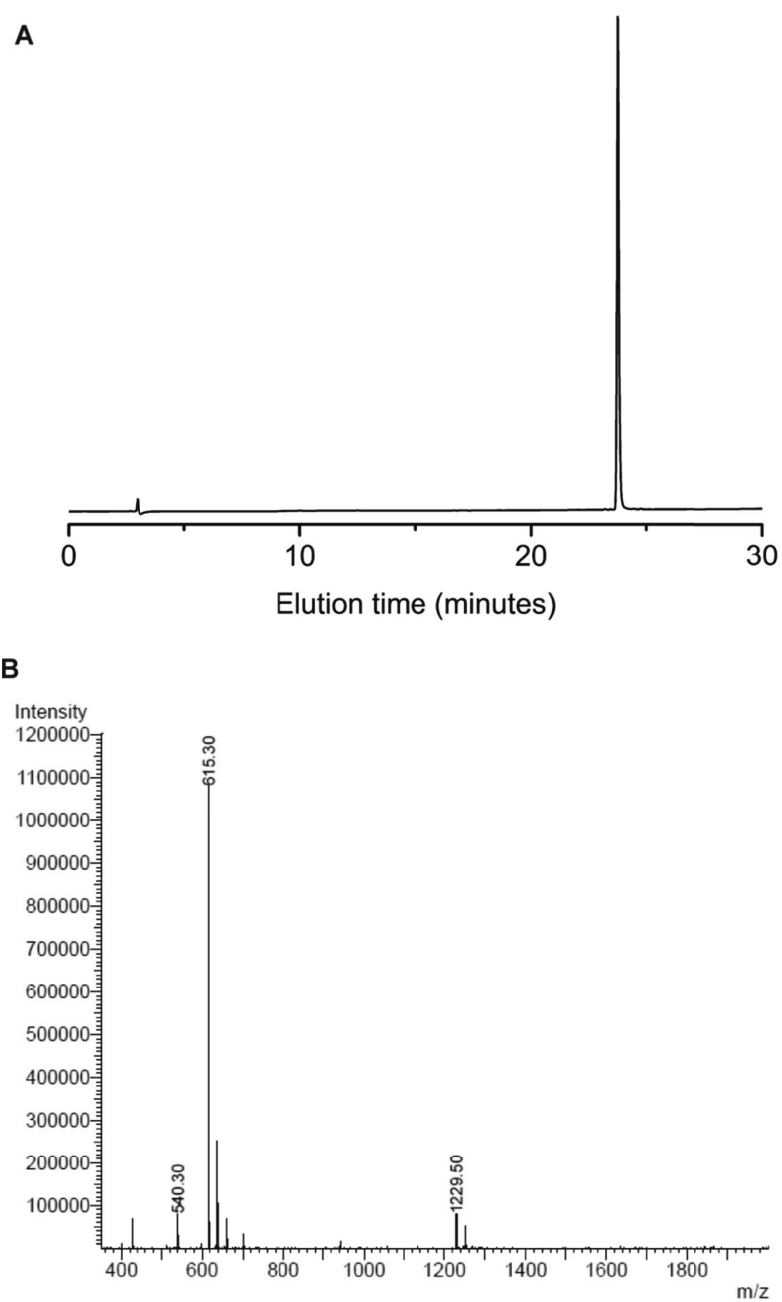
Figure S13. (A) RP-HPLC chromatogram of Fmoc-GFLG-OH and (B) ESI-MS spectrum of Fmoc-GFLG-OH, exact mass [M] = 614.3, measured [M+H$^+$] = 615.3, [M+Na$^+$] = 637.5.
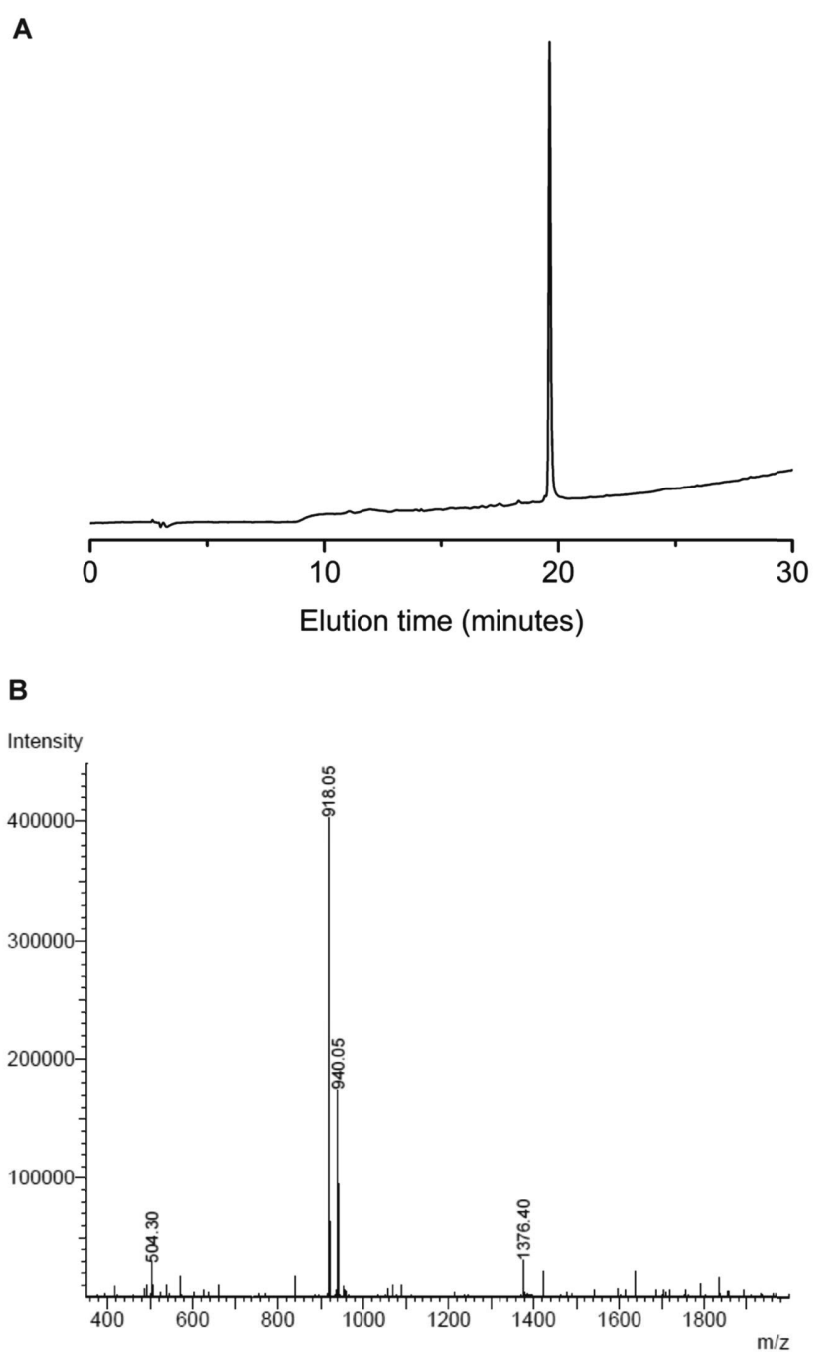
Figure S14. (A) RP-HPLC chromatogram of NH_2-GFLG-Dox and (B) ESI-MS spectrum of NH_2-GFLG-Dox, exact mass [M] = 917.4, measured $[M+H^+]$ = 918.1, $[M+Na^+]$ = 940.1.
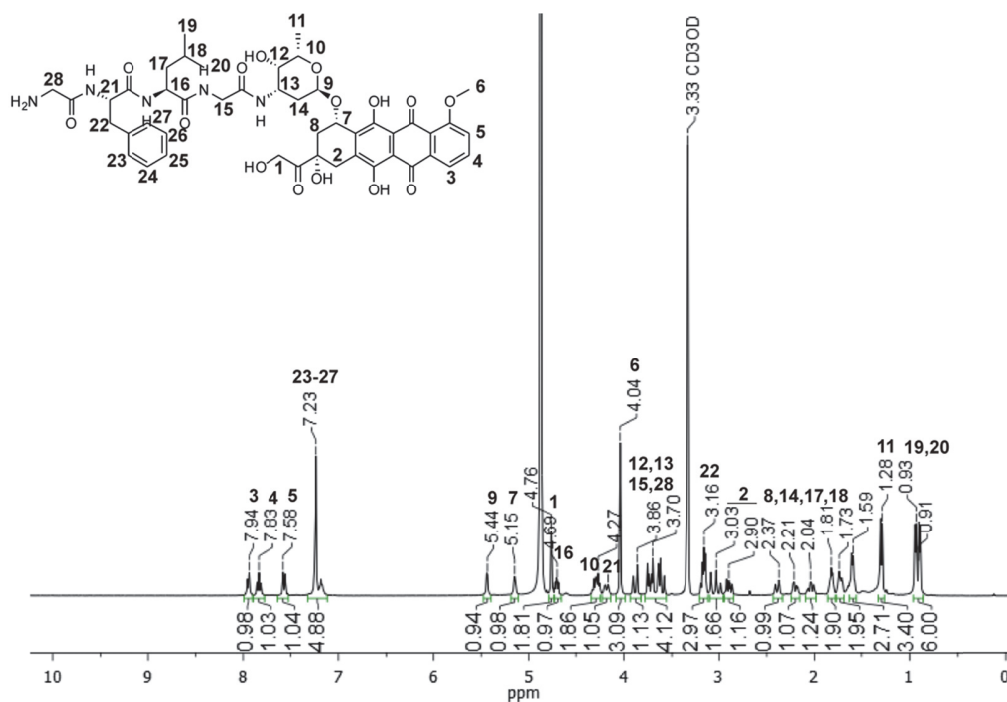
Figure S15. ¹H-NMR spectrum of NH₂-GFLG-Dox in MeOD.
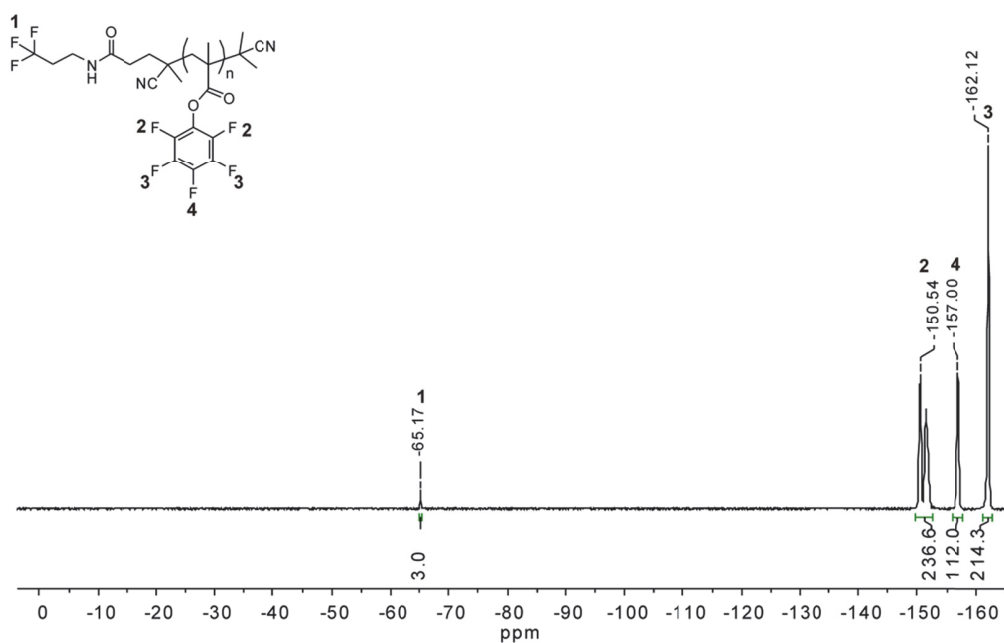
Figure S16. ¹⁹F-NMR spectrum of PPFMA-2 in CDCl₃.
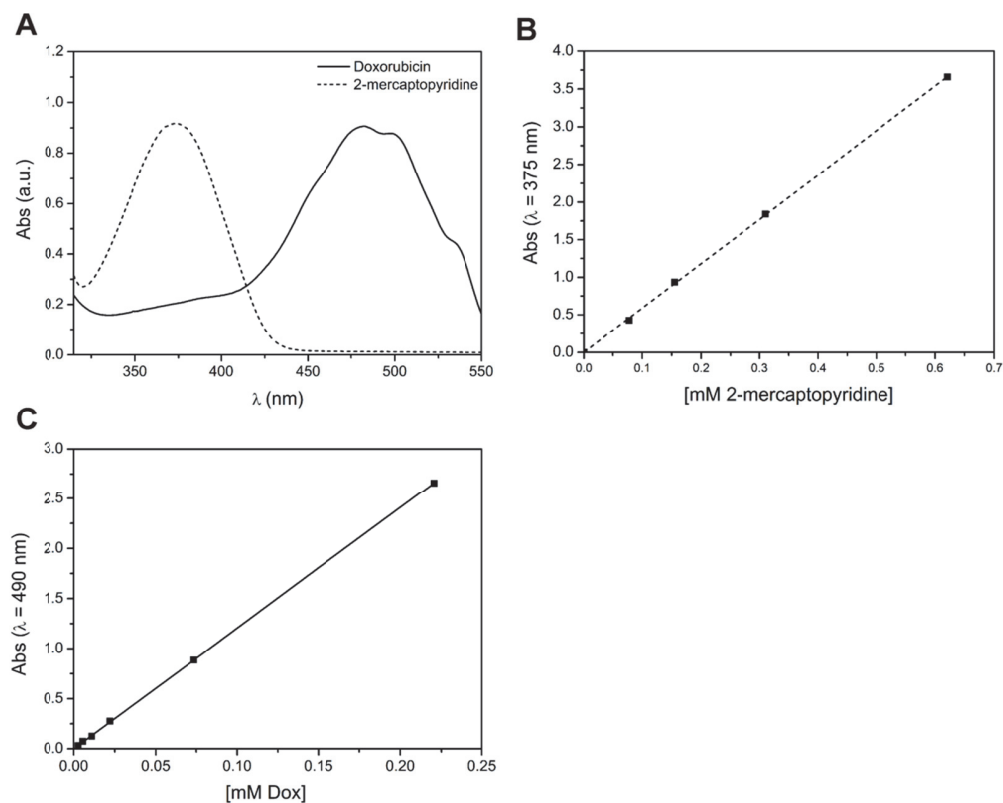
Figure S17. (A) UV spectra of a 0.15 mM solution of 2-mercaptopyridine and a 0.074 mM solution of Dox in DMSO; (B) calibration curve of 2-mercaptopyridine at $\lambda_{max} = 375$ nm in DMSO ($\varepsilon = 5898.6$ cm^{-1} M^{-1}); (C) calibration curve of Dox at $\lambda_{max} = 490$ nm in DMSO ($\varepsilon = 12049.6$ cm^{-1} M^{-1}) (optical length = 1 cm).
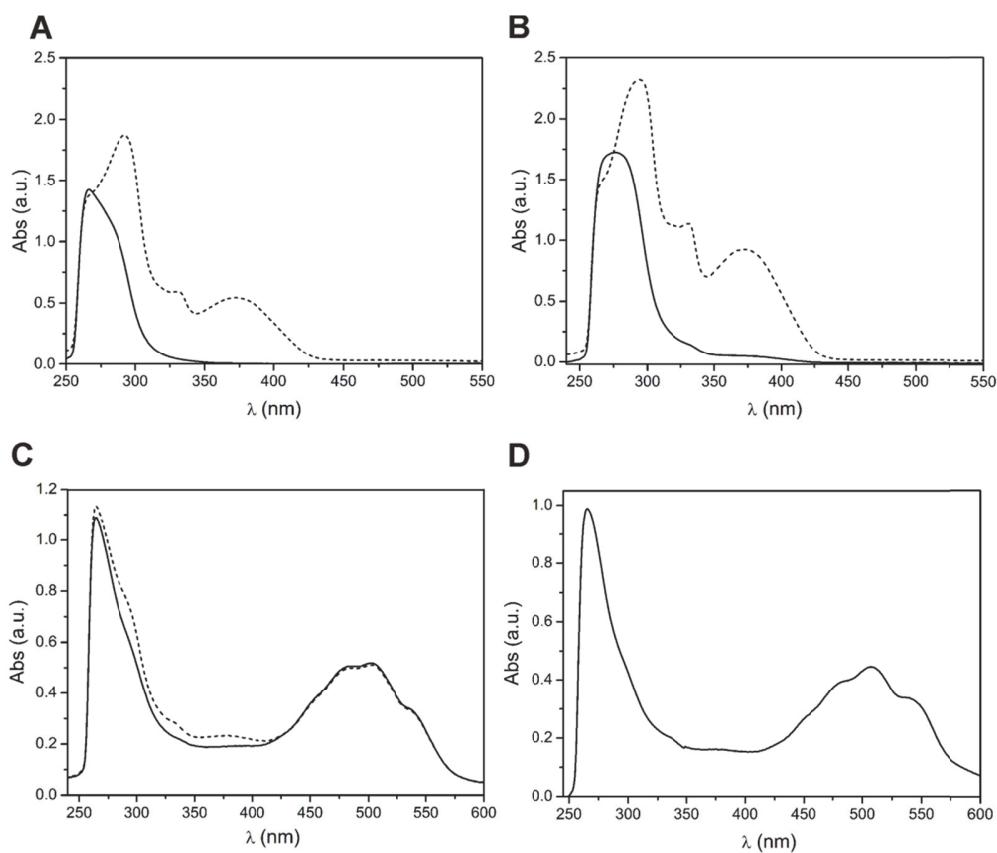
Figure S18. Examples of UV spectra of (A) 0.57 mg/mL PHPMA-PDA-1, (B) 0.53 mg/mL PHPMA-PDA-2 and (C) 0.18 mg/mL PHPMA-Dox-PDA solutions in DMSO before (continuous lines) and after (dashed lines) PDA cleavage. (D) UV spectra of 0.2 mg/mL PHPMA-Dox solution in DMSO. The absorbance peak at λ= 375 nm is characteristic of the released 2-mercaptopyridine whereas the peak at λ = 490 nm is characteristic of Dox.
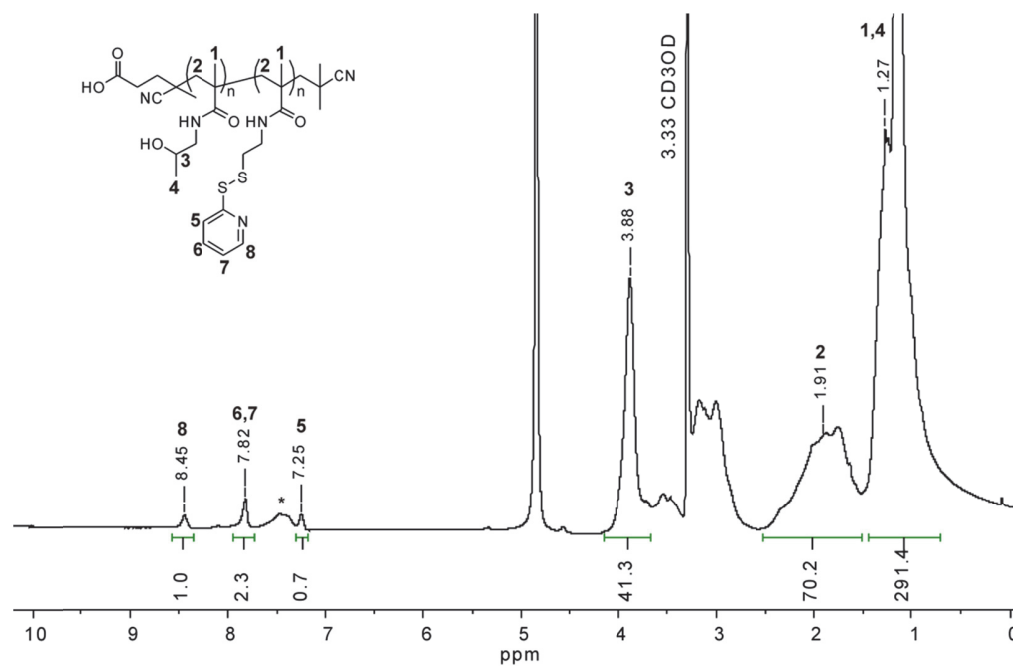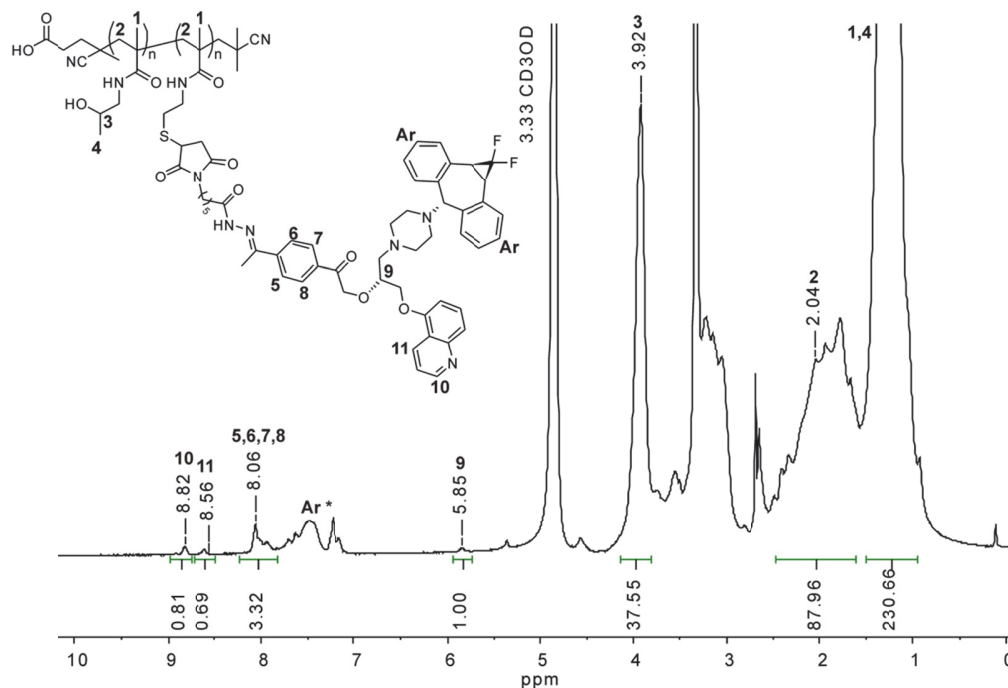
Figure S19. ^{1}H-NMR spectrum of PHPMA-PDA-1 in CD$_3$OD. To calculate the mol % of PDA incorporated in the polymer backbone the integrals of the PDA signals at 8.45 ppm (**8,** 1H), at 7.82 ppm (**6,7**, 2H) and at 7.25 ppm (**5**, 1H) were averaged and compared to the integrals of the polymer signals at 3.88 ppm (**3**), at 1.91 ppm (**2**) and at 1.27 ppm (**1,4**). The result is reported as an average of the mol % obtained using the three different polymer signals. * = peaks associated with the amide protons of the polymer side chains.
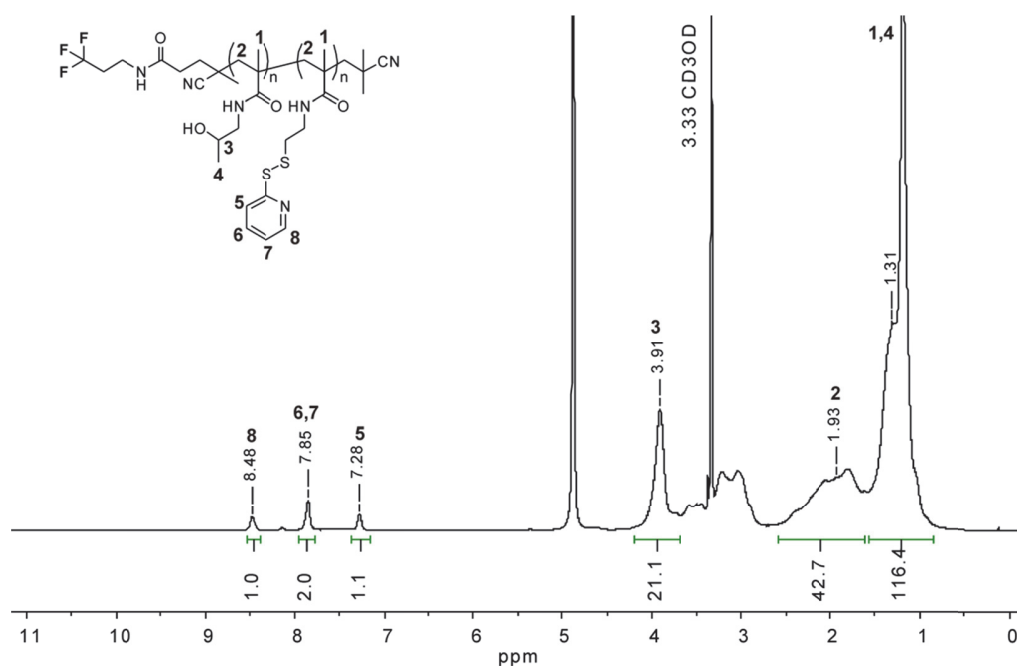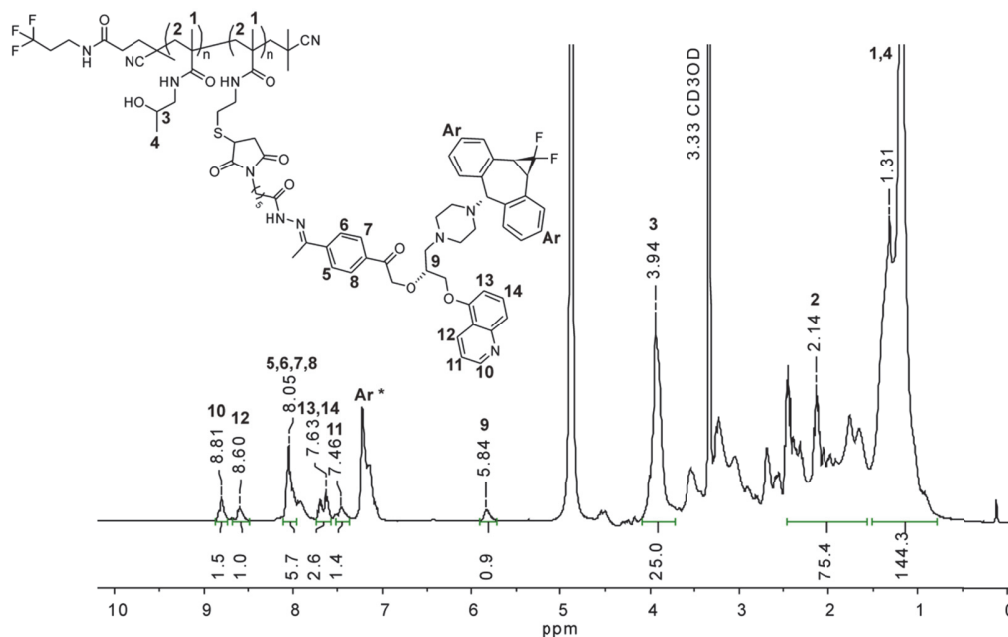
Figure S20. ^{1}H-NMR spectrum of PHPMA-PDA-2 in CD$_3$OD. To calculate the mol % of PDA incorporated in the polymer backbone the integrals of the PDA signals at 8.48 ppm (**8,** 1H), at 7.85 ppm (**6,7,** 2H) and at 7.28 ppm (**5,** 1H) were averaged and compared to the integrals of the polymer signals at 3.91 ppm (**3**), at 1.93 ppm (**2**) and at 1.31 ppm (**1,4**). The result is reported as an average of the mol % obtained using the three different polymer signals.
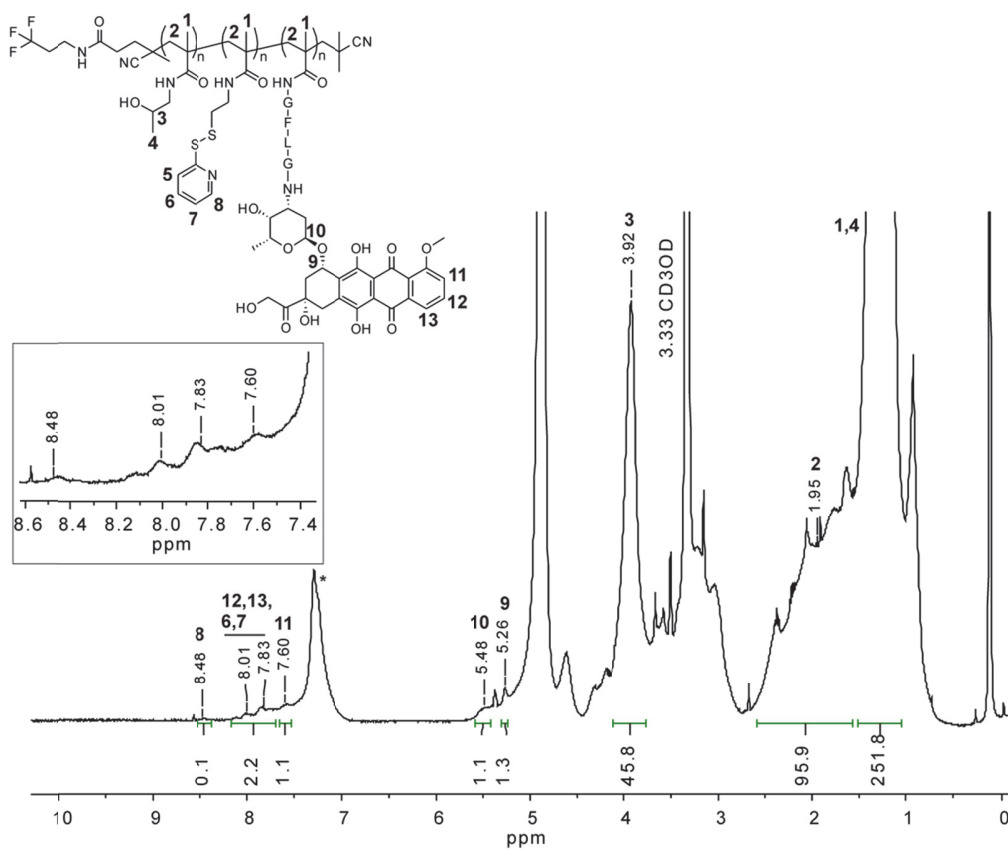
Figure S21. ¹H-NMR spectrum of PHPMA-Dox-PDA in CD₃OD. To calculate the mol % of PDA and Dox incorporated in the polymer backbone the integral of the PDA signal at 8.48 ppm (**8**, 1H), and the average of the integrals of the Dox signals at 8.01-7.83 ppm (**12,13** 2H-Dox and **6,7** 2H-PDA), at 7.60 ppm (**11**, 1H), at 5.48 ppm (**10**, 1H) and at 5.26 ppm (**9**, 1H) were compared to the integrals of the polymer signals at 3.92 ppm (**3**), at 1.95 ppm (**2**) and at 1.27 ppm (**1,4**). The NH₂-GFLG-Dox-derived signals (**Figure S 15**) overlapping with that of the polymer were subtracted from the signals of the polymer (**3**, **2** and **1,4**) used for the calculation. The result is reported as an average of the mol % obtained using the three different polymer signals. * = peaks associated with the amide protons of the polymer side chains and with the amide and aromatic protons of the GFLG linker.
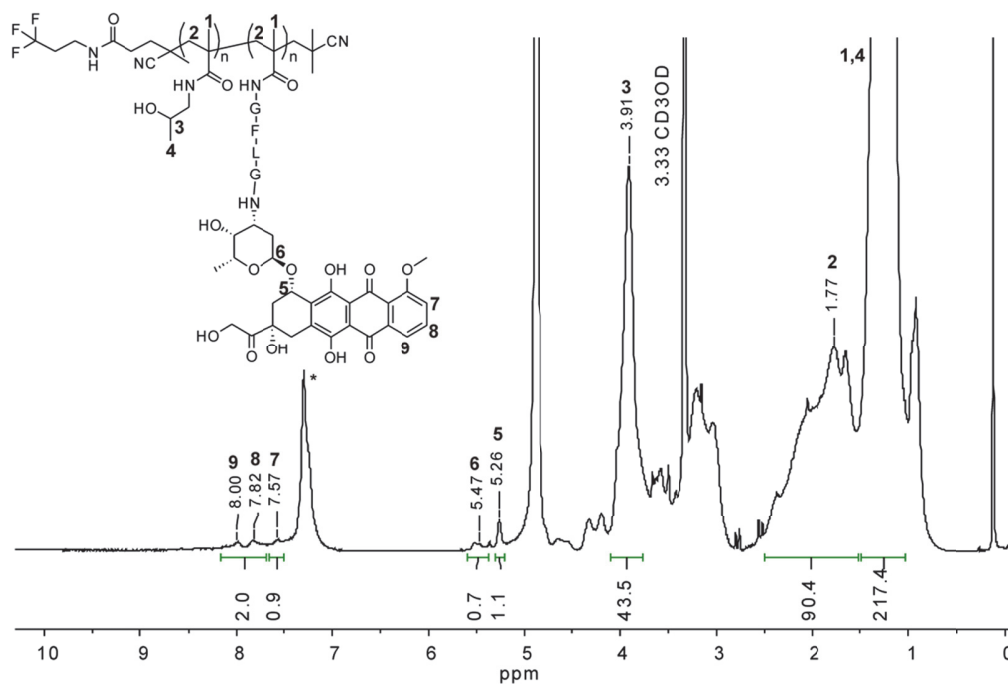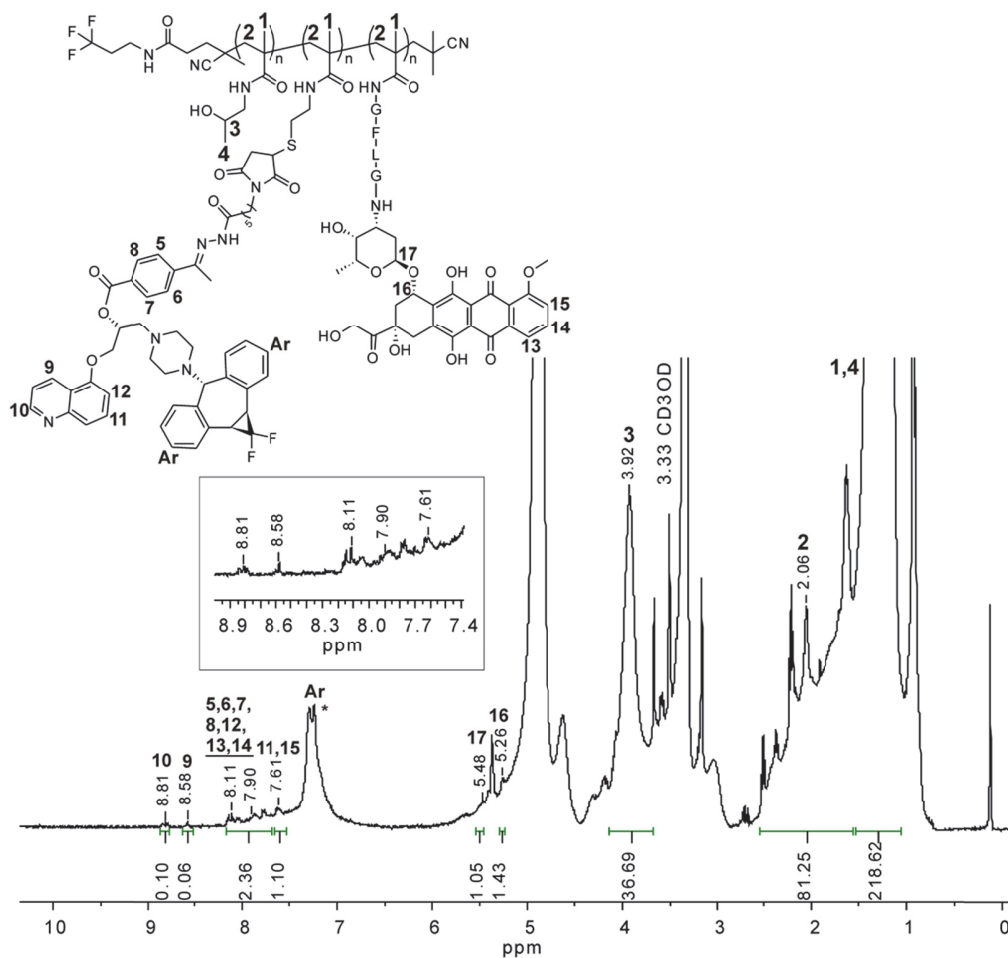
Figure S22. ^{1}H-NMR spectrum of PHPMA-Dox in CD$_3$OD. To calculate the mol % of Dox incorporated in the polymer backbone the integrals of Dox signals at 8.00 ppm (**9**, 1H), at 7.82 ppm (**8**, 1H), 7.57 ppm (**7**, 1H), at 5.47 ppm (**6**, 1H) and at 5.26 ppm (**5**, 1H) were averaged and compared to the integrals of the polymer backbone signals at 3.91 ppm (**3**), at 1.77 ppm (**2**) and at 1.27 ppm (**1,4**). The NH$_2$-GFLG-Dox-derived signals (**Figure S15**) overlapping with that of the polymer were subtracted from the signals of the polymer (**3**, **2** and **1,4**) used for the calculation. The result is reported as an average of the mol % obtained using the three different polymer signals. * = peaks associated with the amide protons of the polymer side chains and with the amide and aromatic protons of the GFLG linker.
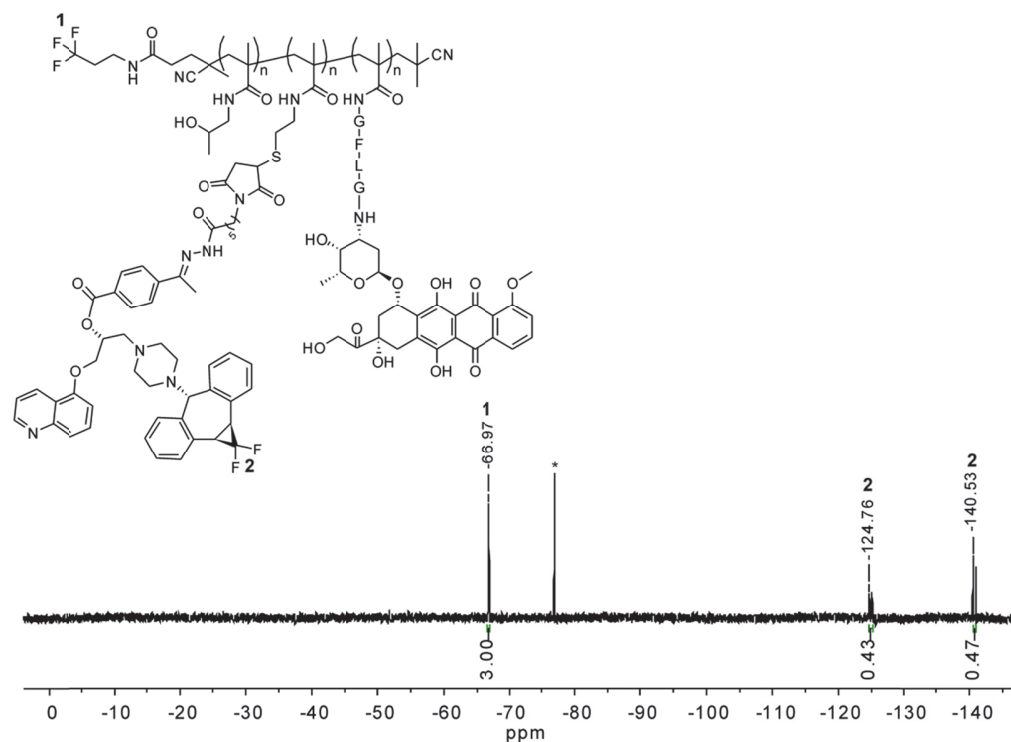
Figure S23. ^{1}H-NMR spectrum of PHPMA-Zos-1 in CD$_3$OD. To calculate the mol % of Zos incorporated in the polymer backbone the integrals of the Zos signals 8.81 ppm (**10**, 1H), 8.60 ppm (**12**, 1H), and at 5.84 ppm (**9**, 1H) were averaged and compared to the integrals of the polymer signals at 3.94 ppm (**3**), at 2.14 ppm (**2**) and at 1.31 ppm (**1,4**). The Zos Mal-derived signals (**Figure S10**) overlapping with that of the polymer backbone were subtracted from the signals of the polymer (**3, 2** and **1,4**) used for the calculation. The result is reported as an average of the mol % obtained using the three different polymer signals. * = peaks associated with the protons of the amide groups in the polymer side chains.

Figure S24. ^{1}H-NMR spectrum of PHPMA-Zos-2 in CD$_3$OD. To calculate the mol % of Zos incorporated in the polymer backbone the integrals of the Zos signals at 8.82 ppm (**10**, 1H), at 8.56 ppm (**11**, 1H), and at 5.85 ppm (**9**, 1H) were averaged and compared to the integrals of the polymer signals at 3.92 ppm (**3**), at 2.04 ppm (**2**) and at 1.31 ppm (**1,4**). The Zos Mal-derived signals (**Figure S10**) overlapping with that of the polymer backbone were subtracted from the signals of the polymer (**3, 2** and **1,4**) used for the calculation. The result is reported as an average of the mol % obtained using the three different polymer signals. * = peaks associated with the protons of the amide groups in the polymer side chains.
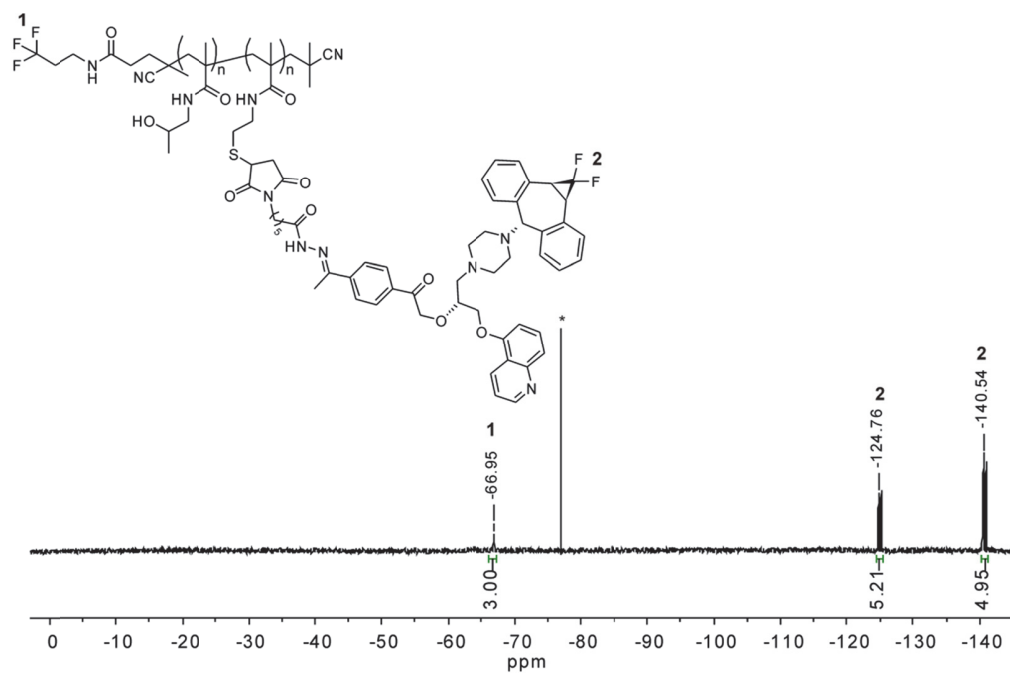
Figure S25. ^{19}F-NMR spectrum of PHPMA-Zos-2 in CD$_3$OD (* = TFA). To calculate the mol % of Zos incorporated in the polymer backbone the integrals of the Zos signals at -124.76 ppm (**2**, 1F) and at -140.54 ppm (**2**, 1F) were compared to the integrals of the polymer end group signal at -66.95 ppm (**1**, 3F) and the result was related to the the degree of polymerization (DP) determined by SEC of the PPFMA-2 polymer precursor. The result is reported as an average of the mol % obtained using the two Zos signals.

Figure S26. ^{1}H-NMR spectrum of PHPMA-Dox-Zos in CD$_3$OD. To calculate the mol % of Dox and Zos incorporated in the polymer backbone the integrals of the Dox signal at 7.61 ppm (**15**, 1H-Dox and **11**, 1H-Zos) and the average of the integrals of the Zos signals at 8.81 ppm (**10**, 1H) and at 8.85 ppm (**9**, 1H) were compared to the integrals of the polymer signals at 3.92 ppm (**3**), at 2.06 ppm (**2**) and at 1.27 ppm (**1,4**). The NH$_2$-GFLG-Dox-derived signal (**Figure S15**) and the Zos Mal-derived signals (**Figure S10**) overlapping with that of the polymer backbone were subtracted from the signal of the polymer (**3**, **2** and **1,4**) used for the calculation. The result is reported as an average of the mol % obtained using the three different polymer signals. * = peaks associated with the amide protons of the polymer side chains and with the amide and aromatic protons of the GFLG linker.

Figure S27. ^{19}F-NMR spectrum of PHPMA-Dox-Zos in CD$_3$OD (* = TFA). To calculate the mol % of Zos incorporated in the polymer backbone the integrals of the Zos signals at -124.76 ppm (**2**, 1F) and at -140.53 ppm (**2**, 1F) were compared to the integrals of the polymer end group signal at -66.97 ppm (**1**, 3F) and the result was related to the the degree of polymerization of the PPFMA-2 polymer precursor determined by SEC. The result is reported as an average of the mol % obtained using the two Zos signals.
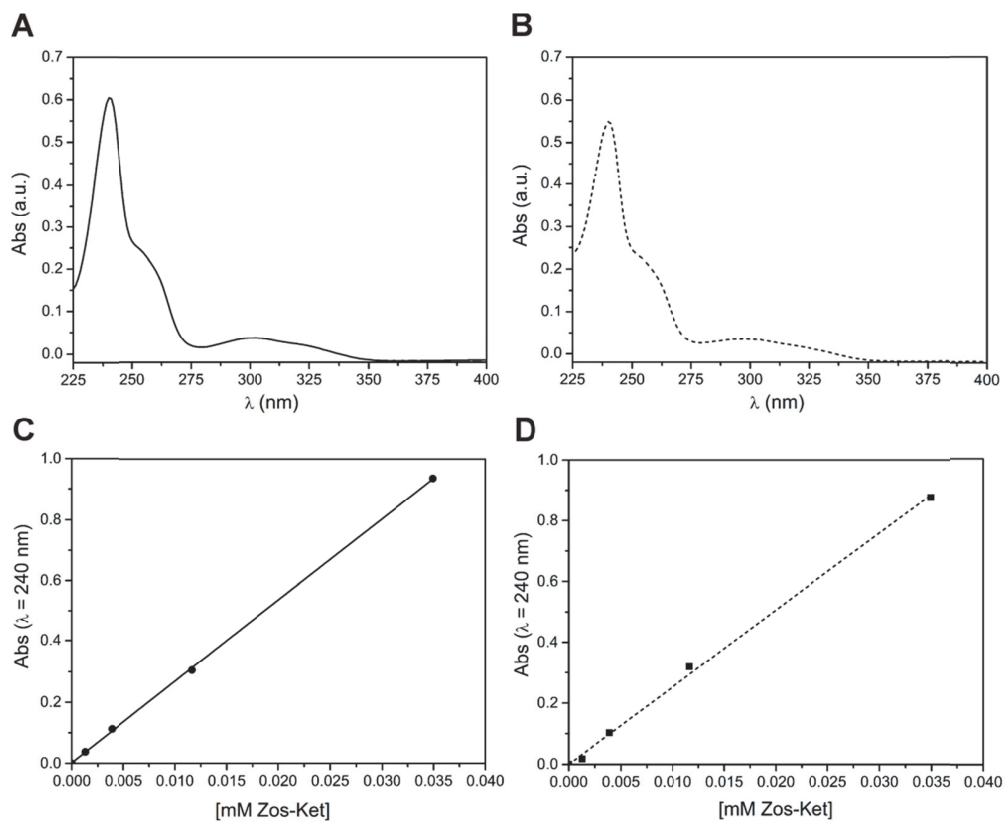
Figure S28. (A) UV spectra of a 0.22 mM solution of Zos-Ket in phosphate citrate buffer containing 30% ethanol at pH 7.4 and (B) 5.5 (optical path = 0.1 cm). (C) Calibration curves of Zos-Ket at λ_{max} = 240 nm in the same buffer solutions at pH 7.4 (ε = 26768 M^{-1} cm^{-1}) and (D) 5.5 (ε = 25313 M^{-1} cm^{-1}) (optical length = 1 cm).
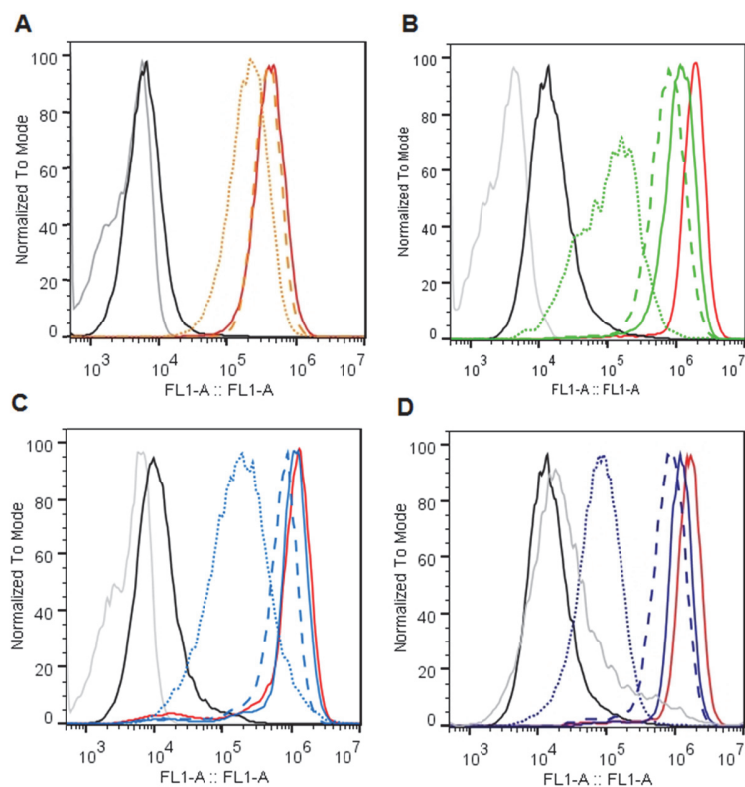
Figure S29. Flow cytometry analysis of (DiOC$_2$(3)) efflux inhibition from A2780ADR cells. CsA (red curve) was used as positive control and untreated cells (grey curves) were used as negative control. Black curves indicate the fluorescence of cells incubated at 37°C without inhibitors. (A) Incubation with Zos at 0.1 (dotted lines) and 1 (dashed lines) µM; (B) incubation with Zos-Ket at 0.1 (dotted lines), 1 (dashed lines) and 5 (continuous lines) µM. (C) Incubation with PHPMA-Zos-1 and (D) -2 at 0.1 (dotted lines), 1 (dashed lines) and 5 (continuous lines) µM of polymer-bound drug.
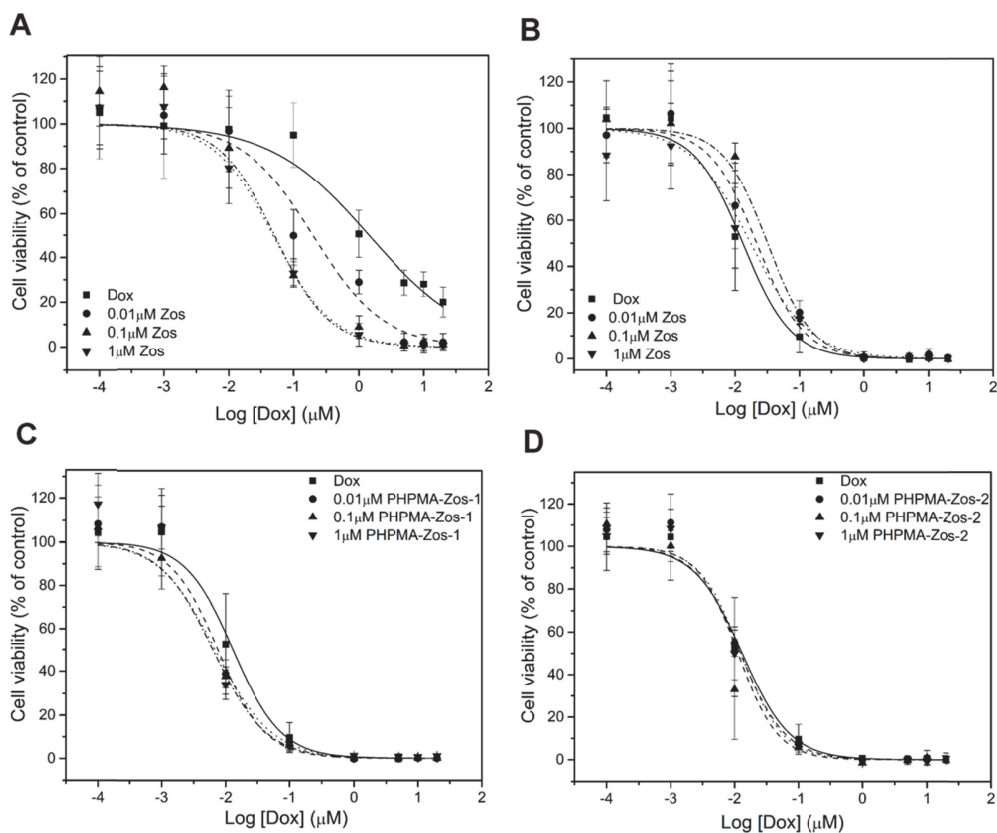
Figure S30. (A) Dox cytotoxicity alone and in combination with increasing concentrations of Zos in A2780ADR and (B) A2780 cells and with increasing concentrations of (C) PHPMA-Zos-1 and (D) -2 in A2780 cells as determined by MTT assay.
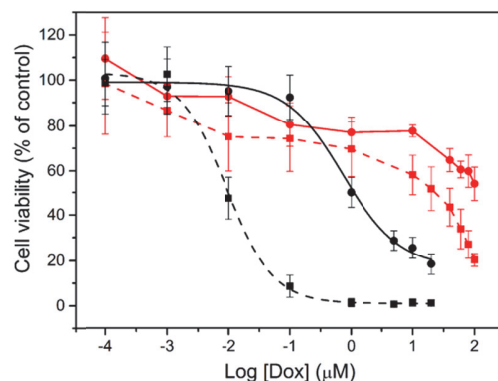
Figure S31. Comparison between the cytotoxicity of the PHPMA-Dox conjugate (red) and free Dox (black) in sensitive A2780 (■) and in resistant A2780ADR (●) cells as determined by MTT assay.
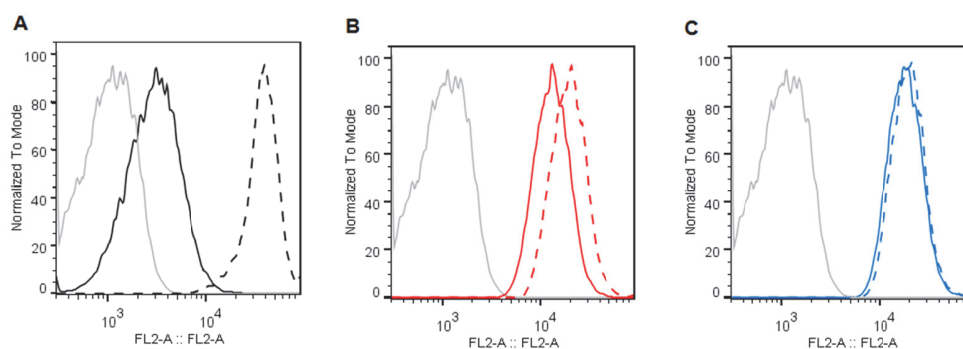
Figure S32. Example of Dox efflux from A2780ADR cells when administered as free drug (A) or delivered as (B) PHPMA-Dox or (C) PHPMA-Dox-Zos conjugates (continuous curves) as determined by flow cytometry. Control cells (gray curves) were used as negative control, cells treated with both Dox/Polymer-Dox conjugates and CsA (dashed lines) were used as positive control.

References for Supporting Information

(1)   Willner, D.; Trail, P. A.; Hofstead, S. J.; King, H. D.; Lasch, S. J.; Braslawsky, G. R.; Greenfield, R. S.; Kaneko, T.; Firestone, R. A., *Bioconjugate Chem.* **1993,** *4* (6), 521.

(2)   Gibson, M. I.; Frohlich, E.; Klok, H. A., *J. Polym. Sci., Part A: Polym. Chem.* **2009,** *47* (17), 4332.

(3)   Perrier, S.; Takolpuckdee, P.; Mars, C. A., *Macromolecules* **2005,** *38* (6), 2033.

4. Monitoring Uptake and Intracellular Trafficking of Poly(*N*-(2-hydroxypropyl) methacrylamide) (PHPMA)

4.1.   Introduction

Polymer nanomedicine is a very attractive approach for the delivery of small molecule therapeutics in particular for the treatment of cancer.[1] The use of polymer conjugates and polymer nanocarriers can help to increase plasma half-life and drug bioavailability,[1,2] while also allowing passive tumor targeting by the enhanced permeation and retention (EPR) effect.[2,3]

Although enhanced drug bioavailability and efficient tumor targeting are important to maximize the efficacy of anticancer drugs and reduce side effects, the location of drug targets in specific well-defined subcellular compartments, makes intracellular transport of polymer nanomedicine a critical step for a successful treatment outcome. After extravasation in the cancer tissue, polymers gain access to the cell interior *via* endocytosis.[4,5] This process starts with the engulfment of the cargo in the cell membrane and results in the formation of intracellular vesicles called early endosomes, which are characterized by slightly acidic pH. The internalized material is then shuttled from the early endosomes to the higher acidic late endosomes, before being finally sorted to the cell lysosomes, where the enzymatic digestion takes place.[6] The physiochemical and biochemical parameters that characterize the endolysosomal compartments have been explored to trigger drug release from the polymer carrier.[5,7] In particular, the highly acidic lysosomal environment and the presence of degradative enzymes have been exploited to trigger intracellular drug release.[7]

Poly(*N*-(2-hydroxypropyl) methacrylamide) (PHPMA)-based carriers, first developed by Kopeček and Duncan in the 1970s, have been extensively used for the preparation of polymer conjugates for the endolysosomal release of anticancer drugs.[8-10] HPMA-doxorubicin, HPMA-camptothecin, HPMA-paclitaxel and HPMA-platinates conjugates

are some examples of HPMA polymer conjugates that have entered clinical trials for therapeutic validation in the last decade.[8,11]

The interest in exploring PHPMA-based conjugates as chemotherapeutics has also triggered a need to study and understand the internalization and intracellular trafficking of these nanomedicines. Based on to the availability of a wide range of chemical functionalities for polymer labeling and to the use of intrinsic fluorescent drugs, fluorescence based techniques have been most frequently used to monitor PHPMA internalization and intracellular trafficking.[5,11] While early attempts to investigate time-dependent PHPMA cellular uptake consisted in the quantification of intracellular fluorescent dyes (PHPMA-dye conjugates)[12] or intrinsic fluorescent drugs (PHPMA-drug conjugates)[13] *via* fluorescence spectroscopy, or *via* radioassay, in the case of I_{125} modified drugs,[13] nowadays flow cytometry is the most utilized method to monitor the cellular uptake of PHPMA. Time and concentration-dependent uptake have been evaluated by detecting the internalized PHPMA-drug conjugates, in case of fluorescent drugs,[14,15] or PHPMA-dye conjugates.[16-18] Whereas flow cytometry is sufficient to give information about cellular uptake, the most used approach to study intracellular trafficking of PHPMA in the endosomal pathway is confocal fluorescence microscopy. Initially, these approaches were based on the subcellular localization of fluorescent drugs. For instance, 6 hours exposure of cells to a PHPMA-mesochlorin e6 (Mce6) conjugate resulted in polymer accumulation in the lysosomes.[19] A similar approach was used to monitor the cleavage of a lysosomal sensitive linker (GFLG) and consequent doxorubicin (Dox) release from PHPMA conjugates.[13] Duncan and co-workers combined subcellular fractionation techniques with confocal microscopy to determine Dox release from a PHPMA-GFLG-Dox conjugate.[14] 5 hours incubation of cells with the polymer conjugate resulted in both punctuate cytoplasmic doxorubicin fluorescence and disperse signal, which was attributed to doxorubicin release from the carrier. While these studies confirmed polymer accumulation in the lysosomes and in some cases drug release by action of lysosomal enzymes after long incubation time, investigation of carrier trafficking in the endolysosomal pathway is also important for further improvement of such delivery systems. Jensen *et al*. monitored time-dependent PHPMA intracellular trafficking by using PHPMA-dye conjugates, however, in this study they did not use endosomal and lysosomal fluorescent markers which allow co-localization studies with the endocytic vesicles.[12] Other reports mainly focused on studying the effect of antibody conjugation or insertion of charged and hydrophobic moieties on the cellular

internalization and accumulation in the late endosomal vesicles of PHPMA copolymers.[17,18] Although these studies have given valuable insight into the early endocytic trafficking of different PHPMA conjugates, the investigation of the complete time-frame of the endocytic process, from early endosomal PHPMA uptake to lysosome loading, would allow an estimation of time-dependent exposure of the polymer to the different endolysosomal environments.

Although detailed co-localization experiments and careful data interpretations can be used for these purposes, it has often been argued that the modification of polymer carriers with fluorescent dyes can lead to several drawbacks. First, exposure of the polymer-dye conjugates to the highly degradative cellular environments can result in the cleavage of the fluorescent dye from the polymer carrier.[20-22] Second, the fluorescent label can interfere with biological processes[23] and finally, concentration- or pH-dependent dye quenching, might lead to additional artifacts.[5,20] Additional challenges arise when this approach is used to monitor, not only polymer intracellular trafficking, but also polymer-mediated drug delivery. In this case, both polymer and drug need to be tracked at the subcellular level. To this end, unless an intrinsic fluorescent drug is used, the drug need to be substituted with a fluorescent dye, therefore further differentiating the system from the designed one. Fluorescent carrier and drug need to be monitored simultaneously and co-localization studies with several stained organelles can result in very complicated assays. Moreover, reported co-localization studies generally lack quantitative information.[5,22] Therefore, the establishment of label-free techniques that can be used in combination with fluorescence-based approaches and that allow both qualitative and quantitative studies are desirable for a deeper understanding of the polymer-cell interaction and for further monitoring intracellular drug delivery processes. Nanoscale Secondary Ion Mass Spectrometry (NanoSIMS) is particularly attractive technique since it allows high spatial resolution (down to 50 nm) and it offers the possibility to obtain quantitative information while also excluding the need for bulky labels.[24] NanoSIMS allows the semi-quantitative analysis of multi-elements and isotopes by sample erosion *via* a focused ion primary beam.[24] Recently, Proetto *et al*. combined NanoSIMS with fluorescence microscopy to image intracellular platinum-based anticancer drugs linked to a ^{15}N-labeled fluorescent polymer carrier.[25] While fluorescence microscopy allowed subcellular carrier co-localization with endocytic vesicles, NanoSIMS analysis was used to simultaneously quantify and compare both internalized carrier and drug. Implementation of this technique in the field of polymer nanomedicines would offer the possibility to use

159

isotopes or elements rather than bulky labels, as well as to quantify polymer-mediated delivery processes.

The first aim of this work is to use fluorescence-based techniques to study PHPMA cellular uptake and to investigate endolysosomal trafficking by determining correlation coefficients with both endosomal and lysosomal vesicles. Additional, the rest of this Chapter demonstrates how NanoSIMS can be used to monitor polymer subcellular localization. PHPMA was prepared from a PPFMA polymer precursor which was obtained *via* reversible-addition fragmentation chain transfer (RAFT) polymerization. In this study, the chain transfer agent (CTA) was used to introduce both a fluorescent label and a fluorinated one at both ω- and α-polymer end groups, these labels enabled polymer detection *via* fluorescence-based techniques and NanoSIMS, respectively. The first part of this work investigates the cellular uptake of PHPMA using flow cytometry analysis and correlates the obtained results with cell division occurring during the time-frame of the experiment. The second part investigates the intracellular trafficking of the polymer by co-localization studies with both early endosomal and lysosomal vesicles *via* confocal fluorescence microscopy. Imaging of several cells per each incubation time, experiment repetitions and calculation of correlation coefficients, was accomplished to determine the PHPMA dynamic profile in the endosomal pathway. Finally, the last part of this work investigates the possibility to use NanoSIMS analysis and transmission electron microscopy (TEM) for co-localization studies of the internalized polymer. While NanoSIMS was used to map the fluorine-containing PHPMA in cells, the combination with TEM enabled the visualization of intracellular vesicles and compartments for polymer subcellular localization. Detailed co-localization studies with endocytic vesicles *via* fluorescence microscopy and the implementation of novel techniques such as NanoSIMS combined with TEM are particularly relevant in the field of polymer nanomedicines since they can allow a fully characterization of intracellular drug delivery processes.

4.2. Experimental Section

4.2.1. Materials

Annexin V-Alexa Fluor 647 conjugate, Annexin buffer, CellLight lysosomes-GFP, CellLight early endosomes-GFP, Rhodamine Red C2 maleimide and CellTrace Violet were purchased from Life Technologies. 1 mM Staurosporine solution in DMSO, 2-(4-amidinophenyl)-6-indolecarbamidine dihydrochloride **(**DAPI), poly-D-Lysine hydrobromide, tris(2-carboxyethyl)phosphine hydrochloride (TCEP), 1-amino-2-propanol (HPA), sodium borohydride (NaBH$_4$), Sephadex G 15 and 1,8-diazabicyclo[5.4.0]undec-7-ene (DBU) were purchased from Sigma-Aldrich. Pentafluorophenol was purchased from MatrixScientific and triethylamine (Et$_3$N) and 1,4-dioxane were from Acros Organics. 3,3,3-Trifluoropropylamine hydrochloride was obtained from Apollo Scientific and dimethylformamide (DMF), from VWR. The solvents were dried using a Pure Solv solvent purification system.

4.2.2. Methods

^{1}H- and ^{19}F-NMR spectra were recorded on a Bruker AV III-400 instrument at room temperature. ^{1}H-NMR spectra of polymers were recorded with a relaxation time (d$_1$) of 10 seconds and at least 256 scans using CD$_3$OD and CDCl$_3$ as solvents. Chemical shifts are reported relative to the residual proton signal of the solvent.Size exclusion chromatography (SEC) of PPFMA in THF was performed using an Agilent 1260 infinity system equipped with a refractive index (RI) Varian 390-LC, two PLgel 5 μm Mixed C (Agilent) columns and a PLgel guard column. THF was used as eluent with a flow rate of 1 mL/min and the temperature was 40 °C. Samples were analysed using conventional calibration with polystyrene (PS) standards ranging from 4910 Da to 549 KDa. UV-Vis spectroscopy was carried out using a Varian Cary 100 Bio spectrometer using quartz cuvettes and flow cytometry was performed using a LSRII cytometer (BD Biosciences) equipped with a violet (405 nm), blue (488 nm), green (561 nm) and red (640 nm) lasers and the data were

analysed using FlowJo software. Cells were imaged using a transmission electron microscope (Tecnai Spirit, FEI).

Confocal microscopy and co-localization studies. Images were acquired on Zeiss LSM700 microscope with a Plan-Apochromat 63x/1.40 Oil objective, a pixel size of 70 nm and pinhole 48 μm. 4 to 6 images were acquired per each incubation time and the experiments were replicated 3 times. Under the microscope, both polymer chains and vesicles resemble disks which suggested to use an object based co-localization analysis. Unfortunately, due to the resolution limit of microscopy, some individual objects could not be distinguished from others. Hence, the object based analysis relying on the measure of distances between closest neighbor objects would have been biased. For this reason, Mander's coefficients were determined at the different time points.[26] Since the different images showed different number of cells per field and the cells could exhibit different size and different levels of expression of the fusion constructs, some "Region Of Interest" (ROIs) were manually drawn to outline the fields of interest. Since different cells expressed different levels of the fusion protein GFP, and the image could present different background due to sample preparation or microscopy variability (staining batch and laser power fluctuation), a global (histogram-derived) thresholding method was used rather than only one cut-off value for all of the images. The chosen methods, selected by visual inspection of thresholded images, were Moments[27] and IsoData[28] respectively for vesicular compartments and polymer images. To perform the analysis, the Fiji distribution of ImageJ,[29] the JACoP plugin[30] and a customized Action Bar "BIOP JACoP Tools" [ref Action bar][31] enabling batch processing, were used.

NanoSIMS. For the subcellular detection of the fluorinated PHPMA, samples were analyzed using a NanoSIMS 50L instrument. For anion analysis, the NanoSIMS uses a Cs^+ primary beam that can be scanned over a squared surface to produce elemental images. The probe size (diameter of the Cs^+ beam) was ~150 nm. During this study, typical images were collected in ultra-high vacuum condition ($5 \cdot 10^{-10}$ mbars). Images size was 38x38 μm with a 256x256 pixel image resolution and a dwell time of 5000 μs per pixel. The NanoSIMS detectors were set up to collect $^{12}C^{14}N^-$, $^{19}F^-$ and $^{32}S^-$ secondary ions simultaneously in the absence of any isobaric interference. Each image was acquired following the same protocol: a phase of pre-implantation where the Cs^+ beam was scanned over the surface in order to remove the gold layer from the area of interest and to implant Cs^+ into the sample; and an acquisition phase consisting of five successive scans

over the surface during which data were collected and were later cumulated during the data reduction.

4.2.3. Procedures

The ^{19}F-CTA and the ^{19}F-PPFMA were synthesized according to the procedure described in **Chapter 1** and **Chapter 2**, respectively. The ^{19}F- and ^{1}H-NMR spectra of ^{19}F-PPFMA are included in **Figure S1** and **S2**. Polymer molecular weight, determined by both NMR and SEC analysis are given in **Table S1**.

^{19}F-PHPMA. 100 mg (0.397 mmol PFMA reactive units) ^{19}F-PPFMA were dissolved in 5 mL dry DMF, 2 equiv. (61 μL) 1-amino-2-propanol (HPA) and 2 equiv. (110 μL) Et_3N were added and the reaction was stirred at 50°C for 20 h. The product was isolated by three precipitations in ice-cold diethyl ether and subsequently dialyzed against water. The ^{1}H-NMR is shown in **Figure S3**.

^{19}F-PHPMA-Rhodamine conjugate. Modification of polymer end group with fluorescent dye was performed as previously reported with some modifications.[32] 20 mg (0.00129 mmol end group) ^{19}F-PHPMA (M_n = 17151 g/mol) were dissolved in 3 mL 0.5 M $NaBH_4$ solution and stirred at room temperature for 2 h. The solution was dialyzed against water for 48 hours and the product was lyophilized. In a second step, 10 mg of product (0.6 μmol end group) were dissolved in dry DMF, 5 equivalents (0.8 mg 0.0032 mmol) neutralized TCEP were added and the solution was stirred overnight under argon. After 20 h, 5 equivalents (2.1 mg) Rhodamine Red C2 maleimide were added together with one drop DBU. The solution was stirred under argon at room temperature for other 24 h. The solution was dialyzed against water overnight using a SpectraPor (MWCO 3.5 KDa) membrane to remove the DMF and finally lyophilized. The product was purified by passing it through a Sephadex G 15 column. The purification was repeated twice.

Cell line and cell culture. HeLa cells were cultured in DMEM (high glucose) medium supplemented with 10 % fetal bovine serum (FBS) (Gibco) and 1% penicillin/streptomycin (Lifetech). Cells were maintained in a humidified atmosphere containing 5 % (v/v) of CO_2 at 37 °C.

Cell preparation for fluorescence microscopy. HeLa cells were seeded on 13 mm sterilized poly-D-Lysine-coated coverslips in 24-well plates at a density of 25000 cells per well and incubated in 450 µL medium for 18 h. 17 µL (PPC 35) CellLight early endosomes GFP and 20 µL (PPC 40) CellLight lysosomes GFP were added to the cell medium and the cells were further incubated for 24 h. During this period, the cell medium was replaced by free phenol red-DMEM medium containing 0.6 mg/mL ^{19}F-PHPMA-Rhodamine and the cells were incubated for 15 h, 4 h, 2 h, 40 min and finally 10 min. For the 15 h incubation sample, the polymer solution was supplemented with the CellLight constructs in order to keep the cell exposure to the constructs constant among the different incubation times. At the end of the time-course experiment, the cells were washed three times with DMEM without phenol red and twice with PBS and finally fixed using 2 % paraformaldehyde and 1 % glutaraldehyde solution in phosphate buffer (PB) (pH 7.4, 0.1 M) for one hour at room temperature. Cells were than washed twice with cacodylate buffer (pH 7.4, 0.1 M) and stained with 0.5 µg/mL DAPI solution in the same buffer for 6 minutes. Cells were washed four times and kept in cacodylate buffer during fluorescence microscopy analysis. Three independent experiments were performed.

Sample preparation for TEM and NanoSIMS analysis. After fluorescence microscopy, cells were post-fixed for 60 minutes in a solution of 1% osmium tetraoxide and 1.5% potassium ferrocyanide in ice-cold cacodylate buffer 0.1 M. This was followed by staining with 0.1 g thiocarbohydrazide in 10 mL double distilled water solution for 20 min at room temperatute. Subsequently, staining with 1% osmium tetraoxide in cacodylate buffer solution was performed for 30 min. Then, the samples were dehydrated in an ascending alcohol series (1 X 50%, 1 X 70%, 2 X 96%, 2 X 100%, 3 minutes each) and resin embedded with Durcupan resin, which was then hardened overnight at 65 ^{o}C. 70 nm-thick sections were cut and placed on TEM finder grids. The grids and sections were gold-coated prior to NanoSIMS analysis to avoid charging effects.

Cell viability assay and polymer internalization kinetics. Cell viability was assessed using Annexin V-Alexa Fluor 647/DAPI assay *via* flow cytometry. Hela cells were seeded and grown in the same conditions used for fluorescence microscopy analysis. Untreated cells were used as negative control and cells treated with Staurosporine were

used as positive control. To this purpose, 1 µL of 1 mM Staurosporine stock solution was add to each mL of medium and cells were incubated for 24 h. Treated cells were incubated with 0.6 mg/mL ^{19}F-PHPMA-Rhodamine for 24 h, 15 h, 4 h, 2 h, 40 min and 10 min. Cells were gently trypsinized, collected in 10 mL tubes and washed with PBS twice. Negative control cells were kept on ice until analysis. Positive control cells and cells treated with the polymer were re-suspended in 100 µL Annexin buffer (1X) containing 1 µg/mL DAPI at a density of 1 x 10^6 cells/mL. 5 µL of Annexin-V-Alexa Fluor 647 was then added to each tube and cells were incubated at room temperature for 15 minutes. Untreated cells stained only with DAPI and only with Annexin V-Alexa Fluor 647 were also prepared and used as controls. After the incubation period, 400 µL of Annexin buffer was added to each tube and cells were kept in ice until analyzed by flow cytometry. Cells were analyzed using FL 9 channel for DAPI and FL 6 for Alexa Fluor 647. In order to determine polymer internalization kinetics, intracellular Rhodamine was detected using FL 2 channel. Two independent experiments were performed and 10000 events were collected.

CellTrace Violet proliferation assay. CellTrace Violet proliferation assay was used to investigate cell division during the time-course of the experiment. To this purpose, cells were trypsinized and incubated at 37°C for 20 min in 5 mL PBS containing 5 µL CellTrace Violet stock solution in DMSO. After this time, 25 mL medium were added and the cells were incubated for further 5 minutes. Cells were centrifuged, resuspended in fresh medium and seeded. One sample of cells was centrifuged, resuspended in PBS and analyzed by flow cytometry using FL 9 channel for CellTrace Violet detection (Seeding time). After 18 hour, cells were treated with the polymer solution for 24 h, 15 h, 4 h, 40 min and 10 min. For each incubation time, prior to adding the polymer solution, one sample of cells was trypsinized, washed with PBS and analyzed by flow cytometry. At the end of the time course experiment, cells incubated with the polymer solution for the different times were collected, washed with PBS and analyzed by flow cytometry (End time). Comparison between CellTrace Violet-cell fluorescence at the "Seeding time", prior to each polymer addition and at the end of the time-course experiment "End time" allowed the determination of the time-dependent cell division occurring during the experiment.

4.3. Results and Discussion

4.3.1. ^{19}F-PHPMA-Rhodamine design and synthesis

The first step of this work consisted in the design of a HPMA polymer containing two different labels that are suitable for both fluorescence-based studies and NanoSIMS analysis. While Rhodamine Red was chosen as fluorescent dye, fluorine, an element not present in biological environments was selected as NanoSIMS probe. Although the aim of this work is to investigate the intracellular trafficking of PHPMA *via* fluorescence microscopy and to demonstrate the feasibility of using NanoSIMS and TEM to track the internalized polymer, the HPMA polymer containing both fluorine and Rhodamine Red (^{19}F-PHPMA-Rhodamine) was synthesized using an approach that would be suitable for further design of polymer-drug conjugates. Two different aspects were taken into account for the selection of the appropriate approach. First, it has been demonstrated that parameters such as polymer chain size and composition need to be carefully considered while studying polymer internalization and trafficking.[16] Based on these results, the preparation of polymers *via* post-polymerization modification offers several advantages in comparison to direct polymerization of functional monomers. This method allows the preparation of polymers characterized by the same chain length distribution and polydispersity, but different side chain functionalities.[33] Moreover, the side chain functionalities can be randomly distributed along the polymer chains therefore avoiding structural heterogeneities that can lead to different polymer architectures[33] and therefore result in different cellular uptake.[16] The second aspect that was considered for the choice of the synthetic approach is the polymer labelling. Although PHPMA-dye conjugates are generally prepared by conjugating the dye to the polymer side chains,[13,16-18] the use of the polymer end groups for label insertion would offer the opportunity to preserve polymer side chains for further drug conjugation. To this purpose, RAFT polymerization is particularly attractive since it allows the synthesis of polymer possessing functional α-ε end groups, that can be used for direct label insertion or that can be used to introduce functionalities.[34] Post-polymerization modification of these functionalities have been proposed as a way to couple labels to the polymer end groups.[32,34]

Hence, ^{19}F-PHPMA was prepared *via* post-polymerization modification of a poly(pentafluorophenyl methacrylate) (PPFMA) precursor. PPFMA was selected since it can be polymerized by RAFT polymerization and since the post-polymerization

modification with different functional amines has been already investigated.[33,34,35] Fluorine was introduced at the α-end group of the polymer *via* modification of the generally used 4-cyano-4-(phenylcarbonothioylthio)pentanoic acid chain transfer agent (CTA) with trifluoropropylamine (^{19}F-CTA). It has been already demonstrated in the **Chapter 2** of this Thesis that insertion of this fluorine tag on the R group of the CTA does not affect PFMA RAFT polymerization behavior. Further post-polymerization modification of the ω-dithiobenzoate polymer moieties (deriving from the Z CTA group) were used to introduce the Rhodamine Red to allow fluorescence-based intracellular trafficking studies. **Scheme 1** illustrates the different synthetic steps for the synthesis of ^{19}F-PHPMA-Rhodamine. First, PFMA RAFT polymerization in presence of ^{19}F-CTA led to the preparation of the fluorinated PPFMA (^{19}F-PPFMA) as described in **Chapter 2**. ^{19}F-PPFMA was subsequently modified to ^{19}F-PHPMA by reaction of the PFMA side chains with an excess of HPA in presence of triethylamine. Subsequently, the ω-dithiobenzoate polymer end groups, were used to introduce the fluorescent label on the polymer backbone. To this purpose, the dithiobenzoate groups were first reduced in presence of NaBH$_4$ and the generated free thiol moieties were reacted with Rhodamine Red C2 maleimide in presence of TCEP and catalytic amount of DBU. The percentage of Rhodamine end-group was determined by UV measurements, using the calibration curve reported in **Figure S4** and taking into account the ^{19}F-PHPMA polymer molecular weight reported in **Table S1** and it was found to be 79.5 %. The ^{19}F-NMR, as well as the UV-Vis spectra of ^{19}F-PHPMA-Rhodamine are shown in **Figure 1A** and **1B**, respectively.
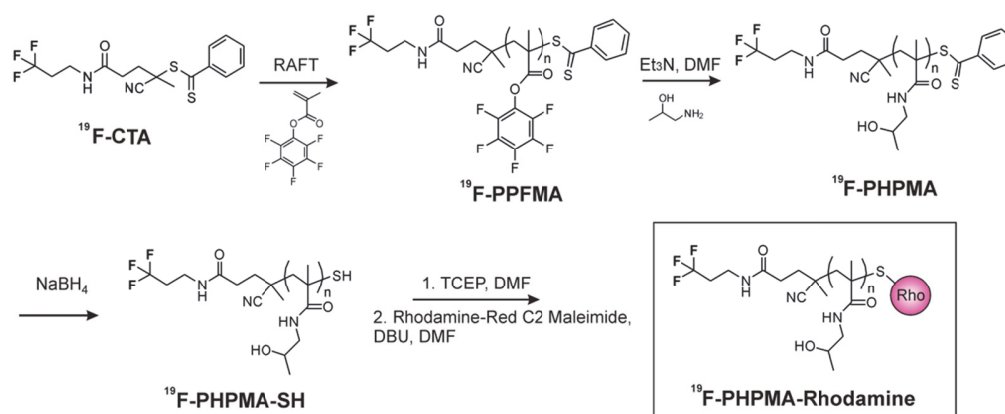
Scheme 1. Synthesis of ^{19}F-PHPMA-Rhodamine.
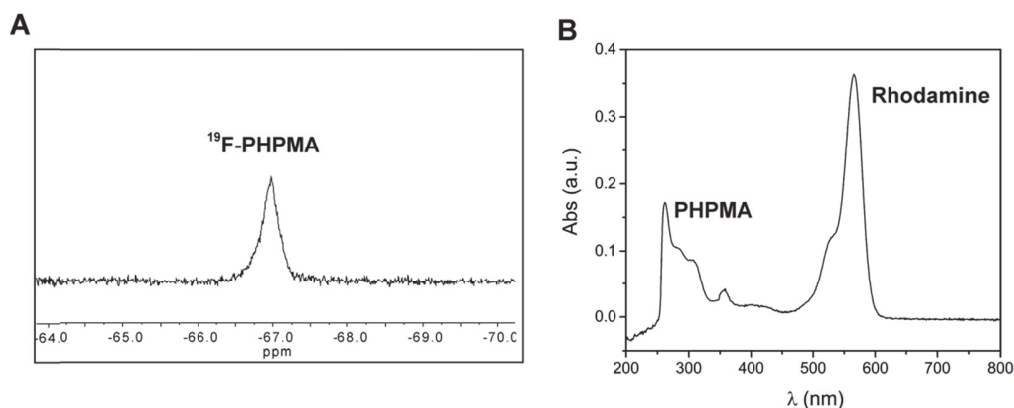
Figure 1. (A)^{19}F-NMR spectra and (B) UV-Vis spectra of ^{19}F-PHPMA-Rhodamine (0.35 mg in 5 mL DMSO).

4.3.2. Cell viability and PHPMA cellular uptake

The fluorescent label introduced in the polymer end group was first used to investigate polymer cellular uptake as a function of time. Hela cells were used as model cell line for this study. In order to assure that the selected polymer concentration (0.6 mg/mL) does not significantly affect cells viability, Annexin V-Alexa Fluor 647/DAPI viability assay was also performed. For this assay cells were treated with the polymer for the selected incubation times (10 min, 40 min, 1 h, 2 h, 4 h, 15 h and 24 h) and incubated prior to flow cytometry analysis with both Annexin V-Alexa Fluor 647 and DAPI, which allow the discrimination between viable, apoptotic and dead cells. While viable cells are stained by none of the two dyes, Annexin V-Alexa Fluor 647 binds to the exposed phospholipids of cells undergoing apoptosis, and DAPI, which is a membrane impermeable DNA binding dye, stains dead cells that have completely lost membrane integrity. The different populations (viable cells, apoptotic cells and dead cells) (**Figure S5**) were determined using control cells stained only with DAPI, only with Annexin V-Alexa Fluor 647 and using control cells treated with the cytotoxic Staurosporine. While the scatter plots of the two independent experiments are reported in Supporting Information in **Figure S5**, the results of two independent experiments are summarized in **Figure 2A** and indicate that viable cell population remained substantially constant over the different incubation times and always above 73 %.
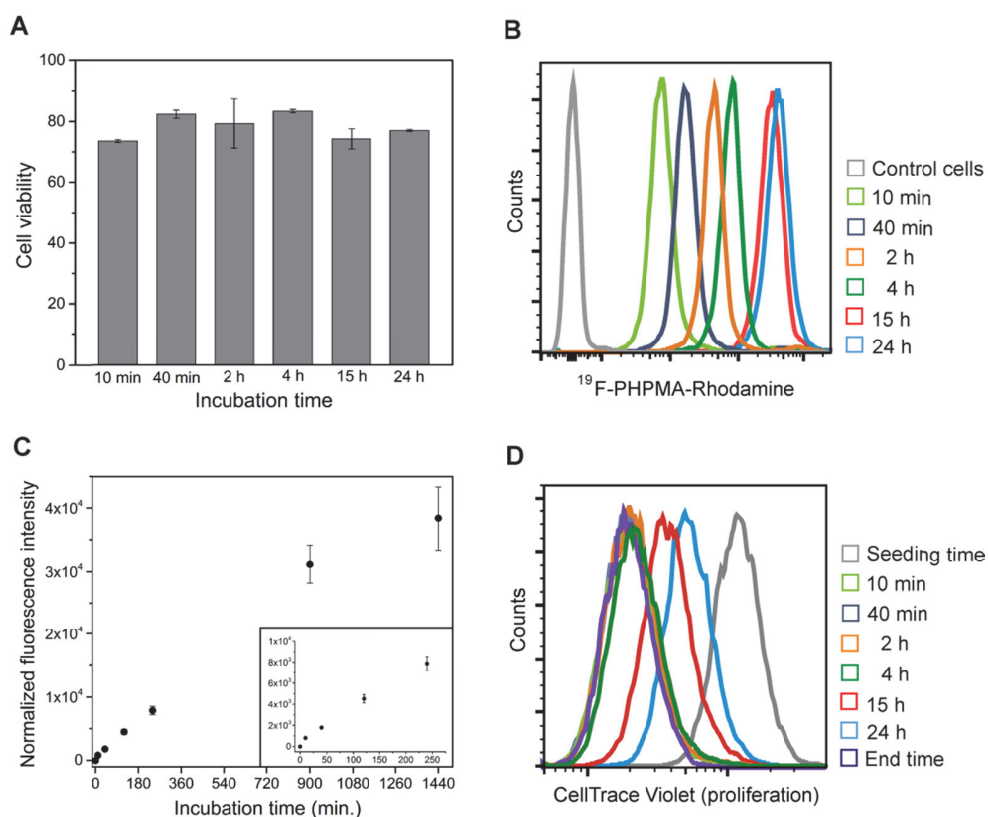
Figure 2. (A) Cell viability after incubation with 0.6 mg/mL ^{19}F-PHPMA-Rhodamine for the different incubation times using Annexin V-Alexa Fluor 647/DAPI assay, as determined by flow cytometry. Results are reported as percentage of viable cell population determined from two independent experiments, error bars represent the standard deviation. (B) Example of cellular uptake of ^{19}F-PHPMA-Rhodamine (0.6 mg/mL) at different incubation times as determined by flow cytometry measurements. (C) ^{19}F-PHPMA-Rhodamine cellular uptake kinetics for the different incubation times (10 min, 40 min, 2 h, 4 h, 15 h, 24 h) as determined by flow cytometry. Results are reported as average geometric mean fluorescence determined from two independent experiments. Error bars represent the standard deviation and geometric mean fluorescence has been normalized to the fluorescence of untreated cells. (D) Shift of CellTrace Violet cell fluorescence deriving from cell division during the time frame of the experiment as determined by flow cytometry. The grey curve represents the initial cell population (Seeding time), while the final population is indicated in violet (End time). The curves labeled with the different time points represent cell fluorescence prior polymer addition for each incubation time.

In the next step, flow cytometry was used to trace the time-dependent polymer uptake. Both concentration-dependent and time-dependent uptake of PHPMA-drug and PHPMA-dye conjugates, as well as PHPMA-derived copolymers have been widely investigated by flow cytometry experiments.[14,16-18] However, cell division during the incubation period was never considered for results interpretation. Cell division has been instead considered for the interpretation of nanoparticles kinetics uptake results.[21,36] Kim *et al*. demonstrated that, especially for long incubation times, cell division can lead to an apparent decrease in polymer uptake.[37] Therefore, the aim of these experiments was to relate the time-dependent polymer uptake to cell division. First, cells were incubated with the polymer for different incubation times and analyzed by flow cytometry to determine time-dependent polymer uptake. Increase in Rhodamine fluorescence over time, as compared to control cells is illustrated in **Figure 2B**, while the result from a duplicate experiment is reported in **Figure S6**. **Figure 2C** summarize the results from these two experiments and represents them as Rhodamine-geometric mean fluorescence intensity (normalized to the geometric mean fluorescence of untreated cells) as a function of time. This plot clearly shows that a prolonged cell exposure to the polymer solution resulted in enhanced polymer uptake. While a rapid fluorescence intensity increase was observed within the first 10 minutes incubation, slower polymer uptake was observed for the subsequent time points and in particular, a consistent decrease in polymer uptake rate was observed between 15 and 24 h incubation. In order to prove that the significant reduced polymer uptake at long incubation time is the result of cell division, a CellTrace violet proliferation assay was performed. CellTrace Violet diffuse into the cells and binds covalently to intracellular amines. Hence, determination of the cell-associated CellTrace Violet fluorescence provides information about cell proliferation. In particular, a decrease in time-dependent fluorescence can be used as an indication of cell division. In order investigate whether cell division occurs during the time frame of the experiment, cells were treated in the same conditions as for the polymer uptake study and flow cytometry was used to detect CellTrace Violet associated fluorescence. **Figure 2D** summarizes the CellTrace Violet assay results, while the complete flow cytometry plots, as well as the correspondent geometric mean fluorescence values, are reported in **Figure S7**. For all experiments, cells were seeded 18 hours before starting the time course polymer incubation. This initial cell population fluorescence is indicated in **Figure 2D** as "Seeding time". Prior polymer addition, for each of the incubation time, one sample of cells was analyzed by flow cytometry in order to determine the cell population fluorescence at the beginning of the time-course experiment. The fluorescence of cells analyzed at the end of

170

the experiment is indicated in **Figure 2D** as "End time". The shift between "Seeding time" and "End Time" fluorescence suggests that during this time frame, the cells underwent at least two division cycles. The geometric mean fluorescence of cells analyzed prior polymer addition for the time points "10 min", "40 min" "2 h" and "4 h" overlaps with that of the cells at the end of the time-course experiment "End time". This result indicates that both cell division cycles occurred prior polymer addition. On the contrary, for the time points "15 h" and "24 h", cell fluorescence values prior polymer addition were found in between the "Seeding time" and "End time" values. This suggests that, in this case, cells underwent at least one division cycle during the polymer incubation period. These results corroborate the kinetics uptake data and suggest that, in presence of continuous source of polymer and at longer incubation time, at least 15 hours in this particular case, the competition between cell division and polymer uptake can result in the establishment of an apparent polymer uptake saturation.

4.3.3. Intracellular trafficking studies of PHPMA *via* confocal microscopy

After determining time-dependent polymer uptake and cell division by flow cytometry, the effect of time-dependent co-localization with the endolysosomal vesicles was investigated. In particular, co-localization studies between Rhodamine-labeled HPMA polymer and early endosomes (EE, initial endocytosis step) and lysosomes (L, final endocytosis step), were performed in order to investigate the endocytosis process time-frame. To this purpose, Hela cells expressing GFP either in the early endosomes or in the lysosomes, were incubated with the polymer for 15 h, 4 h, 2 h, 40 min and 10 min, fixed and imaged by confocal microscopy. Results of co-localization studies after 24 h polymer incubation are not reported since this long incubation period did not lead to any additional information. Representative pictures of observations at 10 min and 4 h polymer incubation for both cells expressing GFP in the EE and L are shown in **Figure 3**. Images of the different time points for one experiment are reported in Supporting Information in **Figure S8** and **Figure S9** for EE and L, respectively. Two different image analysis were performed in order to investigate the dynamic of the endocytosis process and to determine the time dependent polymer co-localization with both endosomal and lysosomal vesicles.

Early Endosomes (EE)
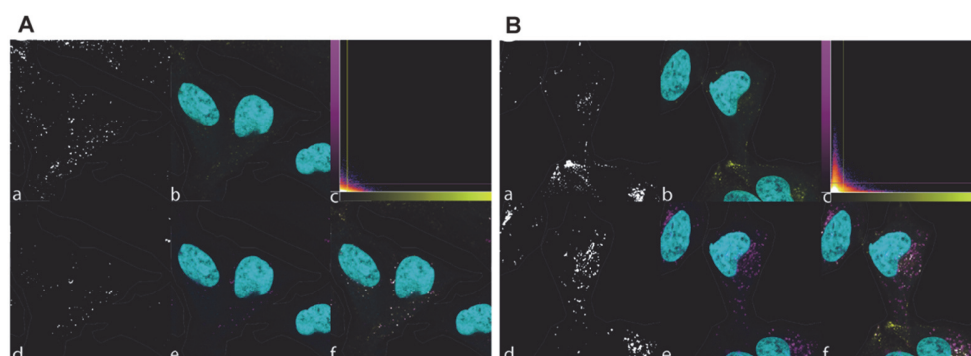
Lysosomes (L)
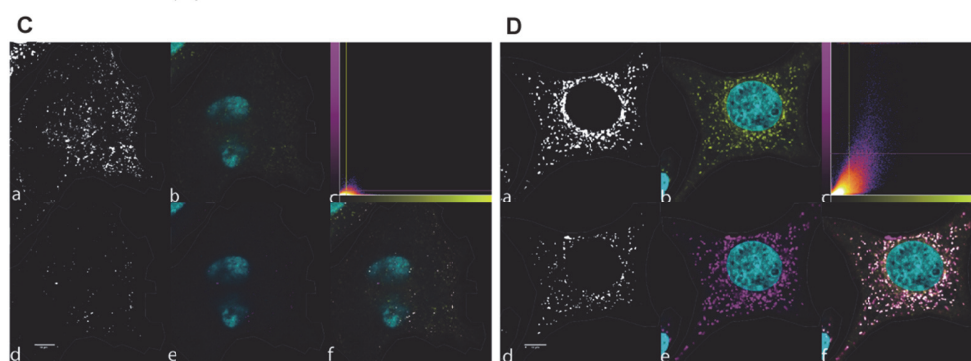
Figure 3. Co-localization studies of ^{19}F-PHPMA-Rhodamine, in magenta, with (A and B) early endosomes expressing GFP and (C and D) lysosomes expressing GFP, both indicated in yellow. Representative pictures of observations at (A and C) 10 min and (B and D) 4 h ^{19}F-PHPMA-Rhodamine incubation (0.6 mg/mL) show the threshold images (a and d), corresponding to endosomal or lysosomal vesicles (b, in yellow) and polymer (e, in magenta), represented together with the DAPI channel (b, e and f, in cyan). The merged channels with the "co-localized" pixel (f), as well as the fluorogram (c) are also reported. The contours of the manually drawn ROIs are shown as a white line.

The first analysis investigated the change in area ratio between endolysosomal vesicles (GFP, Channel 1) or Rhodamine (^{19}F-PHPMA-Rhodamine, Channel 2), with respect to the area of the Regions of Interest (ROIs). **Figure 4** illustrates the area ratio plots. The "Area Threshold in Channel 1 (GFP, EE or L) normalized by the area of the ROI" is shown on the x axis, while the "Area Threshold in Channel 2 (Rhodamine, ^{19}F-PHPMA-Rhodamine) normalized by the Area of the ROI" is shown on the y axis. While panels **A** and **C** illustrate the area subdivision of the plots, panels **B** and **D** represents the results

obtained for the different incubation times, each dot corresponds to an analyzed image from three independent experiments.
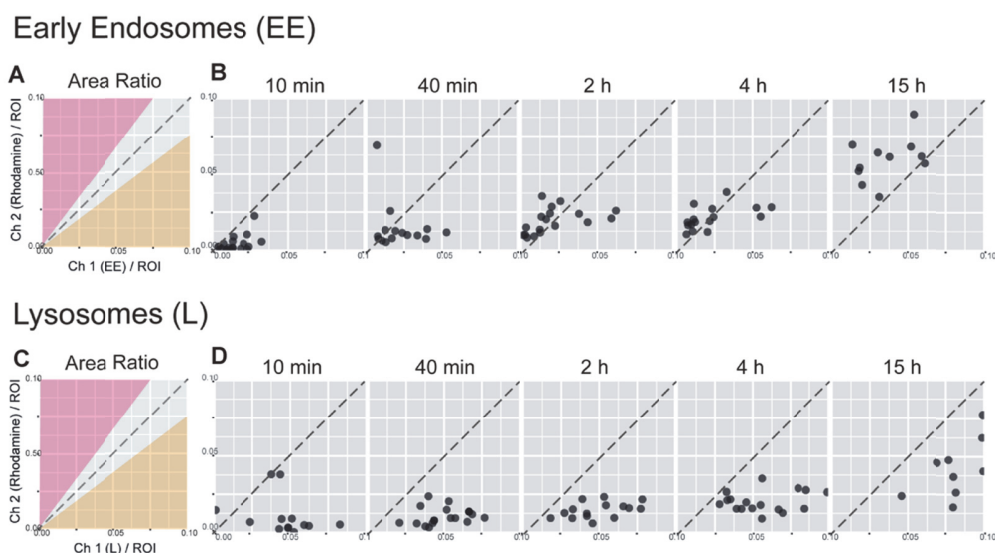
Figure 4. Area Ratio plots for cells with (A, B) Early Endosomes (EE) and (C, D) Lysosomes (L) expressing GFP. "Area Threshold in Channel 2 (Ch2, Rhodamine, ^{19}F-PHPMA-Rhodamine) normalized by the Area of the ROI" is reported on the y axis, while the "Area Threshold in Channel 1 (Ch1, GFP, EE or L) normalized by the Area of the ROI" is shown on the x axis. (A and C) Area Ratio plot subdivision indicating: higher Ch2 (Rhodamine) Area Ratio in magenta, higher Ch1 (GFP, EE or L) Area Ratio in yellow or a comparable Area Ratio between the two channels, in grey. (B and D) Each dot corresponds to the Area Ratio determined for an analyzed image from three independent experiments.

Image analysis revealed that for both early endosomes (**Figure 4B**) and lysosomes (**Figure 4D**), the area of Ch1 (GFP, EE or L) was found to slightly increase over time especially at the latest time point "15 h". This effect was more pronounced in the case of lysosomal staining (**Figure 4D**). Stated that this effect does not derive from the presence of apoptotic cells, as demonstrated from the viability assay, which might decrease the ROIs area due to cells shrinkage,[38] this effect can be explained as the result of increase polymer internalization over incubation time. Prolonged cell exposure to the polymer-containing medium can result in enhanced endolysosomal vesicles formation and

lysosomal vesicles enlargement.[39] This effect was confirmed by the transmission electron microscopy (TEM) image of the cells. **Figure S10** shows representative images of control cells as well as cells treated with the polymer for 4 h as well as 15 h. It was found that cells exposed to the polymer solution resulted in higher amount of lysosomal vesicles as compared to control cells, as indicated by the numerous dark electron rich vesicles observed. Area ratio analysis revealed for both endosomes and lysosomes co-localization experiments a substantial Ch2 (Rhodamine, ^{19}F-PHPMA-Rhodamine) area ratio increase over incubation time. **Figure 4B** and **4D** indicate that more and more polymer enters the cells over the investigated time frame, as already observed by flow cytometry analysis.

The second analysis performed aimed to estimate the co-localization between ^{19}F-PHPMA-Rhodamine and endolysosomal vesicles (EE and L). To this purpose, Mander's coefficients were determined. These coefficients are proportional to the amount of fluorescence of the co-localizing pixels in each channel. Values ranging from 0 to 1 express the fraction of intensity in a channel that is located in pixels where there is above zero (or threshold) intensity in the other channel.[26] Hence, in this particular case, for Ch1 (GFP, EE or L) and for Ch2 (Rhodamine, ^{19}F-PHPMA-Rhodamine), M1 and M2, respectively, are expressed as shown in Equations (1) and (2).[26]

$$M_1 = \frac{\sum_i GFP_{i,coloc}}{\sum GFP_i} \qquad\qquad M_2 = \frac{\sum_i Rho_{i,coloc}}{\sum Rho_i} \qquad\qquad (1, 2)$$

The obtained Mander's coefficient plots are shown in **Figure 5**. In particular, "Mander's Coefficient of Channel 1" (M1, GFP, EE or L) is shown on the x axis, while the "Mander's Coefficient of Channel 2" (M2, Rhodamine, ^{19}F-PHPMA-Rhodamine) is shown on the y axis. While panels **A** and **C** illustrate the area subdivision of the plots, panels **B** and **D** represent the results obtained for the different incubation times. Each dot corresponds to one analyzed image deriving from three independent experiments. **Figure 5B** illustrates the Mander's coefficients determined for images of cells expressing the endosomal GFP. At the earliest time point "10 min", the found M1 values are very low (all below 0.25, mostly below 0.125), suggesting little co-localization of Ch1 intensities (GFP, EE) with the Ch2 (Rhodamine, ^{19}F-PHPMA-Rhodamine). On the other side, higher M2 values were observed, variable from 0 to 1, suggesting that some cells showed little, while other high, co-localization of Ch2 (Rhodamine, ^{19}F-PHPMA-Rhodamine) intensities with Ch1 (GFP, EE). These results suggests that, at the earliest time point, the

174

polymer already entered some of the early endosomes, but just a few vesicles are occupied (M1 values are low). At the time point "40 min" the M1 values shift slightly to the right while the M2 decreases. At the time point "2 h" the M2 values further decreases. Time points "4 h" and "15 h" shows a more variable cell population but always characterized by higher M1 values compared to M2. Hence, after the first time point, while the M1 values slightly increase, suggesting that more EE are involved in the endocytosis process, the M2 values decreases, indicating that more and more of the internalized polymer is not localized inside the endosomal vesicles. This result, together with the increase of the Ch2 area ratio over time (**Figure 4B**) suggests that the internalized polymer chains, firstly detected in the endosomal vesicles, continue their route to another compartment, most probably the cell lysosomes. In order to prove this hypothesis, the same analysis was performed for lysosomal co-localization. Mander's coefficients analysis (**Figure 5D**) revealed that at the earliest time point "10 min", the M1 values are very low (mostly below 0.25), suggesting little co-localization of Ch1 intensities with the Ch2. On the other side, the M2 values are highly variable from 0 to 1. These results suggest that even at the earliest time point, a few polymer chains have already reached some cell's lysosomes (variable M2 values), but just a few of the lysosomes are involved in the process (M1 values are low). At the time point "40 min", M1 and M2 increase and values are more homogenous. This suggests that more polymer chains trafficked to the lysosomes, and therefore more lysosomes have been being occupied. At the following time points "2 h" to "15 h", M1 values increase gradually, suggesting that more and more lysosomes are taking part to the process.
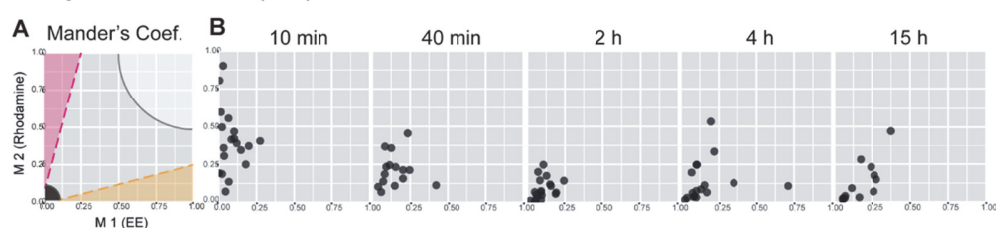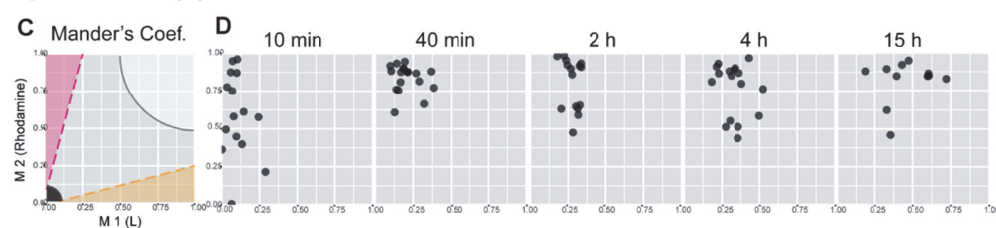
Figure 5. Mander's coefficients plots for cells with (A, B) Early Endosomes (EE) and (C, D) Lysosomes (L) expressing GFP. The "Mander's Coefficient of Channel 2" (M2, Rhodamine, ^{19}F-PHPMA-Rhodamine) is reported on the y axis, while the "Mander's Coefficient of Channel 1" (M1, GFP, EE or L) is reported on the x axis. (A and C) Plot subdivision according the co-localization of channel intensities. The magenta area indicate that most Rhodamine intensities co-localize with EE or L intensities, the yellow area indicate that most GFP intensities (EE or L) co-localize with Rhodamine intensities, both Rhodamine and GFP intensities co-localize with each other (white) and absence of co-localization is defined by the black area. (B and D) Each dot corresponds to the M1 and M2 determined for an analyzed image from three independent experiments.

Fluorescence microscopy studies confirmed the rapid and continuous polymer uptake previously observed *via* flow cytometry experiments. Moreover, it was also observed that, already in the first 10 minutes incubation, some polymer chains were already detected in the cell lysosomes. After 40 min incubation the polymer was detected in both both EE and L vesicles and prolonged incubation resulted in continue polymer internalization *via* the early endocytic vesicles. However, the internalized material was found to only transit through these vesicles to finally accumulate in the lysosomes. Co-localization studies revealed that at least 2 h cell exposure to the polymer allows dominant polymer localization in the cell lysosomes and longer polymer incubation time resulted in higher amount of lysosomal vesicles involved in the process. As already anticipated, understanding the time-dependent accumulation of the polymer in the cell

lysosomes is particularly relevant since the environmental parameters that characterize these vesicles can be exploited to trigger intracellular drug release from PHPMA carriers.[7]

4.3.4. Subcellular polymer localization *via* NanoSIMS and TEM

Although flow cytometry analysis and confocal fluorescence microscopy can estimate polymer uptake and its transit through the endolysosomal pathway, the establishments of new approaches to monitor polymer intracellular trafficking that also offer the possibility to minimize polymer labelling and give quantitative information is of great interest to fully characterize these processes. The last part of this work aims to demonstrate that the insertion of fluorine on the polymer end group allow intracellular polymer detection by NanoSIMS. Further combination with transmission electron microscopy (TEM) was explored as a method to localize the polymer in the endocytic pathway.

For this proof-of-concept study, samples of cells treated with the polymer for 4 and 15 h, which showed a preponderant polymer co-localization with the cell lysosomes were selected. Untreated cells were also used as a control. After confocal microscopy the samples were embedded in resin, cut as 70 nm sections and first imaged by TEM. Representative images are reported in **Figure S10**. As already anticipated, cells exposed to the polymer solution resulted in higher amount of lysosomal vesicles as compared to control cells. Next, samples were analysed by NanoSIMS. Example of secondary ion maps of control cells, as well as cells incubated with the polymer for 4 h and 15 h are shown in **Figure 6** and **Figure S11**. These results suggest that fluorine-containing polymers can be detected as localized signals in the cell cytoplasm and that longer polymer incubation time result in more punctuate cytoplasmic fluorine signals.
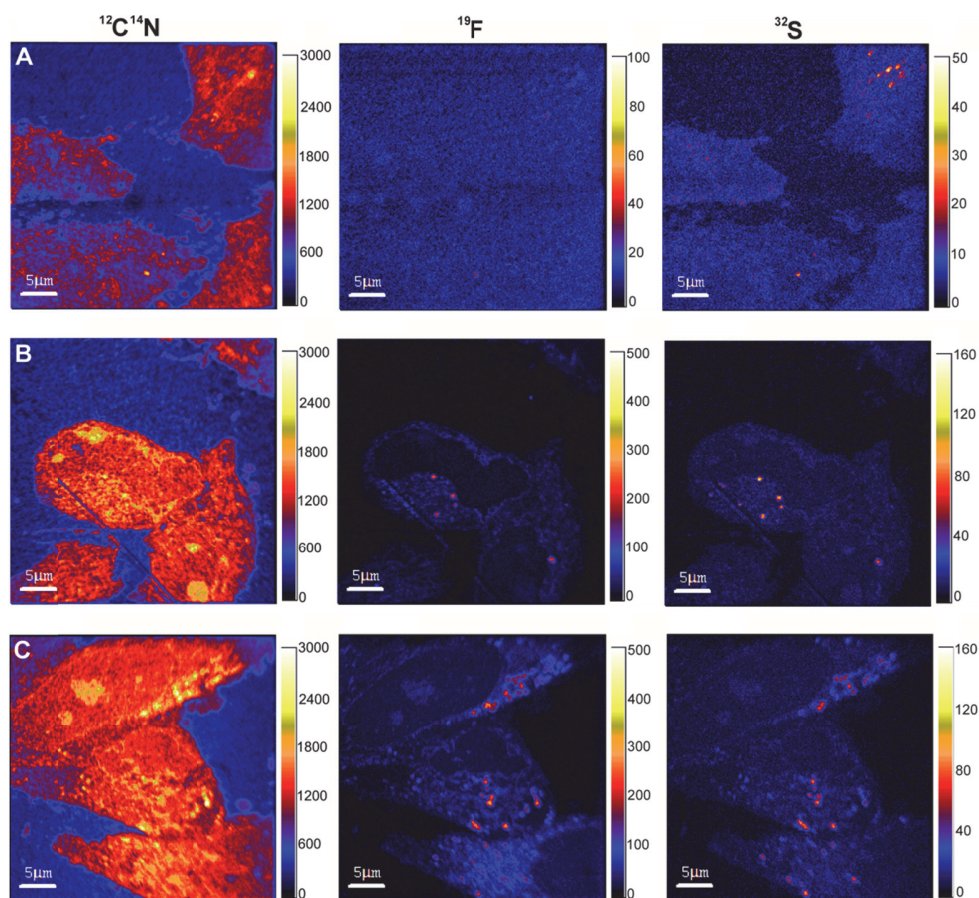
Figure 6. Secondary ion maps of $^{14}N^{12}C^-$, $^{19}F^-$ and $^{32}S^-$ in (A) untreated Hela cells (control cells) and in Hela cells treated with 0.6 mg/mL ^{19}F-PHPMA-Rhodamine for (B) 4 hours and (C) 15 hours.

Interestingly, it was also found that the cytoplasmic fluorine signal strongly correlates with sulphur. Localized sulphur in the cell cytoplasm has been previously observed by NanoSIMS and it has been attributed to sulphur-rich lysosomal vesicles.[40,] This result indicates that NanoSIMS could be used for co-localization studies of polymers with lysosomal vesicles without the need for other imaging techniques. However, combination with TEM analysis would be a very interesting approach to visualize other cellular compartments, for instance, when polymer-mediated delivery need to be investigated. Hence, in a second step, combination of TEM and NanoSIMS was used to confirm the hypothesized co-localization between polymer and lysosomal vesicles and to demonstrate the potential of this method. To this purpose, selected cells were imaged first by TEM and subsequently analysed by NanoSIMS. **Figure 7** illustrates an example of correlation

between TEM and both ^{19}F and ^{32}S secondary ion images. As expected, fluorine signals correlating with sulphur were co-localized with electron dense lysosomal vesicles.
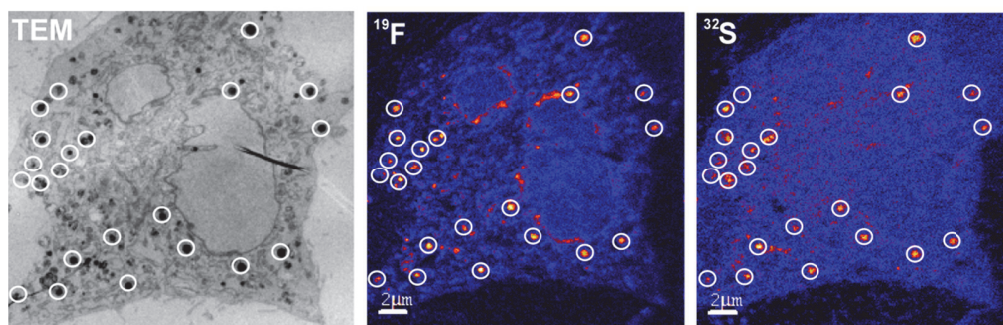
Figure 7. Representative TEM image and the corresponding ^{19}F and ^{32}S secondary ion maps obtained after 15 h incubation of Hela cells with 0.6 mg/mL ^{19}F-PHPMA-Rhodamine. White circles indicate some of the observed correlations between cell vesicles, ^{19}F^{-} and ^{32}S^{-} signals, as an example.

This result confirms the potential of NanoSIMS to monitor polymer accumulation in cell lysosomes and suggest that correlation with TEM images is a powerful approach to visualize intracellular cargo distribution. However, it should be also mentioned that repeated NanoSIMS analysis of the same sample sections resulted in a substantial decrease in fluorine signal over time. We attributed this effect to the high vacuum treatments during TEM and NanoSIMS analysis as well as to the electron beam used during TEM imaging.

4.4.   Conclusions

This work described the design of a dual-labeled PHPMA conjugate containing both a fluorescent and a fluorinated label at the end groups. These labels allowed the study of polymer uptake and intracellular trafficking by fluorescence-based techniques as well as the investigation of new imaging techniques to monitor these processes.

The first part of this work focused on polymer uptake studies by flow cytometry and highlighted the influence of cell division on the polymer uptake kinetics. PHPMA internalization rate was found to be very fast in the first 10 minutes incubation. Longer polymer incubation times led instead to a slower uptake rate and an apparent saturation was observed after 15 hour incubation. Cell proliferation assay suggested that this effect does not derive from a reduced uptake rate but is a consequence of cell division which causes the division of the internalized material between daughter cells.

In a second step, confocal fluorescence microscopy allowed co-localization studies between the internalized polymer and both early endosomal and lysosomal vesicles. Analysis of the area ratio of the polymer-associated Rhodamine signal, as compared to the selected ROIs confirmed an increase polymer uptake over time. Mander's coefficients were calculated and used to estimate the association of the polymer with endosomes and lysosomes expressing GFP. Co-localization studies suggested that the endocytosis process occur very rapidly upon cell incubation with the polymer. While the first 10 minutes incubation resulted in the highest endosomal co-localization, increased polymer incubation resulted in a significant reduction of polymer co-localization with these vesicles. On the contrary, lower correlation with lysosomal vesicles was observed in the first 10 minutes incubation, as compared to longer incubation times. Cell exposure to the polymer solution for at least 2 hours led to almost complete co-localization of the internalized polymer with the lysosomes. Longer cell exposure to the polymer solution resulted in an enhanced correlation between lysosomal vesicles and fluorescent polymer indicating that over time more and more lysosomal vesicles take part to the process.

The last part of this work explored the use of NanoSIMS to map the internalized polymer. First, the fluorine label on the polymer could be detected as subcellular punctuate cytoplasmic fluorine signal. Second, a strong correlation between fluorine and sulfur was observed. Cell imaging *via* TEM prior NanoSIMS analysis confirmed the correlation between both the punctuate sulfur and fluorine signals with electron rich lysosomal vesicles. Although further studies are required, this proof-of-concept study suggests that while NanoSIMS analysis can be used to localize polymer in sulfur rich lysosomes, the combination with TEM is a very promising method to simultaneously map subcellular distribution of internalized polymer in several cell compartments.

Both the optimization of fluorescence-based methods as well as the establishment of new techniques to monitor the subcellular fate of polymer carriers is fundamental for the development of more advance drug delivery systems.

4.5.   References

(1)   Duncan, R., *Nat. Rev. Cancer* **2006**, *6*, 688.

(2)   Wang, A. Z.; Langer, R.; Farokhzad, O. C., *Annu. Rev. Med.* **2012**, *63*, 185.

(3)   Maeda, H.; Nakamura, H.; Fang, J., *Adv. Drug. Deliver. Rev.* **2013**, *65*, 71.

(4)   Akinc, A.; Battaglia, G., *Csh Perspect. Biol.* **2013**, *5*.

(5)   Duncan, R.; Richardson, S. C. W., *Mol. Pharm.* **2012**, *9*, 2380.

(6)   Gruenberg, J., *Nat. Rev. Mol. Cell. Biol.* **2001**, *2*, 721.

(7)   Mura, S.; Nicolas, J.; Couvreur, P., *Nat. Mater.* **2013**, *12*, 991.

(8)   Kopecek, J.; Kopeckova, P., *Adv. Drug. Deliver. Rev.* **2010**, *62*, 122.

(9)   Rihova, B.; Bilej, M.; Vetvicka, V.; Ulbrich, K.; Strohalm, J.; Kopecek, J.; Duncan, R., *Biomaterials* **1989**, *10*, 335.

(10)   Duncan, R.; Kopeckovarejmanova, P.; Strohalm, J.; Hume, I.; Cable, H. C.; Pohl, J.; Lloyd, J. B.; Kopecek, J., *Brit. J. Cancer* **1987**, *55*, 165.

(11)   Lu, Z. R., *Adv. Drug. Deliver. Rev.* **2010**, *62*, 246.

(12)   Jensen, K. D.; Kopeckova, P.; Bridge, J. H. B.; Kopecek, J., *Aaps Pharmsci.* **2001**, *3*.

(13)   Omelyanenko, V.; Gentry, C.; Kopeckova, P.; Kopecek, J., *Int. J. Cancer* **1998**, *75*, 600.

(14)   Seib, F. P.; Jones, A. T.; Duncan, R., *J. Drug Target.* **2006**, *14*, 375.

(15)   Omelyanenko, V.; Kopeckova, P.; Gentry, C.; Kopecek, J., *J. Control. Release* **1998**, *53*, 25.

(16)   Barz, M.; Luxenhofer, R.; Zentel, R.; Kabanov, A. V., *Biomaterials* **2009**, *30*, 5682.

(17)   Liu, J. H.; Bauer, H.; Callahan, J.; Kopeckova, P.; Pan, H. Z.; Kopecek, J., *J. Control. Release* **2010**, *143*, 71.

(18)   Liu, J. H.; Kopeckova, P.; Buhler, P.; Wolf, P.; Pan, H. Z.; Bauer, H.; Elsasser-Beile, U.; Kopecek, J., *Mol. Pharm.* **2009**, *6*, 959.

(19)   Lu, Z. R.; Kopeckova, P.; Kopecek, J., *Nat. Biotechnol.* **1999**, *17*, 1101.

(20)   Richardson, S. C. W.; Wallom, K. L.; Ferguson, E. L.; Deacon, S. P. E.; Davies, M. W.; Powell, A. J.; Piper, R. C.; Duncan, R., *J. Control. Release* **2008**, *127*, 1.

(21)   Salvati, A.; Aberg, C.; dos Santos, T.; Varela, J.; Pinto, P.; Lynch, I.; Dawson, K. A., *Nanomed.-Nanotechnol.* **2011**, *7*, 818.

(22)   Maity, A. R.; Stepensky, D., *Mol. Pharm.* **2016**, *13*, 1.

(23)   Ostrowski, A.; Nordmeyer, D.; Boreham, A.; Holzhausen, C.; Mundhenk, L.; Graf, C.; Meinke, M. C.; Vogt, A.; Hadam, S.; Lademann, J.; Ruhl, E.; Alexiev, U.; Gruber, A. D., *Beilstein J. Nanotech.* **2015**, *6*, 263.

(24)   Hoppe, P.; Cohen, S.; Meibom, A., *Geostand. Geoanal. Res.* **2013**, *37*, 111.

(25)   Proetto, M. T.; Anderton, C. R.; Hu, D.; Szymanski, C. J.; Zhu, Z.; Patterson, J. P.; Kammeyer, J. K.; Nilewski, L. G.; Rush, A. M.; Bell, N. C.; Evans, J. E.; Orr, G.; Howell, S. B.; Gianneschi, N. C., *ACS nano* **2016**, *10*, 4046.

(26)   Manders, E. M. M.; Verbeek, F. J.; Aten, J. A., *J. Microsc-Oxford* **1993**, *169*, 375.

(27)   Tsai, W. H., *Comput. Vision Graph.* **1985**, *29*, 377.

(28)   Ridler, T. W.; Calvard, S., *Ieee T. Syst. Man Cyb.* **1978**, *8*, 630.

(29)   Schindelin, J.; Arganda-Carreras, I.; Frise, E.; Kaynig, V.; Longair, M.; Pietzsch, T.; Preibisch, S.; Rueden, C.; Saalfeld, S.; Schmid, B.; Tinevez, J. Y.; White, D. J.; Hartenstein, V.; Eliceiri, K.; Tomancak, P.; Cardona, A., *Nat. Methods* **2012**, *9*, 676.

(30)   Bolte, S.; Cordelieres, F. P., *J. Microsc-Oxford* **2006**, *224*, 213.

(31)   Mutterer, J.; Custom toolbars and mini applications with Action Bar, **2016**.

(32)   Scales, C. W.; Convertine, A. J.; McCormick, C. L., *Biomacromolecules* **2006**, *7*, 1389.

(33)   Gibson, M. I.; Frohlich, E.; Klok, H. A., *J. Polym. Sci., Part A: Polym. Chem.* **2009**, *47*, 4332.

(34)   Boyer, C.; Bulmus, V.; Davis, T. P.; Ladmiral, V.; Liu, J. Q.; Perrier, S., *Chem. Rev.* **2009**, *109*, 5402.

(35)   Nuhn, L.; Barz, M.; Zentel, R., *Macromol. Biosci.* **2014**, *14*, 607.

(36)   Torrano, A. A.; Brauchle, C., *Beilstein J. Nanotech.* **2014**, *5*, 1616.

(37)   Kim, J. A.; Aberg, C.; Salvati, A.; Dawson, K. A., *Nat. Nanotechnol.* **2012**, *7*, 62.

(38)   Elmore, S., *Toxicol Pathol* **2007**, *35*, 495.

(39)   Appelqvist, H.; Waster, P.; Kagedal, K.; Ollinger, K., *J. Mol. Cell Biol.* **2013**, *5*, 214.

(40)   Legin, A. A.; Schintlmeister, A.; Jakupec, M. A.; Galanski, M.; Lichtscheidl, I.; Wagner, M.; Keppler, B. K., *Chem. Sci.* **2014**, *5*, 3135.

4.6.   Supporting information

Table S1. Molecular weight and polydispersity of ^{19}F-PPFMA and ^{19}F-PHPMA.

Polymer	$M_n^{TH,a}$ (g/mol)	$M_n^{NMR,b}$ (g/mol)	$M_n^{SEC,c}$ (g/mol)	M_n^d (g/mol)	PDI (-)
^{19}F-PPFMA	21180	32976	30225	-	1.4
^{19}F-PHPMA	-	-	-	17151	-

^{a} Theoretical number-average molecular weight (M_n^{TH}) calculated from the conversion determined by ^{19}F-NMR of the crude product.

^{b} Number-average molecular weight (M_n) calculated from ^{19}F-NMR of the purified product.

^{c} Conventional calibration using polystyrene (PS) standards.

^{d} Number-average molecular weight (M_n) calculated from the ^{19}F-PPFMA M_n determined by SEC.
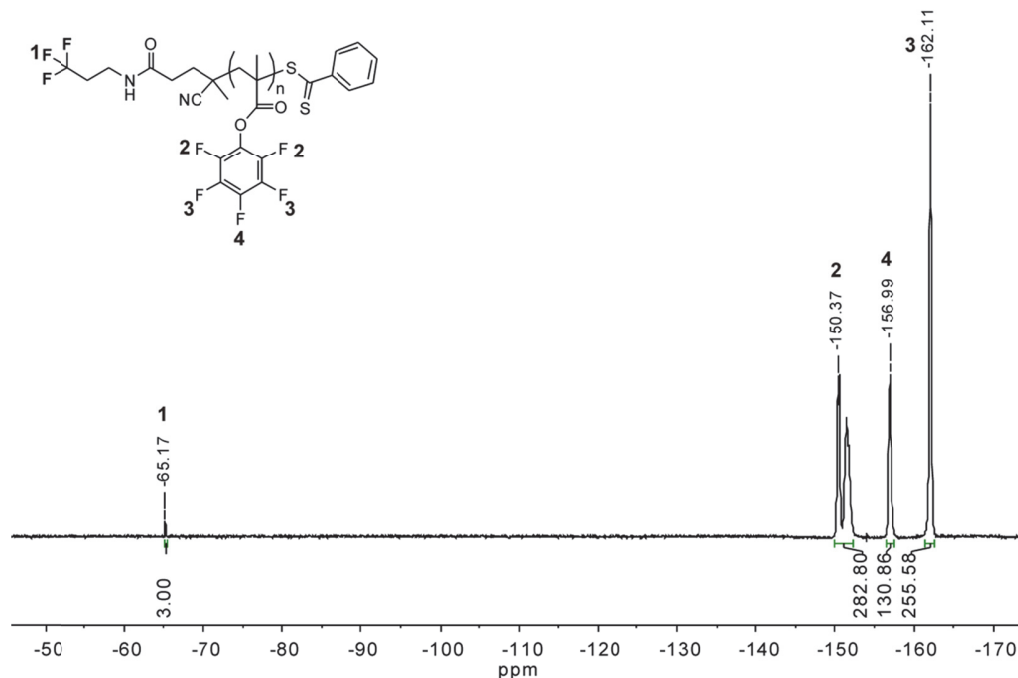
Figure S1. ^{19}F-NMR spectrum of ^{19}F-PPFMA in CDCl$_3$.
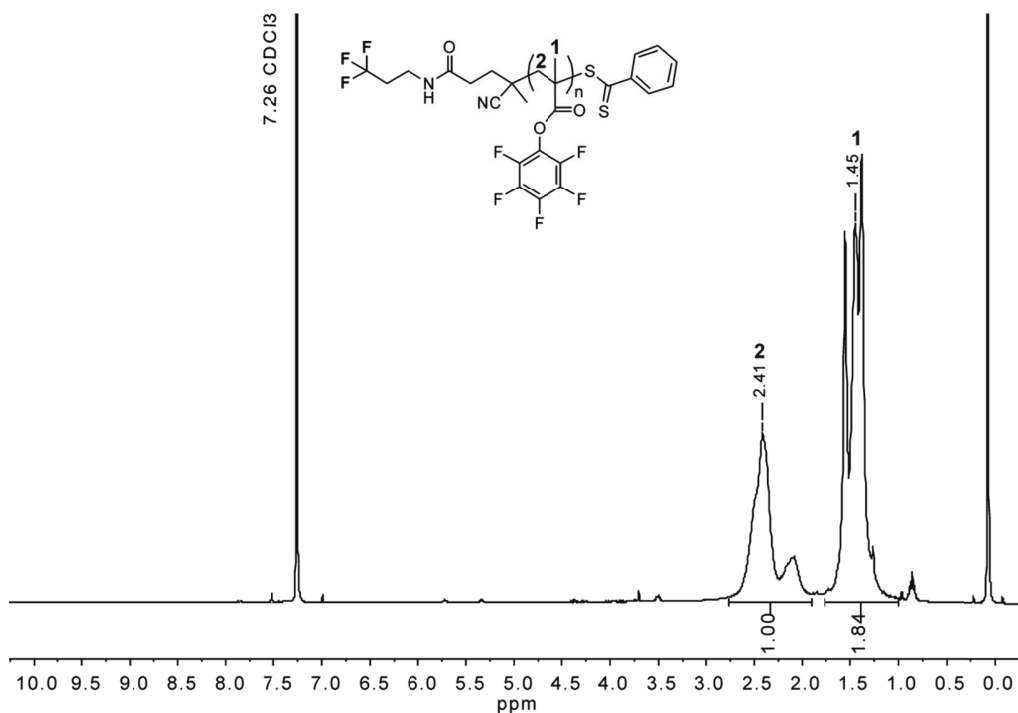
Figure S2. ^{1}H-NMR spectrum of ^{19}F-PPFMA in CDCl[3].
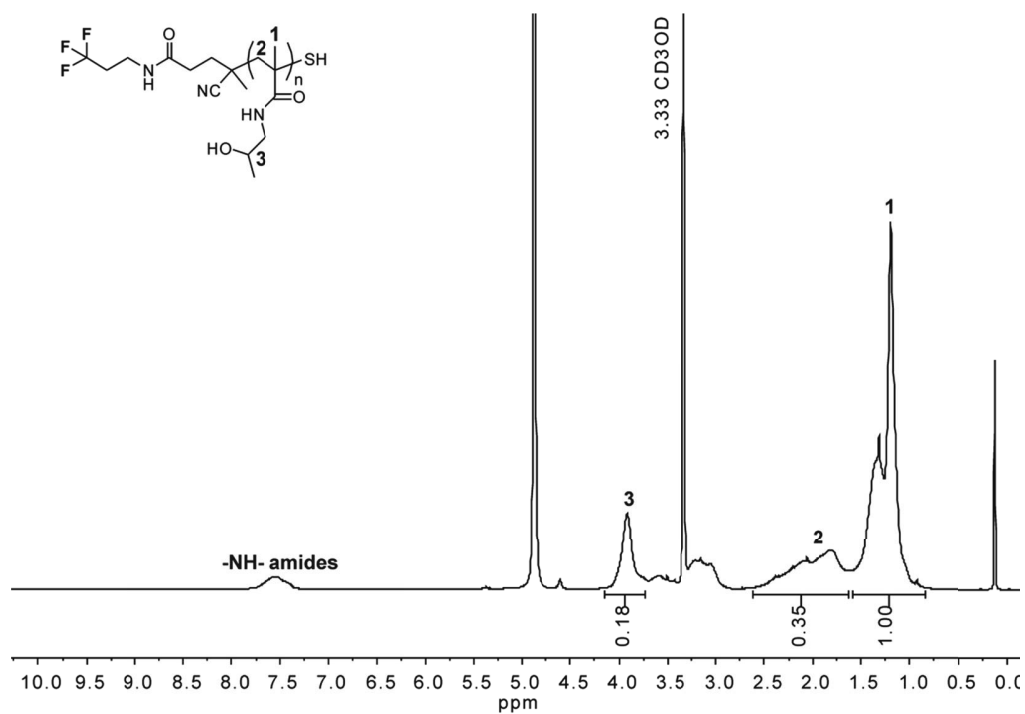
Figure S3. ^{1}H-NMR spectrum of ^{19}F-PHPMA in CD[3]OD.
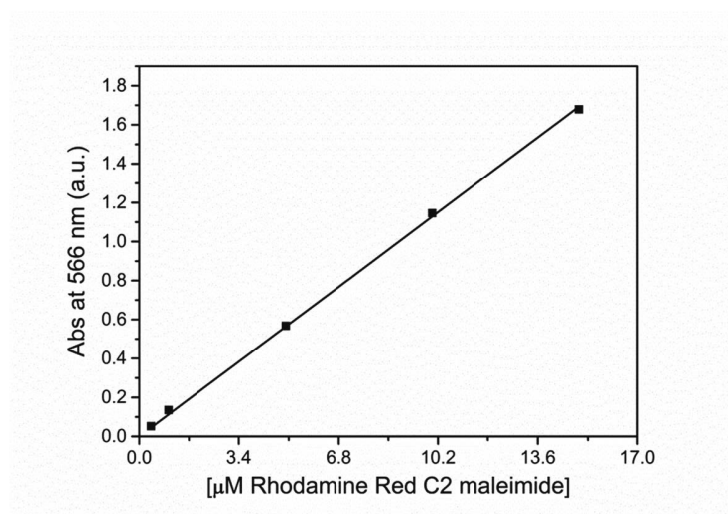
Figure S4. Calibration curve of Rhodamine Red C2 maleimide (ε:112890 M^{-1} cm^{-1}; Solvent DMSO, λ=566 nm).
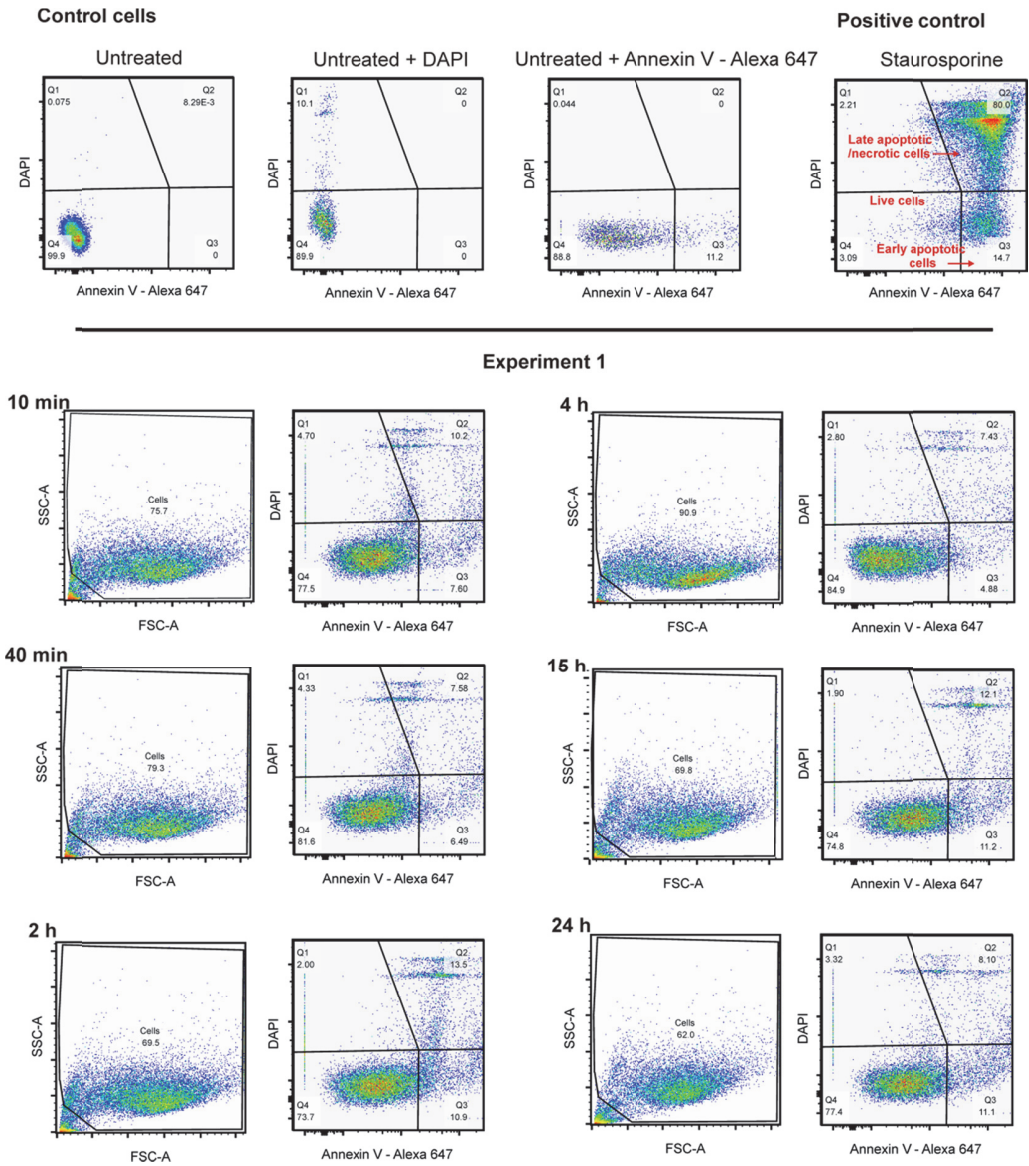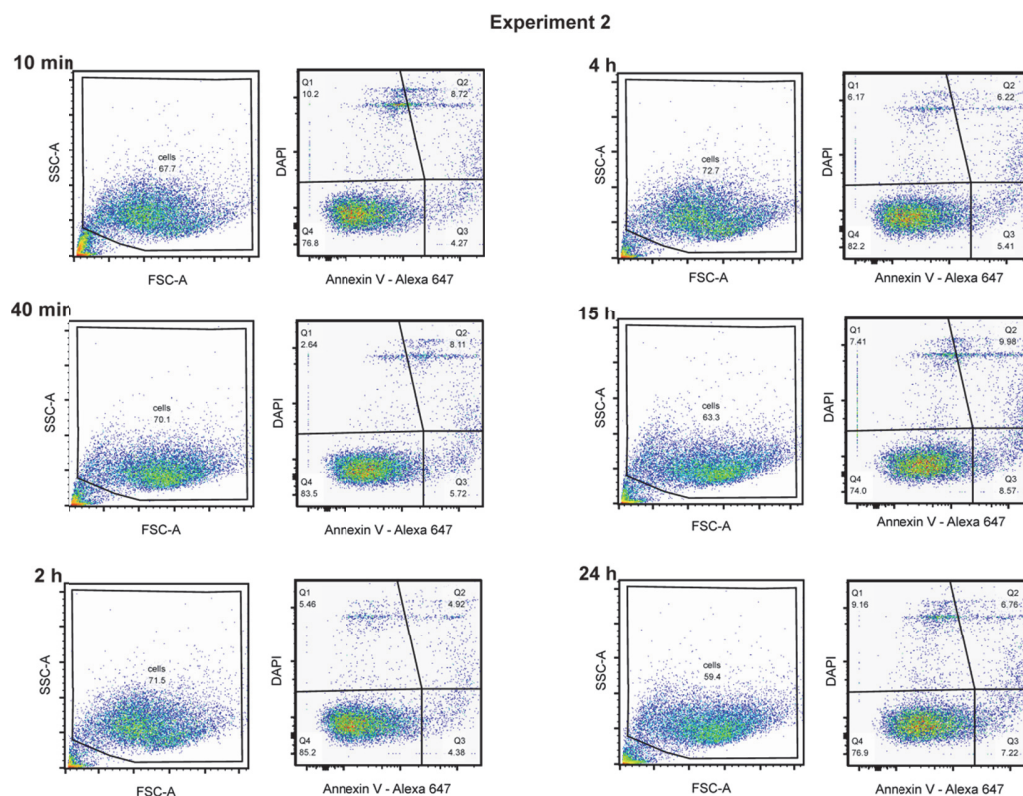
Figure S5. Cell viability after incubation with 0.6 mg/mL ^{19}F-PHPMA-Rhodamine for the different incubation times as determined by flow cytometry using Annexin V-Alexa Fluor 647/DAPI assay. Two independent experiments are reported. Untreated cells (negative control), untreated cells stained only with Annexin V-Alexa Fluor 647 and only with DAPI, as well as cells treated with Staurosporine (positive control) were used to define the different cell populations. Q2,3,4 represents the geometric mean fluorescence determined for the three different cell populations (late apoptotic/necrotic cells, early apoptotic cells and live cells).
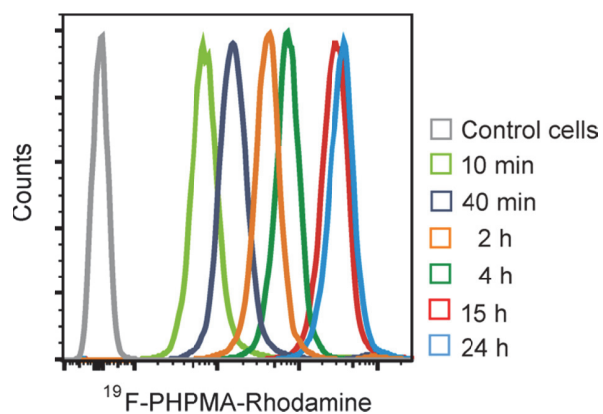
Figure S6. ^{19}F-PHPMA-Rhodamine uptake in Hela cells at different incubation times (10 min, 40 min, 2 h, 4 h, 15 h, 24 h) determined by flow cytometry measurements.
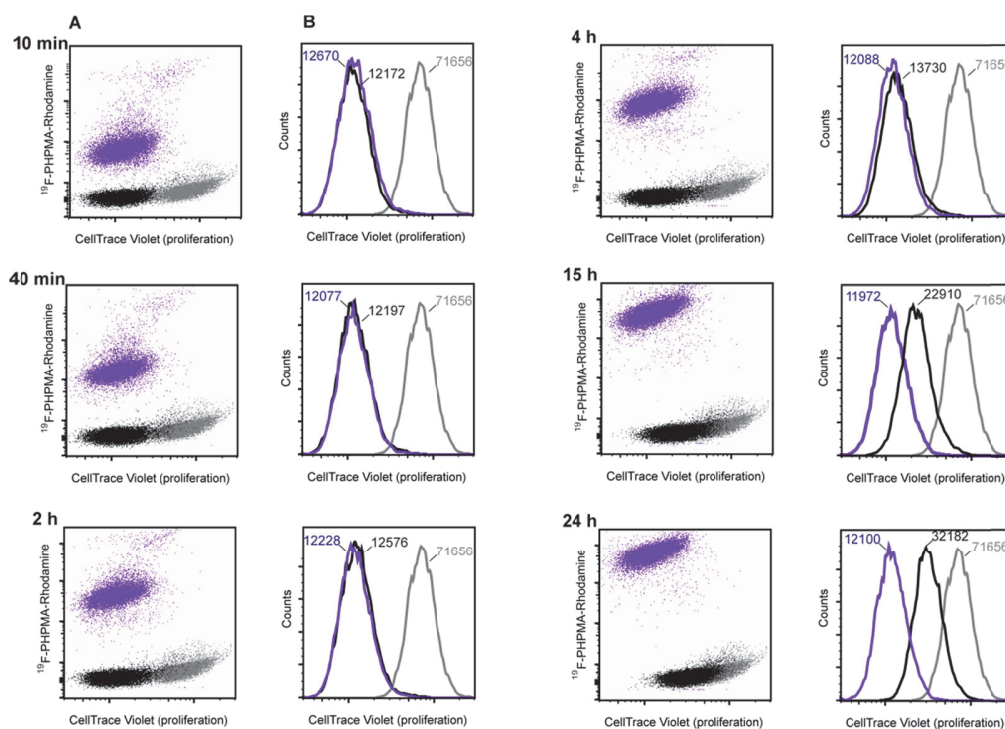
Figure S7. Shift of CellTrace Violet cell fluorescence from the initial (Seeding time, in grey) and the final (End time, in violet) cell fluorescence deriving from cell division during the time frame of the experiment as determined by flow cytometry. Results are represented as both (A) scatter dot plots, which highlights the enhanced ^{19}F-PHPMA-Rhodamine accumulation in cells over time and as (B) histogram plots, which also report the geometric mean fluorescence values.
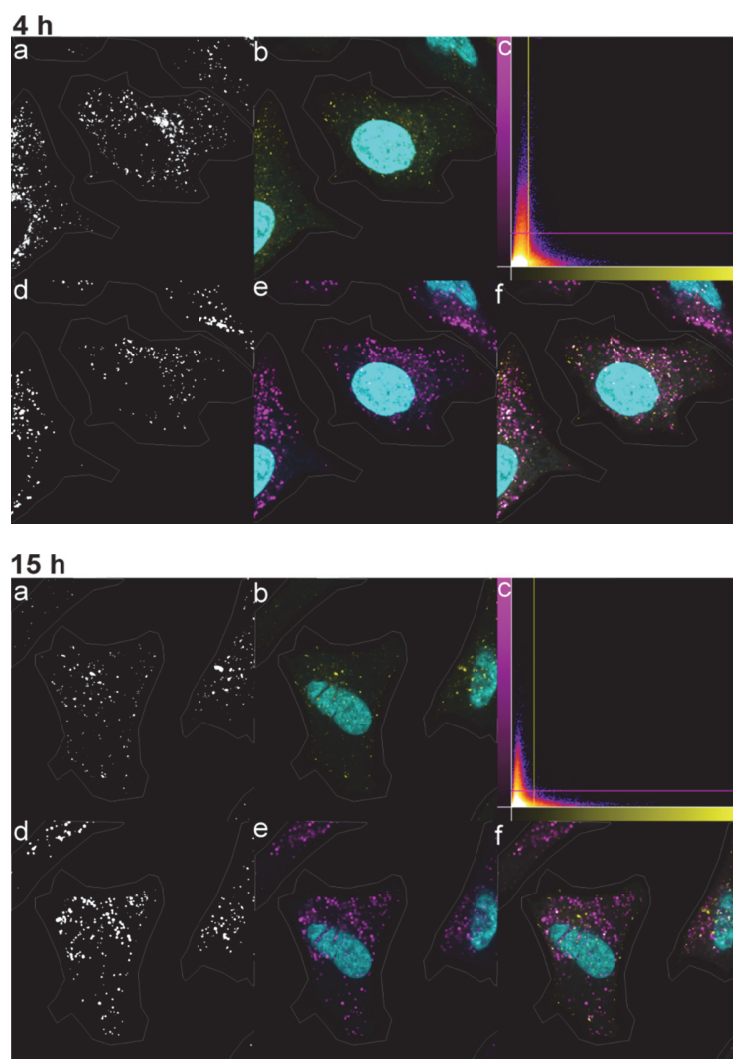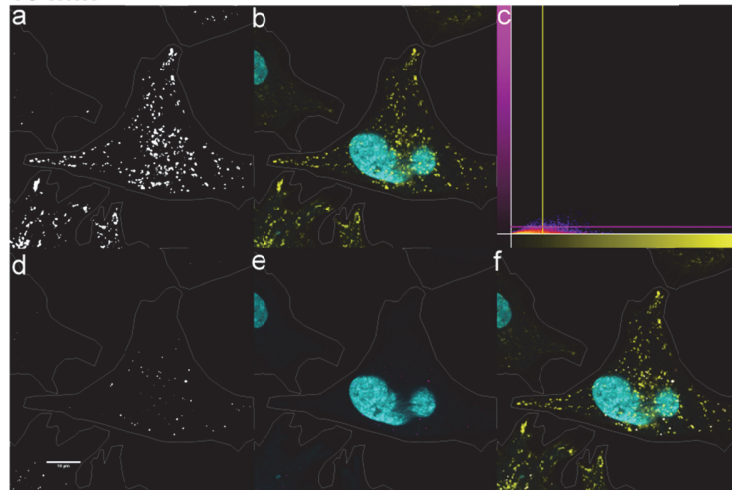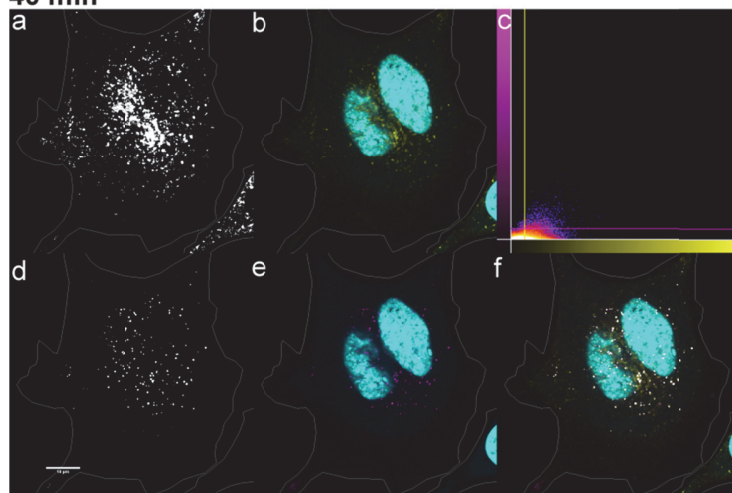
Eearly Endosomes (EE)
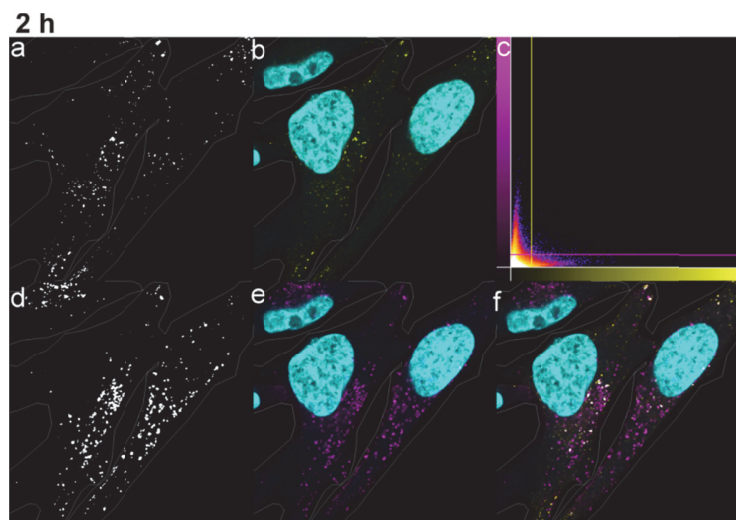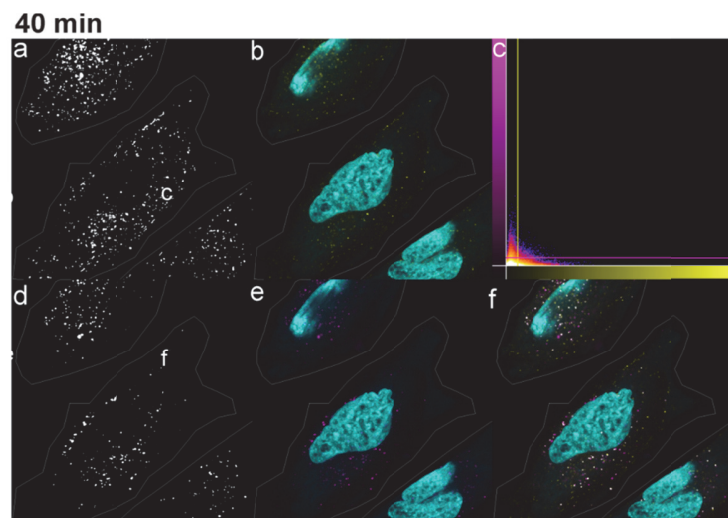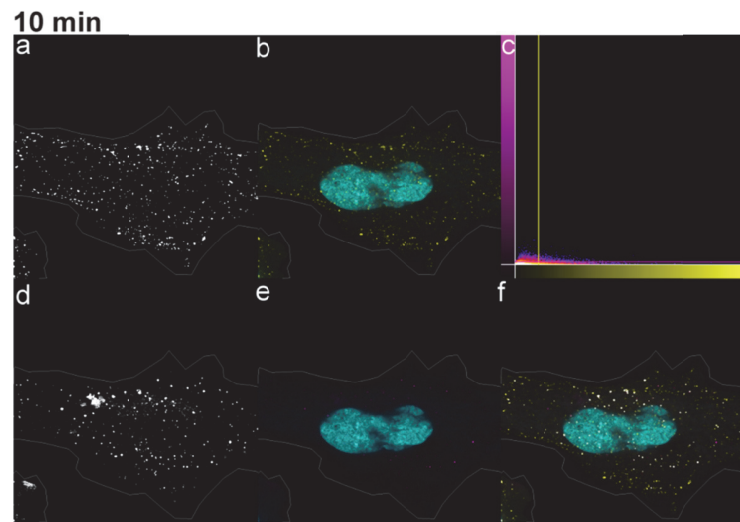
Figure S8. Co-localization studies of ^{19}F-PHPMA-Rhodamine (magenta) with GFP-EE (yellow) for 10 min, 40 min, 2 h, 4 h and 15 h ^{19}F-PHPMA-Rhodamine incubation (0.6 mg/mL) for one single experiment. Representative observations show the threshold images (a and d), corresponding to endosomal vesicles (b, in yellow) and polymer (e, in magenta), represented together with the DAPI channel (b, e and f, in cyan). The merged channels with the "co-localized" pixel (f), as well as the fluorogram (c) are also reported. The contours of the manually drawn ROIs are shown as a white line.
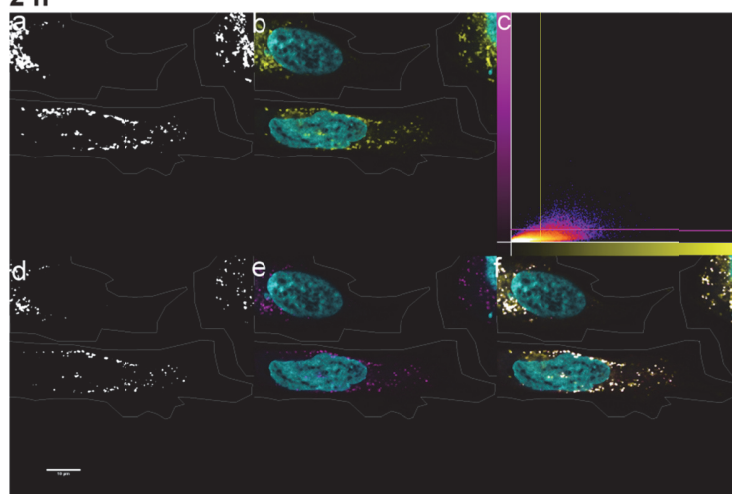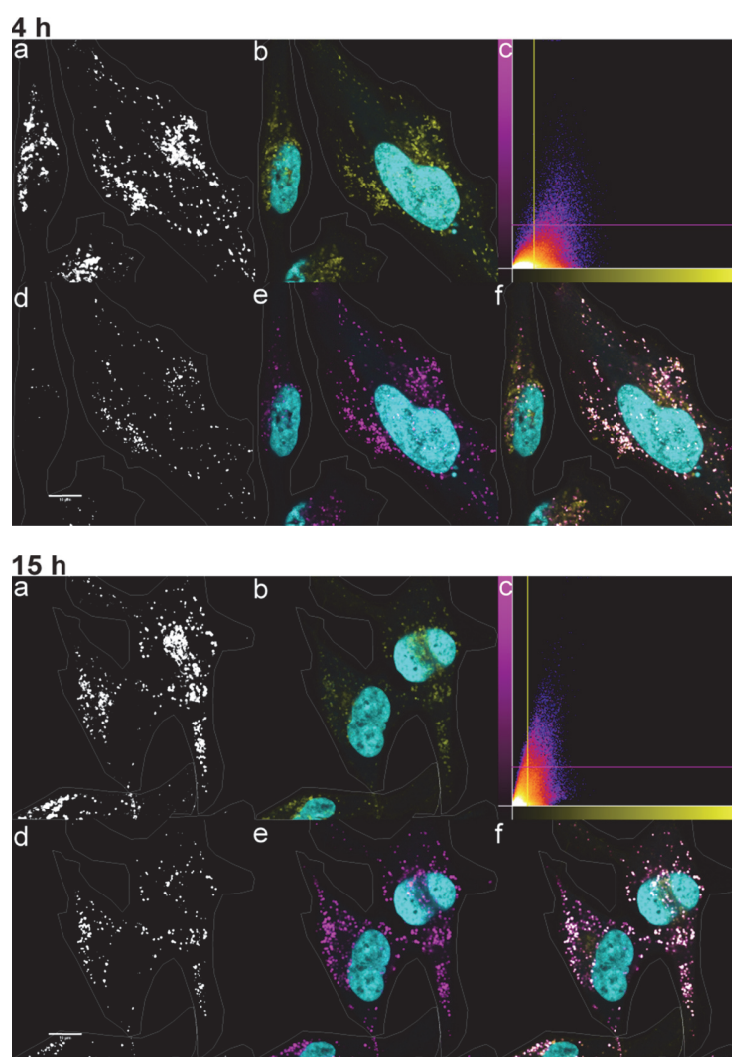
Figure S9. Co-localization studies of ^{19}F-PHPMA-Rhodamine (magenta) with GFP-EE (yellow) for 10 min, 40 min, 2 h, 4 h and 15 h ^{19}F-PHPMA-Rhodamine incubation (0.6 mg/mL) for one single experiment. Representative observations show the threshold images (a and d), corresponding to lysosomal vesicles (b, in yellow) and polymer (e, in magenta), represented together with the DAPI channel (b, e and f, in cyan). The merged channels with the "co-localized" pixel (f), as well as the fluorogram (c) are also reported. The contours of the manually drawn ROIs are shown as a white line.
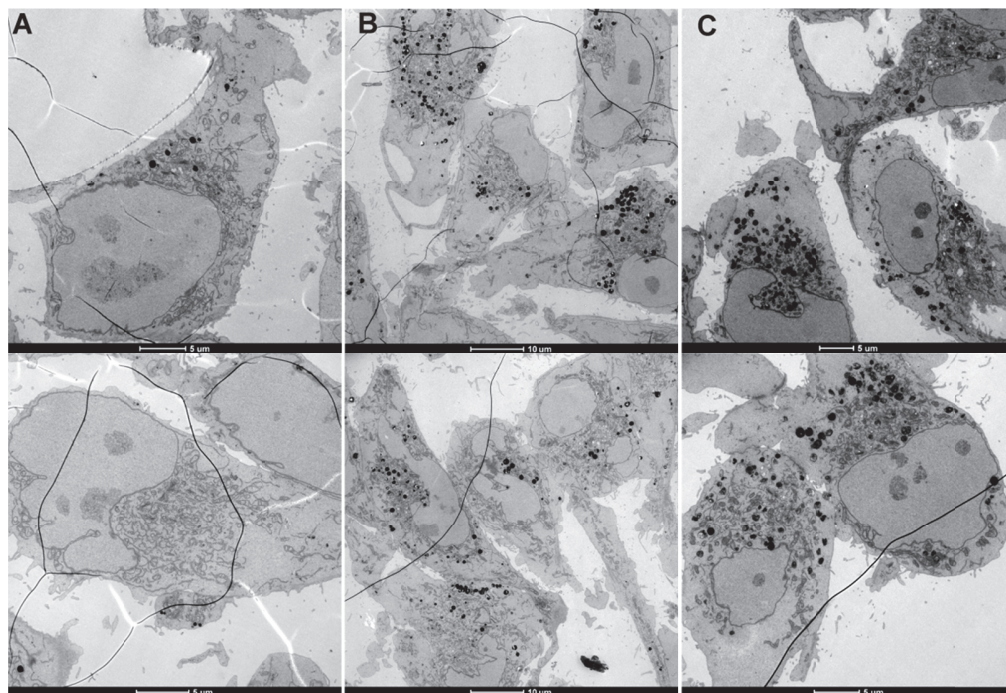
Figure S10. Representative TEM images of (A) control cells, as well as cells incubated for (B) 4 h and (C) 15 h with ^{19}F-PHPMA-Rhodamine.
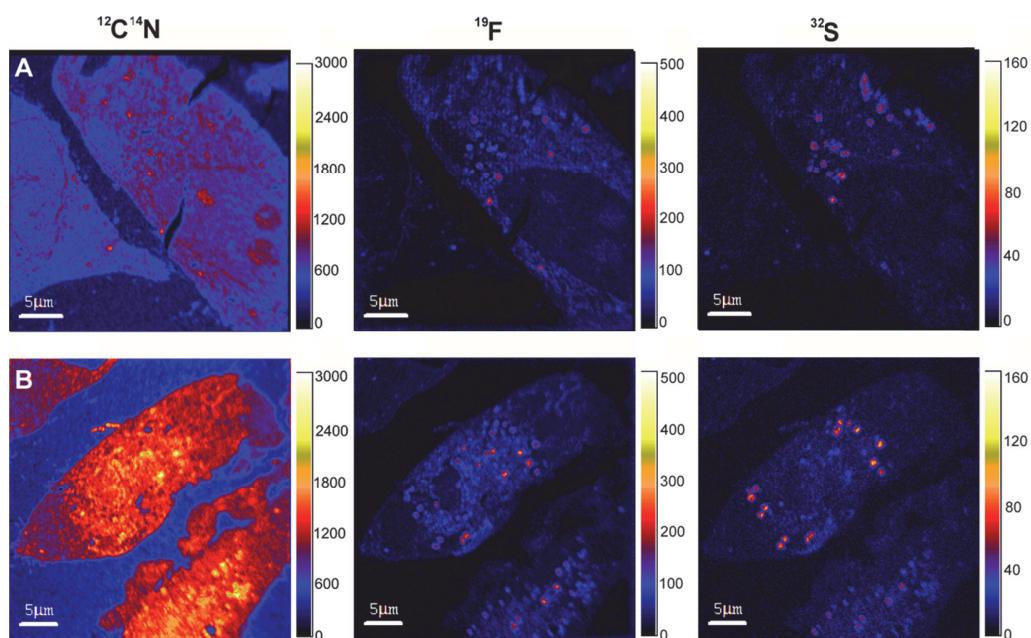

Figure S11. Secondary ion maps of ^{14}N^{12}C$^-$, ^{19}F$^-$ and ^{32}S$^-$ in Hela cells treated with 0.6 mg/mL ^{19}F-PHPMA-Rhodamine for (A) 4 hours and (B) 15 hours.

5. Conclusions and Perspectives

Polymer nanomedicine is a rapidly expanding field that has found application in the treatment of cancer as well as other diseases. Both the use of controlled radical polymerization techniques as well as the development of new methods and tools to monitor intracellular trafficking and delivery of polymers are essential for the design of more advanced delivery systems. This Thesis described the use of RAFT polymerization for the preparation of dual functional PHPMA polymers that allow to control the intracellular delivery of anticancer drug combinations and to monitor PHPMA intracellular trafficking.

Following an introduction to the field of polymer nanomedicine, which presented the different approaches that have been proposed to control and monitor intracellular polymer-mediated anticancer drug delivery in **Chapter 1**, **Chapter 2** described the preparation of α- and α,ω-fluorinated PPFMA by using CTAs containing a fluorinated label in the R (F-CTA-1) or in both R and Z (F-CTA-2) groups. While the use of F-CTA-1 led to the preparation of α-fluorinated PPFMA and was used to determine the experimental polymer molecular weights as well as transfer constants *via* ^{19}F-NMR studies, the second CTA derivative (F-CTA-2) was used for the preparation of the α,ω-fluorinated PPFMA in order to determine α,ω-end group fidelity. It was demonstrated that the use of F-CTAs for the RAFT polymerization of FPMA does not affect the polymerization behavior therefore suggesting that this is a suitable method for the preparation of α- and α,ω-labeled PPFMA derivatives. The α-fluorinated PPFMA was later used as a precursor polymer for the preparation of PHPMA polymers in **Chapter 3** and **Chapter 4**. This method is not only limited to PPFMA or fluorinated polymers, but can be applied to a wide range of polymers prepared by RAFT polymerization. Insertion of the fluorinated labels at the polymer α- and ω-end groups can be used as a general method to study CTA consumption as well as end group fidelity during the polymerization process *via* ^{19}F-NMR studies.

In **Chapter 3**, post-polymerization modification of the precursor PPFMA led to the preparation of a dual-functional PHPMA conjugate for the endolysosomal release of the anticancer drug doxorubicin (Dox) and the third generation P-gp inhibitor zosuquidar (Zos) by using two orthogonal cleavable linkers. First, PHPMA conjugates bearing a Zos derivative connected to the polymer carrier *via* a hydrazone linker was tested. *In vitro*

activity studies using both resistant A2780ADR and sensitive A2780 ovarian carcinoma cells revealed that this is an effective polymeric system to overcome Dox efflux in resistant ovarian cancer cells. The second part of this work investigated the activity of the dual delivery system in which both drugs were conjugated to the PHPMA *via* orthogonal cleavable linkers. *In vitro* activity studies of two different conjugates containing either the anticancer drug Dox alone (PHPMA-Dox) or in combination with Zos (PHPMA-Dox-Zos) demonstrated that the presence of the two drugs attached to the polymer backbone *via* orthogonal cleavable linkers can enhance P-gp inhibition and therefore Dox cytotoxicity in the resistant cancer cells.

In **Chapter 4**, post-polymerization modification of the α-fluorinated PPFMA prepared in **Chapter 1** allowed the synthesis of a dual-labeled PHPMA conjugate containing the fluorinated label as well as a fluorescent dye in the polymer end groups. While the fluorescent label allowed to study polymer uptake and intracellular trafficking using fluorescence-based techniques, the fluorinated label was used for NanoSIMS studies. Both flow cytometry and confocal microscopy suggested a very rapid PHPMA cellular uptake upon cell exposure to the polymer solution. The investigation of cell proliferation during the time-frame of the experiment revealed that the apparent polymer uptake saturation after long incubation time derives from division of the internalized polymer between daughter cells. Co-localization studies with endosomal and lysosomal vesicles expressing GFP confirmed the early endosomal trafficking of the PHPMA and the final accumulation of the polymer in the cell lysosomes. Preponderant polymer localization in the cell lysosomes was observed after 2 hours incubation and longer exposure of the cells to the polymer solution resulted in an increase amount of lysosomal vesicles involved in the process. The last part of this Chapter demonstrated the feasibility of using NanoSIMS to map the subcellular distribution of the fluorinated PHPMA. Combination with TEM confirmed the correlation of polymer-associated fluorine signals with sulfur rich lysosomal vesicles and demonstrated the potential of this method to map the subcellular polymer distribution with several cell compartments simultaneously.

NanoSIMS and its combination with TEM was found a very promising approach to monitor PHPMA intracellular trafficking. However, this proof-of-concept study represents only a first step toward the implementation of this technique in the field of polymer nanomedicine. First, the screening of different nonessential elements and isotope-labelled PHPMA, the investigation of time-dependent polymer trafficking and quantitative analysis are necessary to fully estimate the potential of this technique.

Second, the use of this technique to monitor not only intracellular trafficking, but also intracellular drug release should be considered. The approach presented in this Thesis offered the opportunity to prepare precursor PPFMA polymers containing labels at the polymer end groups, while at the same time preserving polymer side chains for further modification to PHPMA-anticancer drug conjugates. Hence, the use of isotope-labelled drugs would offer the opportunity to track both carrier and drugs at the subcellular level. This would be particularly interesting to investigate delivery systems such that described in **Chapter 3**, in which multiple drugs are linked to the polymer carrier and are designed to be release in a stepwise manner and to interact with different intracellular targets. Analysis *via* both NanoSIMS and TEM would allow to address multiple objectives such as (i) the determination of polymer intracellular trafficking time-frame, (ii) the simultaneous visualization of polymer and drugs in the endolysosomal compartments, (iii) the quantification of drug release kinetics from the polymer carrier as a response to the different endolysosomal environments and (iv) the determination of the ultimate intracellular fate of both carrier and drugs.

Finally, it is worth to emphasize that this approach is not limited to PHPMA-based polymers, but it can be applied to a wide range of polymers of different composition and architecture that are prepared *via* RAFT polymerization. The development of a general method to address the above mentioned objectives is of great impact in the field of polymer nanomedicines since the establishment of techniques and methods able to simultaneously map several intracellular compartments and that allow for quantitative analysis, while avoiding the use of bulky labels are object of constant investigation.

Claudia Battistella

Rue de la Borde 37
1018 Lausanne
Switzerland
+41 78 673 40 12
claudia.battistella@epfl.ch
OrcID 0000-0002-5426-6205

EDUCATION

Jun 2012 – Apr 2017	Ph.D. in Materials Science **Ecole polytechnique fédérale de Lausanne (EPFL), Switzerland**
Oct 2008 – Dec 2010	M.Sc. in Industrial Chemistry **University of Padua, Italy** Final grade: 110/110 cum laude
Oct 2005 – Dec 2008	B.Sc. in Industrial Chemistry **University of Padua, Italy** Final grade: 108/110

EXPERIENCE

Ph.D. Thesis

Title	**Controlling and monitoring Intracellular drug delivery using PHPMA-based polymer nanomedicines**
Supervisor	Prof. Harm-Anton Klok
Description	Design, synthesis and *in-vitro* evaluation of poly(pentafluorophenyl methacrylate) (PPFMA)-derived polymer therapeutics:

- Design, preparation and evaluation of fluorinated chain transfer agents to (i) investigate the RAFT polymerization kinetics of pentafluorphenyl methacrylate *via* ^{19}F-NMR spectroscopy and (ii) to prepare ^{19}F-end labelled polymer therapeutics
- Preparation of poly(*N*-2-(hydroxypropyl)methacrylamide) (PHPMA)-zosuquidar conjugates *via* post-polymerization modification of PPFMA and *in-vitro* evaluation of these conjugates for their ability to reverse multidrug resistance in ovarian carcinoma cells
- Development of a label-free method to monitor uptake and intracellular trafficking of ^{19}F-labelled PHPMA polymer conjugates *via* NanoSIMS-TEM analysis (Collaboration with Prof. Anders Meibom, Laboratory for biological geochemistry, EPFL)

Student supervision	- Fall 2013: Master semester project. Preparation of disulfide linked

PHPMA polymer conjugates *via* post-polymerization modification. Fall 2014: Master semester project. Optimization of the chain end functionalization of PHPMA copolymers with fluorescent moieties

Teaching assistant
- Fall 2013: Bachelor course "Life-science" (Prof. Harm-Anton Klok)

M.Sc. Thesis

Title
Synthesis, characterization and conformational studies of analogues of the peptide antibiotic trichogin GA IV, containing the amino acid *p*F-Phe

Supervisor
Dr. Cristina Peggion – (Laboratory of Prof. Claudio Toniolo)

Description
- Synthesis of trichogin GA IV analogues containing fluorinated labels *via* solid phase peptide synthesis
- Conformational studies using circular dichroism, 2D ^{1}H-NMR, ^{19}F-NMR and FTIR spectroscopy
- Investigation of peptide-phospholipid membranes interaction *via* the liposome leakage assay

Research Experience

May 2011 – Nov 2011
Research Assistant
National Research Council (CNR), Padua, Italy

- Research carried out in the laboratory of Dr. Sergio Tamburini on the grafting of organic moieties on silica surface for the selective sequestration of heavy metals from liquids

Jan 2011 – Apr 2011
Research Assistant
University of Padua, Italy

- Research carried out in the laboratory of Prof. Claudio Toniolo under the supervision of Dr. Cristina Peggion on the optimization of the synthesis of fluorinated trichogin GA IV

PUBLICATIONS

3   **C. Battistella**, H.-A. Klok, "**Controlling and monitoring intracellular delivery of polymer nanomedicines**", *Macromolecular Bioscience*, Accepted

2   **C. Battistella**, H.-A. Klok, "**Reversion of P-gp-mediated drug resistance in ovarian carcinoma cells with PHPMA-zosuquidar conjugates**" Submitted to *Biomacromolecules*

1   C. Peggion, B. Biondi, **C. Battistella**, M. De Zotti, S. Oancea, F. Formaggio and C. Toniolo**, "Spectroscopically labeled peptaibiotics. Synthesis and properties of selected trichogin GA IV analogs bearing a side-chain monofluorinated aromatic amino acid for ^{19}F-NMR analysis**", *Chem. Biodivers.* 2013, 10, 904-919

b

SCIENTIFIC SKILLS

Cell biology skills	Cell culture ● Proliferation and viability assays ● Cell transduction
Cell biology techniques	Optical and fluorescence microscopy ● Confocal laser scanning microscopy (CLSM) ● Flow cytometry
Animal experiments	Introduction to animal experimentation, practical aspects (FELASA category B) –February 2012
	Introductory course in laboratory animal science, theory – June 2012
Synthetic skills	Organic synthesis ● Controlled polymerization and post-polymerization modification techniques ● Solid phase peptide synthesis (SPPS)
Analytical techniques	High pressure liquid chromatography (HPLC) ● Mass spectrometry (MS) ● Nuclear magnetic resonance (NMR) ● Dynamic light scattering (DLS) ● UV-Vis spectroscopy ● Size exclusion chromatography (SEC) ● Fourier transform infrared spectroscopy (FTIR) ● Circular dichroism spectroscopy (CD) ● Electron microscopy
IT skills	ImageJ ● ChemDraw Bio ● MestReNova ● OriginPro ● CorelDRAW ● Endnote ● MS Office ● Flow-Jo

AWARDS

May 2011	**National Research Council (CNR), Padua, Italy**
	● Awarded postgraduate fellowship "**Selective sequestration of heavy metals from industrial processes using functionalized silica**" – Laboratory of Dr. Sergio Tamburini
Jan 2011	**University of Padua, Italy**
	● Awarded postgraduate fellowship "**A bridge between modern spectroscopic techniques and peptide chemistry: application on membrane-active peptides**" – Laboratory of Prof. Claudio Toniolo under the supervision of Dr. Cristina Peggion

LENGUAGES

Italian	Native proficiency
English	Full professional proficiency
French	Limited working proficiency